Durham E-Theses

Analysis of crystal defects by simulation of x-ray section topographs

Holland, Anthony James

How to cite:

Holland, Anthony James (1993) *Analysis of crystal defects by simulation of x-ray section topographs*, Durham theses, Durham University. Available at Durham E-Theses Online: http://etheses.dur.ac.uk/5589/

Use policy

The full-text may be used and/or reproduced, and given to third parties in any format or medium, without prior permission or charge, for personal research or study, educational, or not-for-profit purposes provided that:

- a full bibliographic reference is made to the original source
- a link is made to the metadata record in Durham E-Theses
- the full-text is not changed in any way

The full-text must not be sold in any format or medium without the formal permission of the copyright holders.

Please consult the full Durham E-Theses policy for further details.

Academic Support Office, Durham University, University Office, Old Elvet, Durham DH1 3HP
e-mail: e-theses.admin@dur.ac.uk Tel: +44 0191 334 6107
http://etheses.dur.ac.uk

Analysis of Crystal Defects by Simulation of X-ray Section Topographs

Anthony James Holland, B.Sc., M.Sc. (Dunelm)

A thesis submitted to the University of Durham in candidature for the degree of Doctor of Philosophy

April 1, 1993

The copyright of this thesis rests with the author.
No quotation from it should be published without
his prior written consent and information derived
from it should be acknowledged.

- 5 MAY 1993

Abstract

This thesis is concerned with the simulation of the contrast in X-ray section topographs due to the strains induced in silicon single crystals by various types of technologically relevant crystal defect. A general introduction to the field of X-ray topography is presented, illustrating that this technique is well suited to the characterisation of defect induced strain in highly perfect crystals. A review of X-ray dynamical theory is given, culminating in Takagi's equations for a crystal containing a defect. Techniques for simulating X-ray section topographs, based on Takagi's equations, are discussed. Computer simulation of section topographs has been used throughout this work to deduce the microscopic strains from the X-ray topographic images.

The volume of oxygen precipitates in MCZ silicon was found to increase linearly as lnT, where T is the annealing temperature of the sample. Results suggest that the vast majority of precipitates which survive to maturity are nucleated at approximately the same time, subsequently growing at the same rate. An industrial role for simulation in conjunction with experiment is proposed, in the evaluation of the precipitate depth and the deformation parameter, C, representing the precipitate strain magnitude. The technological relevance of these two quantities is discussed. The effect of surface relaxation on the structure of images due to precipitates has been investigated. The critical depth z_{crit} at which the effect of surface relaxation became negligible was found to increase linearly with lnC. Simulations have been generated for crystals containing oxygen precipitate distributions, with denuded zones. Characteristic image features have been discussed. Studies on precipitate resolvability revealed that the critical separation for two precipitates to be just resolved increases linearly as lnC.

An extensive study of intrinsic gettering has been undertaken, in terms of decorated dislocations. The strain distribution due to precipitate decoration was modelled by the *cylindrical inclusion* model. It was shown that even for very low precipitate strains, precipitate decoration is distinguishable from the associated dislocation by section topography. Hence, an industrial role is proposed for simulation, in conjunction with experiment, in the parameterisation of the strain induced by decorated dislocations. To fully explore the use of the cylindrical inclusion model in this way, the variation in the inclusion strain magnitude was determined as a function of the precipitate strain and density, and the size of the precipitate distribution. It was found that the strain magnitude of the equivalent cylindrical inclusion must increase more rapidly relative to the precipitate deformation parameter for low-order reflections than for high-order reflections. Decorated dislocations have been shown to be resolvable by section topography even in the most dislocation-rich silicon samples. The industrial usefulness of this characteristic is discussed. A study was made of the critical deformation parameter, C_{crit}, for decorated dislocations to be just resolved, as a function of the separation, κ, of the dislocations. For κ greater than about $45\mu m$, the variation of $ln(C_{crit})$ with κ was linear. For smaller separations, the linearity breaks down because of the increasingly important strain contribution

due to the dislocations.

The strains induced by oxide films and devices in the silicon substrates onto which they are formed have been investigated. Experimental section topographs of oxide edge regions and devices on silicon have been simulated, and the visibility of the *extra* set of fringes found in simulations by another worker has been examined. The variation in image strucure with device position on the entrance and exit surfaces has been investigated. An absolute minimum on device width detectable by section topography of $1\mu m$ has been found. However, this minimum was found to depend on device-induced strain, and for values of strain characteristic of contemporary devices, the minimum detectable device width was found to be at least $3.5\mu m$. This is above the limits set by the geometric and other constraints of the experimental technique. A thorough study has been made of the cancellation of opposing strains due to opposite edges of a device. The total distortion induced by the device was found to be minimised by reducing the device width and increasing the force per unit length, S, along the device edges. Quantitative information has been obtained on this process. It was found that the fractional increase in lattice parameter at a fixed point, due to device-induced strain, increases linearly with S, with increasing gradient for increasing device width. It was shown that the narrower the device, the faster the relative fall-off in fractional increase in lattice parameter with increasing displacement from one edge of the device.

Dedicated to my parents

Acknowledgements

I would like to acknowledge financial support for this project from the Science and Engineering Research Council and Bede Scientific Instruments, through a C.A.S.E. studentship. I am grateful to Professor A. W. Wolfendale and Professor A. D. Martin for the provision of the facilities at Durham University Physics Department.

I would like to thank my supervisors, Professor B. K. Tanner and Dr. G. S. Green, for their enthousiastic support and for many useful discussions. In addition, I am indebted to Dr. S. Cottrell for his assistance and advice on computational aspects of this work. I am grateful to Professor Z. H. Mai, Dr. R. Matyi, Dr. S. Halder and Dr. W. Spirkl, for interesting and productive conversations on the subject of X-ray topography.

The advice and assistance of the technical and secretarial staff of Durham University Physics Department is gratefully acknowledged. In particular, I would like to thank Miss V. Greener and Mrs. P. A. Russell for the preparation of photographs and diagrams, respectively. I also thank my colleagues in the Solid State Physics Group at Durham University, Mr. C. M. Friend, Mr. C. I. Gregory, Mr. J. Hudson, Mr. R. Luscombe and Mr. S. M. Westwood, for contributing to a friendly and relaxed working environment.

Finally, I would like to thank my parents for their constant support and encouragement.

Declaration

I declare that the work contained in this thesis has not been submitted for a degree at this University or any other. All the work presented herein was conducted by the author, unless stated otherwise.

A.J. Holland

April, 1993.

Copyright © 1993 by Anthony James Holland.

The copyright of this thesis rests with the author. No quotation from it should be published without the author's prior written consent. Information derived from this thesis should be acknowledged.

Publications

Part of the work presented in Chapter 4 has been published as:

A. J. Holland, G. S. Green, B. K. Tanner and Z. H. Mai, (1991), Mat. Res. Soc. Symp. Proc., **209**, 475.

Part of the work presented in Chapter 6 is to be published:

A. J. Holland and B. K. Tanner, J. Phys. D, in press.

Contents

1 Introduction to X-ray Diffraction Topography **1**

1.1 Background and Relevance of Topography 1

1.2 Underlying Physical Processes 1

1.3 Experimental Techniques 3

1.4 Industrial Applications 7

2 Dynamical Theories of X-ray Diffraction in Crystals **10**

2.1 Introduction and Motivation for Dynamical Theory 10

2.2 Dynamical Theory for a Perfect Crystal 12

2.2.1 Development of the Fundamental Equations 12

2.2.2 The Dispersion Surface 14

2.2.3 Anomalous Transmission 15

2.2.4 The Pendellösung Effect 16

2.3 Takagi's Theory for an Imperfect Crystal 18

2.3.1 Background and Basic Postulates 18

2.3.2 The Electron Case 21

2.3.3 The X-ray Case 22

2.3.4 General Formulation of the Diffraction Equations 23

3 Simulation of X-ray Topographs **24**

3.1 Background and Motivation 24

3.2 Derivation of the Iterative Algorithm 25

3.3 Integration of Takagi's Equations 27

3.4 Simulation of Real Topographs 28

4 Investigation of the Strain Effects Associated with Oxygen Precipitates in Silicon **30**

4.1 Formation and Growth of Precipitates 30

4.2 Simulation Code for a Precipitate 34
4.3 Simulation of Experimental Section Topographs due to Oxygen Precipitates in MCZ Silicon 37
4.3.1 Introduction 37
4.3.2 Results 37
4.3.3 Discussion 39
4.4 Investigation of the Effect of Surface Relaxation on Precipitate Images 41
4.5 Investigation of the Effect of Crystal Curvature on Precipitate Images 41
4.5.1 Introduction 41
4.5.2 Results 42
4.5.3 Discussion 42
4.6 Image Structure due to a Crystal with Denuded Zones 43
4.7 Resolvability of Precipitates as a Function of Strain 44
4.8 General Discussion and Industrial Implications 45

5 Intrinsic Gettering of Transition Metal Impurities at Dislocations in Silicon 47

5.1 Background and Context 47
5.1.1 Introduction 47
5.1.2 Statement of Approach 50
5.2 Development of the Strain Code for a Cylindrical Inclusion 50
5.2.1 Strain Equations for a Cylindrical Inclusion 50
5.2.2 Transformation of Coordinates from Experimental System to Inclusion System 51
5.2.3 Derivation of Takagi's Differential Expression 53
5.2.4 Derivation of Inclusion Orientation 55
5.2.5 Boundary Conditions of the Inclusion 56
5.2.6 Lattice Mismatch Parameter 57
5.2.7 Expressing the Equations in Computer Code 58
5.3 Comparison Between Corresponding Dislocation and Cylindrical Inclusion Images 58
5.3.1 Preliminary Comments 58
5.3.2 $\bar{1}31$ Reflection 59
5.3.3 $\bar{4}40$ Reflection 60
5.3.4 $3\bar{3}\bar{3}$ Reflection 61

5.4 Development of the Strain Code for a Cylindrical Distribution of Precipitates 62
5.4.1 Statement of Problem 62
5.4.2 Derivation of the Transformation Equations 63
5.4.3 Construction of the Strain Code 64
5.5 Variation of Cylindrical Inclusion Strain as a Function of Precipitate Strain 64
5.5.1 Statement of Approach 64
5.5.2 Edge Dislocation Results 65
5.5.3 60° and Screw Dislocation Results 67
5.5.4 Discussion 67
5.6 Variation of Strain with Precipitate Density 70
5.7 Variation of Strain with Radius of Precipitate Distribution 72
5.8 Reversal of the Strain Associated with a Cylindrical Inclusion 73
5.9 Resolvability of Two Decorated Dislocations as a Function of Strain . 74
5.9.1 Introduction 74
5.9.2 Results 74
5.9.3 Discussion 75
5.10 General Discussion and Industrial Implications 76

6 Investigation of Device-Induced Strain in Silicon Substrates 79
6.1 Background and Context 79
6.1.1 Technological Motivation 79
6.1.2 Blech and Meieran's Strain Equations 80
6.2 Transformation of the Strain Equations into Computer Code 83
6.2.1 Extension of Kato and Patel's Treatment 84
6.2.2 Development of the Strain Code 85
6.3 Simulation of Experimental Images due to Oxide Film Edges 86
6.3.1 Introduction 86
6.3.2 Results 87
6.3.3 Discussion 88
6.4 Simulation of Images due to a Device on a Silicon Substrate 89
6.4.1 Introduction 89
6.4.2 Results 89
6.4.3 Convergence Criteria 90
6.4.4 Conclusions 91

6.5 Image Structure for Devices on the Entrance and Exit Surfaces 92
6.5.1 Statement of Method 92
6.5.2 Position (a) 92
6.5.3 Position (b) 92
6.5.4 Position (c) 92
6.5.5 Position (d) 93
6.5.6 Position (e) 93
6.5.7 Position (f) 93
6.6 Distinguishability of Devices in X-ray Section Topography 93
6.6.1 Introduction 93
6.6.2 Results 94
6.6.3 Discussion 95
6.7 Variation in Lattice Distortion with Device-Induced Strain 95
6.7.1 Introduction 95
6.7.2 Results 96
6.7.3 Increase in Substrate Lattice Parameter with Device-Induced Strain 99
6.8 General Discussion and Industrial Implications 102

7 Conclusions 104

Appendix A 110

Appendix B 111

Appendix C 112

Appendix D 113

Appendix E 114

Appendix F 115

Appendix G 116

Appendix H 117

Appendix I 118

Appendix J 119

Appendix K 120

Appendix L 121

Bibliography 122

Chapter 1

Introduction to X-ray Diffraction Topography

1.1 Background and Relevance of Topography

X-ray Diffraction Topography is a well established tool in the analysis of microscopic defects in crystals, and in the analysis of 3-5 lasers and 2-6 IR detectors. The technique is of direct relevance to the semiconductor industry, because of its applications to quality control in wafer manufacture.

X-ray topography is, as will be shown later, closely related on a fundamental level to the technique of transmission electron microscopy. However, X-ray topography has the advantage of being a non-destructive technique, so that it can be used many times on the same sample, without damaging that sample. In addition, X-ray topography can be used to visualise a much larger volume of crystal than is possible using the electron technique. Finally, X-ray methods are much more sensitive to microscopic strains in crystals, and this confirms X-ray topography in a very specific niche for the characterisation of crystal defects.

1.2 Underlying Physical Processes

The images due to defects, found in topographs, result from two fundamental processes. These are *orientation contrast* and *extinction contrast*.

Consider a beam of monochromatic X-radiation incident upon a crystal, Fig. 1.1. The intensity diffracted from the crystal is allowed to fall onto a photographic film, giving a topograph. Now, suppose the crystal contains a region in which the lattice planes are misoriented relative to the rest of the bulk, Fig. 1.1(a). If the Bragg condition is satisfied throughout the rest of the crystal, then it cannot simultaneously be satisfied in the misoriented region. Consequently, there will be a part of the recording film which will show no intensity, due to null diffraction from the misoriented region, and this is known as *orientation contrast*.

Orientation contrast may also be observed if the same crystal is subject to poly-

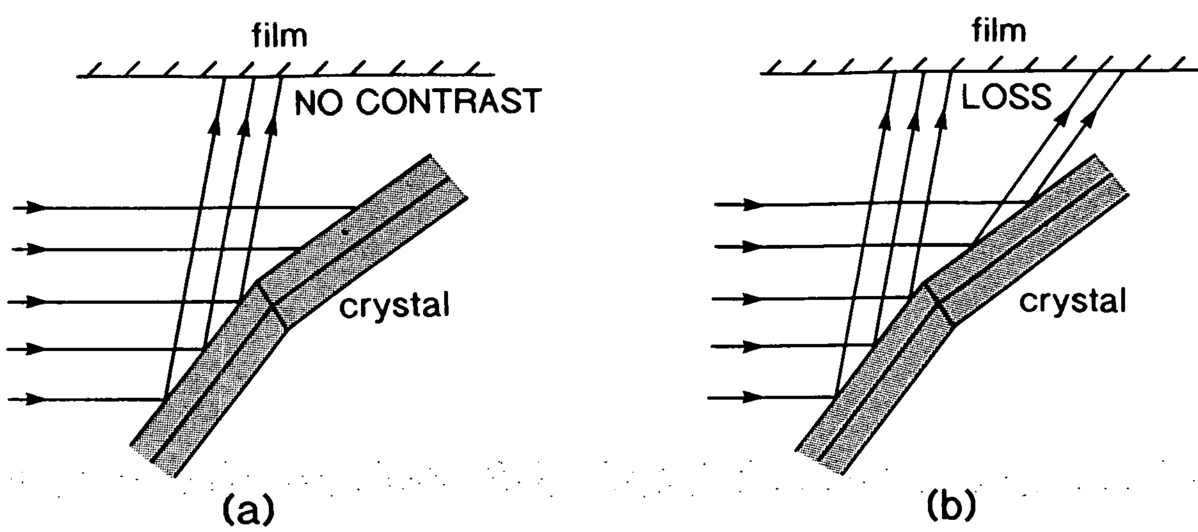

Fig. 1.1: Orientation contrast from a monochromatic, collimated X-ray beam, (after Tanner).

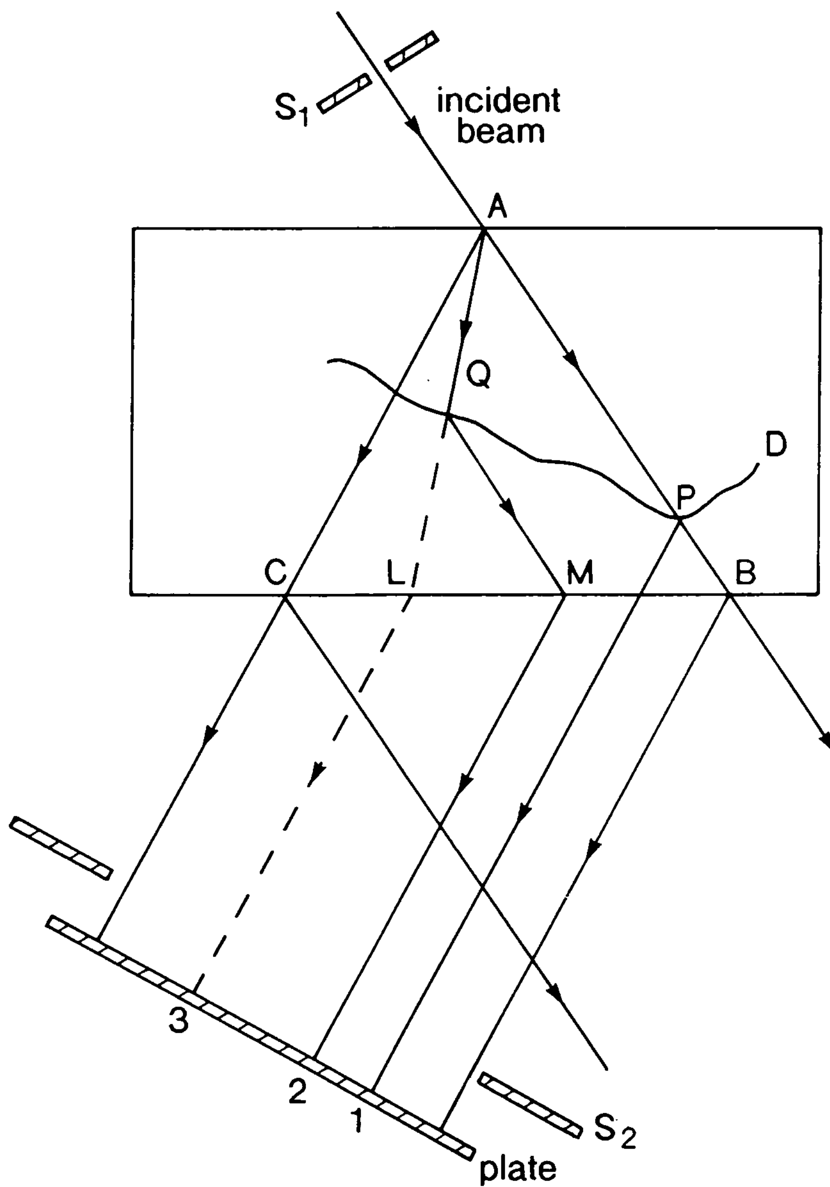

Fig. 1.2: Image structure due to a dislocation in transmission geometry, (after Authier).

chromatic radiation, Fig. 1.1(b). In this case, radiation of different wavelengths will diffract from the two regions at different angles. Hence, the photographic film will show an area of reduced or enhanced contrast, corresponding to the discontinuous interface between the two regions.

Orientation contrast results from the presence of discontinuous misorientations of sets of lattice planes. *Extinction contrast* results from the elastic distortion of the crystal lattice around a defect. The diffraction conditions in the vicinity of the defect are different from those in the rest of the crystal. So, the intensity scattered from the defect region is different from that scattered by the rest of the crystal, and this shows up on the photographic film.

Let us now consider the structure of the image in a topograph corresponding to a specific type of defect, the dislocation. The image can be thought of as having three parts; the *direct image*, *intermediary image* and *dynamical image*. These three images are formed by distinct, characteristic processes, which are described in detail by Authier [1].

Consider Fig. 1.2. The figure shows an X-ray beam, collimated by slit S_1, striking the crystal surface at point A. The direct beam is attenuated very slightly as it undergoes diffraction at each successive Bragg plane. The diffracted waves collectively form the diffracted beam, which is allowed to fall onto the photographic film via slit S_2.

The direct beam intersects the dislocation at point P, where the lattice planes are distorted because of the defect. Lattice planes which would not satisfy the Bragg condition in the perfect crystal are able to do so in the distorted region around the defect. The high-intensity direct beam is diffracted strongly and strikes the photographic film at point 1. The result is a localised dark spot at position 1, and this spot is known as the *direct image*.

The defect disturbs the flow of energy in the so-called *Borrmann fan*, ABC, and this causes a reduced intensity of radiation to propagate along direction QL, for example. The effect of this redistribution of energy across the Borrmann fan causes a shadow of low-intensity to fall onto the film around position 3. This is manifest as a bright region around position 3, known as the *dynamical image*.

When wavefields strike the dislocation, new wavefields are created and propagate along line QM, for example. Such wavefields interfere with existing wavefields, and the result is a set of bright and dark fringes around position 2 on the film. These interference fringes form the *intermediary image*.

The direct, intermediary and dynamical images collectively form the defect image. The defect image is seen, on a topograph, superimposed on a background of alternate bright and dark, parallel, vertical bands, known as the *Pendellösung fringes*. The mechanism of formation of these fringes can be understood in terms of *dynamical theory*, which will be presented in the following chapter.

1.3 Experimental Techniques

Next, we will investigate the means by which topographs are obtained experimentally. Several thorough reviews have been presented [2,3,4].

In order to obtain a topograph, a sample is subject to an X-ray beam, and the resulting diffracted beam is allowed to fall onto a recording medium, usually photographic film. This can be done in one of two ways, illustrated in Fig. 1.3, which describes one of the early techniques called the *Berg-Barrett method* [5], which still finds extensive application.

In Fig. 1.3(a), the Bragg planes are oriented so that the beam is diffracted away from the crystal, and therefore only interacts with the surface layer. This is called the reflection (Bragg) geometry. In Fig. 1.3(b), the diffracted beam passes through the crystal and is allowed to fall onto a photographic film, via a slit which blocks the primary transmitted beam. This is called the transmission (Laue) geometry.

In both cases, the diffracted beam is allowed to fall onto a photographic film, to generate a topograph. The reflection geometry is useful in the study of surface effects, whilst the transmission geometry allows the experimenter to probe the structure of the bulk. The work presented in this thesis is associated exclusively with the transmission geometry.

The foremost laboratory technique, developed by Lang in the late 1950's, is illustrated in Fig. 1.4. The *Lang technique* is desirable because of its high sensitivity to both orientation and extinction contrast. It is common practice to use K_α radiation to obtain topographs. This *line* is in fact a closely spaced doublet, and so the beam is collimated so as to diffract only the stronger K_{α_1} line. Hence, the problem of double-imaging is avoided.

First of all, let us disregard the arrows of Fig. 1.4. A narrow, collimated beam of radiation is allowed to fall onto the crystal and undergoes diffraction from the Bragg planes indicated schematically in the figure. The diffracted beam emerges from the crystal and is filtered through a slit which blocks the primary transmitted beam, before falling onto the photographic film. The image so recorded is a *section topograph* [6].

If the crystal and film are traversed together across the incident beam, indicated by arrows in Fig. 1.4, then a *projection topograph* is obtained [7,8]. This topograph represents a *projection* of the entire crystal.

Kato and Lang [9] used section and projection topography to study the Pendellösung fringes in topographs of wedge-shaped crystals. They used measurements of the fringe spacings to calculate the structure amplitudes of the reflections. The section and projection methods have been discussed by Lang [10], where he assesses the relative merits of each.

One important advantage of section topography is that it can be used to locate the position of a defect in a crystal. Consider Fig. 1.5. The narrow incident beam strikes the defect at point I. The direct image of this point lies at I′ on the film. Hence, the ratio of lengths A′I′/A′B′ is equal to AI/AB. Thus, if the crystal thickness

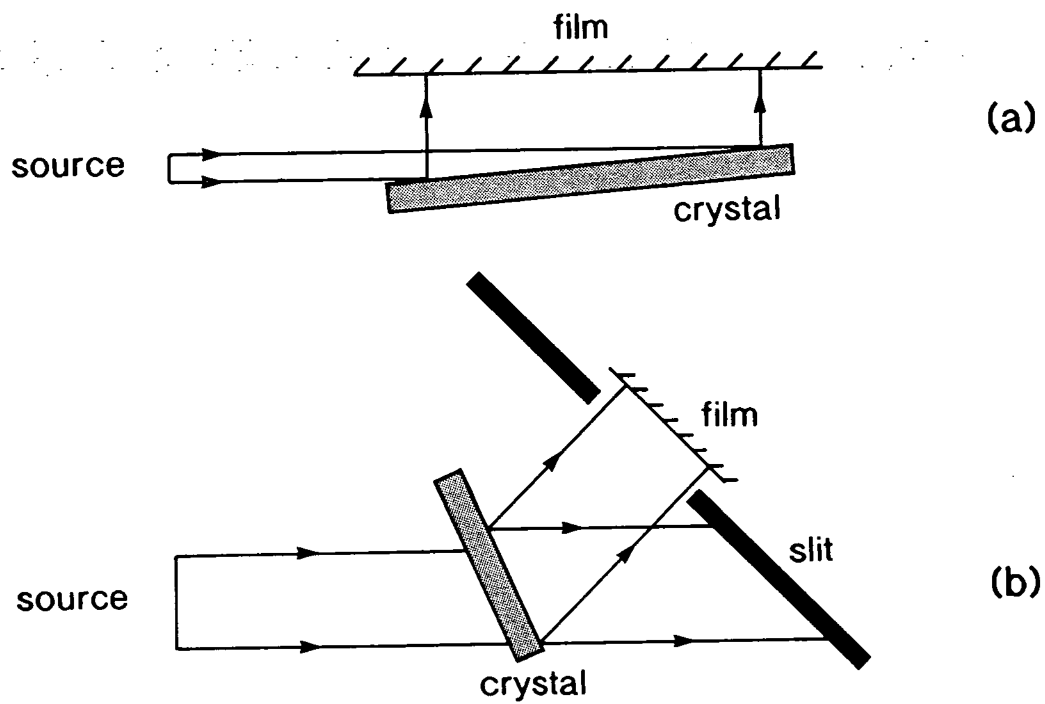

Fig. 1.3: The Berg-Barrett method, (after Tanner).
(a) reflection (Bragg) geometry.
(b) transmission (Laue) geometry.

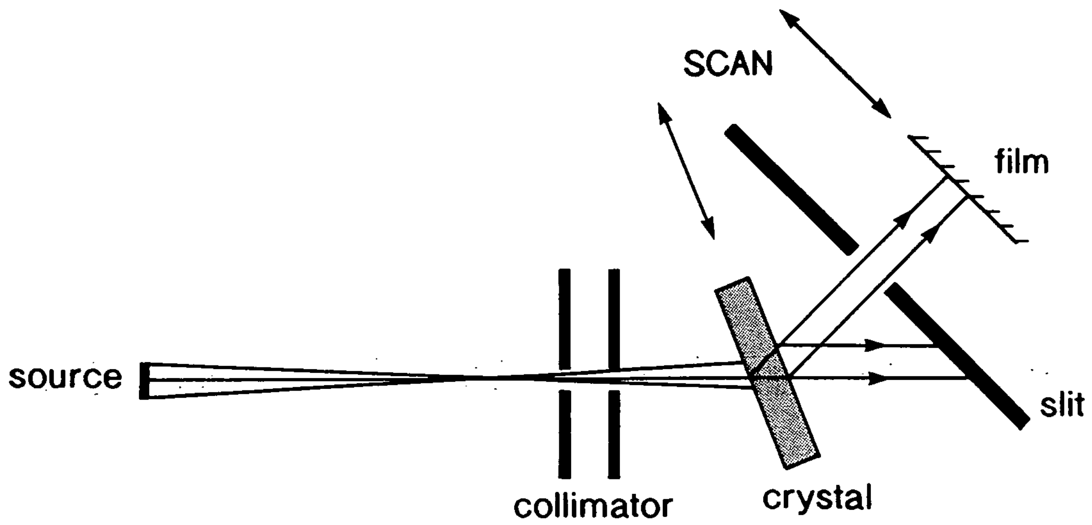

Fig. 1.4: Lang's transmission technique (after Tanner).

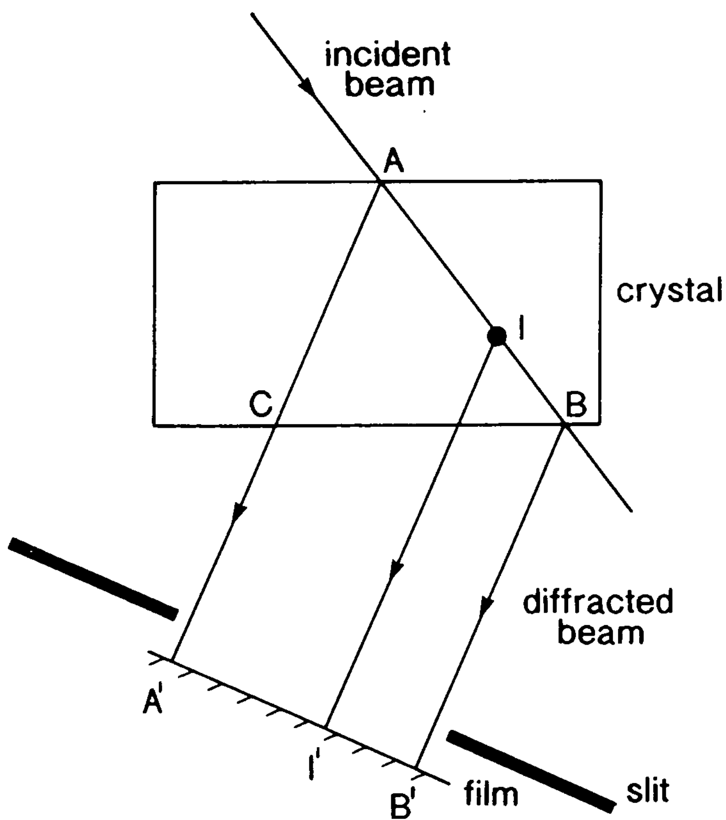

Fig. 1.5: Use of section topography to determine the depth of a defect.

and angle of incidence are known, the depth of the defect can be calculated. It is important that the incident beam should be as narrow as possible, in order to maximise the accuracy of determination of depth by this method.

The main advantage of projection topography is that one can image a dislocation, for example, across the whole of its length. However, defects at different depths will give rise to overlapping images on the topograph, and this hinders the extraction of useful information from the topograph. The experimenter would preferentially use section topography when the defect density is too high to allow the resolution of individual defects by the projection technique.

The contrast of individual dislocations on projection topographs is not as high as on section topographs. However, the diffraction conditions can be fixed so that the defect image is still distinguishable from the background. The source slits of the incident beam for projection topography need not be as small as for section topography. So, even though the length of specimen scanned is longer in the projection case, the time taken may not be significantly greater.

A variant of projection topography is the *limited projection topograph* [11], illustrated in Fig. 1.6. Only a part of the diffracted beam is allowed to fall on the film. In the simple case of Fig. 1.6, only those defects between depths d_1 and d_2 will be imaged. This is useful in the case of crystals which are surface-damaged, with interesting defect distributions beneath the damaged layer. In addition, by examining a sample layer by layer, it is possible to resolve defect images which would be hopelessly overlapped in a standard projection topograph. In using this method, it is crucial to arrange a very narrow incident beam, in order to ensure good resolution of sampling depth.

Both section and the equivalent of projection topography can be undertaken using the *double crystal method* [12,13], illustrated in Fig. 1.7. Here, the direct beam undergoes diffraction from a perfect reference crystal, and the resulting diffracted beam is then allowed to fall onto the sample crystal. For highest strain sensitivity, it is necessary that the lattice planes in the two crystals are parallel and equally spaced. It is often found desirable to arrange for the reference crystal to be cut so that the Bragg planes are inclined to the crystal surface, Fig. 1.7. In this way, it is possible to obtain a diffracted beam from the reference crystal of much greater width than the original direct beam. This, in turn, allows a larger volume of sample to be investigated.

The beam diffracted by the sample will be of appreciable intensity only if the Bragg condition is fulfilled simultaneously by both crystals. Suppose the sample is rotated or *rocked* slightly, relative to the reference crystal. Then the intensity, I, of the final diffracted beam falls off rapidly with angular deviation, $\Delta\theta$, from the exact Bragg condition. Plots of I against $\Delta\theta$ are called *rocking curves*, and the rocking curve for the double crystal arrangement is very sharp, Fig. 1.7. The reference crystal is assumed to be perfect, so that any changes in diffracted intensity are due to lattice imperfections in the sample. Because of the rapid variation of I with $\Delta\theta$, the double crystal method is much more sensitive to small variations in lattice parameter than either section or projection topography. The high accuracy of the double crystal method was utilised as long ago as 1926 [14], to study the

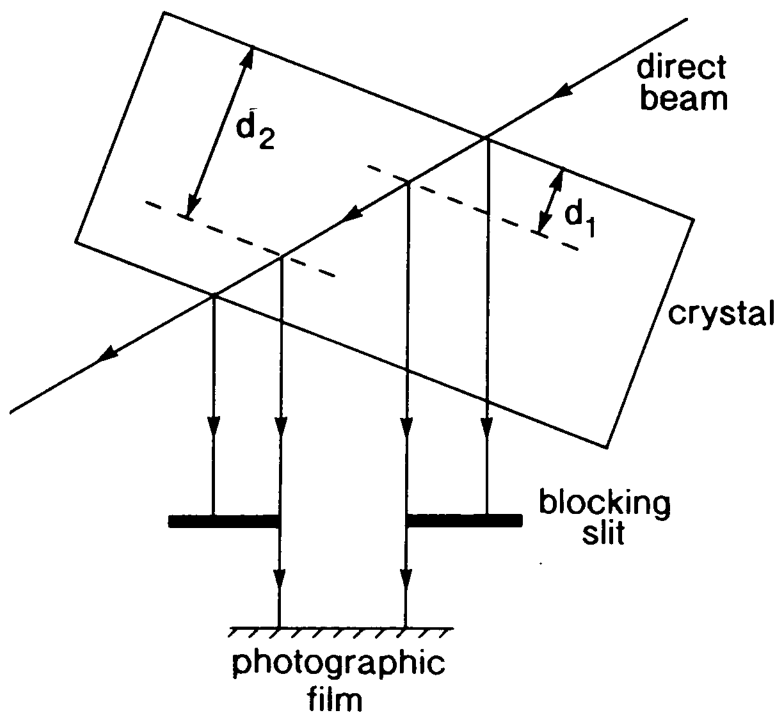

Fig. 1.6: Limited projection topography.

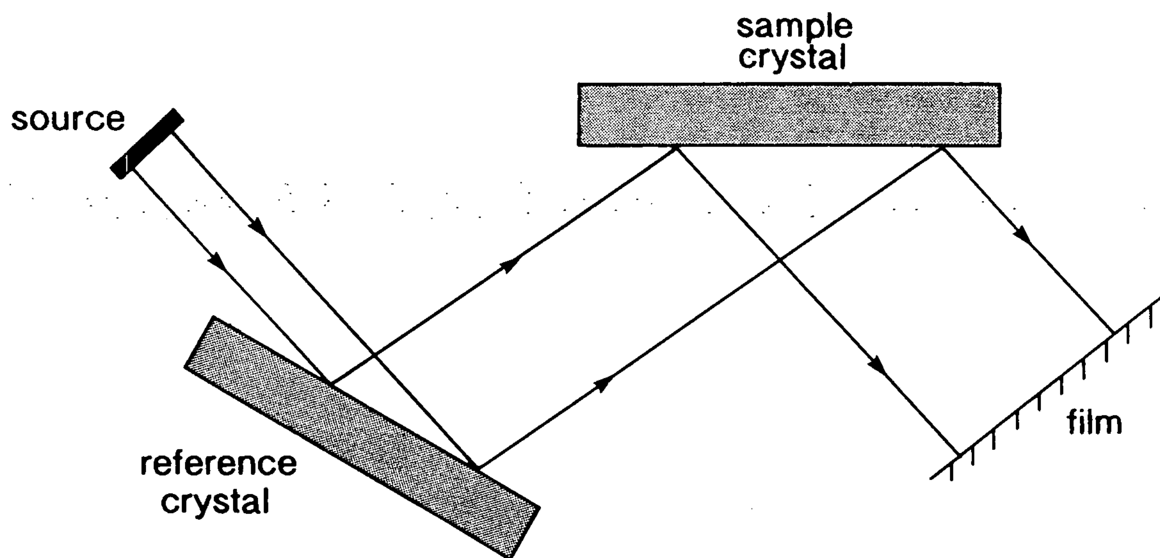

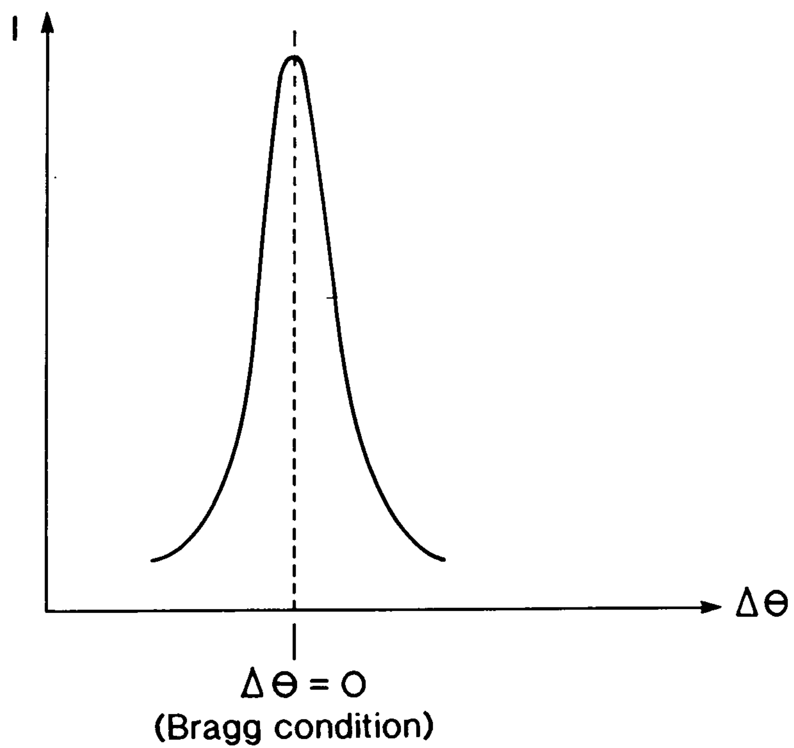

Fig. 1.7: Rocking curve analysis.

refraction of X-rays in a prism.

In addition to section and projection topography, the experimenter nowadays has at his disposal the technique of *synchrotron radiation topography.* Tuomi et al. [15,16] introduced the idea of using a beam of intense synchrotron radiation as the source in topography experiments. The intensity of the diffracted beam is recorded in the usual way, on photographic film. The field has been reviewed comprehensively by Bowen [17] and by Tanner and Bowen [18].

Synchrotron radiation is a highly intense form of electromagnetic radiation, extending from the hard X-ray to the microwave region of the spectrum. This radiation is obtained by confining electrons to a roughly circular path, by means of bending magnets. The radiation is almost totally plane polarised in the plane of the electron orbit. Templeton et al. [19] pointed out that total plane polarisation is prevented by the distributions of vertical positions and directions of electrons near the source point. However, because of the relativistic speeds of the electrons, the radiation is seen in the laboratory frame as a cone, tangential to the electron orbit.

One of the foremost synchrotron facilities is the storage ring source (S.R.S.) at S.E.R.C.'s Daresbury Laboratory. The system is illustrated schematically in Fig. 1.8. Electrons are first of all generated, and then accelerated in a 10 MeV linear accelerator, before being injected into a 600 MeV booster. The electrons are then fed into the main ring, in time with a radio-frequency accelerating field. Several beam lines can be built up in the storage ring, to supply several experiments each with a different beam. The electrons move in a closed, polygonal path, with a bending magnet at each apex of the polygon. At each apex, electrons emit radiation as they are accelerated by the bending magnet. Clearly, the beam loses energy each time this happens, but this energy is replaced by the action of the electrons passing through the r.f. accelerating field. Since electrons travel in bunches in the ring, the radiation derived from them is pulsed.

Synchrotron radiation is continuous, so that each lattice plane may select a particular wavelength for diffraction, and a Laue pattern of *spots* is observed on the resulting topograph. Each *spot* is in fact a topograph of the sample, and the same defect distribution is visible in each. Docherty et al. [20] have studied twin domains in crystals, using synchrotron topography. The Laue patterns of topographs which they obtained provide a striking illustration of the symmetry relations between the twin domains. Hohlwein et al. [21] have developed a double crystal monochromator for synchrotron radiation, allowing a selective reduction in bandwidth, whilst retaining high intensity. The result is an intense beam of well-collimated, broadband radiation.

Stock et al. [22] have studied a silicon wafer containing a laser-drilled hole. The characterisation of the strain around such a hole requires the simultaneous recording of many topographs. The authors developed a multiple slit for use in synchrotron topography, to allow the simultaneous recording of up to ten section topographs. They successfully used this device to visualise the strain field around a laser-drilled hole in a silicon wafer.

Synchrotron topography has numerous advantages over the conventional labo-

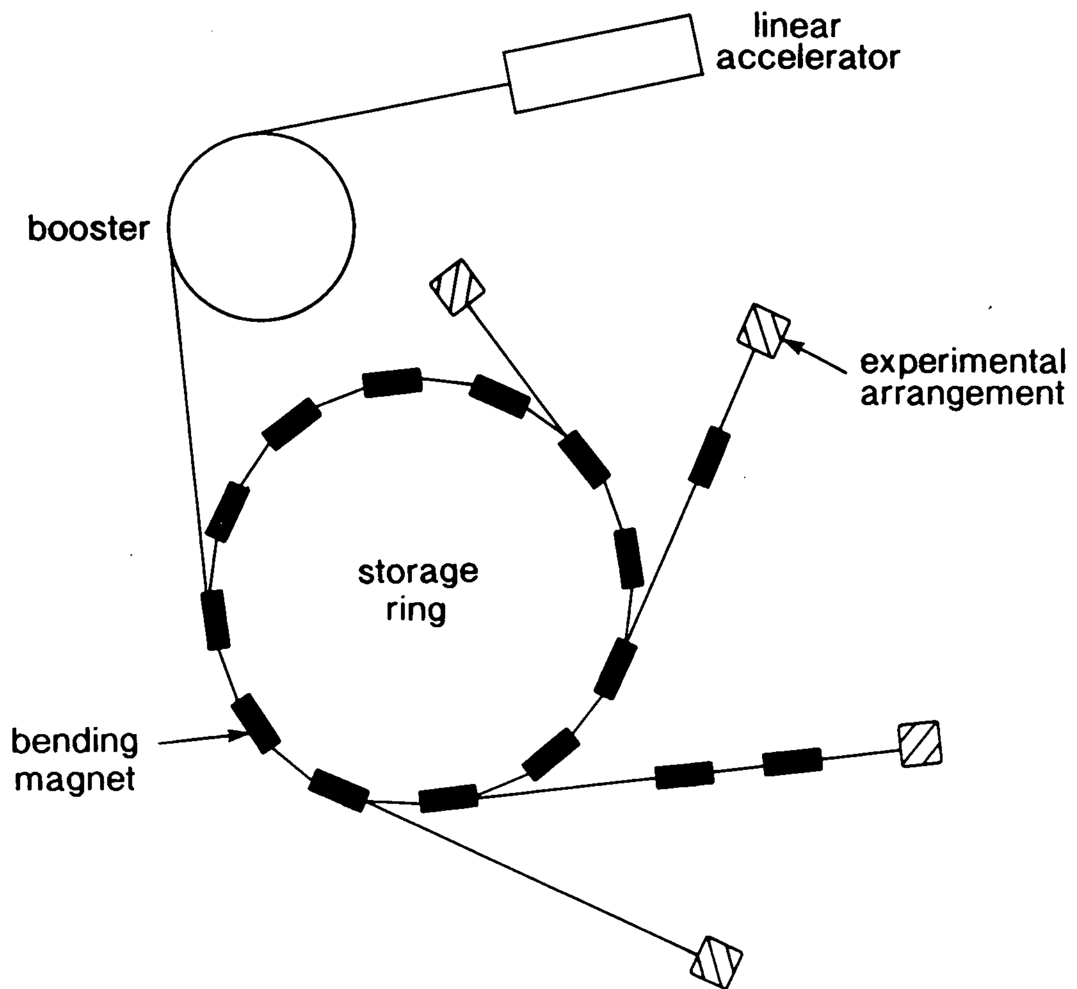

Fig. 1.8: Generation of synchrotron radiation by means of a storage ring source.

ratory techniques. Let us consider some of these.

One of the main advantages of synchrotron topography is the high intensity of the direct beam. This has allowed the observation of real-time processes such as the deformation resulting from acoustic waves in acoustic wave devices [23], and dislocation motion in InP crystals as a result of mechanical deformation [24]. High beam intensity allows very good resolution on the final topograph. This will be commented upon later. Also, the intensity of the beam means that exposure times can be preferentially lower than in the case of laboratory methods; seconds rather than hours.

Next, it is important to note that the synchrotron beam is wide. Hence, projection topographs of whole crystals can be obtained in one exposure.

Tanner et al. [25] have used the inherent good resolution of synchrotron topography to study the motion of magnetic domain walls. They found that for a resolution equivalent to that of the Lang method, they could place the specimen ten times as far from the recording film as in the Lang case. This is due to the minimal beam divergence of synchrotron radiation, and is very helpful, since it allows more experimental apparatus to be packed into the space around the sample.

Hart [26] has used synchrotron radiation to study grain boundaries in LiF samples. The defect images obtained were found to be much wider on synchrotron topographs than on Lang topographs. This is because the synchrotron technique is much more sensitive to local strain variations. This characteristic is of great importance in the characterisation of lattice defects, since these are visualised by means of the strains associated with them.

The sensitivity of synchrotron topography to variations in lattice strain has been used by Chikaura et al. [27] to image microdefects in thinned crystals of silicon. The contrast of the defect image is much sharper than in the Lang case. The authors proposed that when the wafer is thinned, the strain field around the defect spreads because of stress relief at the wafer surface, to an extent detectable by synchrotron topography.

Recently, it has been shown [28] that synchrotron topography in the grazing Bragg-Laue geometry is the ideal means of characterising dislocations in the interfaces of heterostructures. The authors demonstrated that it is necessary to take into account surface relaxation in the determination of dislocation depth by this method.

The aforementioned advantages of synchrotron radiation have been summarised in an article describing the European Synchrotron Radiation Facility in Grenoble, France [29].

It is necessary to complete the survey of experimental methods by looking at the means by which topographs are recorded photographically.

In order to obtain good resolution, one would use a thin photo-emulsion with very small grain size. However, photographic emulsion is a poor X-ray absorber, and it is necessary to compensate for this by increasing the thickness of the emulsion.

Ilford L4 Nuclear Emulsion is taken as the standard for use in X-ray topography. This substance contains a high concentration of silver halide, which allows high X-

ray absorption with minimum emulsion thickness.

Following exposure, the emulsion is made to swell by soaking in water. This facilitates rapid diffusion of developer into the emulsion. Lang [3] and Epelboin et al. [30] have shown that the best resolution on the final topograph is obtained by developing at low temperature. However, this does necessitate a long exposure time. The average size of a developed grain of Ilford L4 emulsion is about $0.25\mu m$. This is ideal for topography, since the smallest dislocation image will be of order $1\mu m$ in width.

After developing, the emulsion is treated with a weak solution of acetic acid, prior to fixing. After fixing, the plates are washed in cold, running water and dried in warm air, preferably filtered.

The finished topograph is enlarged to form a micrograph, using a projection microscope. The topograph is placed under the microscope and illuminated with visible light. Hence, an enlarged image of the topograph is recorded on optical photographic film.

Background noise can reduce the visibility of defect images. A remedy is to use longer exposures, so increasing the signal-to-noise ratio corresponding to the defect image. Such long exposures will inevitably cause increased blackening on the topograph, hindering the visual interpretation of the resulting micrograph. It has been found [31] that details which would otherwise have been lost in overexposed topographs can be reclaimed by viewing the topograph in reflected rather than transmitted light.

1.4 Industrial Applications

The comment was made earlier that X-ray topography finds considerable use in the semiconductor industry. In an early paper, Segmüller [32] illustrated the use of topography to study the defects introduced in Ge by basic device manufacturing steps. The author illustrated, with the aid of topographs, the generation of dislocations as a result of thermal stresses induced during growth. Deposition of an oxide layer onto a substrate is a standard industrial technique in the preparation of devices. The deposition is done at high temperature so that, upon cooling, the substrate and the oxide layer contract at different rates. This causes the crystal to bend. Segmüller used topography to investigate the bending of a Ge wafer after deposition of a layer of SiO_2. Also, by interpreting the contrast on topographs of antimony-doped Ge topped with an epitaxial layer of boron-doped Ge, he analysed the stresses induced by the epitaxial layer.

It has been shown that the presence of defect distributions can have a detrimental effect upon the electrical performance [33] and mechanical resilience [34] of crystals used for devices. Mechanical working of a Si wafer, for example, by cutting with a diamond-blade saw, can introduce serious imperfections into the surface layer of the crystal. The strains induced by these imperfections can have a deleterious effect upon the electrical properties of the wafer. Auleytner et al. [35] have used X-ray

section topography to determine the thickness of the damaged layer at the surface of such a Si wafer.

Scott [36] has commented that X-ray topography has played a major role in the understanding of defect generation mechanisms, with reference to the developments in the growth of $GaAs$ substrates. The author showed a Lang topograph of a Si-doped $GaAs$ ingot, and he associated specific image features with the process of Si segregation during growth. He then used topography to investigate a device-processed wafer. A combination of topography and device performance analyses, on an In-doped $GaAs$ wafer with devices built onto it, showed that the variation in threshold voltage in the wafer was linked to the variation in crystal defect density.

A standard industrial method for producing *silicon-on-insulator* (SOI) wafers is the *wafer bonding technique*, illustrated in Fig. 1.9. The bonded wafer is oxidised to form a 1μ SiO_2 layer on its surface. This wafer is then brought into contact with the Si base wafer at 1100°C and a very tight bonding is obtained. The bonded wafer is subsequently thinned in order to form the active layer for device preparation. During the bonding of the SiO_2 and Si surfaces, it is possible for voids to form, due to incomplete bonding. Such voids render the SOI wafer useless for device purposes, since unbonded silicon is unstable with heat treatment. Abe et al. [37] have detected these voids using X-ray topography, and have found that void formation is linked to the degree of surface roughness of the silicon base wafer.

Meieran [38] has reviewed the use of X-ray and other methods in quality control in the semiconductor industry. He comments on the application of Lang topography in visualising very clearly the presence of surface damage and also of precipitates in silicon crystals. As mentioned earlier, section topography can even be used to map the spatial distribution of precipitates, which is of great value.

Sometimes, certain kinds of defect are artificially introduced into the lower portion of a crystal, to act as *gettering centres.* Upon heat treatment, metal contaminants in the surface layer of silicon will preferentially migrate to dislocation loops, and other oxygen-related defects, in the bulk. The dislocation loops here are the gettering centres, and their effect is to remove metallic impurities from the surface layer, leaving it suitable for device preparation. The metallic contaminants would otherwise have a negative effect upon device performance. Falster and Bergholz [39] have used X-ray topography to investigate the gettering efficiency of oxygen-related defects in silicon. Hahn et al. [40] have highlighted the beneficial effect of intrinsic gettering on the electrical performance of devices fabricated on Si wafers, in a study involving the use of synchrotron radiation section topography.

The *open-wafer process* is used in industry to relieve stress in semiconductor wafers. The technique involves etching a hole through the wafer, making a cut from the outer to the inner edge, and then cleaning the wafer. Tänzer et al. [41] subjected ordinary and open wafers to a heat treatment associated with standard industrial processing, and took Lang projection topographs of the resulting wafers. They found that whereas the ordinary wafers showed widespread dislocation distribution and slippage, the open wafers were undamaged except for a very localised area around the etched hole.

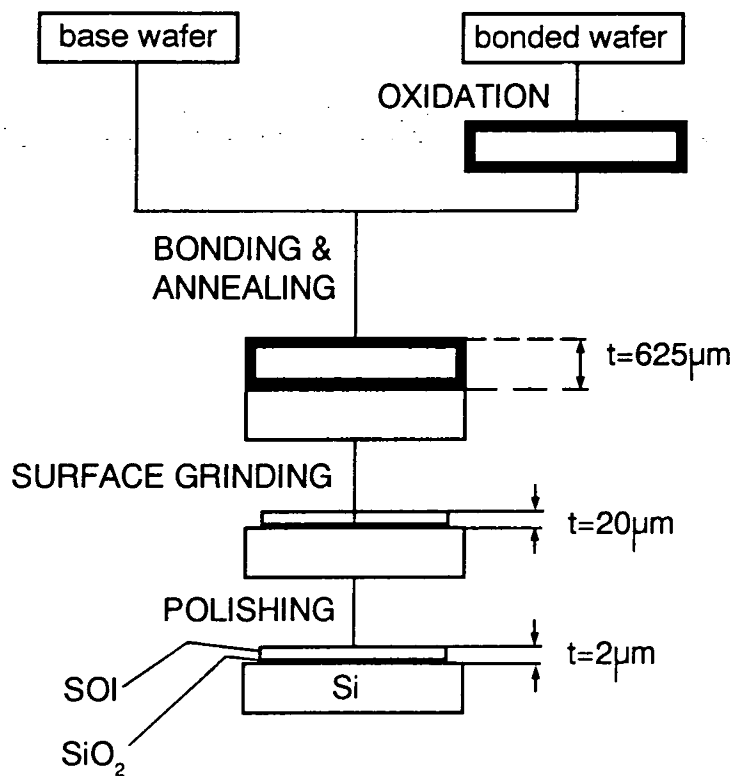

Fig. 1.9: Wafer bonding technique for silicon-on-insulator wafer fabrication, (after Abe and Matlock).

This is an excellent example of the use of topography to illustrate how a well-defined technique can benefit the semiconductor industry.

Chapter 2

Dynamical Theories of X-ray Diffraction in Crystals

2.1 Introduction and Motivation for Dynamical Theory

In 1912, Laue, Fridrich and Knipping [42] discovered the process of X-ray diffraction in crystals. This was of importance in two major respects. First of all, it highlighted the wave nature of X-rays, and confirmed X-radiation as a part of the electromagnetic spectrum. Secondly, this discovery provided striking evidence of the periodic structure of crystals.

It soon became apparent that X-rays could be used to analyse the structure of materials, and an enormous amount of experimental data was built up in the following years. This provided the motivation for the development of a theory of X-ray diffraction in crystals, to account for the experimental results within a consistent theoretical framework. So it was that Laue developed a theory of diffraction and interference, known as *kinematical theory*, which we will now consider.

We imagine the electron content of each atom to be smeared out across the atomic volume. Consider scattering from two points within an atom, Fig. 2.1. The wave vectors of the incident and scattered waves are $\underline{k}$ and $\underline{k}'$, respectively. The phase difference between waves scattered at points O and P is:

$$\delta_j = 2\pi(\underline{k}' - \underline{k}).\underline{r}_j,$$

$$\text{where} \quad \underline{r}_j = \overrightarrow{OP}\ .$$

Hence, the scattered amplitude for an atom is:

$$A = \sum_j A_e \exp(i\delta_j),$$

where A_e = amplitude scattered by one electron,

and j takes values 1 up to z, where z = atomic number.

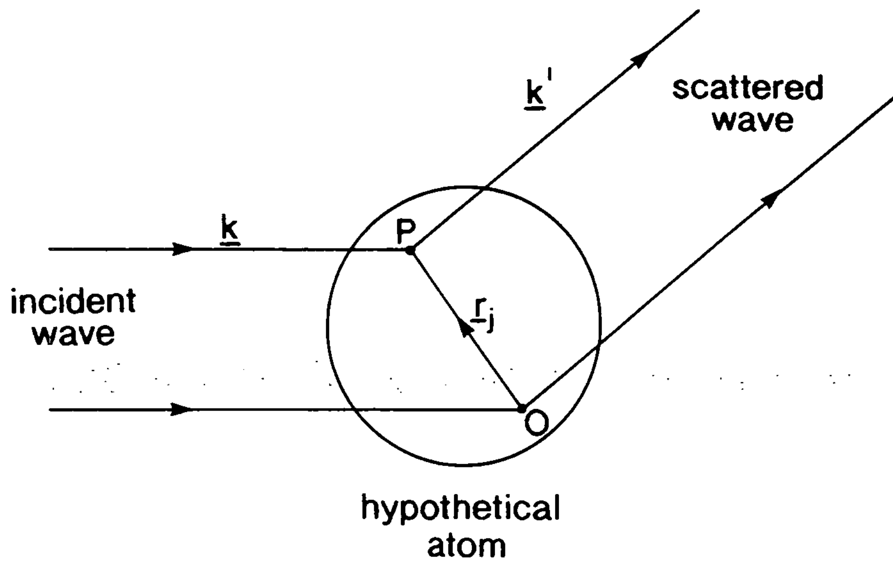

Fig. 2.1: Scattering of radiation from a single atom.

Fig. 2.2: Scattering of radiation from a periodic array of atoms.

The *atomic scattering amplitude*, f, is defined as the amplitude scattered by an atom divided by the amplitude scattered by a single electron.

Then, from above:

$$f = \sum_j \exp(i\delta_j) = \sum_j \exp[i2\pi(\underline{k} - \underline{k}').\underline{r}_j]. \tag{2.1}$$

Our goal is to calculate the amplitude scattered from a periodic array of atoms. The approach is to consider scattering from a unit cell, and then add the contributions due to all unit cells.

Consider Fig. 2.2. The unit cells have *origins* with position vectors $\underline{r}_1$, $\underline{r}_2, ...,$ $\underline{r}_i$. Within a unit cell, the atomic coordinates are given by $\underline{R}_1$, $\underline{R}_2, ...,$ $\underline{R}_t$, with respect to the origin of that unit cell. The total scattered amplitude is then:

$$A = \sum_i \sum_t f_t \exp[-2\pi i(\underline{r}_i + \underline{R}_t).\delta\underline{k}],$$

where $\delta\underline{k} = \underline{k}' - \underline{k}$.
Hence,

$$A = F_K \sum_i \exp[-2\pi i \underline{r}_i.\delta\underline{k}], \tag{2.2}$$

where the *geometrical structure factor*,

$$F_K = \sum_t f_t \exp[-2\pi i \underline{R}_t.\delta\underline{k}]. \tag{2.3}$$

The scattered intensity, I, is given by:

$$I = A^* A,$$

so that:

$$I \alpha \mid F_K \mid^2 . \tag{2.4}$$

The kinematical theory was able to satisfy the requirements of contemporary studies of the atomic structure of crystals. However, flaws soon became apparent. For example, the intensity dependence given in equation (2.4) was found to be at variance with the relation $I \alpha \mid F_K \mid$, obtained empirically. In addition, the theory assumes that the amplitudes of the diffracted waves are small compared to the amplitude of the transmitted wave. This assumption is valid for small crystals or mosaic crystals, but not for large, perfect, single crystals, where the diffracted amplitude can be appreciable.

Essentially, the main drawback of kinematical theory is that it fails to take into account the interaction of the transmitted wavefield with the diffracted wavefields.

What was needed was a theory which would allow a *dynamic* interchange of energy between the transmitted and diffracted wavefields. In 1914, Darwin [43] proposed such a *dynamical theory*, into which he attempted to incorporate multiwave scattering. An alternative theory was presented by Ewald [44] in 1916, in which each lattice point is represented by a dipole, which can be set into oscillation by

an electromagnetic field within the crystal. The oscillating dipoles themselves emit radiation, giving rise to a radiation field. This model proved to be very fruitful in the interpretation of experimentally observed scattering phenomena. In 1931, Laue [45] introduced a theory based on that of Ewald. Instead of a dipole at each lattice point, Laue proposed a localised positive charge. These positive charges sit in a continuous distribution of negative charge. The electromagnetic field associated with the radiation causes polarisation within this medium, and the polarisation is proportional to the local electric field. In the next section, we will pursue this approach used by Laue.

The field of dynamical theories has been extensively reviewed by several authors [46,47,48,49].

2.2 Dynamical Theory for a Perfect Crystal

2.2.1 Development of the Fundamental Equations

Using the Laue model, outlined above, the problem reduces to the solution of Maxwell's Equations in a periodic medium.

According to Maxwell's Equations:

$$\underline{\nabla} \times \underline{E} = \frac{-1}{c}\frac{\partial \underline{B}}{\partial t}, \tag{2.5}$$

$$\text{and} \quad \underline{\nabla} \times \underline{H} = \frac{1}{c}\frac{\partial \underline{D}}{\partial t}, \tag{2.6}$$

$$\begin{aligned}
\text{where magnetic induction,} \quad \underline{B} &= \mu \underline{H}, \\
\text{and electric displacement,} \quad \underline{D} &= \varepsilon \underline{E}, \\
\text{where} \quad \mu &= \text{permeability of medium}, \\
\varepsilon &= \text{permittivity of medium}, \\
\underline{H} &= \text{magnetic field}, \\
\text{and} \quad \underline{E} &= \text{electric field}.
\end{aligned}$$

Equation (2.5) then becomes:

$$\begin{aligned}
\frac{1}{\varepsilon}\underline{\nabla} \times \underline{D} &= \frac{-1}{c}\frac{\partial \underline{B}}{\partial t} \\
&= \frac{-\mu}{c}\frac{\partial \underline{H}}{\partial t}.
\end{aligned}$$

Taking the curl of both sides:

$$\frac{1}{\varepsilon}\underline{\nabla} \times \underline{\nabla} \times \underline{D} = \frac{-\mu}{c}\frac{\partial}{\partial t}(\underline{\nabla} \times \underline{H}).$$

Using (2.6), this becomes:

$$\frac{1}{\varepsilon}\underline{\nabla} \times \underline{\nabla} \times \underline{D} = \frac{-\mu}{c^2}\frac{\partial^2 \underline{D}}{\partial t^2}. \tag{2.7}$$

$$\begin{aligned} \text{Now,} \quad \varepsilon &= 1 + \chi, \\ \text{where} \quad \chi &= \text{dielectric susceptibility.} \end{aligned}$$

Then, making the approximation

$$\frac{1}{\varepsilon} \cong 1 - \chi, \text{for } |\chi| \ll 1,$$

equation (2.7) becomes:

$$\underline{\nabla} \times \underline{\nabla} \times (1 - \chi)\underline{D} = \frac{-1}{c^2}\frac{\partial^2 \underline{D}}{\partial t^2}. \tag{2.8}$$

In a periodic medium, as specified by Laue, the susceptibility is periodic and can be expressed in terms of a Fourier series:

$$\chi = \sum_h \chi_h \exp(-2\pi i \underline{h}.\underline{r}), \tag{2.9}$$

$$\text{where} \quad \chi_h = \frac{-e^2\lambda^2}{\pi m c^2 V} F_h,$$

$$\begin{aligned} \text{where} \quad e &= \text{electronic charge,} \\ \lambda &= \text{wavelength,} \\ m &= \text{electron mass,} \\ c &= \text{velocity of light,} \\ V &= \text{unit cell volume,} \\ \text{and} \quad F_h &= \text{structure factor.} \end{aligned}$$

The solution of the wave equation (2.8) can be expressed as a Bloch wave:

$$\underline{D} = \sum_h \underline{D}_h \exp(-2\pi i \underline{K}_h.\underline{r}). \tag{2.10}$$

This solution is a linear combination of plane waves, each with wave vector $\underline{K}_h$, and represents the multiwave solution sought after by the pioneers of dynamical theory. The wave vectors, $\underline{K}_h$, are linked by the *Laue equation*:

$$\underline{K}_h = \underline{K}_o + \underline{h}, \tag{2.11}$$

where $\underline{h}$ is a reciprocal lattice vector. Substitution of (2.10) and (2.9) into (2.8) gives:

$$\sum_g \{\chi_{h-g}(\underline{K}_h.\underline{D}_g)\underline{K}_h - \chi_{h-g}(\underline{K}_h.\underline{K}_h)\underline{D}_g\} = (k^2 - \underline{K}_h.\underline{K}_h)\underline{D}_h, \tag{2.12}$$

where $k = |\underline{k}|$, and $\underline{k}$ = wave vector in vacuum.

Equations (2.12) are the fundamental equations of dynamical theory.

2.2.2 The Dispersion Surface

Next we will borrow a concept from kinematical theory, namely the *Ewald sphere.* Consider a sphere of radius k, in reciprocal space, centred on the reciprocal lattice point L, Fig. 2.3. Suppose the sphere cuts the point O, so that $\overrightarrow{LO}$ represents the wave vector, $\underline{K_o}$, of the refracted wave in a crystal. The point O is then considered to be the origin of the reciprocal lattice. Now, each reciprocal lattice point is associated with a set of planes in the real crystal lattice, specified by a set of Miller indices. Strong diffraction will occur from the lattice planes with Miller indices (h, k, l) associated with point H, Fig. 2.3, if the sphere also cuts the point H. In this case, $\overrightarrow{LH}$ denotes the wave vector, $\underline{K_h}$, associated with this diffracted wave. The sphere described here is the *Ewald sphere*, and the point L is called the *Laue point.*

The fact that the Ewald sphere must cut reciprocal lattice points $O(0,0,0)$ and $H(h,k,l)$ is an embodiment of the Laue equation, (2.11), since any two reciprocal lattice points are connected by a reciprocal lattice vector, $\underline{h}$.

Kinematical theory assumes no loss of energy in the incident wave through the crystal, and no multiple scattering, i.e. $|\underline{K_o}| = k$. However, in reality $|\underline{K_o}| = nk$, where the refractive index,

$$n = 1 + \frac{\chi_o}{2},$$

and χ_o = susceptibility of free space.

Hence, the Ewald sphere must be re-drawn, with radius nk. In fact, in the X-ray case, the curvature of the sphere is large, so that the probability of more than two reciprocal lattice points being cut is small. Hence, we only need to consider the refracted wave and one diffracted wave. In this *two-beam* case, equation (2.10) becomes:

$$\underline{D} = \underline{D_o} \exp(-2\pi i \underline{K_o}\cdot\underline{r}) + \underline{D_h} \exp(-2\pi i \underline{K_h}\cdot\underline{r}). \tag{2.13}$$

Also, equations (2.12) reduce to:

$$\alpha_o \alpha_h = \frac{1}{4} k^2 C^2 \chi_h \chi_{\overline{h}}, \tag{2.14}$$

$$\begin{aligned}
\text{where}\quad \alpha_o &= \frac{1}{2k}\{\underline{K_o}.\underline{K_o} - k^2(1+\chi_o)\},\\
\alpha_h &= \frac{1}{2k}\{\underline{K_h}.\underline{K_h} - k^2(1+\chi_o)\},\\
C &= 1, \text{ for } \sigma \text{ - polarisation},\\
C &= \cos 2\theta_B, \text{ for } \pi \text{ - polarisation},\\
\theta_B &= \text{Bragg angle},
\end{aligned}$$

and χ_h, $\chi_{\overline{h}}$ are the h and $\overline{h}$ Fourier components of the susceptibility.

Equation (2.14) is the equation of the *dispersion surface*, and its importance will become apparent. In the dynamical case, there is no longer a single Ewald sphere

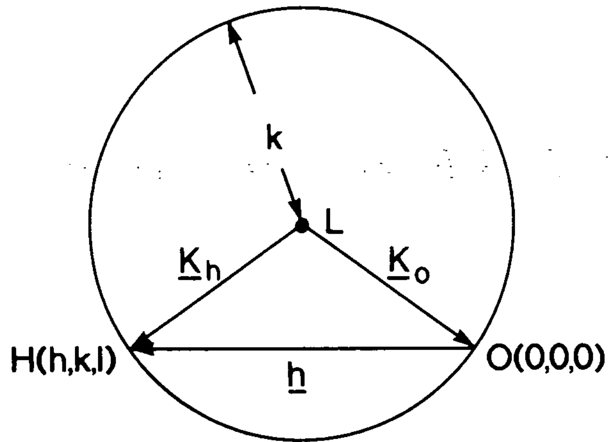

Fig. 2.3: The Ewald sphere.

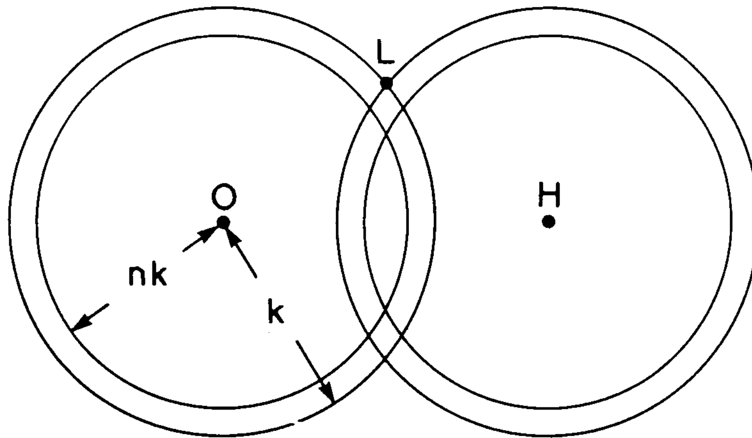

Fig. 2.4: Spheres in reciprocal space, centred upon lattice points O and H.

associated with an incident wave. The dispersion surface represents the loci of the centres of allowed Ewald spheres.

Consider Fig. 2.4, which shows two pairs of spheres, of radii k and nk, centred on the reciprocal lattice points O and H. The Laue point, L, of the kinematical case is indicated. Fig. 2.5 shows a magnification of the area around the point L. Here, the arcs AB and $A'B'$ correspond to the spheres of radius k, and CD and $C'D'$ to the spheres of radius nk.

Equation (2.14) defines a hyperboloid of revolution, whose projection onto the paper in Fig. 2.5 is a hyperbola. On the scale of Fig. 2.5, the arcs CD and $C'D'$ approximate to lines, and these lines are the asymptotes of the hyperbola. Each branch of the hyperbola has two parts, corresponding to σ- and π- polarisation. Each *tie point*, P, on the dispersion surface defines a pair of wave vectors, $\underline{K}_o$ and $\underline{K}_h$, corresponding to an allowed reflection. Tie points on the vertical axis YY' correspond to strong diffraction at the Bragg condition. It will be seen that, far from the Bragg condition, the σ and π dispersion surfaces merge with the spheres centred on O and H.

The parameters α_o and α_h in equation (2.14) are in fact the perpendicular distances of the tie point, P, from the spheres of radius nk. It can be shown that the amplitude ratio:

$$R_i = \frac{D_{h_i}}{D_{o_i}} = \sqrt{\frac{\alpha_{o_i}}{\alpha_{h_i}}}, \qquad (2.15)$$

where $i = 1, 2$ denotes the branch (1 or 2) of the dispersion surface.

To summarise, the importance of the dispersion surface is two-fold. First of all, it enables one to determine the wave vectors, $\underline{K}_o$ and $\underline{K}_h$, associated with the refracted and diffracted waves, respectively. Also, equation (2.15) allows the calculation of the amplitude ratio, R, of the diffracted and refracted wave components of the total wave field.

Having discussed the dispersion surface, let us see how the dynamical theory describes two well known physical effects.

2.2.3 Anomalous Transmission

Consider the rocking curve experiment illustrated in Fig. 2.6, for a thin crystal, (a), and a thick crystal, (b). Fig. 2.6(c) is a plot of transmitted intensity, I_T, against angle of incidence, θ, for the two crystals. In case (a), there is a predictable dip in I_T around the Bragg condition, corresponding to an increase in diffracted intensity. However, in the high-absorption domain of case (b), there is a peak in I_T around the Bragg condition. Evidently, there is some mechanism whereby the intensity of the refracted beam is not appreciably attenuated in passing through the crystal. This effect was first discovered by Borrmann in 1941, and is known as *anomalous transmission* or the *Borrmann effect*.

Consider next the equation, (2.13), for the wave amplitude in the two-beam case:

$$\underline{D} \;=\; \underline{D}_o \exp(-2\pi i \underline{K}_o . \underline{r}) + \underline{D}_h \exp(-2\pi i \underline{K}_h . \underline{r}),$$

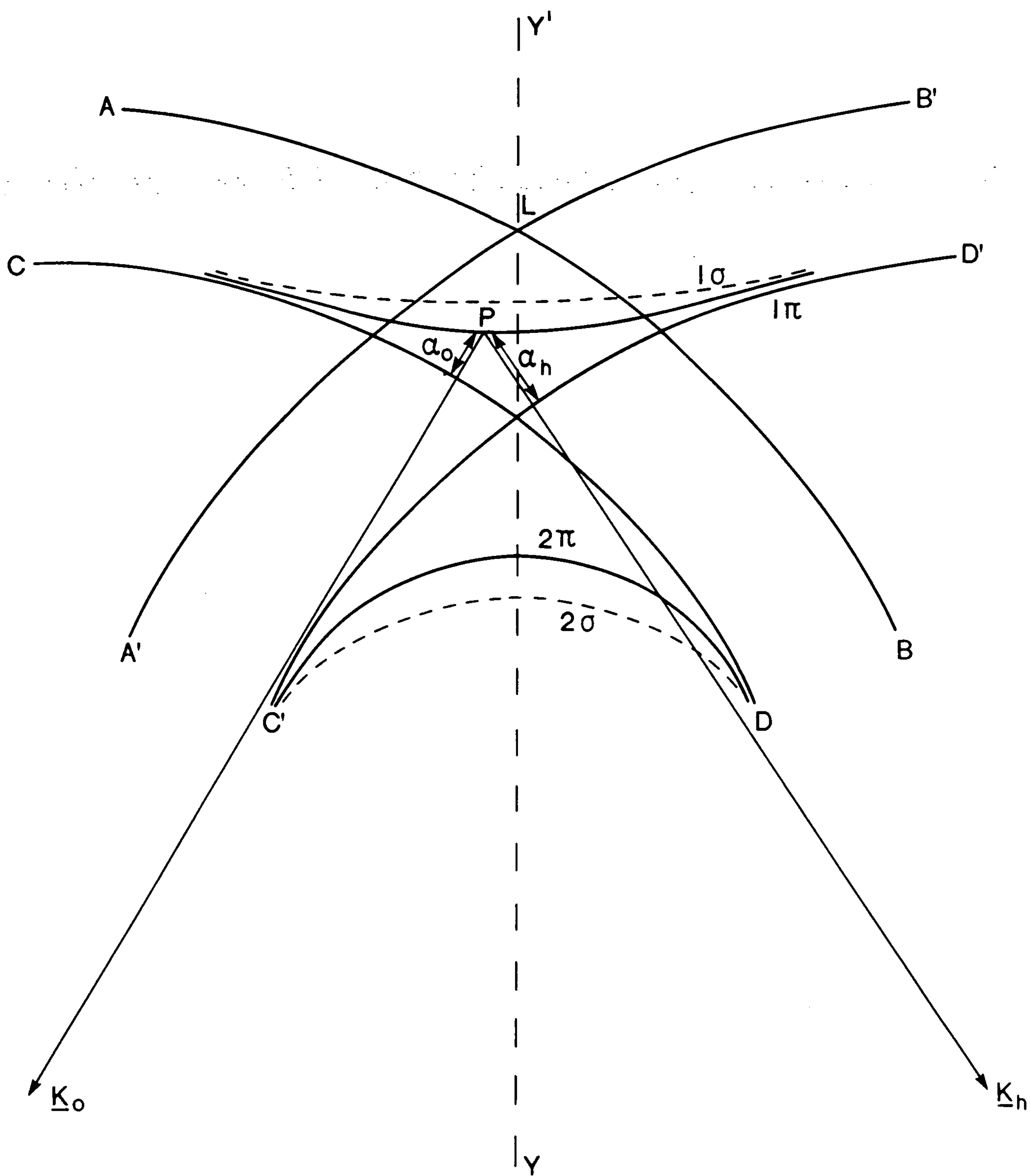

Fig. 2.5: The dispersion surface construction, (after Tanner).

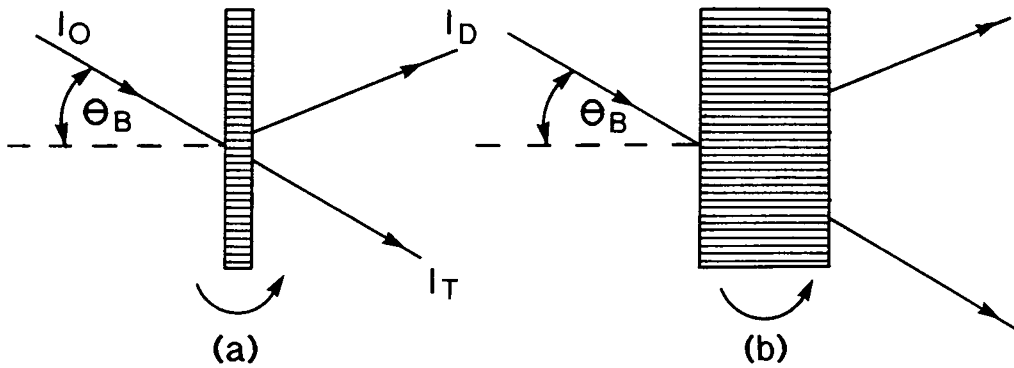

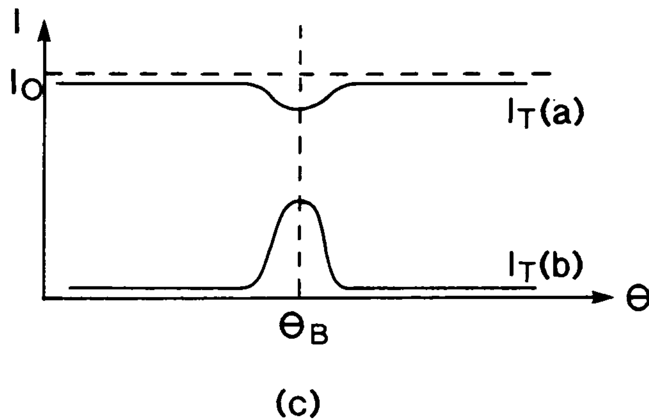

Fig. 2.6: Demonstration of Anomalous Transmission.
(a) thin crystal.
(b) thick crystal.
(c) transmitted intensity, I_T, vs. angle of incidence, θ, for the two crystals.

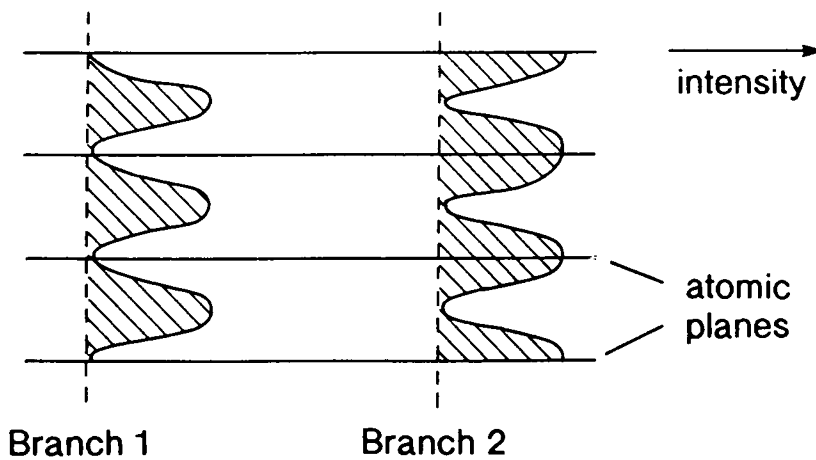

Fig. 2.7: Bloch waves with tie points on opposite branches of the dispersion surface.

$$= \{\underline{D}_o + \underline{D}_h \exp(-2\pi i \underline{h}.\underline{r})\}. \exp(-2\pi i \underline{K}_o.\underline{r}). \qquad (2.16)$$

The corresponding intensity is given by:

$$\begin{aligned} I &= \underline{D}^*.\underline{D}, \\ &= D_o^2\{1 + R^2 + 2RC\cos(2\pi \underline{h}.\underline{r})\}, \end{aligned} \qquad (2.17)$$

where C is given in (2.14) and R in (2.15).

Hence, the intenity is maximum, for $\sigma-$polarisation ($C = 1$), when $\underline{h}.\underline{r} = N$, and minimum when $\underline{h}.\underline{r} = (2N + 1)/2$, where N is integral. This means that the maxima and minima of the standing wavefield lie either at or half way between the atomic planes, since $\underline{h}.\underline{r} = N$ corresponds to a plane of atoms. The sign of R determines whether maxima or minima occur at the atomic planes. The sign of R is opposite for Bloch waves with tie points on opposite branches of the dispersion surface. Consequently, one Bloch wave will have intensity maxima, while the other will have minima, at the atomic planes. This is illustrated schematically in Fig. 2.7, where the branch 1 wave is taken to have minima at the atomic planes. Photoelectric absorption, which plays the major role in attenuation, is very strong for the wave whose maxima lie at the atomic planes, and very weak for the other wave. In the case of Fig. 2.7, the 1σ wave only, at the exact Bragg condition, will be appreciably transmitted. Thus, the process of anomalous transmission is accounted for by dynamical theory.

2.2.4 The Pendellösung Effect

One of the most important phenomena described by dynamical theory is the Pendellösung effect [9], mentioned in the previous chapter. Pendellösung fringes are clearly visible in Fig. 2.8, which is an experimental topograph of a perfect crystal.

For a plane wave, of unit amplitude, incident upon the entrance surface of a crystal, Fig. 2.9, the boundary conditions are:

$$\begin{aligned} 1 &= D_{o_1} + D_{o_2}, \\ 0 &= D_{h_1} + D_{h_2}, \end{aligned} \qquad (2.18)$$

where $i = 1, 2$ denotes the branch of the dispersion surface.

The amplitude ratio R_i, equation (2.15), can be written:

$$R_i = \frac{D_{h_i}}{D_{o_i}} = \eta \pm (1 + \eta^2)^{\frac{1}{2}}, \qquad (2.19)$$

where η = deviation parameter, a measure of the angular deviation from the exact Bragg condition.

The plus sign in (2.19) corresponds to branch 1 and the minus sign to branch 2 of the dispersion surface.

Fig. 2.8: Experimental section topograph of a perfect crystal, showing an undistorted set of Pendellösung fringes.

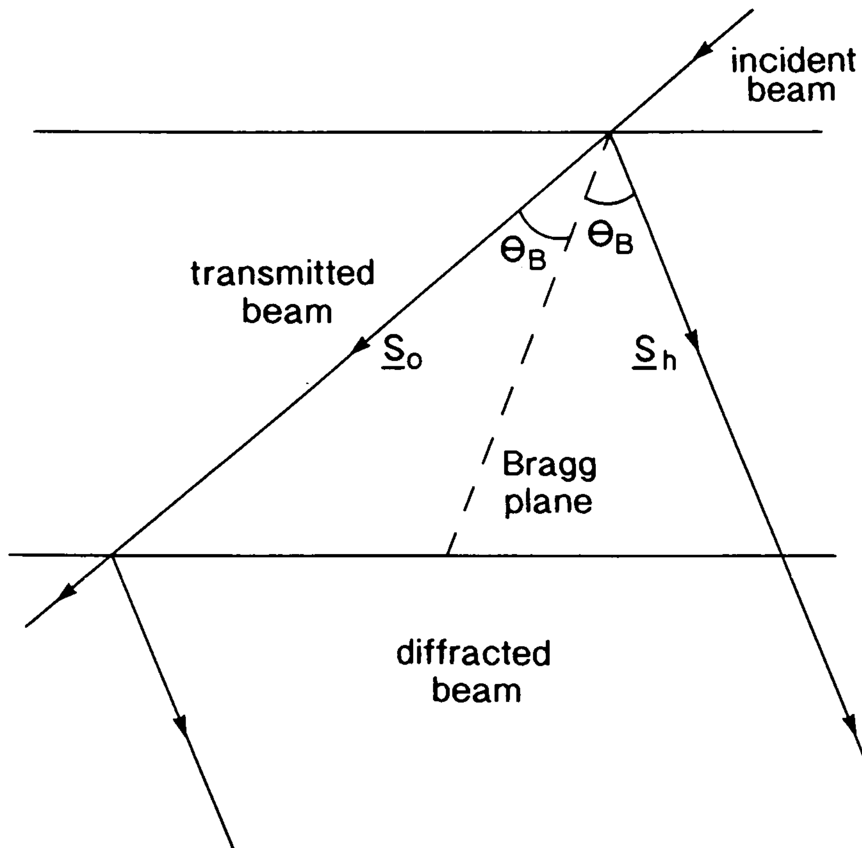

Fig. 2.9: Characteristic diffraction geometry for a wave incident on the surface of a crystal.

Introducing a parameter β, such that

$$\eta = \cot\beta,$$

and using (2.18) and (2.19), we obtain:

$$\begin{aligned} D_{o_1} &= \cos^2\tfrac{\beta}{2} & D_{o_2} &= \sin^2\tfrac{\beta}{2} \\ D_{h_1} &= -\sin\tfrac{\beta}{2}\cos\tfrac{\beta}{2} & D_{h_2} &= \sin\tfrac{\beta}{2}\cos\tfrac{\beta}{2}. \end{aligned} \tag{2.20}$$

For a crystal of thickness t, the Bloch waves at the exit surface have additional phase factors:

$$D_i(t) = D_{o_i}\exp(-2\pi it\underline{K}_{o_i}\cdot\hat{\underline{n}}) + D_{h_i}\exp(-2\pi it\underline{K}_{h_i}\cdot\hat{\underline{n}}), \tag{2.21}$$

where D_{o_i} and D_{h_i} are the components at the entrance surface, and $\hat{\underline{n}}$ is a unit vector perpendicular to the surface.

The boundary conditions at the exit surface are:

$$\begin{aligned} D_o^e &= D_{o_1}(t) + D_{o_2}(t), \\ D_h^e &= D_{h_1}(t) + D_{h_2}(t). \end{aligned}$$

The intensity, I_h, in the diffracted beam is given by:

$$\begin{aligned} I_h &= D_h^{e*}D_h^e \\ &= \{D_{h_1}\exp(2\pi it\underline{K}_{h_1}\cdot\hat{\underline{n}}) + D_{h_2}\exp(2\pi it\underline{K}_{h_2}\cdot\hat{\underline{n}})\}\times \\ &\quad \{D_{h_1}\exp(-2\pi it\underline{K}_{h_1}\cdot\hat{\underline{n}}) + D_{h_2}\exp(-2\pi it\underline{K}_{h_2}\cdot\hat{\underline{n}})\}, \\ &= D_{h_1}^2 + D_{h_2}^2 + D_{h_1}D_{h_2}\{\exp[2\pi it(\underline{K}_{h_2} - \underline{K}_{h_1})\cdot\hat{\underline{n}}] + \exp[-2\pi it(\underline{K}_{h_2} - \underline{K}_{h_1})\cdot\hat{\underline{n}}]\}, \\ &= D_{h_1}^2 + D_{h_2}^2 + 2D_{h_1}D_{h_2}\cos[2\pi t(\underline{K}_{h_2} - \underline{K}_{h_1})\cdot\hat{\underline{n}}]. \end{aligned}$$

Substituting for D_{h_1} and D_{h_2} from (2.20) gives:

$$\begin{aligned} I_h &= 2\sin^2\frac{\beta}{2}\cos^2\frac{\beta}{2} - 2\sin^2\frac{\beta}{2}\cos^2\frac{\beta}{2}.\cos[2\pi t(\underline{K}_{h_2} - \underline{K}_{h_1})\cdot\hat{\underline{n}}], \\ I_h &= \frac{1}{2}\sin^2\beta\{1 - \cos[2\pi t(\underline{K}_{h_2} - \underline{K}_{h_1})\cdot\hat{\underline{n}}\}. \end{aligned} \tag{2.22}$$

From equation (2.22), it is seen that there is interference between the Bloch wave components associated with opposite branches of the dispersion surface, and that this interference depends on depth. This process is the mechanism of formation of the Pendellösung fringes seen in wedge-shaped crystals and in section topographs. The interference beat depends on the difference, $(\underline{K}_{h_2} - \underline{K}_{h_1})$, between the wave vectors.

Using the relation

$$(\underline{K}_{h_2} - \underline{K}_{h_1})\cdot\hat{\underline{n}} = \Lambda_o(1+\eta^2)^{\frac{1}{2}},$$

where Λ_o = diameter of dispersion surface,
and substituting for β, we obtain:

$$I_h = \frac{\sin^2[\pi\Lambda_o t(1+\eta^2)^{\frac{1}{2}}]}{1+\eta^2}, \quad (2.23)$$

$$I_o = 1 - \frac{\sin^2[\pi\Lambda_o t(1+\eta^2)^{\frac{1}{2}}]}{1+\eta^2}. \quad (2.24)$$

Clearly, from (2.23) and (2.24), the intensity of both the diffracted and transmitted beams varies periodically with depth. Furthermore, the period is the same for both beams, and is given by a depth:

$$[\Lambda_o(1+\eta^2)^{\frac{1}{2}}]^{-1}.$$

This depth has a maximum value for $\eta = 0$, i.e. the Bragg condition. In this case, the depth corresponding to one period is called the *extinction distance*, ξ_h, given by:

$$\xi_h = \Lambda_o^{-1}.$$

Again, the usefulness of the dispersion surface is seen, this time in providing a value for the extinction distance. For values of $\eta \neq 0$, the effective extinction distance is:

$$\xi'_h = \frac{\xi_h}{(1+\eta^2)^{\frac{1}{2}}}.$$

Equations (2.23) and (2.24) illustrate the complementarity of the diffracted and transmitted intensities. Photographic plates placed in the two beams will show opposite contrast. This complementarity serves to underline the fact that the diffracted and refracted waves are really parts of the same wave field. Ewald compared the oscillation of energy between the refracted and diffracted waves to the periodic oscillation of energy between two coupled pendulums; hence the name *Pendellösung.*

The Pendellösung fringes seen in X-ray topographs are very similar to the parallel bright and dark bands observed much earlier in electron micrographs [50]. This similarity highlights the close relationship between X-ray diffraction and electron diffraction. In fact, the two processes can be described by the same set of equations, as will be shown later.

2.3 Takagi's Theory for an Imperfect Crystal

2.3.1 Background and Basic Postulates

In the 1950's and 60's, several theories were proposed to account for electron diffraction in an imperfect crystal. Cowley and Moodie introduced a *lamellar theory* [51],

in which the crystal is divided into a set of thin sheets or *lamellae*, parallel to the surface. They derived the relations between wave functions at successive lamellae, and showed how these relations could be used iteratively to obtain the wave function at the exit surface. In the *column approximation* of Hirsch, Howie and Whelan [52], the lamellar crystal is divided again into columns, perpendicular to the lamellae. The columns must be sufficiently narrow that the part of each lamella within a column may be considered perfect. In this case, the theory is applied to each column individually, to obtain the wave function at the exit surface. Howie and Whelan [53,54] used this theory to calculate electron micrographs due to dislocations in crystals.

One of the most successful theories of this period was developed independently by Takagi [55,56] and Taupin [57]. The theory describes both electron and X-ray diffraction within a common mathematical formulation, and is applicable to both perfect and imperfect crystals.

Takagi proposed that the Fourier components, $\underline{D}_h$, in equation (2.10) be allowed to vary slowly with position. It is then possible to take into account variations in the wave field induced by crystal lattice distortions.

Extending this idea, the wave function in a distorted crystal can be written:

$$\psi(\underline{r}) = \sum_g \psi_g(\underline{r}) \exp(-2\pi i \underline{k}_g.\underline{r}), \tag{2.25}$$

$$\begin{array}{lll} \text{where} & \underline{k}_g & = \underline{k}_o + \underline{g}, \\ \text{and} & \underline{g} & \text{is a reciprocal lattice vector.} \end{array} \tag{2.26}$$

The ψ_g in (2.25) can be replaced by Fourier components ψ'_g, based on a local reciprocal lattice associated with the distortion, provided the exponential term is multiplied by a suitable phase factor. Hence,

$$\psi(\underline{r}) = \sum_g \psi'_g(\underline{r}) \exp[-2\pi i S_g(\underline{r})], \tag{2.27}$$

where

$$S_g(\underline{r}) = \underline{k}_g.\underline{r} - \underline{g}.\underline{u}(\underline{r}_o). \tag{2.28}$$

The function $\underline{u}(\underline{r})$ represents the displacement of a lattice point due to a distortion. Consequently, a point $\underline{r}_o$ in the perfect crystal is displaced to a point $\underline{r}$ in the distorted crystal, given by:

$$\underline{r} = \underline{r}_o + \underline{u}(\underline{r}_o). \tag{2.29}$$

Takagi defined the wave vector $\underline{k}'_g$, such that:

$$\underline{k}'_g = \underline{\nabla} S_g(\underline{r}) = \underline{k}_g - \underline{\nabla}(\underline{g}.\underline{u}). \tag{2.30}$$

Consider a reciprocal lattice vector, $\underline{g}'$, associated with the local reciprocal lattice of the distorted region. It can be shown that:

$$\underline{g}' = \underline{g} - \underline{\nabla}[\underline{g}.\underline{u}(\underline{r}_o)]. \tag{2.31}$$

Combining (2.30) and (2.31), we have:

$$\underline{k}'_g = \underline{k}_o + \underline{g}'. \tag{2.32}$$

ψ_g and ψ'_g are now functions of position, so that any small change, $\Delta\underline{k}_o$, in $\underline{k}_o$ can be compensated for by multiplying $\psi_g(\underline{r})$ or $\psi'_g(\underline{r})$ by a factor $\exp(2\pi i\Delta\underline{k}_o.\underline{r})$, without affecting their spatial variation. This is true so long as $\Delta\underline{k}_o$ is sufficiently smaller than any reciprocal lattice vector. The possibility of ambiguity in $\underline{k}_o$ is removed by setting

$$\mid \underline{k}_o \mid = nk = n \mid \underline{k} \mid, \tag{2.33}$$

where n = mean refractive index,
and $\underline{k}$ = wave vector in vacuum.

Takagi introduced a function called the *crystalline field*, $\chi(\underline{r})$, defined such that:

$$\text{(a). in the electron case,} \quad \chi_e(\underline{r}) = \frac{V(\underline{r})}{E}, \tag{2.34}$$

where $V(\underline{r})$ = electrostatic potential in crystal,
and E = accelerating voltage of electron,

$$\text{(b). in the X-ray case,} \quad \chi_x(\underline{r}) = \frac{-e^2\lambda^2}{\pi mc^2}.n(\underline{r}), \tag{2.35}$$

where	e	=	electronic charge,
	λ	=	wavelength,
	m	=	electron mass,
	c	=	velocity of light,
and	$n(\underline{r})$	=	density of electrons at point $\underline{r}$.

The periodicity of χ enables us to write:

$$\chi(\underline{r}) = \sum_g \chi_g \exp(-2\pi i\underline{g}.\underline{r}). \tag{2.36}$$

Using (2.29), the crystalline field in the distorted crystal is:

$$\chi'(\underline{r}) = \chi[\underline{r} - \underline{u}(\underline{r}_o)]. \tag{2.37}$$

Combining (2.36) and (2.37), we obtain:

$$\chi'(\underline{r}) = \sum_g \chi_g \exp[-2\pi i(\underline{g}.\underline{r} - \underline{g}.\underline{u})]. \tag{2.38}$$

Using the above, we now consider electrons and X-rays separately and derive, for each, the appropriate equation for diffraction in a crystal.

2.3.2 The Electron Case

The Schrödinger Equation for an electron in an electrostatic potential $V(\underline{r})$, given by (2.34), can be written:

$$\nabla^2\psi(\underline{r}) + 4\pi^2k^2[1+\chi'(\underline{r})]\psi(\underline{r}) = 0, \tag{2.39}$$

where k is defined in (2.32).

The periodicity of the crystalline potential, $V(\underline{r})$, is embodied in the definition, (2.38), of $\chi'(\underline{r})$.

Substituting (2.27) and (2.38) into (2.39) gives:

$$\begin{aligned}\sum_g\{\nabla^2\psi'_g(\underline{r}) + 2\pi i\nabla^2(\underline{g}.\underline{u})\psi'_g(\underline{r}) - 4\pi i[\underline{k}'_g.\underline{\nabla}\psi'_g(\underline{r})]\\ + 4\pi^2[k^2(1+\chi_o) - \underline{k}_g^2]\psi'_g(\underline{r})\\ + 4\pi^2k^2\sum_{g'\neq g}\chi_{g-g'}\psi'_{g'}(\underline{r})\}.\exp[-2\pi i(\underline{k}_g.\underline{r} - \underline{g}.\underline{u})]\\ = 0.\end{aligned} \tag{2.40}$$

The spatial variation of $\psi'(\underline{r})$ and $(\underline{g}.\underline{u})$ is significant only on a macroscopic scale of the order of atomic dimensions. Hence, the first and second terms in the curly bracket of (2.40) can be neglected. The remaining terms are also of such macroscopic variation, and can be taken out of the integral when (2.40) is mutiplied by $\exp[2\pi i(\underline{k}_h.\underline{r} - \underline{h}.\underline{u})]$ and integrated with respect to $\underline{r}$ over a unit cell, where $\underline{h}$ is a reciprocal lattice vector. Upon doing this, the only non-vanishing term in the summation is for $g = h$, and we obtain:

$$[\underline{k}'_h.\underline{\nabla}\psi'_h(\underline{r})] = -i\pi[k^2(1+\chi_o) - \underline{k}'^2_h]\psi'_h(\underline{r}) - i\pi k^2\sum_{h'\neq h}\chi_{h-h'}\psi'_{h'}(\underline{r}). \tag{2.41}$$

For strong diffraction, $k \cong |\,\underline{k}'_h\,|$, so dividing through (2.41) by k gives:

$$[\underline{S}_h.\underline{\nabla}\psi'_h(\underline{r})] = i2\pi k\beta'_h(\underline{r})\psi'_h(\underline{r}) - i\pi k\sum_{h'\neq h}\chi_{h-h'}\psi'_{h'}(\underline{r}), \tag{2.42}$$

where $\underline{S}_h$ is the unit vector in the direction of $\underline{k}_h$, and

$$\beta'_h = \beta_h - \frac{1}{k}\frac{\partial}{\partial S_h}[\underline{h}.\underline{u}(\underline{r})], \tag{2.43}$$

$$\text{where}\quad \beta_h = \frac{|\,\underline{k}_h\,|^2 - |\,\underline{k}_o\,|^2}{2k^2}.$$

Equation (2.42) is the fundamental equation of electron diffraction in a crystal, and includes the equations derived from lamellar theories as a special case.

2.3.3 The X-ray Case

The electric displacement, D, induced by X-rays in a crystalline medium is given by the wave equation:

$$\nabla^2 \underline{D} + 4\pi^2 k^2 \underline{D} + 4\pi \underline{\nabla} \times \underline{\nabla} \times \underline{P} = 0, \tag{2.44}$$

where $\underline{k}$ is defined in (2.33).

Furthermore, the electric polarisation, $\underline{P}$, is given by:

$$4\pi \underline{P} = \chi' \underline{D}, \tag{2.45}$$

where χ' represents the quantity in (2.35), for an imperfect crystal.

Expressing $\underline{D}$ in a form analogous to equation (2.27), we obtain:

$$\underline{D}(\underline{r}) = \sum_g \underline{D}'_g(\underline{r}) \exp[-2\pi i(\underline{k}_g.\underline{r} - \underline{g}.\underline{u})], \tag{2.46}$$

where $\underline{k}_g$ is defined in (2.26), and the $\underline{D}'_g$ are associated with a distorted crystal. Similarly for $\underline{P}$:

$$\begin{aligned} \chi'(\underline{r})\underline{D}(\underline{r}) &= 4\pi \underline{P}(\underline{r}) \\ &= 4\pi \sum_g \underline{P}'_g(\underline{r}). \exp[-2\pi i(\underline{k}_g.\underline{r} - \underline{g}.\underline{u})], \end{aligned} \tag{2.47}$$

where $\underline{P}'_g(\underline{r})$ is given by:

$$4\pi \underline{P}'_g(\underline{r}) = \sum_{g'} \chi_{g-g'}(\underline{r}) \underline{D}'_{g'}(\underline{r}). \tag{2.48}$$

After some manipulation, Takagi showed that:

$$\begin{aligned} \underline{\nabla} \times \underline{\nabla} \times \underline{P} &= -4\pi^2 \sum_g [\underline{k}_g \times [\underline{k}_g \times \underline{P}'_g]] \\ &\quad \times \exp[-2\pi i(\underline{k}_g.\underline{r} - \underline{g}.\underline{u})], \end{aligned} \tag{2.49}$$

and

$$\begin{aligned} \nabla^2 \underline{D} &= \sum_g \{-4\pi i(\underline{k}'_g.\underline{\nabla})\underline{D}'_g - 4\pi^2 \underline{k}'^2_g \underline{D}'_g\} \\ &\quad \times \exp[-2\pi i(\underline{k}_g.\underline{r} - \underline{g}.\underline{u})]. \end{aligned} \tag{2.50}$$

Substitution of (2.49) and (2.50) into (2.44) gives:

$$\begin{aligned} &\sum_g \{-4\pi i(\underline{k}_g.\underline{\nabla})\underline{D}'_g + 4\pi^2(\underline{k}^2 - \underline{k}'^2_g)\underline{D}'_g \\ &+ 4\pi^2 \sum_{g'} \chi_{g-g'}[\underline{D}'_{g'}]_g\}. \exp[-2\pi i(\underline{k}_g.\underline{r} - \underline{g}.\underline{u})] \\ &= 0, \end{aligned} \tag{2.51}$$

$$\text{where} \quad [\underline{D}'_{g'}]_g = \frac{-1}{|\underline{k}'_g|}[\underline{k}'_g \times [\underline{k}'_g \times \underline{D}'_{g'}]], \tag{2.52}$$

and denotes the component vector of $\underline{D}'_{g'}$ perpendicular to $\underline{k}_g$.

If we multiply (2.51) by $\exp[2\pi i(\underline{k}_h.\underline{r} - \underline{h}.\underline{u})]$ and integrate with respect to $\underline{r}$ over a unit cell then, as with the derivation of (2.41) from (2.40), we obtain:

$$(\underline{S}_h.\underline{\nabla})\underline{D}'_h = i2\pi k\beta'_h\underline{D}'_h - i\pi k \sum_{h' \neq h} \chi_{h-h'}[\underline{D}'_{h'}]_h. \tag{2.53}$$

Equation (2.53) is the fundamental equation of X-ray diffraction in a crystal.

2.3.4 General Formulation of the Diffraction Equations

It will be seen that the equations (2.42) and (2.53) are of the same form. Takagi showed that, in the two beam case, equations (2.42) and (2.53) reduce to:

$$\begin{aligned} \frac{\partial \psi'_o}{\partial S_o} &= -i\pi k C\chi_{\bar{h}}\psi'_h \\ \frac{\partial \psi'_h}{\partial S_h} &= -i\pi k C\chi_h\psi'_o + i2\pi k\beta'_h\psi'_h, \end{aligned} \tag{2.54}$$

where β'_h is given by (2.43).

There are three distinct cases of polarisation:

1. the electron case,
2. the X-ray case where both $\underline{D}'_o$ and $\underline{D}'_h$ are perpendicular to the plane of incidence, defined by $\underline{k}_o$ and $\underline{k}_h$, and
3. the X-ray case where both $\underline{D}'_o$ and $\underline{D}'_h$ are parallel to the plane of incidence.

The polarisation factor, C, in (2.54) is given by:

$$\begin{aligned} C &= 1, \text{ for cases 1 and 2,} \\ \text{and} \quad C &= \cos 2\theta_B, \text{ for case 3.} \end{aligned}$$

In the X-ray case, ψ'_o and ψ'_h can be replaced by $\underline{D}'_o$ and $\underline{D}'_h$, respectively. Hence, the fundamental equations describing X-ray diffraction in a crystal are:

$$\begin{aligned} \frac{\partial \underline{D}'_o}{\partial S_o} &= -i\pi k C\chi_{\bar{h}}\underline{D}'_h \\ \frac{\partial \underline{D}'_h}{\partial S_h} &= -i\pi k C\chi_h\underline{D}'_o + i2\pi k\beta'_h\underline{D}'_h. \end{aligned} \tag{2.55}$$

Chapter 3

Simulation of X-ray Topographs

3.1 Background and Motivation

An experimental topograph is a map of the intensity distribution across the beam diffracted by the crystal under investigation. As we have seen already, the presence of a defect inside the crystal imbues the resulting image with a rich structure.

A knowledge of the amplitude and phase of the radiation at the exit surface is sufficient to allow the calculation of the diffraction processes inside the crystal. Unfortunately, the topograph can only provide the modulus of the amplitude and not the phase, so that it is impossible to parameterise the defect by reference to the topograph alone. Consequently, it is necessary to introduce an elastic strain model for the defect, and to use this in conjunction with Takagi's equations (2.55) to simulate the diffraction processes within the crystal. The response of the recording medium must then be taken into account in order to obtain a simulation of the topograph itself. Careful adjustment of the parameters associated with the strain model and the crystal itself allows matching of simulation with experiment, and hence a direct evaluation of the real physical parameters associated with the defect. The simulation process outlined above will be used extensively in the following chapters for the characterisation of various crystal defects, and the field of X-ray topography simulation has been reviewed thoroughly by Epelboin [58,59].

An essential feature of the simulation technique is the solution of Takagi's equations (2.55). Analytical solutions have been established for a perfect, unbent crystal in the Laue geometry [56] and in the Bragg geometry [60]. In addition, substantial work has been done [61,62,63] to establish specific solutions for the case of a crystal bent by a uniform strain gradient. In general, however, it is necessary to integrate Takagi's equations by means of an iterative algorithm. The preferred, and widely used, method is that of Authier et al. [64]. It is a half-step derivative method, and has been shown [65] to be the fastest method of integrating Takagi's equations.

3.2 Derivation of the Iterative Algorithm

The principle will be to impose a regularly spaced array of points on the Borrmann fan and to work out, from point to point, the local values of the wave amplitudes, D_o and D_h. Fig. 3.1 illustrates how this may be done.

The wave amplitudes at point P on the exit surface are defined by the diffraction processes in the triangle ABP. A set of *characteristic lines* is drawn in this triangle, parallel to the $\underline{S}_o$ and $\underline{S}_h$ directions. The point of intersection of two characteristic lines is called a *node*, and the spacing of two adjacent nodes in the $\underline{S}_o$ and $\underline{S}_h$ directions is p and q, respectively. The vertical separation of nodal layers is represented by the variable $ELEM$, and the horizontal separation of adjacent nodes by the variable $TRANSV$.

Let us represent the wave amplitudes, D_o and D_h, by a continuously differentiable function $f(x)$, Fig. 3.2. Provided the variation of f with x is slow, the gradient of the curve at B is approximately equal to the gradient of the line AC, so that:

$$\left(\frac{df}{dx}\right)_{x+\frac{p}{2}} \approx \frac{f(x+p)-f(x)}{p}. \tag{3.1}$$

Rearranging (3.1):

$$f(x+p) \approx f(x) + p\left(\frac{df}{dx}\right)_{x+\frac{p}{2}}. \tag{3.2}$$

Consider Takagi's equations, (2.55):

$$\begin{aligned} \frac{\partial D_o'(r)}{\partial S_o} &= -i\pi kC\chi_{\bar{h}}D_h'(r) && \ldots(a) \\ \frac{\partial D_h'(r)}{\partial S_h} &= -i\pi kC\chi_h D_o'(r) + 2i\pi k\beta_h' D_h'(r) && \ldots(b) \end{aligned} \tag{3.3}$$

Henceforth, we will consider an imperfect crystal, so the primes can be removed. In the following derivation, the polarisation factor, C, is set to unity, since the π-component only is taken into account in numerical integration, to minimise the computational time. Multiplying (3.3a) by p and (3.3b) by q, and replacing r by the oblique coordinates (S_o, S_h), we obtain:

$$\begin{aligned} p\frac{\partial}{\partial S_o}D_o(S_o,S_h) &= 2AD_h(S_o,S_h) && \ldots(a) \\ q\frac{\partial}{\partial S_h}D_h(S_o,S_h) &= 2BD_o(S_o,S_h) + 2W(S_o,S_h)D_h(S_o,S_h), && \ldots(b) \end{aligned} \tag{3.4}$$

$$\begin{aligned} \text{where } A &= \frac{-1}{2}i\pi pk\chi_{\bar{h}}, \\ B &= \frac{-1}{2}i\pi qk\chi_h, \\ \text{and } W(S_o,S_h) &= i\pi qk\beta_h', \end{aligned}$$

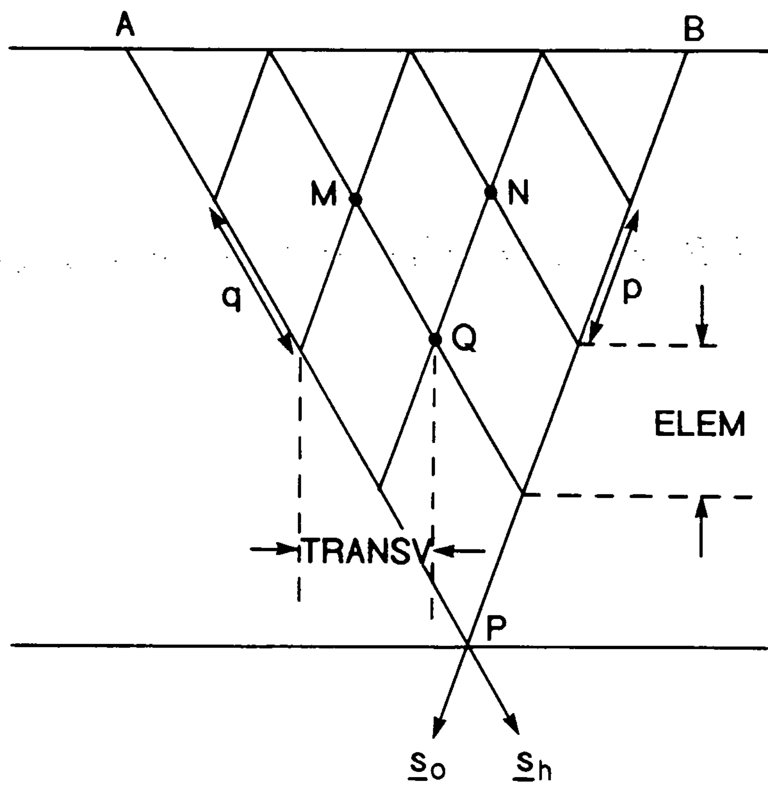

Fig. 3.1: Regularly spaced array of nodes within the Borrmann fan.

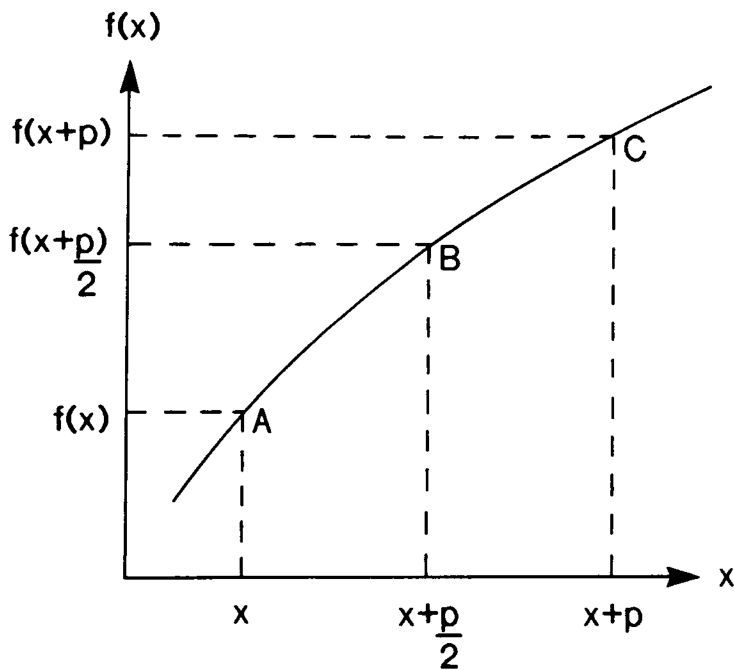

Fig. 3.2: Variation af a continuously differentiable, slowly varying function of the hypothetical variable x.

where β'_h is given in equation (2.43).

Expressing D_o, D_h in the half-step derivative form of (3.1) leads to:

$$\begin{aligned} p\frac{\partial}{\partial S_o}D_o(S_o-\frac{p}{2},S_h) &= D_o(S_o,S_h)-D_o(S_o-p,S_h), \\ q\frac{\partial}{\partial S_h}D_h(S_o,S_h-\frac{q}{2}) &= D_h(S_o,S_h)-D_h(S_o,S_h-q). \end{aligned}$$

Combining with equations (3.4) gives:

$$\begin{aligned} D_o(S_o,S_h) &= D_o(S_o-p,S_h)+2AD_h(S_o-\tfrac{p}{2},S_h) & \ldots(a) \\ D_h(S_o,S_h) &= D_h(S_o,S_h-q)+2BD_o(S_o,S_h-\tfrac{q}{2}) \\ &\quad +2W(S_o,S_h-\tfrac{q}{2})D_h(S_o,S_h-\tfrac{q}{2}). & \ldots(b) \end{aligned} \tag{3.5}$$

Now, provided f varies slowly with x, we can write:

$$\begin{aligned} f(x+\frac{p}{2}) &= \frac{f(x)+f(x+p)}{2}, \\ \text{so that}\quad 2f(x+\frac{p}{2}) &= f(x)+f(x+p). \end{aligned} \tag{3.6}$$

Assuming that the wave amplitudes D_o, D_h vary slowly in the Takagi equations, we may use (3.6) to re-write (3.5) as:

$$\begin{aligned} D_o(S_o,S_h) &= D_o(S_o-p,S_h)+AD_h(S_o-p,S_h)+AD_h(S_o,S_h) & \ldots(a) \\ D_h(S_o,S_h) &= D_h(S_o,S_h-q)+BD_o(S_o,S_h-q) \\ &\quad +BD_o(S_o,S_h)+W\left(S_o,S_h-\tfrac{q}{2}\right)D_h(S_o,S_h-q) \\ &\quad +W\left(S_o,S_h-\tfrac{q}{2}\right)D_h(S_o,S_h). & \ldots(b) \end{aligned} \tag{3.7}$$

Substituting for $D_h(S_o,S_h)$ from (3.7b) into (3.7a) gives:

$$\begin{aligned} D_o(S_o,S_h) &= E\{C_2D_o(S_o-p,S_h)+AC_2D_h(S_o-p,S_h) \\ &\quad +ABD_o(S_o,S_h-q)+AC_1D_h(S_o,S_h-q)\}, \end{aligned} \tag{3.8}$$

$$\begin{aligned} \text{where}\quad C_1 &= 1+W, \\ C_2 &= 1-W, \\ E &= \frac{1}{1-W-AB}, \\ \text{and}\quad W &= i\pi kq\beta'_h\left(S_o,S_h-\frac{q}{2}\right). \end{aligned}$$

Similarly, substituting for $D_o(S_o, S_h)$ from (3.7a) into (3.7b) gives:

$$\begin{aligned} D_h(S_o, S_h) &= E\{BD_o(S_o - p, S_h) + ABD_h(S_o - p, S_h) \\ &\quad + BD_o(S_o, S_h - q) + C_1 D_h(S_o, S_h - q)\}. \end{aligned} \tag{3.9}$$

Equations (3.8) and (3.9) can be expressed in matrix form:

$$\begin{bmatrix} D_o(S_o, S_h) \\ D_h(S_o, S_h) \end{bmatrix} = E \begin{bmatrix} C_2 & AC_2 & AB & AC_1 \\ B & AB & B & C_1 \end{bmatrix} \begin{bmatrix} D_o(S_o - p, S_h) \\ D_h(S_o - p, S_h) \\ D_o(S_o, S_h - q) \\ D_h(S_o, S_h - q) \end{bmatrix}. \tag{3.10}$$

Using equations (3.10), the values of D_o and D_h at any point T in the integration network, Fig. 3.3, can be calculated, given the corresponding values at R and S, and the value of the term W at point W.

In practice, a computer program based on equations (3.10) is used to calculate the amplitudes D_o and D_h at all points throughout the integration network. The intensity distribution of the diffracted beam striking the film may then be calculated, using the values of D_h at the exit surface.

3.3 Integration of Takagi's Equations

A spherical incident wave is simulated by considering a single point source of radiation at the entrance surface. Using this model, the amplitude distribution of the diffracted beam at the exit surface of a perfect crystal is given by the J_o Bessel function, illustrated in Fig. 3.4. The edges K and M of the curve in Fig. 3.4 correspond to the $\underline{S_o}$ and $\underline{S_h}$ directions. Close to the Borrmann fan edges, the diffracted wavefield has high intensity and rapid spatial variation. The horizontal step, $TRANSV$, must be sufficiently small to take these effects into account. Too few nodes in the region between K and L will have two undesirable effects. First of all, much of the intensity in this region will be missed by the simulation program, and the resulting direct image will be unrealistically bright. Also, the derivation of the previous section assumed a slow variation in wave amplitude between successive nodes. If $TRANSV$ is too large, this condition will cease to be fulfilled, and the simulation program will no longer be reliable.

A plane wave is modelled by many coherent point sources ranged across the entrance surface. In this case, the value of $TRANSV$ must be sufficiently small that the variation in phase between two successive nodes is small. In practical terms, the integration step should be as small as possible to maximise the accuracy of the simulation, and as large as possible to minimise the computation time. For each simulation, a compromise between these two considerations must be found.

Originally, simulations were performed using *constant step algorithms* (C.S.A.'s), in which the integration steps p and q, Fig. 3.3, are constant. This is satisfactory for simulation of section topographs where the direct image is not of interest. In

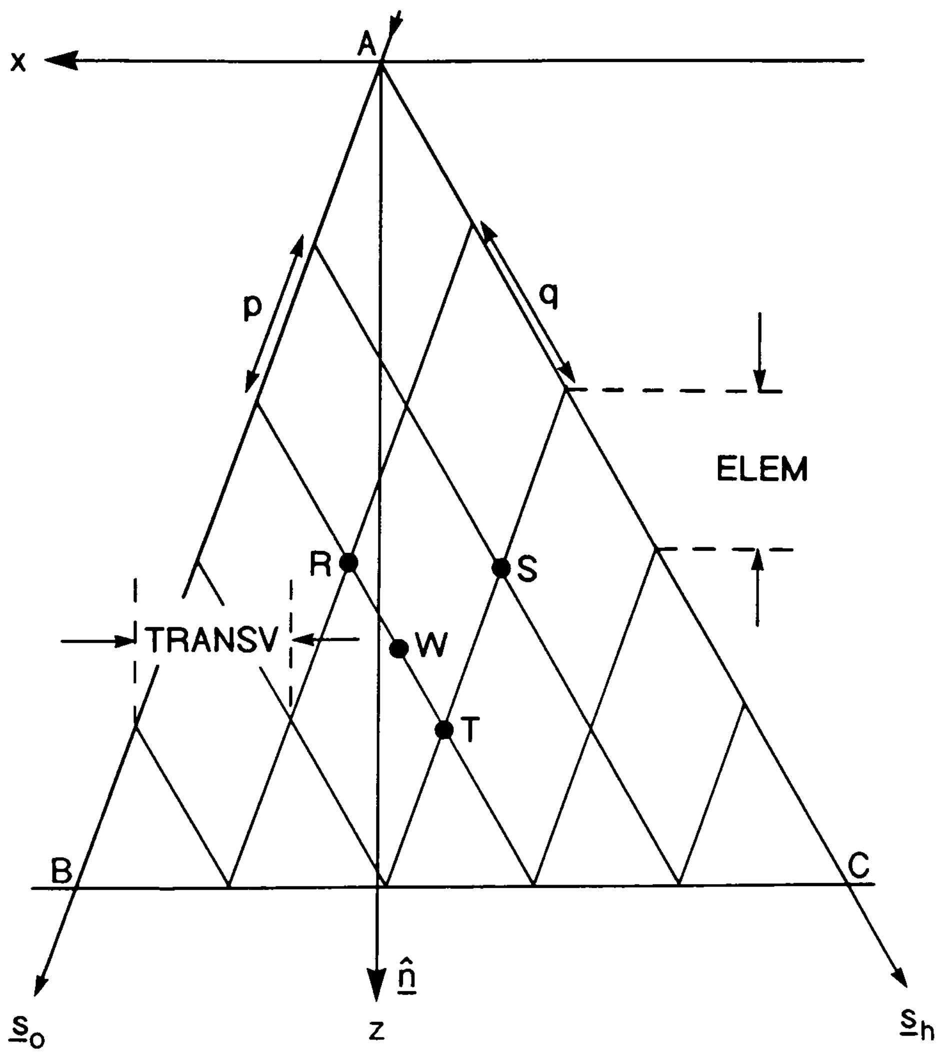

Fig. 3.3: Integration network within the Borrmann fan.

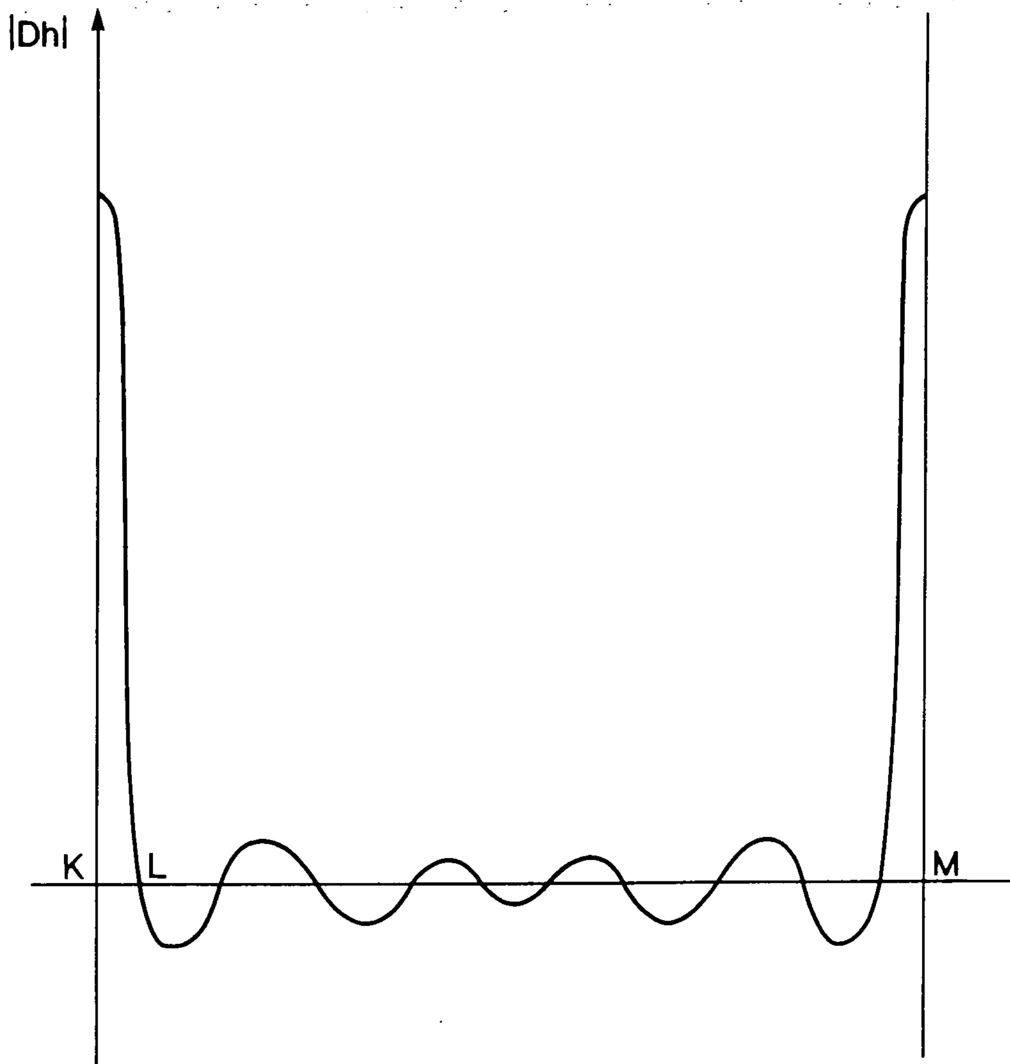

Fig. 3.4: Schematic variation of the diffracted wave amplitude, $\mid D_h \mid$, along the exit surface, for a perfect crystal.

traverse topographs, most of the contrast arises from integration of the direct image. In this case, and others where the direct image is significant, the constant horizontal and vertical integration steps of the C.S.A. are not necessarily sufficient to accommodate the variation in wave amplitudes near the Borrmann fan edges. For these cases, Petrashen [66] proposed a *varying step algorithm* (V.S.A.), in which the steps p and q are reduced near the Borrmann fan edges. Epelboin [67,68] devised a V.S.A. in which the integration steps are chosen throughout the Borrmann fan so as to reflect faithfully the local variation in wave amplitudes. Epelboin comments that the position of the perfect crystal extinction fringes, Fig. 3.5, given by the zeros of the J_o Bessel function, is a guide to the variation in wave amplitudes. The number density of nodes across the exit surface is chosen locally to suit the variation in wave amplitudes between adjacent zeros of J_o, Fig. 3.6. The integration steps are automatically increased in regions of the Borrmann fan where the amplitude variation is slow. In this way, it is possible to generate a V.S.A. network with fewer nodes than the corresponding C.S.A. arrangement. This combines increased accuracy with decreased computation time. The simulations in this thesis are exclusively associated with section topographs, and the intermediary image is by far the most sensitive to such strains, providing the most useful information. Consequently, a C.S.A. has been used throughout the simulation work in the following chapters.

3.4 Simulation of Real Topographs

To complete this survey of simulation techniques, it is necessary to consider some practical aspects which will turn the integration method above into a working simulation tool. The network of Fig. 3.3 assumes an infinitesimally narrow incident beam. Clearly, this is not practical, since experimental section topography utilises beams of width in excess of $10\mu m$. The solution is illustrated in Fig. 3.7. Several point sources are ranged across the entrance surface, over a distance corresponding to the beam width, and each point source gives rise to an elementary section topograph. The resultant topograph is a superposition of these elementary contributions. It will be seen that the greater the required resolution, the greater the number of elementary section topographs. In the case of a V.S.A., the situation is more complicated, since the distance between two computed points is no longer constant. The solution is to increase the array of computed intensities. Intermediate points are calculated by interpolation, the distance between two such points being equal to the minimum separation of adjacent nodes in the integration network. An apodisation process is used to reduce the total number of calculated intensity points along the exit surface, to be consistent with the required resolution of the simulation. To simulate a traverse topograph, the method, Fig. 3.8, is to add the intensity of the section topographs due to a discrete distribution of sources between X and Y.

The response of the photographic emulsion must be incorporated into the simulation process, in order to convert the raw intensity data into a visual representation of the final topograph. Details such as the emulsion thickness, exposure time and development temperature should be taken into account. The influence of these fac-

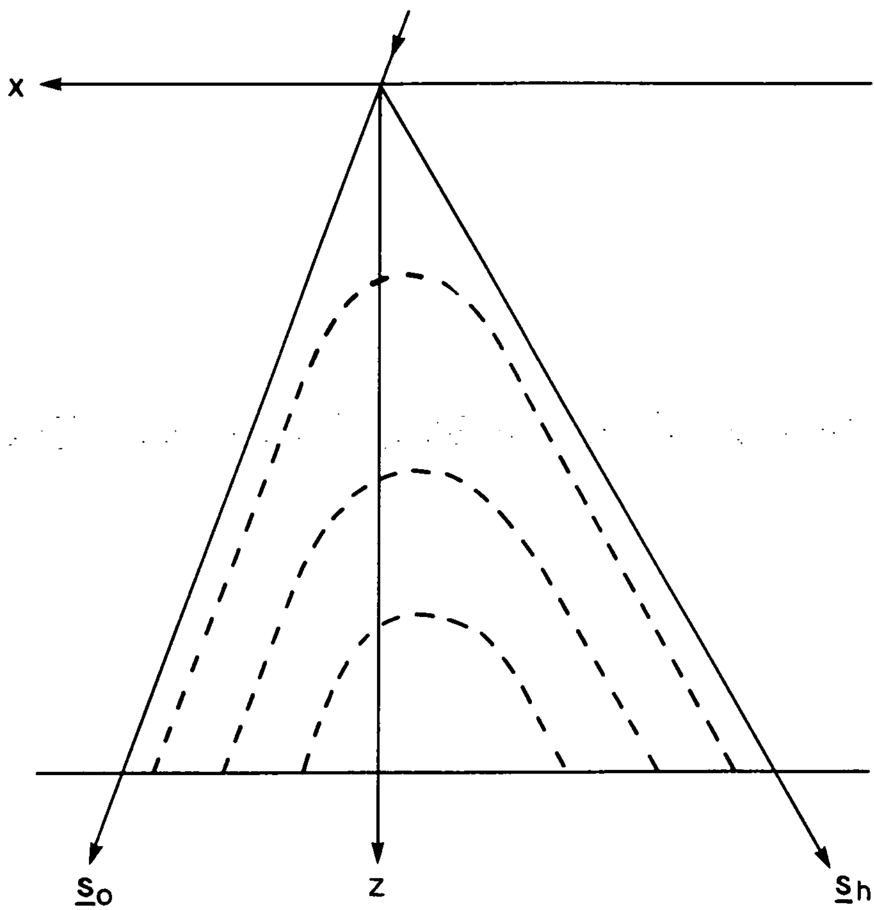

Fig. 3.5: Schematic representation of the positions of the perfect crystal extinction fringes, (after Epelboin).

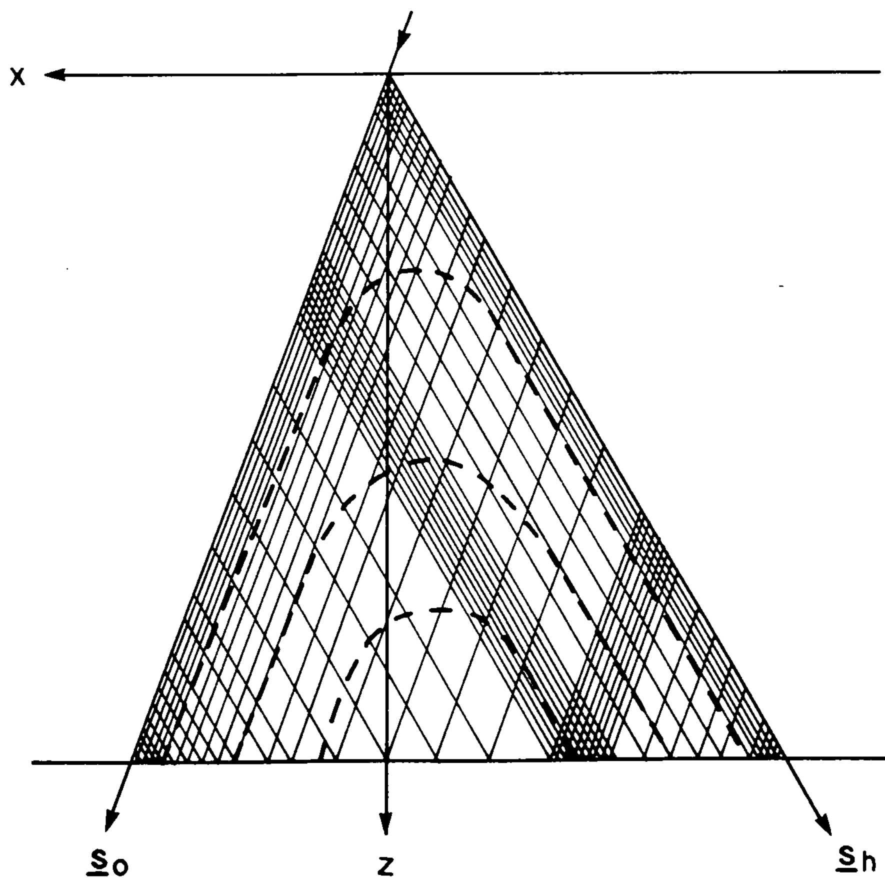

Fig. 3.6: The V. S. A. integration network, (after Epelboin).

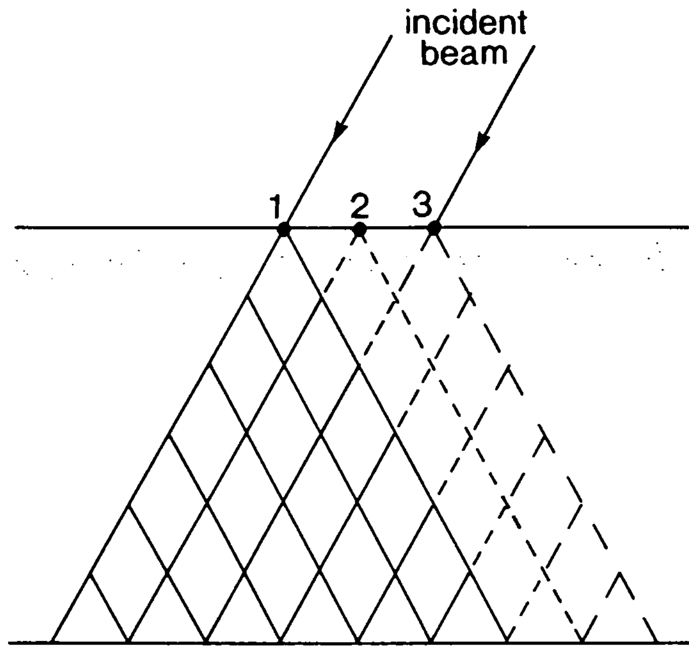

Fig. 3.7: Simulation of a real section topograph, taking into account finite beam width, (after Epelboin).

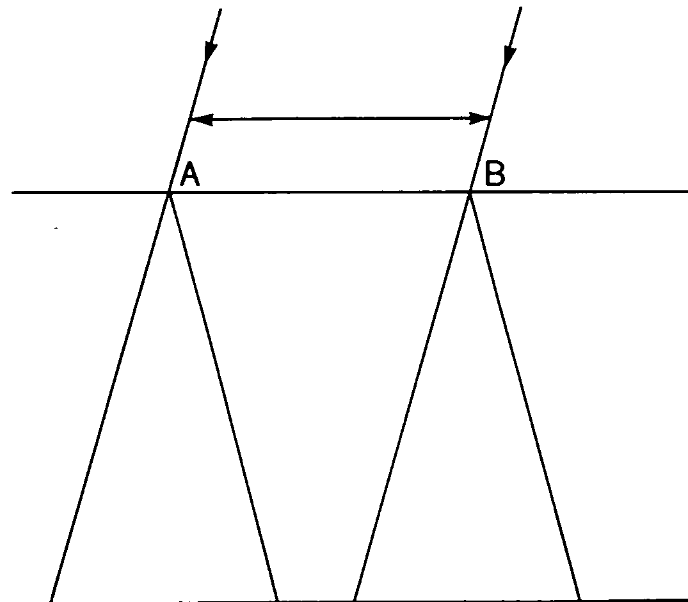

Fig. 3.8: Simulation of a real traverse topograph, (after Epelboin).

tors on image quality has already been discussed in Chapter 1. The photographic response is characterised by the relation between the density of grey levels, D, and the illumination, E, defined by:

$$\begin{aligned} E &= It, \\ \text{where } I &= \text{intensity of source radiation,} \\ \text{and } t &= \text{exposure time.} \end{aligned}$$

The photo-representation program used in the current work is due to Dr. S. Cottrell, formerly of Durham University. The relation between D and E was taken as linear, as this is a very good approximation for a wide range of illumination values. Only in the representation of the direct image does this linearity break down. This point will be considered at length in Chapter 6. The photo-representation program selects a range of illumination values, consistent with the conditions associated with each simulation. Deepest black is then associated with the maximum illumination in this range, whilst brightest white is associated with the minimum illumination. Hence, the response of the photographic film is simulated.

Various techniques have been used to generate paper prints of simulations. The first X-ray topography simulation was produced in 1967 by Balibar and Authier [69]. The calculation required 24 hours of computation time, and the final image, Fig. 3.9, was drawn by hand.

Subsequently, line printers were used, where different levels of grey were rendered by overprinting. Increased sophistication has allowed simulations to be viewed on a monitor, and adjusted, prior to printing.

The simulations in this thesis were performed on a SUN4 workstation. The raw intensity data is converted into a simulation of the topograph itself by means of the photo-representation program. The simulation may be viewed on a monitor, prior to submission to a laser printer as a *postscript* image file. The printer renders grey levels by suitable variation in the size of the black area within each pixell. This is illustrated in Fig. 3.10, which shows a blow-up of part of the simulation in Fig. 4.9 from the following chapter.

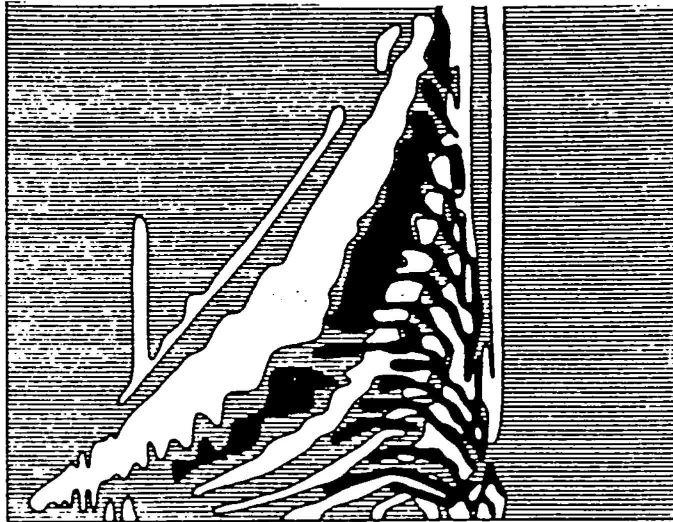

Fig. 3.9: The first simulation of an X-ray topograph, for the case of a dislocation, (after Balibar and Authier).

Fig. 3.10: Blow up of part of a simulation generated on the laser printer used in the current work. Levels of grey are defined by the proportion of black in each pixell.

Chapter 4

Investigation of the Strain Effects Associated with Oxygen Precipitates in Silicon

4.1 Formation and Growth of Precipitates

Single crystal silicon, for use in solid-state device manufacture, is grown by two standard techniques. These are the *Czochralski* (CZ) method and the *float-zone* (FZ) method, which have been reviewed thoroughly [70,71].

Consider Fig. 4.1, which illustrates the CZ method. The initially polycrystalline Si is contained in a, usually quartz, crucible. The charge can be heated above the melting point of Si by means of an r.f. coil which encloses the system envelope, Fig. 4.1. A single crystal seed, attached to a pull-rod by a chuck, is lowered to the surface of the molten Si, whose temperature is adjusted until a meniscus can be supported by the seed. The pull-rod is then slowly rotated and lifted, resulting in the growth of a cylindrical single crystal of Si. The diameter of the crystal can be selected in advance by careful adjustment of the rotation rate of the pull-rod.

Now consider Fig. 4.2, which illustrates the FZ method. A molten zone is held between a vertically mounted seed crystal and a charge rod by surface tension forces. The molten zone is moved slowly along the rod, by traversing the system envelope with an r.f. coil. The action of traversing the molten zone in this way tranforms the Si sample into a single crystal. During the traverse of the molten zone, the opposite ends of the Si rod are rotated in opposite senses, resulting in a smooth, cylindrical final crystal.

Hurle [71] has discussed the relative merits of the two techniques. The advantages of the CZ method are:

(a). the growing crystal is not in contact with a mould,
(b). crystals of different orientations can be grown by suitable selection of the orientation of the seed,
(c). industrially useful dopants can be added to the melt during growth,

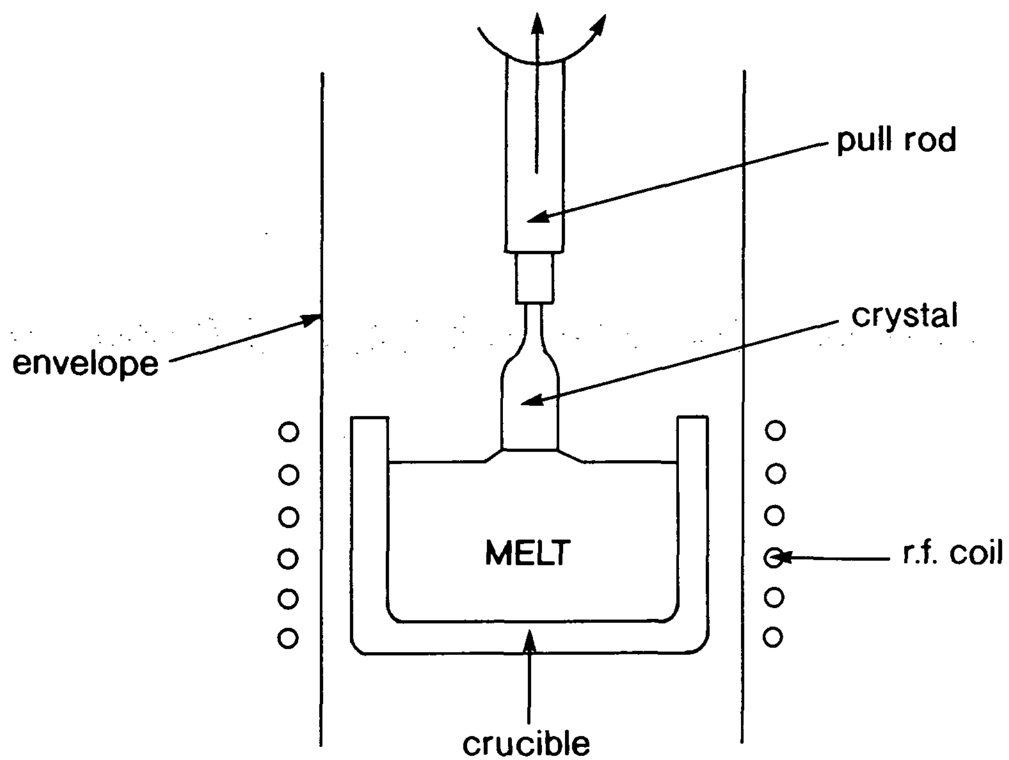

Fig. 4.1: The Czochralski (CZ) method of crystal growth.

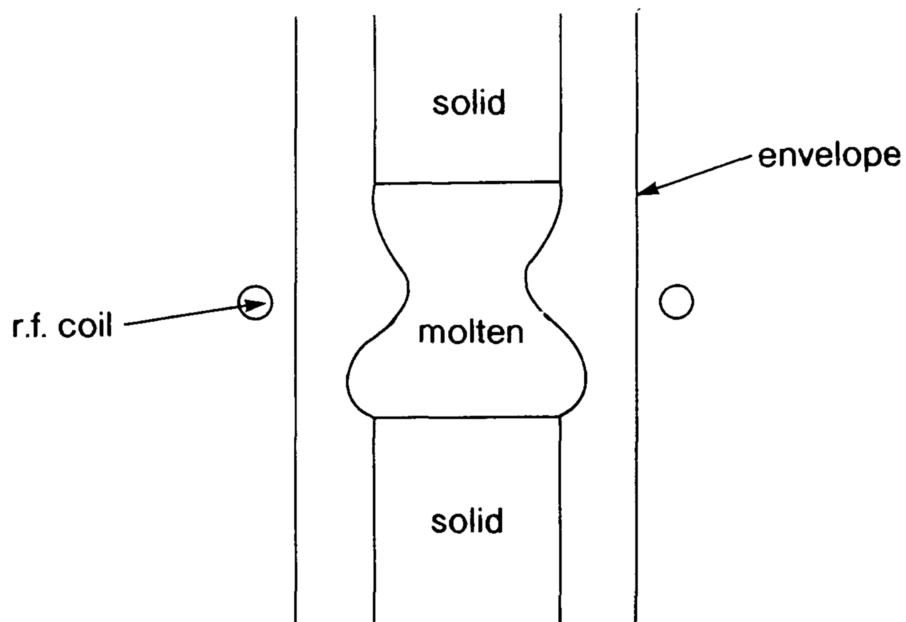

Fig. 4.2: The float-zone (FZ) method of crystal growth.

(d). the crystal can be viewed during growth, and
(e). it is possible to grow large diameter crystals.

The main advantage of the FZ method is that the Si melt is in contact only with its own solid, so that there is no risk of absorption of contaminants from a crucible. In addition, the solubility of impurities is higher in molten than in solid Si, so that repeated traversing of the molten zone results in most of the impurities being transported to one end of the rod. This end can then be cut off, using a diamond saw, leaving a rather pure crystal.

A feature common to both the CZ and the FZ methods is the incorporation of oxygen into the crystal during growth. During the CZ growth of Si, silicon dioxide from the quartz crucible reacts with Si in the melt, according to the reaction:

$$Si + SiO_2 \rightarrow 2SiO.$$

As a result of this, CZ Si can exhibit oxygen concentrations of the order of 10^{18} atoms cm^{-3}. In the FZ technique, Si also absorbs oxygen from the atmosphere surrounding the growing crystal during high temperature heat treatment, although the oxygen concentration is typically two orders of magnitude lower than for CZ Si. The presence of oxygen in Si can have both harmful and beneficial effects, as will be pointed out in due course.

It has been found that by applying a transverse [72,73,74] or vertical [75] magnetic field to the Si charge during CZ growth, the quality of the resulting crystal is enhanced in a number of important ways. This process, known as the *magnetic Czochralski* (MCZ) method, is illustrated for a transverse applied field in Fig. 4.3. Hoshi et al. [72] have shown that turbulent convection in Si melts during CZ growth can be suppressed upon application of a transverse magnetic field of 2000 gauss. They pointed out that MCZ Si is characterised by a lower and more uniform oxygen concentration than would be possible by the standard CZ method. In addition, they also commented that resistivity variation along the radius of the Si rod was more uniform than that found in FZ Si samples. On an industrial level, the advantages of the MCZ method are clear. Oxygen concentration can be selected within the range 0.5 - $12 \times 10^{17} cm^{-3}$, defect generation is inhibited and wafer warping during subsequent heat treatment is also reduced. Hoshikawa [75] has shown that MCZ growth in a vertical magnetic field has certain advantages over the standard transverse technique, above. The vertical field MCZ method is illustrated in Fig. 4.4. The magnetic field can be generated by a small-size, light solenoid, Fig. 4.4, and the field strength required to suppress thermal convection is less than for the tranverse method. In addition, the rotation conditions of the crystal and crucible can be selected independently, to adjust the oxygen concentration in the final crystal. To summarise, crystals can be grown by the MCZ method to a higher quality than would be possible by FZ growth, defining an important industrial niche for the MCZ method.

It has been known for some time [76,77] that Si crystals containing oxygen exhibit an infrared absorption peak at the $9 \mu m$ wavelength. This was explained [76,77] by associating the absorption peak with stretching of the $Si - O$ bond, in the configuration shown in Fig. 4.5. Here, the single oxygen atom acts as an interstitial,

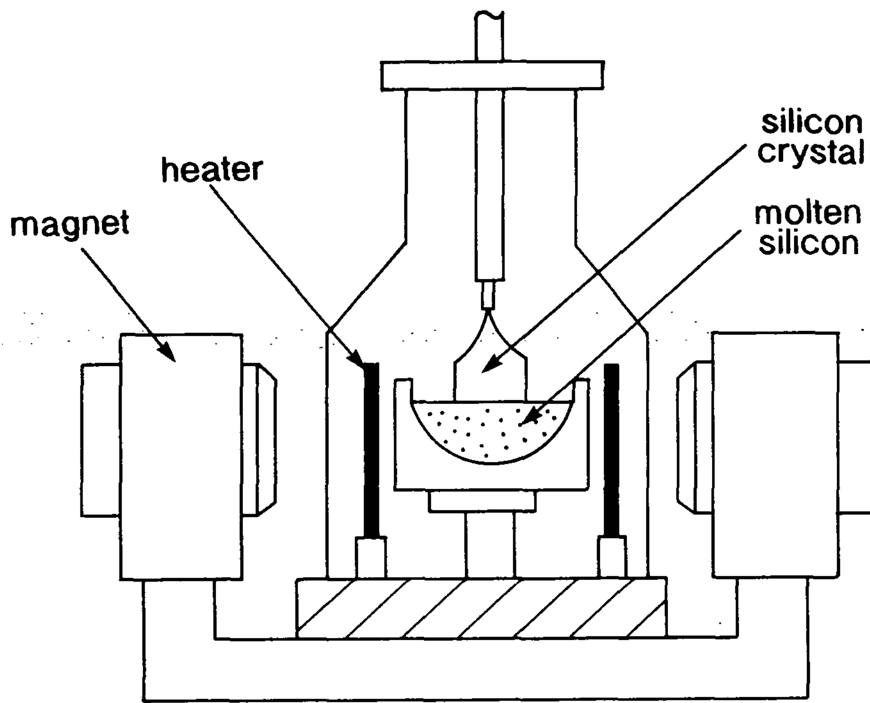

Fig. 4.3: The magnetic Czochralski (MCZ) method, in a transverse magnetic field.

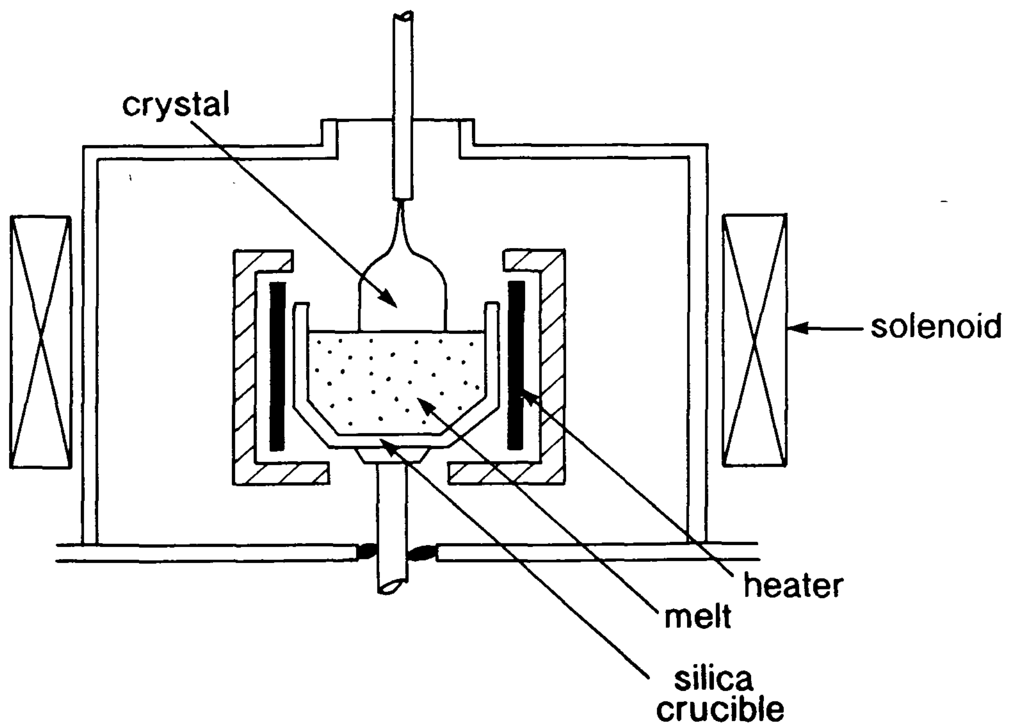

Fig. 4.4: The magnetic Czochralski (MCZ) method, in a vertically applied magnetic field.

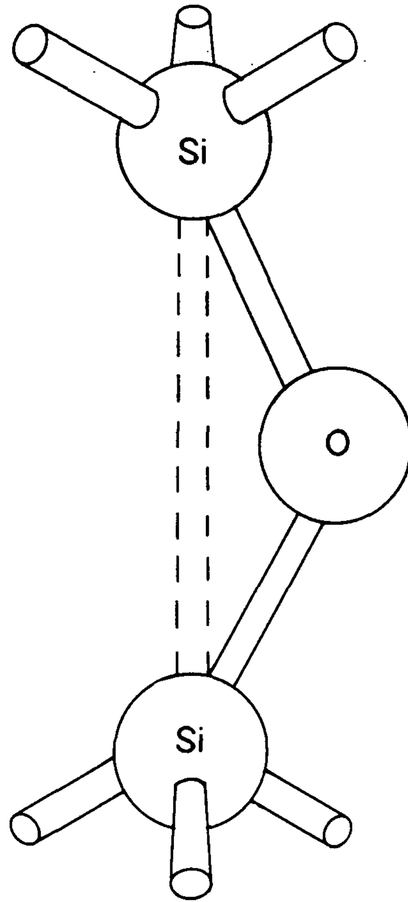

Fig. 4.5: Interstitial configuration of oxygen in the silicon lattice, (after Corbett et al.)

interrupting the normal $Si - Si$ valence bond. This hypothesis was strongly supported by the work of Bond and Kaiser [78], which showed a relative increase in lattice parameter in oxygen rich Si samples, consistent with the interstitial configuration of Fig. 4.5.

It is crucial to understand how oxygen, incorporated into the Si lattice in this way, behaves when the Si crystal is heat treated as part of device processing. At high temperatures, it may be expected that the $Si - O$ activation energy is exceeded by the thermal vibrational energy, so that oxygen is free to diffuse into the Si lattice. In 1957, Kaiser [79] presented the first experimental demonstration that oxygen atoms, liberated in this way, cluster together to form silicon oxide *precipitates.* He found that, following prolonged heat treatment at 1000°C, the $9\mu m$ infrared absorption band reduced, whilst the overall oxygen concentration remained constant, consistent with oxygen clustering.

Following Kaiser's discovery of oxygen precipitation in Si, a vast literature has accumulated on the subject [80,81,82,83,84], motivated in part by the clear industrial significance of this process. Patel [85] used X-ray anomalous transmission to show a reduction in perfection of Si crystal heated at 1000°C, due to defects induced by oxygen precipitates. Bender [86] has commented that these defects can have both harmful and beneficial effects on device performance. The undesirable effects include the formation of lattice defects in the active device region and wafer warpage during heat treatment. On the positive side, device quality is enhanced by wafer hardening due to reduced dislocation mobility, and the diffusion of oxygen out of the surface layer during heat treatment, leaving a defect-free *denuded zone.* Oxygen precipitates remaining in the bulk are used to remove harmful metallic impurities from the active device layer. This process is known as *intrinsic gettering* and will be the subject of the next chapter.

Section topography has been used successfully to measure the denuded zone depth in CZ Si and to determine the distribution and form of oxygen precipitates. Recently, the technique of *light scattering microscopy* (LSM) has been used [87] to reveal precipitates smaller than the limit detectable by X-ray section topography. Partanen et al. [87] have used LSM to identify precipitates with volumes down to about $1 \times 10^5 nm^3$.

The size and rate of growth of oxygen precipitates in Si is determined by the diffusion of oxygen atoms in the lattice during annealing, and by the duration of the annealing. Diffusion-based precipitate growth kinetics has been treated thoroughly and rigorously by Ham [88] and Flynn [89]. Wada et al. [90,91] have studied the growth kinetics of square-plate oxygen precipitates in CZ Si. They showed that the precipitate volume, V, is given by:

$$V(T,t) = \frac{8\pi\sqrt{2}}{3}\left[\frac{C_I - C_E}{C_S - C_E} D(T)t\right]^{\frac{3}{2}}, \quad (4.1)$$

where T, t are the annealing temperature and duration, respectively, C_I, C_E are the initial and equilibrium concentrations of oxygen interstitials, respectively, C_S is the oxygen atomic concentration in the precipitate and $D(T)$ is the oxygen diffusion coefficient.

The diffusion coefficient is a function of temperature, and is given [92] by;

$$\begin{aligned} D &= D_0 \exp\left[-\frac{E_m}{kT}\right], \\ \text{where } k &= \text{Boltzmann's constant}, \\ T &= \text{annealing temperature}, \end{aligned} \tag{4.2}$$

D_0 is a constant, and E_m is the energy required for a point defect to jump between adjacent lattice sites.

From equation (4.1), it is seen that the precipitate volume is proportional to $(Dt)^{\frac{3}{2}}$. Wada et al. [90,91] used this relation semi-empirically to investigate the nucleation and growth of oxygen precipitates in CZ Si. Messoloras et al. [93] have used the diffusion theory of Ham [88], in conjunction with their own infrared absorption measurements, to determine the number density and spherical radii of oxygen precipitates in Si. They studied samples with a grown-in oxygen concentration of $\sim 7\times10^{17} cm^{-3}$. After heating to saturation at 1050°C, the number density of precipitates was found to be $1.1\times10^{9} cm^{-3}$ and the spherical radius was 1,359Å. Using a similar approach, Binns et al. [94] calculated the number density of precipitates as a function of the diffusion coefficient, D, and a time constant defining the rate of incorporation of oxygen atoms into the precipitates. The theory of diffusion-based precipitate growth tends to be expressed in terms of spherical precipitates, which remain spherical as they grow. However, various workers have observed oxygen precipitates in Si with square-plate [95], ribbon-like [84] and even octahedral [96] form. However, it was noted [96] that the difference in volume between octahedral and spherical precipitates was small, and that [93] the growth equations for a spherical precipitate can be applied with good accuracy to other forms. These studies of precipitate growth are important, since the size of a precipitate determines its potential to generate harmful strain-induced defects.

It is also important to understand the nucleation of oxygen precipitates, as a step towards controlling the rate of precipitate formation. Furuya et al. [81] showed that *latent nuclei*, formed at temperatures in excess of 1200°C, change into active *defect nuclei* at temperatures below 800°C, which then grow into oxygen precipitates. It was proposed [81] that the latent nuclei are clusters of crystal point defects, and that the defect nuclei are tiny oxygen precipitates which grow as a result of annealing. The results indicated that latent nuclei are unstable during annealing in the temperature range 900-1100°C, with a correspondingly low precipitate density in the processed sample. Further work [82] showed that the presence of carbon in CZ Si enhances the precipitation of oxygen, and was explained in terms of the nucleation mechanism outlined above. Carbon atoms attach themselves to latent nuclei, increasing their thermal stability in the 1100-900°C temperature range. At temperatures below 800°C, oxygen atoms attach themselves to the carbon clusters to form the active defect nuclei. Gupta et al. [83] have recently shown that the presence of boron in CZ Si can also enhance the precipitation of oxygen. Small angle neutron scattering (SANS) showed [83] that oxygen precipitates out of the lattice in boron-doped samples at a much faster rate than in the undoped Si. This means that precipitates have a better chance of survival during subsequent heat treatment. Bergholz et al. [97] have shown that the overall number density of

oxygen precipitates in a CZ Si sample can decrease with annealing time, as large precipitates grow at the expense of smaller ones.

In the following sections, a study has been made of the effect of annealing temperature on precipitate size, by means of simulation in conjunction with experimental section topography. First of all, it is necessary to describe the operation of the computer code which has been used to simulate section topographs of precipitates in Si.

4.2 Simulation Code for a Precipitate

In the previous chapter, it was shown how a section topograph could be simulated by numerical integration of Takagi's equations (2.55) at all nodes of a network inside the Borrmann fan. Equations (3.8) and (3.9) give the wave amplitudes D_o and D_h at point T in the integration network, Fig. 3.3, in terms of the corresponding values at point W. A computer program to implement these equations iteratively from point to point in an integration network was written by Dr. G. S. Green, formerly of Durham University. The program is written in Pascal, based on code originally due to Epelboin [58,59], and this program, including the changes made by the current author, is presented as $GENERAL.P$ in APPENDIX A.

In equations (3.9), $D_h(S_o, S_h)$ is worked out in terms of D_o, D_h at the appropriate points, some constant terms and some terms dependent on the variable:

$$\begin{aligned} W &= i\pi kq\beta_{h'}\left(S_o, S_h - \frac{q}{2}\right), \\ &= i\pi kq\left[\beta_h - \frac{1}{k}\frac{\partial}{\partial S_h}\{\underline{h}.\underline{u}(\underline{r})\}\right], \end{aligned}$$

from equation (2.43).

Before calculating W, it is necessary to work out Takagi's differential expression, given by the term dsh, such that:

$$dsh = \frac{\partial}{\partial S_h}\left[\underline{h}.\underline{u}(\underline{r})\right],$$

from equation (2.43).

Eshelby [98] and Teodosiu [99] have studied the spherically symmetric strain field due to a point strain centre, and this will be taken as a model for precipitate strain distribution in the current work. The validity of this model will be confirmed in section 4.3. The strain field due to a precipitate is defined in terms of the *deformation parameter*, C, whose value is directly proportional to the volume of a coherent, spherical precipitate. The strain-induced displacement, $\underline{u}(\underline{r})$, due to the precipitate is then given by:

$$\underline{u}_r(\underline{r}) = \frac{C}{r^2}\hat{\underline{r}}, \qquad (4.3)$$

where r is the radial displacement from the point strain centre.

Hence,

$$\begin{aligned}\frac{\partial}{\partial S_h}\left[\underline{h}.\underline{u}(\underline{r})\right] &= C\frac{\partial}{\partial S_h}\left[\underline{h}.\underline{r}/r^3\right], \\ &= C\left(\frac{\partial}{\partial x}\frac{\partial x}{\partial S_h}+\frac{\partial}{\partial y}\frac{\partial y}{\partial S_h}+\frac{\partial}{\partial z}\frac{\partial z}{\partial S_h}\right) \\ &\quad \left(\frac{h[1].x+h[2].y+h[3].z}{(x^2+y^2+z^2)^{\frac{3}{2}}}\right).\end{aligned} \tag{4.4}$$

The terms x, y, z in (4.4) refer to the experimental x, y, z-axes illustrated in Fig. 4.6, whose origin is the origin of the integration network. The terms $h[1,2,3]$ are components of the diffraction vector, $\underline{h}$, in the x, y, z-directions so defined.

The differentials $\frac{\partial x}{\partial S_h}$, $\frac{\partial y}{\partial S_h}$ and $\frac{\partial z}{\partial S_h}$ are represented by the terms shx, shy and shz, respectively, and it is seen from Fig. 4.6 that:

$$\begin{aligned} shx &= \underline{\hat{x}}.\underline{\hat{S}_h} = -\sin(dir), \\ shy &= \underline{\hat{y}}.\underline{\hat{S}_h} = 0, \\ shz &= \underline{\hat{z}}.\underline{\hat{S}_h} = \cos(dir), \end{aligned} \tag{4.5}$$

where dir is the angle between the z-axis and the S_h-direction.

Hence, shx and shz give the components of S_h in the x and z-directions, respectively. shy is equal to zero, since planes of incidence are perpendicular to the y-axis.

Carrying out the differential operations in equation (4.4) gives dsh as:

$$\begin{aligned} dsh &= \frac{C}{r^3}\left[shx\left(h[1]-\frac{3x}{r^2}H\right)+shz\left(h[3]-\frac{3z}{r^2}H\right)\right], \\ \text{where } H &= h[1].x+h[2].y+h[3].z. \end{aligned} \tag{4.6}$$

A procedure called $DIFFPOINT$ (APPENDIX B) has been constructed by Green to calculate dsh, according to equation (4.6).

Having found dsh, it is then possible to calculate the term W in equation (2.43), and implement equations (3.8) and (3.9). The term β, equation (2.43) is worked out in section α of $GENERAL.P$ (APPENDIX A), using equations (10) and (11) of Epelboin's 1985 review [58]. In section β of $GENERAL.P$, the variable $W1$ is set to $-\pi kq\beta_h$ and the real parts of variables $c1$ and $c2$ are both set to unity. Each time $DIFFPOINT$ is called from within the integration procedure, section γ of $GENERAL.P$, the value of dsh is calculated at the appropriate node and multiplied by $q\pi$. In section δ of $GENERAL.P$, the modified dsh is modified again to give:

$$\begin{aligned} dsh &= q\pi\frac{\partial}{\partial S_h}\left[\underline{h}.\underline{u}\right]-\pi kq\beta_h, \\ &= -\pi q\left(k\beta_h-\frac{\partial}{\partial S_h}\left[\underline{h}.\underline{u}\right]\right), \end{aligned}$$

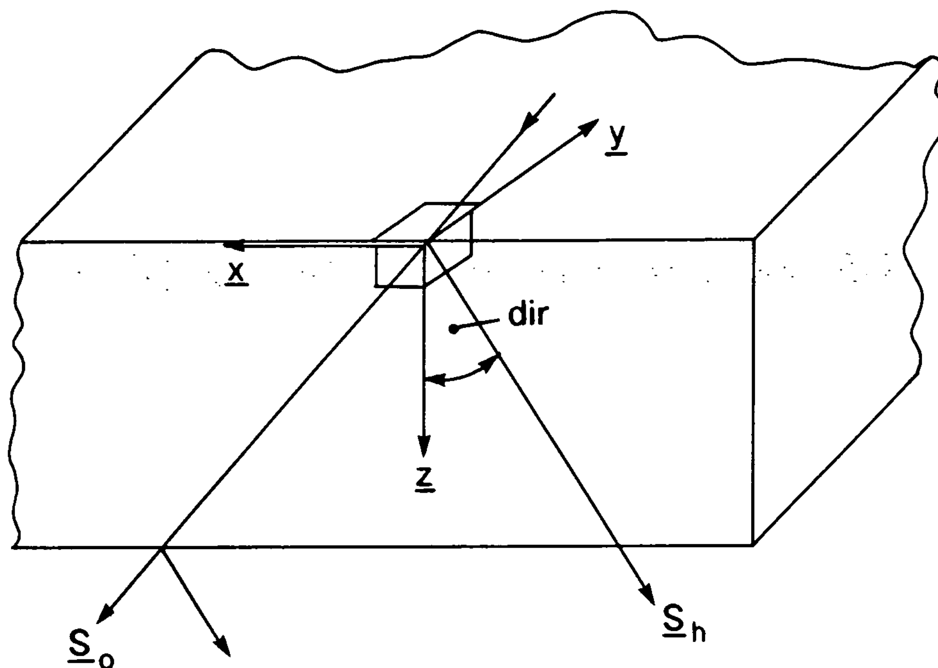

Fig. 4.6: Illustration of the experimental x, y, z-axes.

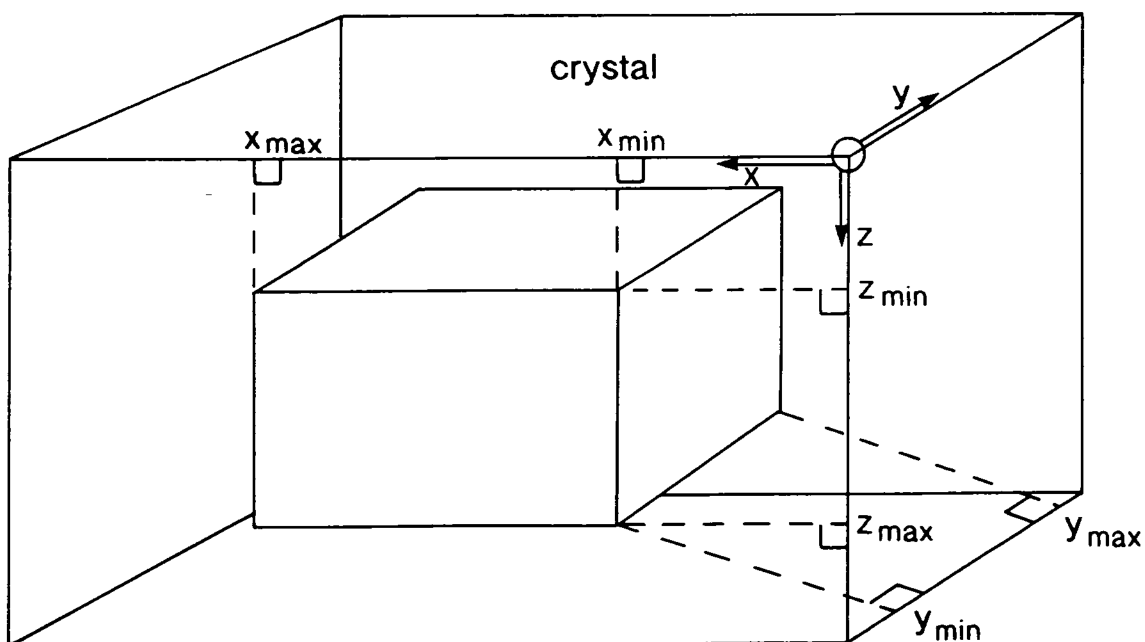

Fig. 4.7: Illustration of an imaginary rectilinear box constructed within a crystal to contain a precipitate distribution.

which is the modulus of the required expression for W from (2.43).

Subsequently, the imaginary parts of $c1$ and $c2$ are set to dsh and $-dsh$, respectively. These are used in section ϵ of $GENERAL.P$ to calculate D_o and D_h by a series of complex algebraic operations. The calculated values of D_o and D_h are stored in the array elements $\phi[1, ks]$ and $\phi[2, ks]$, respectively, where ks represents the ordinal number of a node in a row. The integration procedure has been constructed by Green so that, ultimately, the values along the exit surface are obtained for each plane of incidence.

The procedure $POINTDEF$ (APPENDIX B) to read the defect paramaters into the simulation program has been constructed by Green, with small modifications by the current author. In section α of $POINTDEF$, the deformation parameter, C, and the total number of precipitates, $prlim$, are read in. The code has been constructed by the current author so that the precipitates can be confined to an imaginary rectilinear box, whose faces are defined by the (x, y, z) coordinates $x_{min}, x_{max}, y_{min}, y_{max}, z_{min}$ and z_{max}, Fig. 4.7. The coordinates of each of the $prlim$ precipitates are defined in section β of $POINTDEF$, using the variable $random(0)$, which is a random number between 0 and 1. In this way, it is possible to simulate for a random distribution of precipitates confined to a specific rectilinear volume within the crystal. This is useful in section 4.6, in the study of denuded zones. In the case of a single precipitate, $prlim$ is set to unity and the difference between x_{min} and x_{max} is set to $0.2\mu m$. Each coordinate value is stored in an element of a one-dimensional array, where each array corresponds to one of the three coordinate directions. These array entries are fed back into the main program when $DIFFPOINT$ is called, for each precipitate, in section γ of $GENERAL.P$. The parameters of the reflection and the crystal are input via procedure $SETUP$ within $GENERAL.P$. A typical input data file to be read by $POINTDEF$ is shown in APPENDIX H1.

Green has written the procedure $CURVE.P$ (APPENDIX C) to incorporate crystal bending into the simulation process. Linear elasticity theory [99] was assumed, so that the total dsh value is obtained by adding the dsh contributions due to the long range strain due to curvature and the short range precipitate strain. This is accomplished by including a single entry in the input data file of APPENDIX H1 to indicate the crystal radius of curvature, following the precipitate-specific parameters. This method has been used [100] to simulate experimental topographs due to curved crystals.

Real crystals exhibit the property of *surface relaxation*, whereby the crystal lattice planes relax at all points along the surface. The result of this is that the normal component of strain is zero everywhere along the surface. This has been incorporated into the current work via the *Method of Images*, Fig. 4.8. The strain field due to the precipitate, depth z below the crystal surface, is added to that due to an *image precipitate*, distance z above the surface. The result is a cancellation of normal strain components at all points along the surface. Surface relaxation is incorporated into the simulation process by calling $DIFFPOINT$ a second time in section γ of $GENERAL.P$, and adjusting the z-argument appropriately for the image precipitate. The dsh-values due to the two precipitates are then added to represent the total strain.

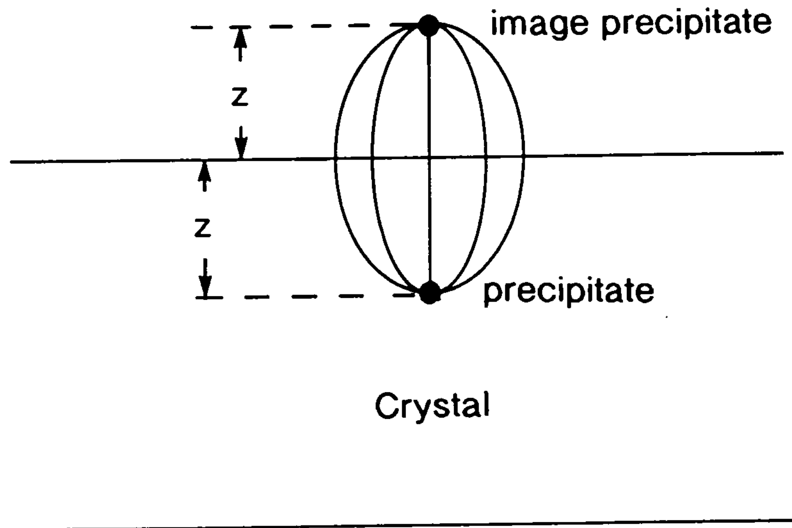

Fig. 4.8: Method of Images.

The simulation technique above assumes isotropic elasticity theory, and this has been shown to be satisfactory for the simulation of section topographs due to hydrogen precipitates in Si [101,102].

It has already been pointed out that oxygen precipitates in Si can take a variety of different forms [84,95,96]. However, it was noted that the volume of even the octahedral precipitates observed by Yang et al. [96] was very similar to that of the equivalent spherical precipitates of diffusion theory [88,89]. In addition, it has been shown [93] that the growth equations for a spherical precipitate can be applied to precipitates with other forms. Hence, it is suggested that the spherical strain model of equation (4.3) can be applied to oxygen precipitates in general, to a good approximation. The veracity of this assertion is tested in the following section.

4.3 Simulation of Experimental Section Topographs due to Oxygen Precipitates in MCZ Silicon

4.3.1 Introduction

The simulation of section topographs due to precipitates is a comparatively recent development. Lefeld-Sosnowska et al. [103] have simulated the effect on image structure of the position of spherical inclusions relative to the Borrmann fan. Green et al. [101] have simulated section topographs due to hydrogen precipitates in FZ Si. They found that the image height, h, in the experimental y-direction, Fig. 4.6, was related to the deformation parameter, C, by the equation:

$$h = A \, lnC, \tag{4.7}$$

where A is a constant.

In the current work, the simulation technique of section 4.2 has been applied [104] to experimental section topographs due to oxygen precipitates in MCZ Si. The experimental topographs were obtained by Prof Z. H. Mai, Institute of Physics, Chinese Academy of Sciences, Beijing, P. R. China, when in Durham under a Royal Society academic exchange programme. Wafers of nominal thickness $430\mu m$ were cut from a (001) oriented Si crystal grown by the MCZ method. Section topographs were taken after annealing for 18 hours at 450°C, 650°C and 800°C. All topographs were taken using MoK_{α_1} radiation and recorded on Ilford L4, $50\mu m$ thick nuclear plates.

4.3.2 Results

The section topographs of annealed wafers all indicated a low density of defects [74], permitting individual defects to be examined. Of the reflections examined in the current study, the asymmetric 333 and symmetric 440 reflections were found to give the most readily distinguishable contrast from the oxygen precipitates. Fig. 4.9 shows an example of the excellent matching between simulation and experiment in

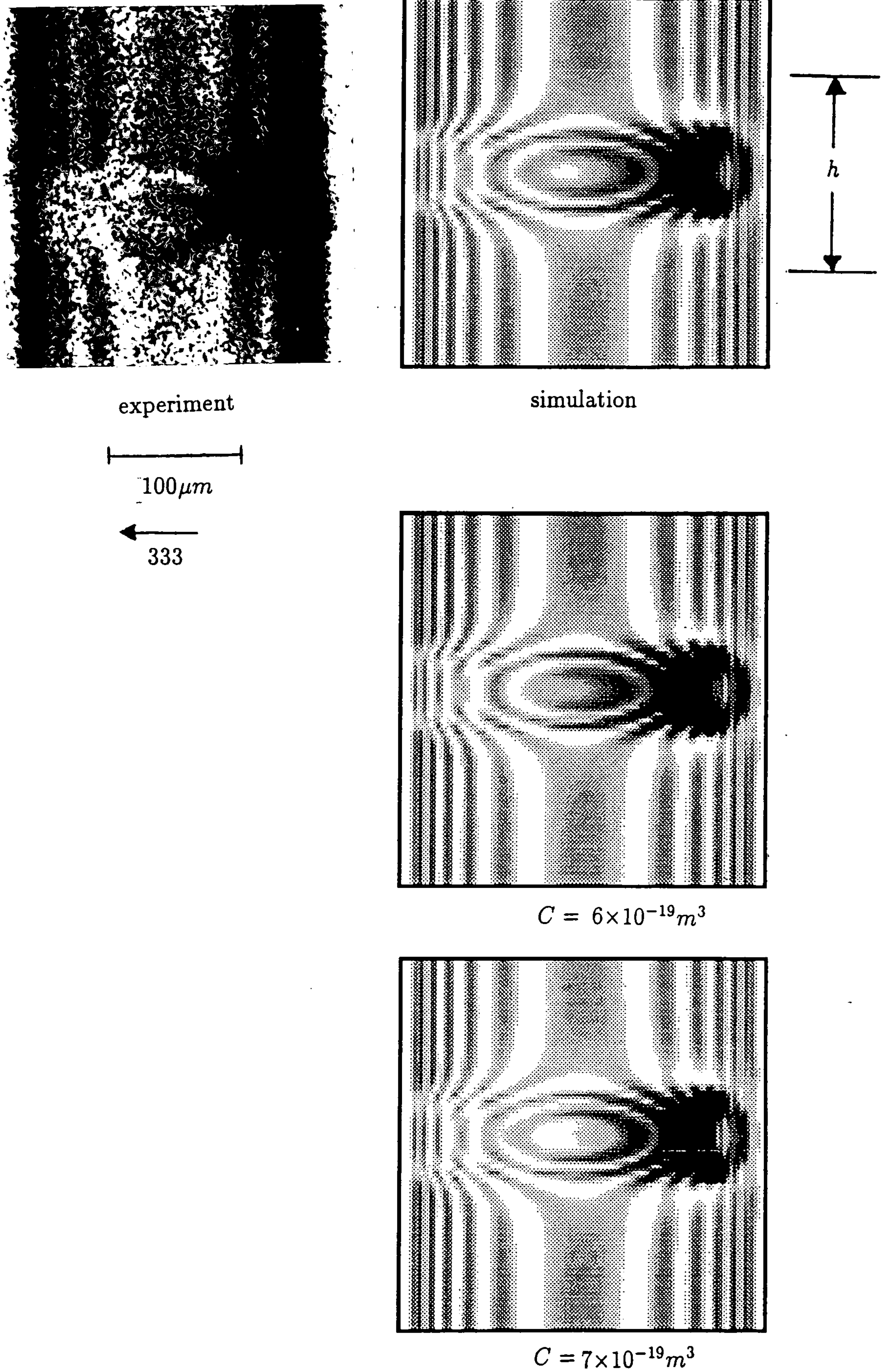

Fig. 4.9: Simulation vs. experimental section topograph, for an oxygen precipitate formed in an MCZ silicon sample annealed for 18 hours at 800°C, imaged using MoK_{α_1} radiation in the 333 reflection. Experimental topograph obtained by Prof. Z. H. Mai of the Chinese Academy of Sciences, Beijing, P. R. China. Matching was obtained for a deformation parameter, C, of $6.5\times10^{-19}m^3$. Also indicated are equivalent simulations for C-values of $6\times10^{-19}m^3$ and $7\times10^{-19}m^3$.

the case of a sample which was annealed at 800°C and imaged using the 333 reflection, APPENDIX I1. All the simulations in this section were generated assuming the spherically symmetric strain field of equation (4.3), and using the surface relaxation model outlined in the previous section. Matching was obtained by adjusting the entries in the input data file corresponding to the deformation parameter, C, and the precipitate position. Equation (4.7) due to Green et al. [101] describes how the image height, h, increases with C. The width of the image is determined by the depth of the precipitate, given by its z-coordinate, Fig. 4.6. The distance of the defect image from the edge of the section pattern is given by the lateral position of the defect relative to the Borrmann fan, expressed in terms of the x-coordinate, Fig. 4.6, of the defect. The structure of a precipitate image is thus determined uniquely by its x, z and C-values. Hence, it is possible to determine unambiguously the x, z and C-values associated with a precipitate by matching of simulated and experimental topographs. The image of Fig. 4.9 corresponds to a precipitate close to the X-ray entrance surface and near the direct beam. Remarkably different images can be produced from identical strain centres at different positions in the crystal [101,102,103]. The purpose of the two extra images in Fig. 4.9, for C-values of $6\times10^{-19}m^3$ and $7\times10^{-19}m^3$, will be explained shortly.

Fig. 4.10 shows examples of defect images from samples annealed at different temperatures, taken in the 440 reflection, APPENDIX I2. In each case, an excellent match can be obtained, provided a different value of the deformation parameter is used for each of the three temperatures.

Fig. 4.11 shows the topograph due to a precipitate which was so large that its strain field was no longer spherically symetric, as evidenced by the lack of a horizontal axis of symmetry. As the simulation program associates a spherically symmetric strain field with the precipitate, it is impossible to obtain matching in this case. This result, and its implications, will be discussed in section 4.3.3. Similar effects were observed in studies of hydrogen precipitates in Si [105], when precipitates became very large and began to punch out prismatic dislocation loops.

Table 4.1 shows corresponding values of C and T for the four cases in Figs. 4.9 and 4.10. The deformation parameter, C, was found to increase monotonically with annealing temperature, T, Fig. 4.12, showing that the lattice surrounding the precipitate was in compression. This agrees with the previous deduction of Mai et al. [106]. A linear relation between C and lnT was found empirically, Fig. 4.12. There is a question as to the reliability of this relation, given that data is only available for three temperatures. However, the two results for the 800°C case, taken for different precipitates and in different reflections, show striking agreement in the value of C obtained by comparison of simulation with experiment. This indicates that the individual data points are reliable, and supports the conclusion that C varies linearly with lnT.

The error bars in Fig. 4.12 were determined by examining pairs of simulations with C-values on either side of the best-fit case, and determining the change necessary for a *just noticeable difference* (JND) in the image. The JND has been assessed in terms of the effect of the deformation parameter on the height, h, Fig. 4.9, in the simulations over which the Pendellösung fringes are distorted away from their per-

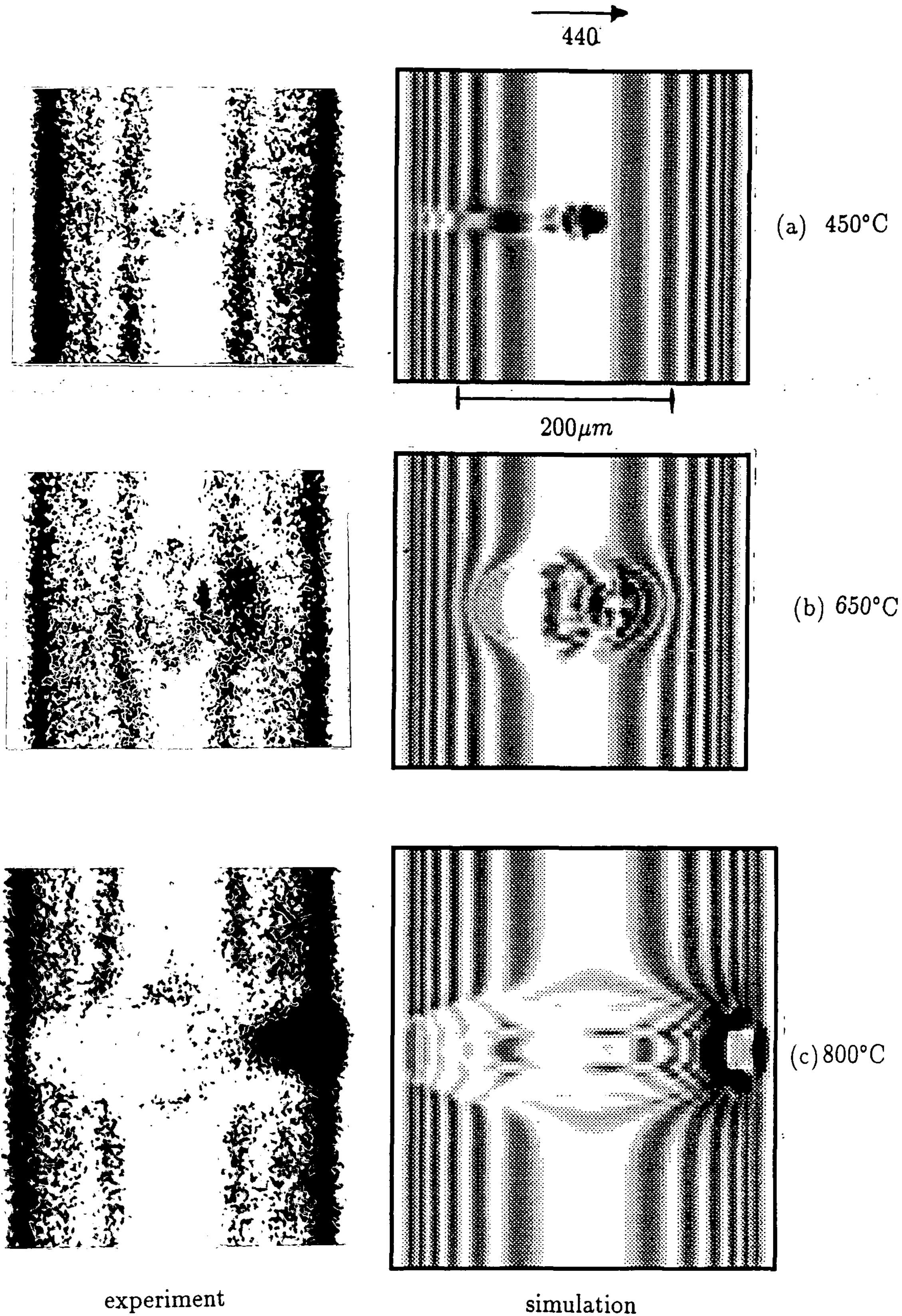

Fig. 4.10: Simulation vs. experimental section topographs, for oxygen precipitates formed in MCZ silicon samples annealed for 18 hours at 450°C, 650°C and 800°C, imaged using MoK_{α_1} radiation in the 440 reflection. Experimental topographs obtained by Prof. Z. H. Mai of the Chinese Academy of Sciences, Beijing, P. R. China.

Fig. 4.11: Section topograph of a very large precipitate, whose strain field has ceased to be spherically symmetric.

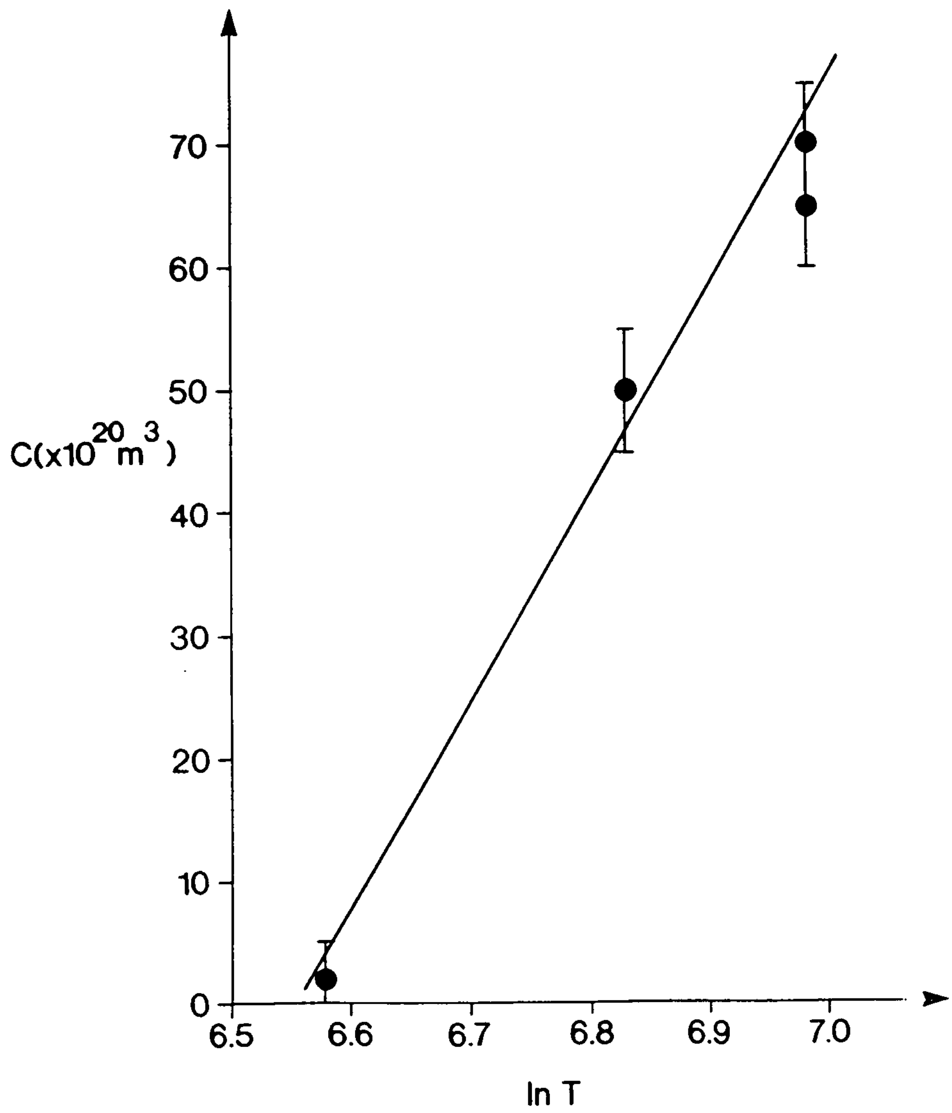

Fig. 4.12: Variation of deformation parameter, C, with annealing temperature, T.

$C(\times 10^{20} m^3)$	$T(K)$	$\ln T$
2	723	6.58
50	923	6.83
70 (440)	1073	6.98
65 (333)	1073	6.98

Table 4.1: Deformation parameter, C, as a function of annealing temperature, T, for an 18 hour anneal using the 333 and 440 reflections.

fect crystal configuration. The criterion for a JND has been taken as an increased (or decreased) deviation from the perfect crystal configuration of $1mm$. A pair of simulations corresponding to a JND is shown in Fig. 4.9, together with the original simulation of the experimental image.

4.3.3 Discussion

Excellent matching of simulation with experiment was found for two different reflections and three different annealing temperatures, Figs. 4.9 and 4.10. This indicates that the spherically symmetric strain model of equation (4.3) is, in general, a very good approximation for oxygen precipitates in Si. This is an important point, since oxygen precipitation is a ubiquitous feature of industrially manufactured Si single crystals.

It was not possible to simulate the topograph of Fig. 4.11, since the precipitate had become so large that its strain field was no longer spherically symmetric. Cui et al. [105] showed that hydrogen precipitates in Si adopt a spherical form following nucleation, since this is the configuration with least associated potential energy. They pointed out, however, that as the precipitate grows, it adopts a torus shape in order to minimise the total elastic potential energy. It is proposed here that a related mechanism might be at work in the formation of the precipitate imaged in Fig. 4.11. It might be expected that annealing at a specific temperature for a certain duration would generate precipitates with a whole range of sizes and strains. However, the two results of Table 4.1 for the 800°C case show a remarkable convergence in precipitate strain (and hence size). This is in agreement with the results of Green et al. [101], which showed a striking uniformity in the strains associated with a large number of hydrogen precipitates in an annealed FZ Si sample. A possible explanation is that the vast majority of precipitates which grow to maturity are nucleated at approximately the same time, shortly after the onset of heat treatment. Subsequent growth of these precipitates would then take place at the same rate, resulting in uniformity of precipitate sizes after the end of the treatment.

The process of early nucleation and subsequent growth proposed above is supported by the results of Gupta et al. [83]. They showed that early nucleation and growth of oxygen precipitates in CZ Si is induced by the presence of boron impurities. Various impurities exist in as-grown Si which may affect precipitate growth in

$C,(\times 10^{20} m^3)$	$T(K)$	$\ln(C \times 10^{20})$	$1/T(\times 10^4 K^{-1})$
2	723	0.69	13.8
50	923	3.91	10.8
70	1073	4.25	9.3
65	1073	4.17	9.3

Table 4.2: Corresponding Values of $ln(C \times 10^{20})$ and $1/T$, where C is the precipitate deformation parameter and T is the annealing temperature.

this way.

Matching of simulation and experiment in Figs. 4.9 and 4.10 generated the results of Table 4.1, which are plotted in Fig. 4.12, showing a linear relation between C and lnT. This implies that the precipitate volume, V, increases linearly with lnT, since for a coherent precipitate the deformation parameter, C, is directly proportional to V.

According to the diffusion theory of precipitate growth, the volume, V, of a precipitate is related to the annealing temperature, T, and duration, t, by equations (4.1) and (4.2). It is important to remember that equation (4.1) was developed by Wada et al. [90,91] for a square-plate precipitate. The comment has already been made that the growth equations for a spherical precipitate can be applied with good accuracy to other forms of precipitate, and it is of interest to see if the spherical oxygen precipitates imaged in Figs. 4.9 and 4.10 follow the functional form of equation (4.1). Combining equations (4.1) and (4.2), it is seen that:

$$V = A \exp\left(\frac{-B}{T}\right),$$

where A and B are constants, so that:

$$\ln V = D - \frac{B}{T}, \tag{4.8}$$

where D is another constant.

Of course, for a coherent spherical precipitate, C is directly proportional to V, so that, on the basis of equation (4.8), it is expected that $\ln C$ should be inversely proportional to $1/T$. The values of these quantities, for the values of C and T from Table 4.1, are displayed in Table 4.2. The corresponding graph of lnC vs. $1/T$, Fig. 4.13, shows that these two quantities are not, in fact, inversely proportional, for the spherical precipitates imaged in Figs. 4.9 and 4.10. Hence, it is clear that the equation (4.1) developed by Wada et al. [90,91] to describe the growth kinetics of square-plate precipitates cannot be applied to the spherical oxygen precipitates in MCZ Si studied here.

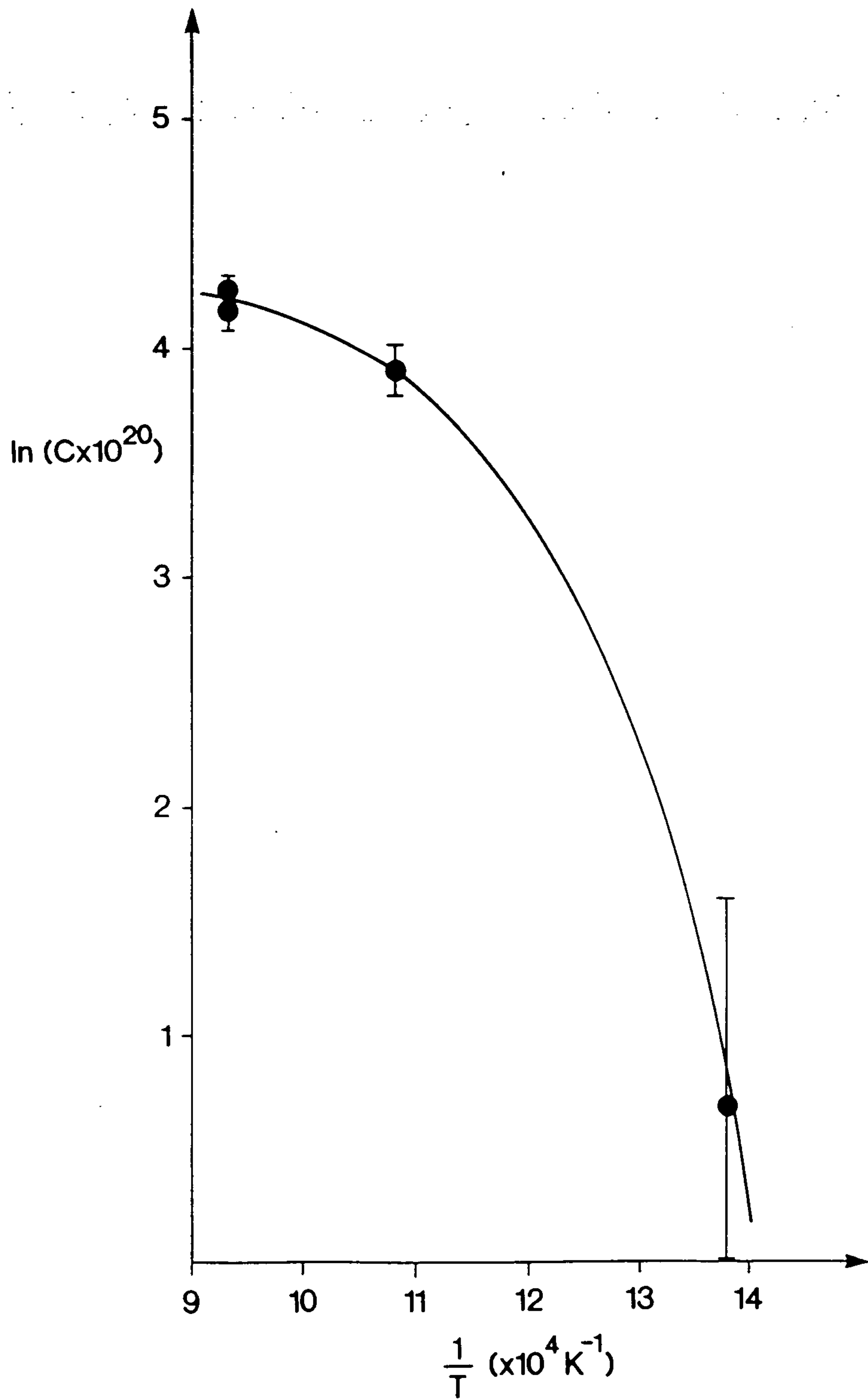

Fig. 4.13: Variation of $\ln C$ with $1/T$. Deformation parameter, C, is expressed in m^3 and annealing temperature, T, in K.

z_{crit}, (μm)	C, ($\times 10^{20} m^3$)	$ln(C \times 10^{20})$
20	2	0.69
40	5	1.61
60	10	2.30
80	30	3.40
90	60	4.09

Table 4.3: Critical depth, z_{crit}, at which the effect of surface relaxation becomes negligible as a function of deformation parameter, C.

4.4 Investigation of the Effect of Surface Relaxation on Precipitate Images

The simulated images of section 4.3 were generated assuming surface relaxation. It is of interest to study the influence of surface relaxation on the images due to oxygen precipitates with C-values in the range defined by the results of section 4.3. Especially significant is the effect of surface relaxation as a function of depth in the crystal.

The simulations of Figs. 4.14, 4.15, 4.16, 4.17 and 4.18 were taken for precipitates at different depths, with and without surface relaxation, for five different values of deformation parameter, C. The crystal and reflection of Fig. 4.10 were assumed, and the precipitates were always located in the direct beam. In each case, the critical depth, z_{crit}, at which the effect of surface relaxation becomes negligible was determined. The results are displayed in Table 4.3

The results of Table 4.3 are plotted in Fig. 4.19. The depth at which the effect of surface relaxation becomes negligible increases, as expected, with increasing deformation parameter. Furthermore, the variation of z_{crit} with lnC is linear.

Clearly, it is important that surface relaxation be incorporated into the simulation process, for precipitates close to the crystal surface. Otherwise, the simulation program cannot be reliably used in conjunction with experiment to assign values to the deformation parameter and the precipitate coordinates.

4.5 Investigation of the Effect of Crystal Curvature on Precipitate Images

4.5.1 Introduction

Growth of an oxide layer onto the surface of a Si wafer at high temperature has become a standard feature of device manufacture. As the wafer is cooled to room temperature, the differential thermal expansion coefficients of the SiO_2 film and the Si substrate cause the wafer to bow. The purpose of the current section is to

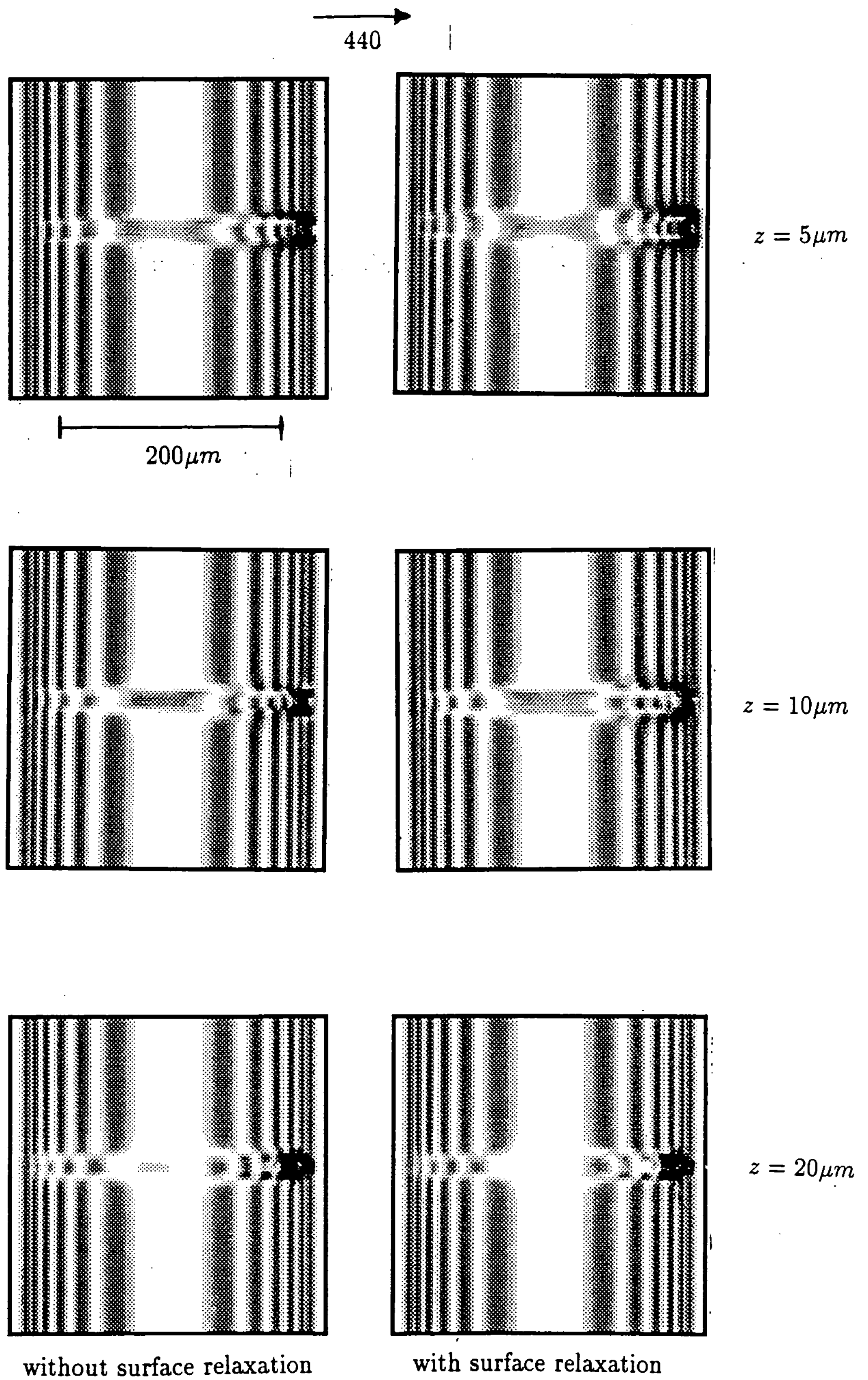

Fig. 4.14: Simulations for precipitates at different depths, taken with and without surface relaxation; deformation parameter, $C = 2 \times 10^{-20} m^3$.

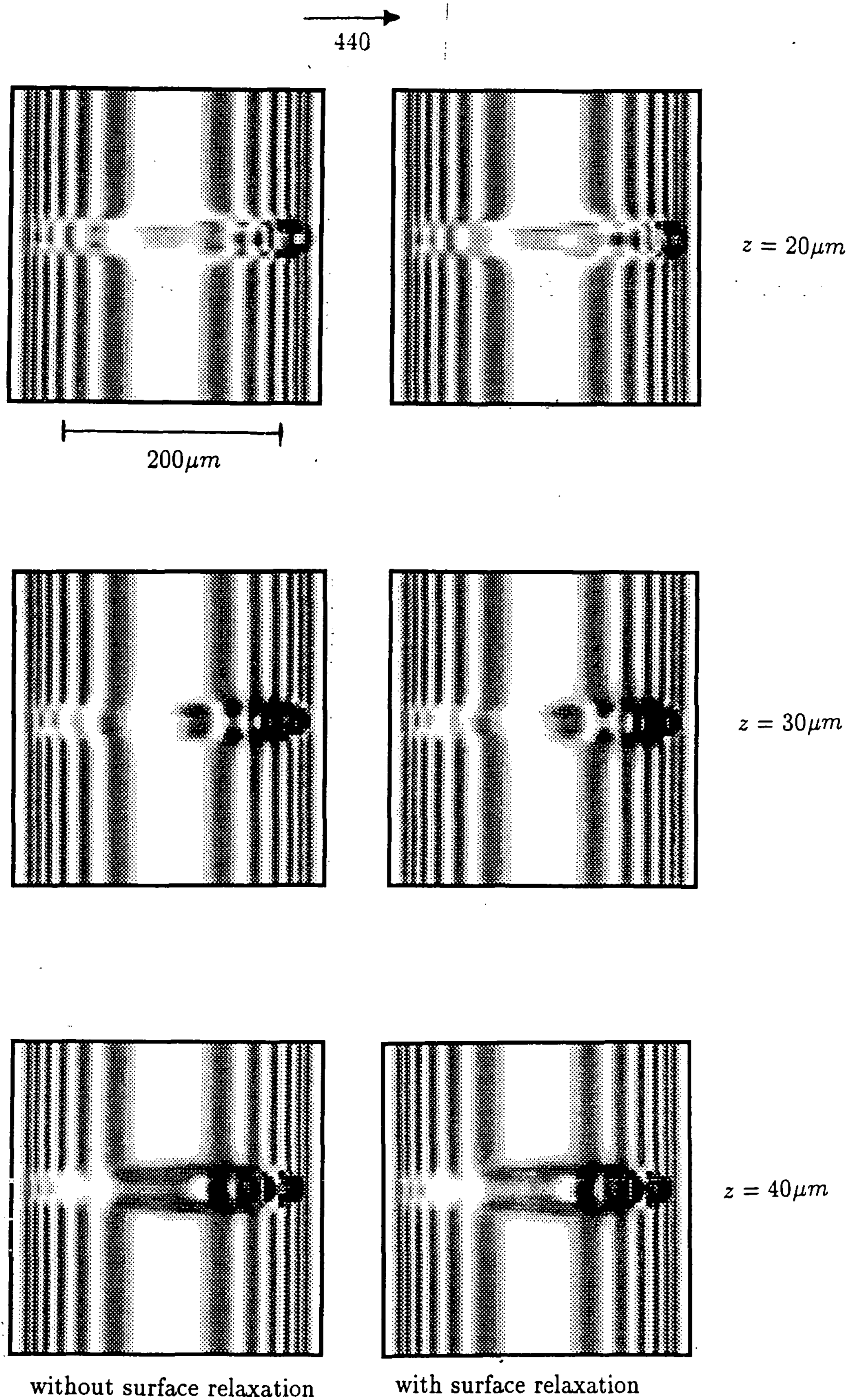

Fig. 4.15: Simulations for precipitates at different depths, taken with and without surface relaxation; deformation parameter, $C = 5 \times 10^{-20} m^3$.

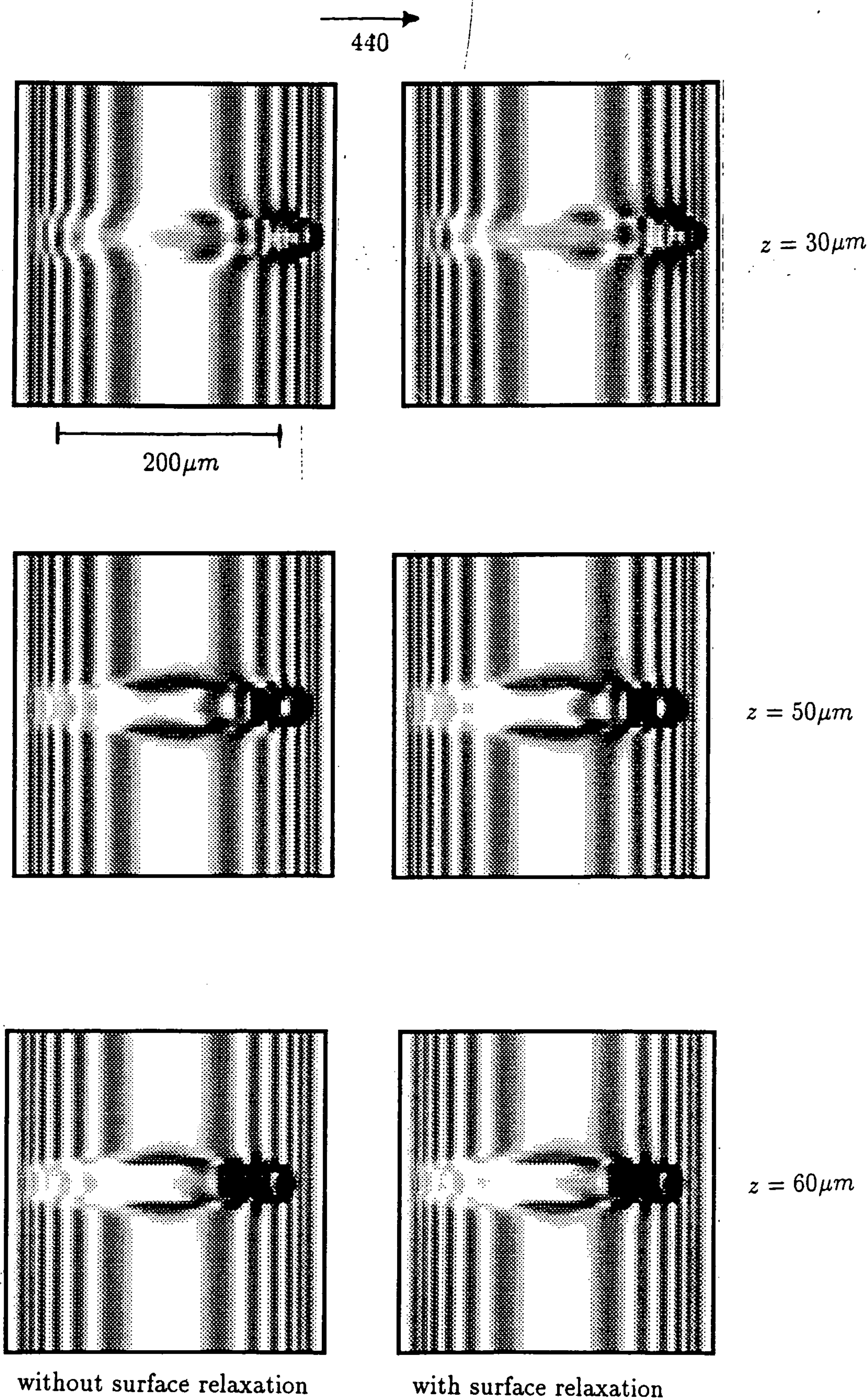

Fig. 4.16: Simulations for precipitates at different depths, taken with and without surface relaxation; deformation parameter, $C = 1 \times 10^{-19} m^3$.

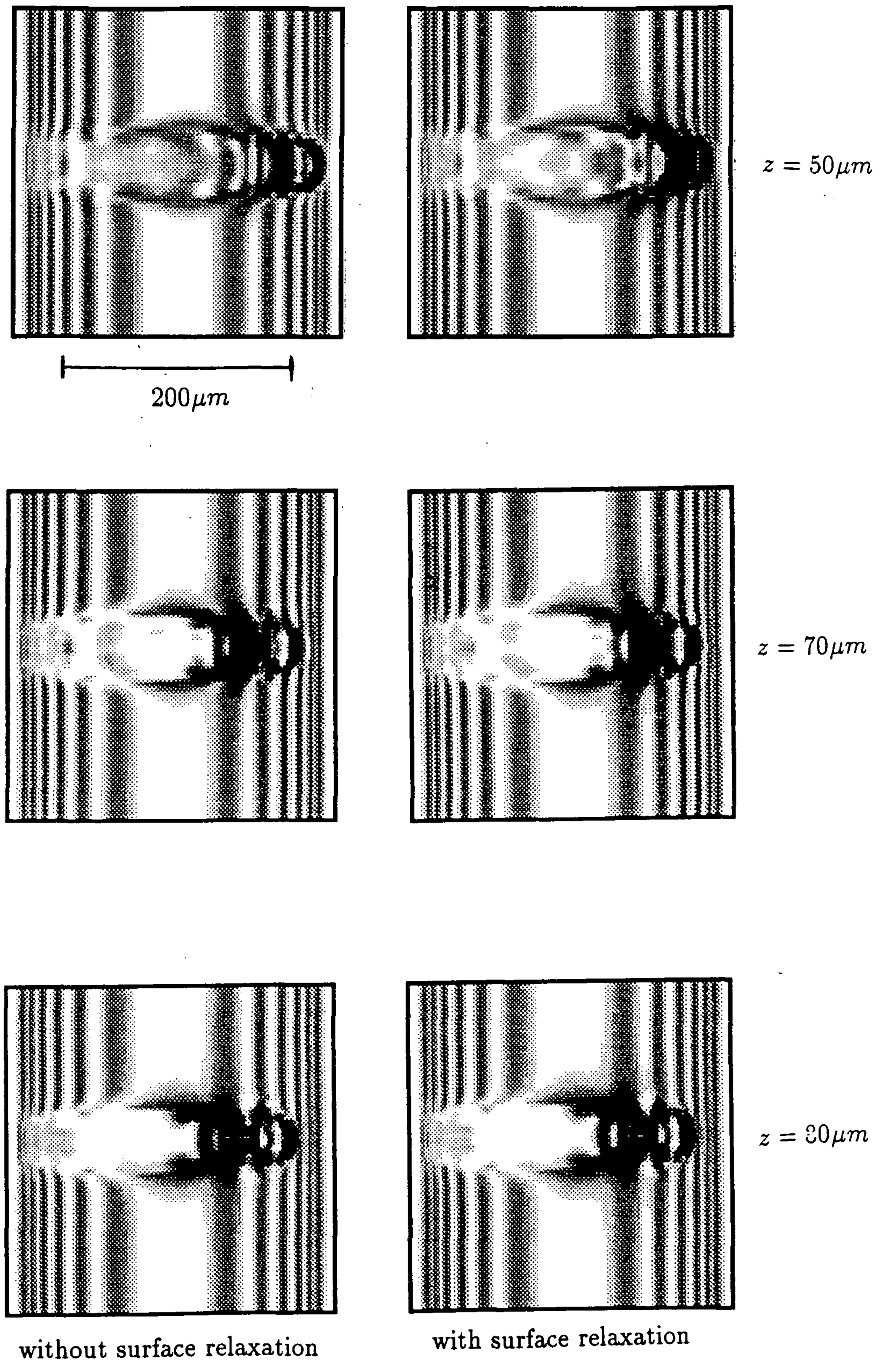

Fig. 4.17: Simulations for precipitates at different depths, taken with and without surface relaxation; deformation parameter, $C = 3 \times 10^{-19} m^3$.

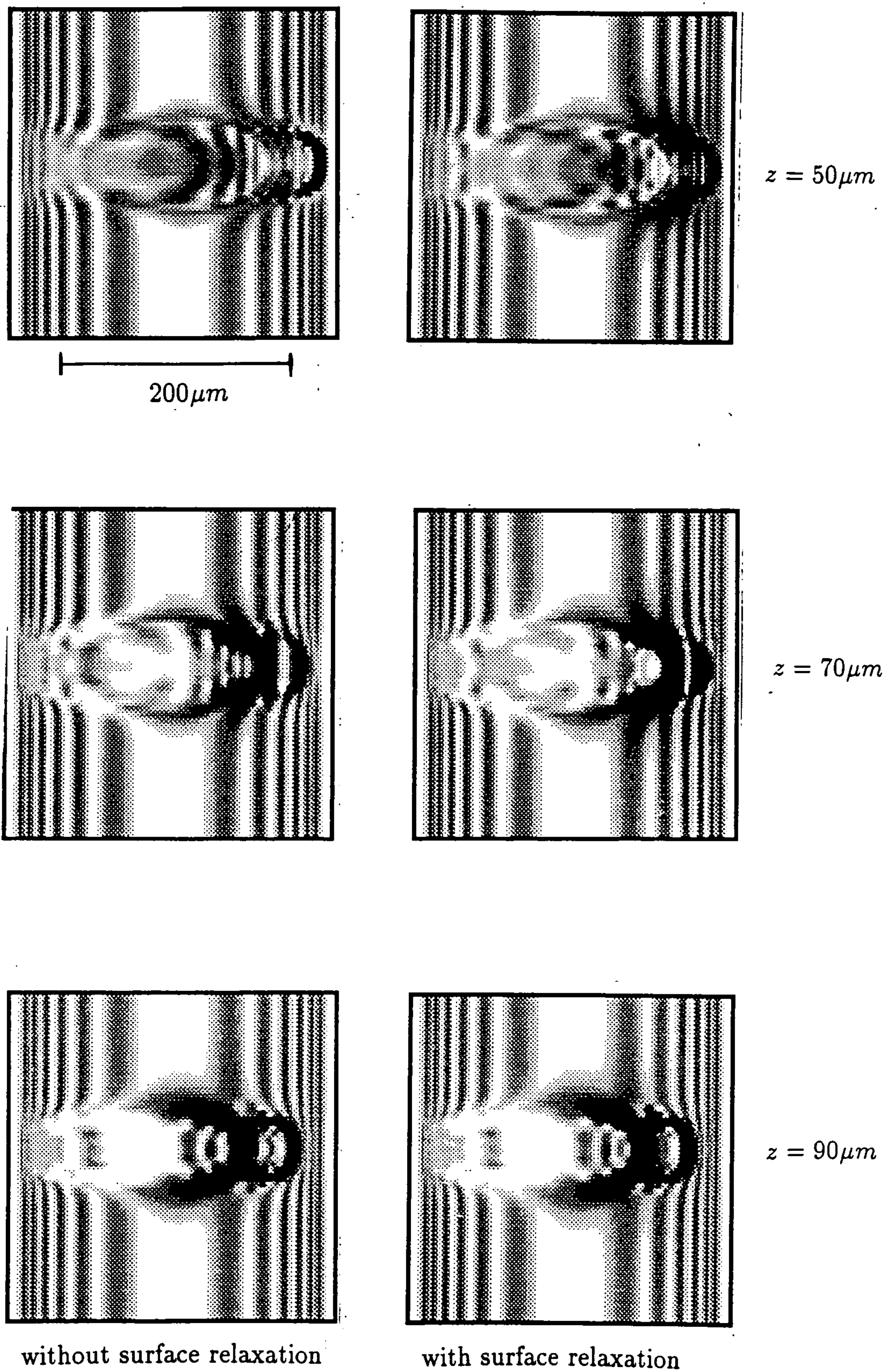

Fig. 4.18: Simulations for precipitates at different depths, taken with and without surface relaxation; deformation parameter, $C = 6 \times 10^{-19} m^3$.

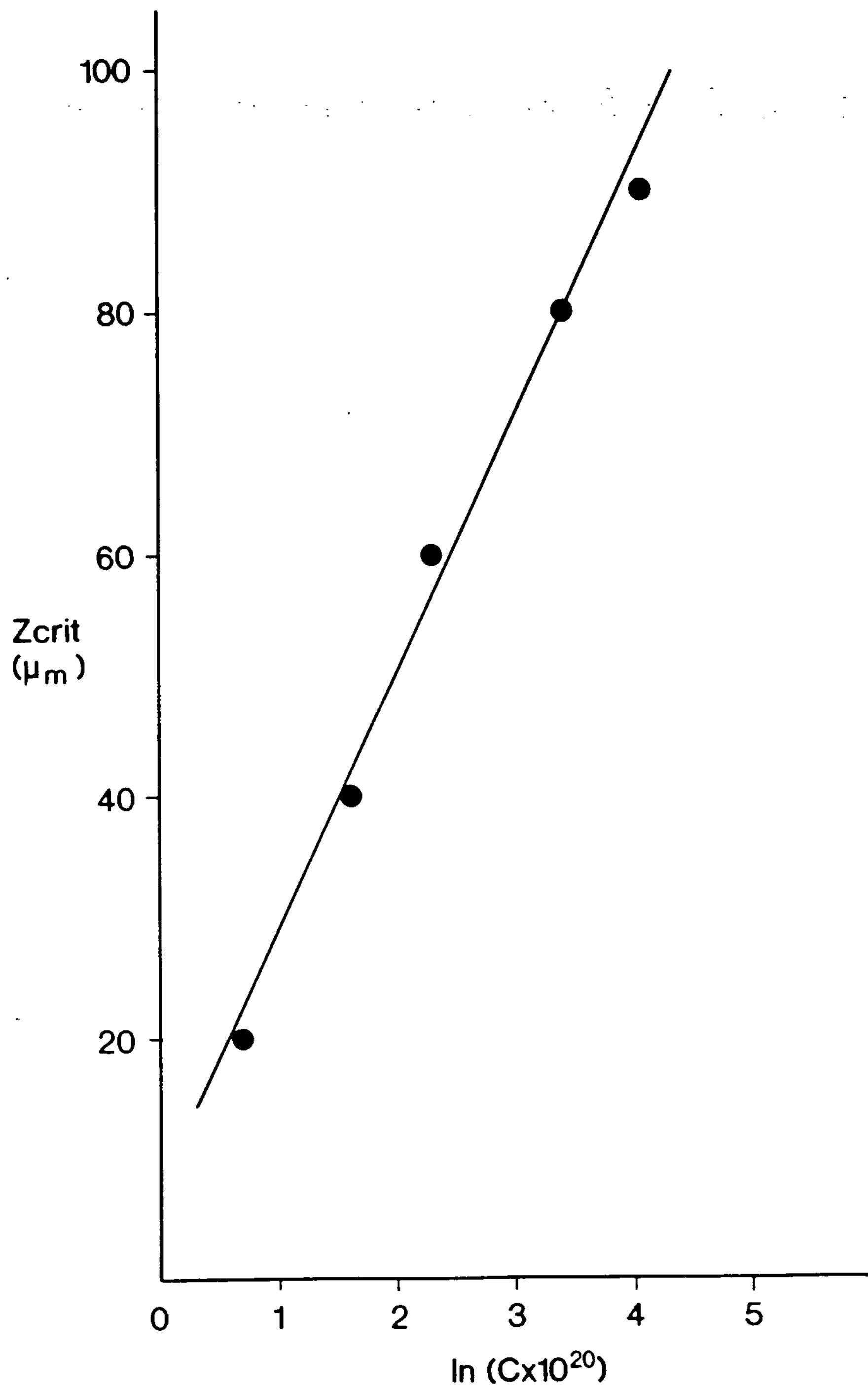

Fig. 4.19: Depth at which the effect of surface relaxation becomes negligible, z_{crit}, as a function of deformation parameter, C, where C is measured in m^3.

examine the change in image contrast as a result of wafer curvature. The procedure $CURVE.P$ (APPENDIX C) has been used to calculate the long range strain induced by wafer curvature. The code was written on the basis of cylindrical curvature of the crystal about an axis perpendicular to the planes of incidence of the incident radiation. Consider polar coordinates (r, θ) relative to the bending axis. The radial and tangential components of the strain-induced displacement are given by:

$$
\begin{aligned}
u_r &= 0, \\
\text{and } u_\theta &= (r - r_0)\theta,
\end{aligned}
$$

where r_0 is the radius of the *neutral plane*, in which the circumferential distance between points in the lattice remains unchanged.

In addition, the crystal was assumed to be isotropic.

4.5.2 Results

The simulations of Figs. 4.9 and 4.10 have been repeated, taking into account the effect of crystal curvature. Fig. 4.20 shows the simulation of Fig. 4.9, for the asymmetric 333 reflection, for radii of curvature equal to $1000m$, $500m$ and $100m$. Even for the highest radius of curvature, the effect on image structure is pronounced. The central band of the Pendellösung pattern has increased in width and the structure of the intermediary image is very different. As the radius of curvature is decreased to $100m$, the integrated intensity increases, manifest by the washing out of the Pendellösung fringes, and the spacing of adjacent Pendellösung fringes decreases. Fig. 4.21 shows the simulation of Fig. 4.10(c) for the symmetric 440 reflection, for much smaller radii of curvature from $100m$ down to $20m$. It is seen that in the symmetric reflection, the effects of wafer bending begin to manifest themselves at $20m$ radius of curvature.

4.5.3 Discussion

The enhanced diffracted intensity due to a curved crystal in the asymmetric reflection has been investigated by Meieran and Blech [107]. The effect can be understood in terms of Kato's spherical-wave dynamical theory [108,109]. According to this theory, the intensity diffracted from Bragg planes increases rapidly with the curvature of the planes. The Bragg planes involved in an asymmetric reflection bend as a result of wafer curvature, resulting in enhanced diffracted intensity. The increase in diffracted intensity is clearly seen in Fig. 4.20, as the radius of curvature is decreased to $100m$. However, in a symmetric reflection, the planes remain flat, fanning out so that the total misorientation is zero. Hence, it is expected that a curved crystal in a symmetric reflection would show no enhanced diffracted intensity. Clearly, this is not true for a radius of curvature of $20m$ in Fig. 4.21. Hart [110] made a study of the effect of crystal curvature on the Pendellösung fringe pattern due to a wedge-shaped Si crystal. He showed that the strain induced by curvature causes a displacement in the Pendellösung fringes and a reduction in the spacing of adjacent fringes. Experimental work by White and Chen [111] showed that such Pendellösung fringe

333

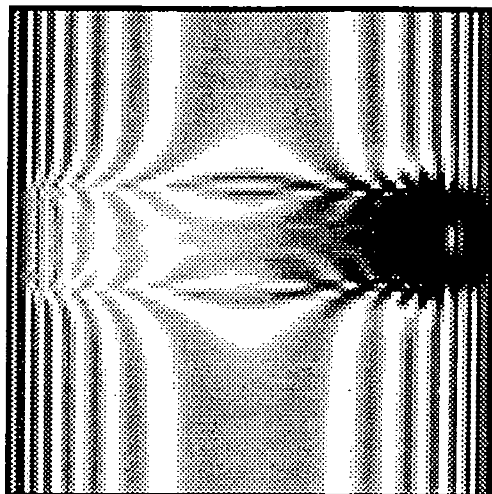

1000m

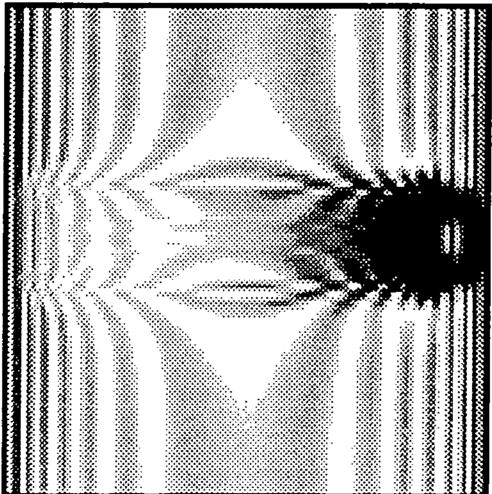

500m

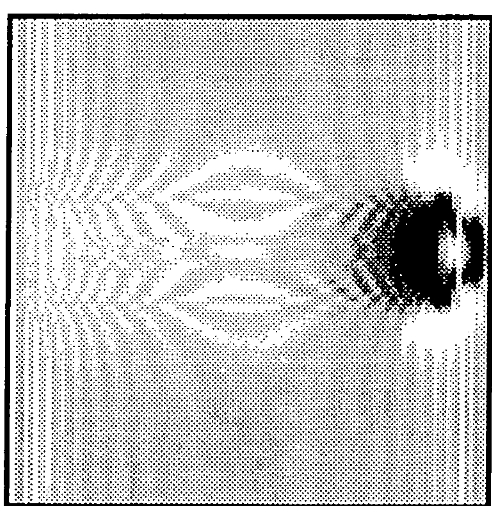

100m

$100 \mu m$

Fig. 4.20: Repetition of the simulation of Fig. 4.9, for the asymmetric 333 reflection, for a curved crystal with different radii of curvature.

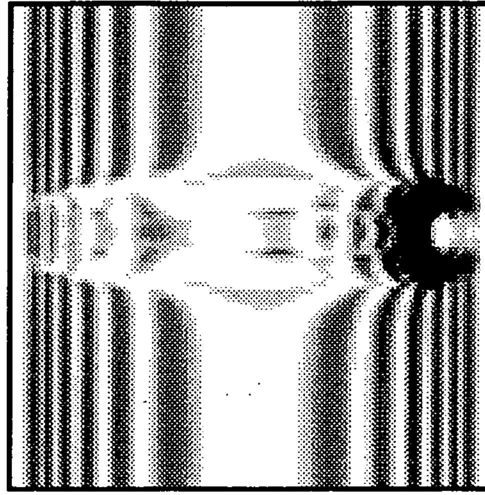

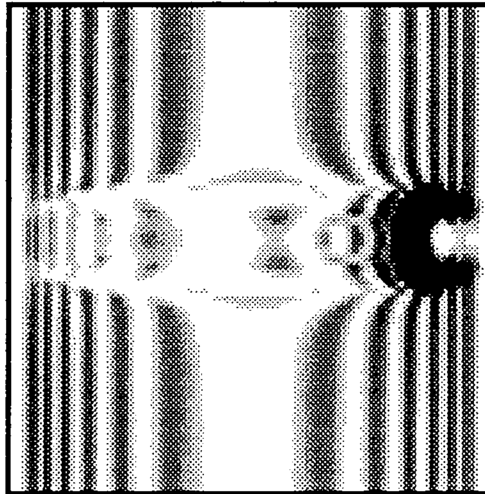

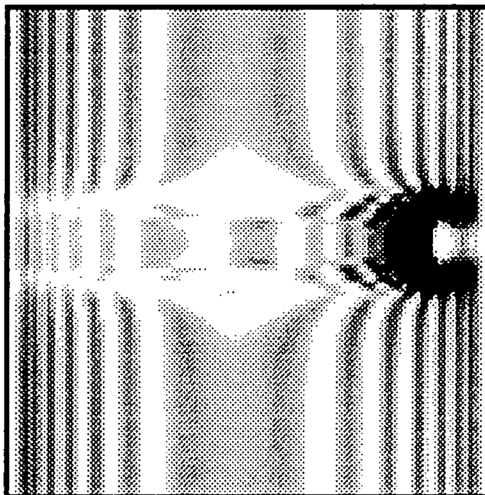

Fig. 4.21: Repetition of the simulation of Fig. 4.10(c), for the symmetric 440 reflection, for a curved crystal with different radii of curvature.

displacements are manifest for curved crystals even in symmetric reflections, and this result was reproduced in the simulations of Green and Tanner [112]. The physical origin of these processes can be seen in the ray optics theory of Chukhovskii and Petrashen [62,113], which includes second order terms neglected by Kato [108,109], and predicts the results described above for symmetric reflections. These effects are based on phase changes in the wavefields inside a curved crystal. The simulations of Fig. 4.21 clearly indicate the Pendellösung fringe displacements predicted by Chukhovskii and Petrashen's theory [62,113]. In addition, the changes in the structure of the intermediary image with decreasing radius of curvature illustrate the sensitivity of this part of the image to the variation in long range strain induced by wafer bending.

4.6 Image Structure due to a Crystal with Denuded Zones

Outdiffusion of oxygen from the surface layers of a Si crystal, upon heating in a non-oxygen ambient, is an important and useful step in device manufacture. This process results in the formation of a relatively defect free denuded zone beneath the crystal surface, which is then ready for device fabrication. The depth of a denuded zone formed in this way is typically a few tens of microns. In addition, oxygen precipitates left in the bulk act as gettering centres, to remove harmful impurities from the active device region. The depth of the denuded zone, and the gettering efficiency, have been studied by several workers [40,114,115] for different denuding treatments, using section topography.

The means by which a section topograph can be used to determine the denuded zone depth is illustrated in Fig. 4.22. Fig. 4.22(a) is an experimental section topograph of a crystal with a denuded zone at the top and bottom surfaces, and Fig. 4.22(b) illustrates the corresponding experimental geometry. Diffracted rays incident on the recording film between D and E have been subject to interference effects in the part of the crystal containing the precipitate distribution. Consequently, the region DE of the film contains information on the defect content of the crystal. However, rays in the direct beam which are diffracted between A and B propagate through crystal which is essentially perfect. Hence, the region CD of the film shows a perfect crystal Pendellösung fringe pattern. These effects are clearly seen in the experimental topograph of Fig. 4.22(a). The width, CE, of the topograph can be calculated, given the reflection, crystal surface normal and crystal thickness. Hence, the thickness of the denuded zone is obtained by measuring the ratio of lengths CD/CE from the final photographic image.

Fig. 4.23 shows simulations for a hypothetical crystal, containing a precipitate distribution with denuded zones of depth $30\mu m$ at top and bottom. The precipitate density was taken as $10^8 cm^{-3}$, consistent with the results of Wada et al. [90] for oxygen precipitates in CZ Si, formed as a result of a 1050°C anneal. A $300\mu m$ thick, (001) oriented crystal, imaged in the 440 reflection was assumed. Three simulations were performed, corresponding to three different values of deformation

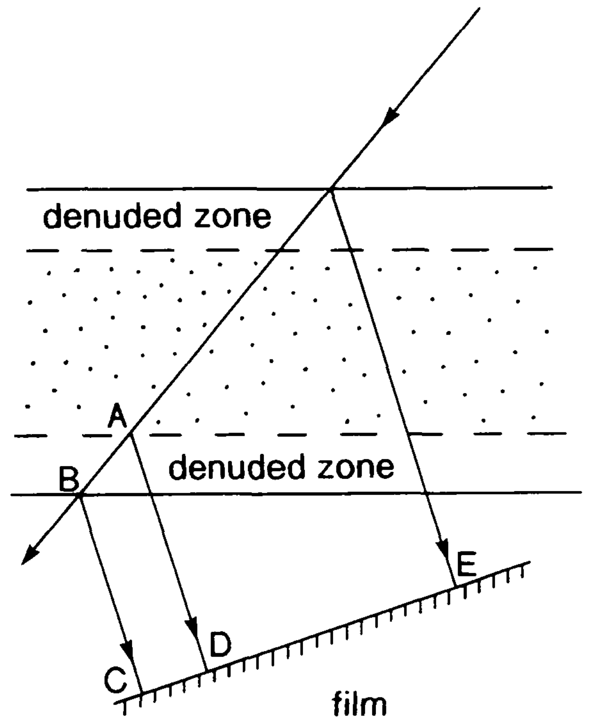

Fig. 4.22: Experimental section topograph (a) and corresponding experimental geometry (b) of a crystal containing oxygen precipitates, with denuded zones at the top and bottom surfaces.

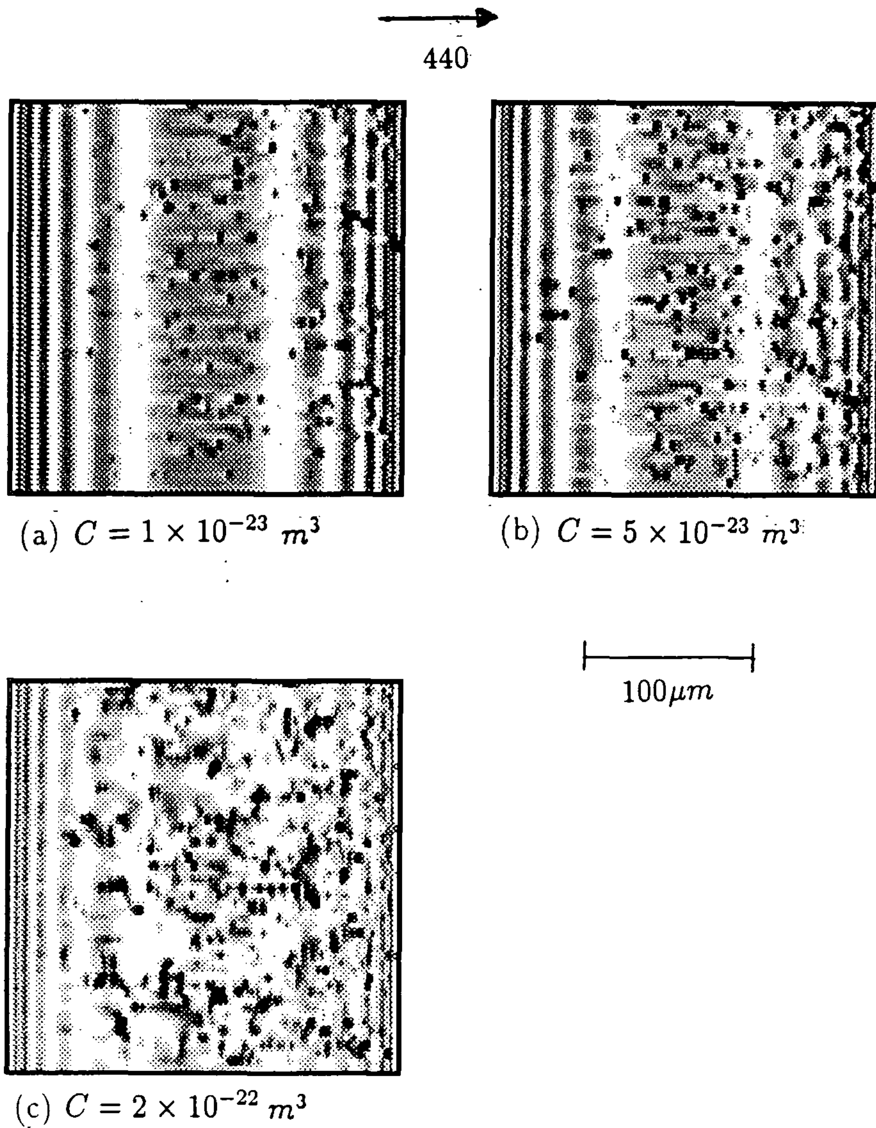

Fig. 4.23: Section topograph simulations for a silicon crystal containing oxygen precipitates, with $30\mu m$ denuded zones at the top and bottom surfaces. A (001) oriented Si wafer of thickness $300\mu m$ was assumed, and the symmetric 440 geometry was taken. Each simulation corresponds to a specific value of precipitate deformation parameter, C.

parameter, C. A typical input data file is shown in APPENDIX H2.

Several key features are manifest in the images of Fig. 4.23. First of all, the region CD of Fig. 4.22(b) is well defined as a set of undisturbed Pendellösung fringes at the extreme left-hand side of the simulation frame. The simulation frame width corresponds to a topograph width of $222\mu m$. The width of the perfect crystal portion of Fig. 4.23(c) is approximately $7mm$ on the simulation, corresponding to a denuded zone depth of approximately $30\mu m$, as specified in the input data file.

It is seen that for a C-value of $1\times10^{-23}m^3$, individual precipitate images are clearly discernible. As the deformation parameter is increased to $5\times10^{-23}m^3$, the precipitate images are more pronounced, but still individually resolvable. However, at a C-value of approximately $2\times10^{-22}m^3$, the precipitate images have become so large that individual defects are no longer resolvable. This critical deformation parameter is two or three orders of magnitude lower than the C-values found for real oxygen precipitates in section 4.3. It is clear that the intermediary and dynamical images of precipitates formed during a typical thermal processing of CZ Si, as reported by Wada et al. [90], cannot be resolved by section topography. Only the more localised direct images show up experimentally. The fact that oxygen precipitates in MCZ Si, imaged in Figs. 4.9 and 4.10, are still clearly resolved for C-values up to $7\times10^{-19}m^3$ serves as a good illustration of the perfection of MCZ Si relative to CZ Si.

4.7 Resolvability of Precipitates as a Function of Strain

The resolvability of precipitates can be examined more precisely by imaging just two precipitates and determining the critical separation for which the two precipitates are just resolved. This has been done in the current section, using the simulation code of the previous sections, for five different values of deformation parameter, C. A moment's consideration of the geometry of Fig. 4.6 confirms that the clearest criterion for resolvability is obtained by considering precipitates which are mutually displaced in the experimental y-direction. In the current section, the minimum y-separation of two precipitates to be just resolved, $(\Delta y)_{crit}$, is determined as a function of deformation parameter, C.

Figs. 4.24, 4.25, 4.26, 4.27 and 4.28 each show, for a particular C-value, simulations of a pair of precipitates with different separations, (Δy). The C-values used here correspond to the range found for real oxygen precipitates from Figs. 4.9 and 4.10. For each case, the value of $(\Delta y)_{crit}$ has been determined by visual inspection. The corresponding results are displayed in Table 4.4.

The results of Table 4.4 are plotted in Fig. 4.29, which shows a linear relation between $(\Delta y)_{crit}$ and lnC. Clearly, it is the image height, h, in the y-direction which determines the resolvability of two precipitate images. Green et al. [101] showed that h is given by:

$$h = A\ lnC,$$

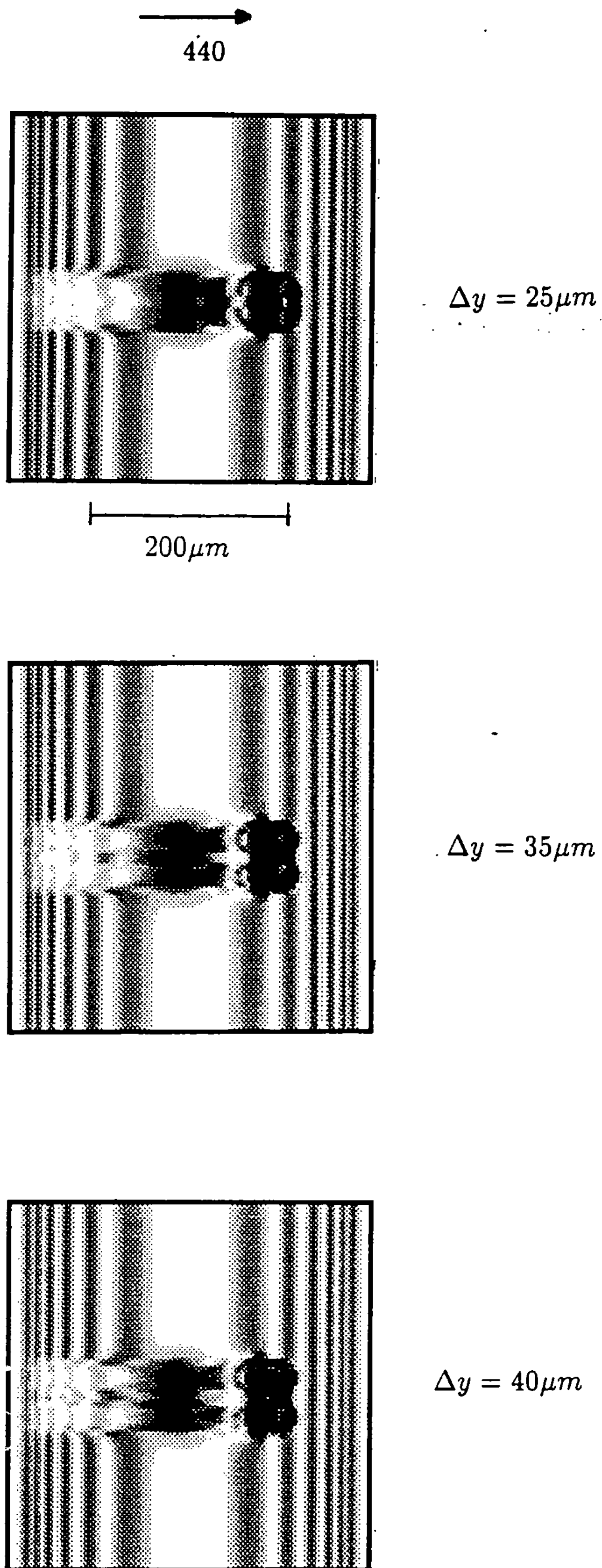

Fig. 4.24: Simulations for a pair of precipitates with different separation, Δy, in the experimental y-direction; deformation parameter, $C = 5 \times 10^{-20} m^3$ throughout.

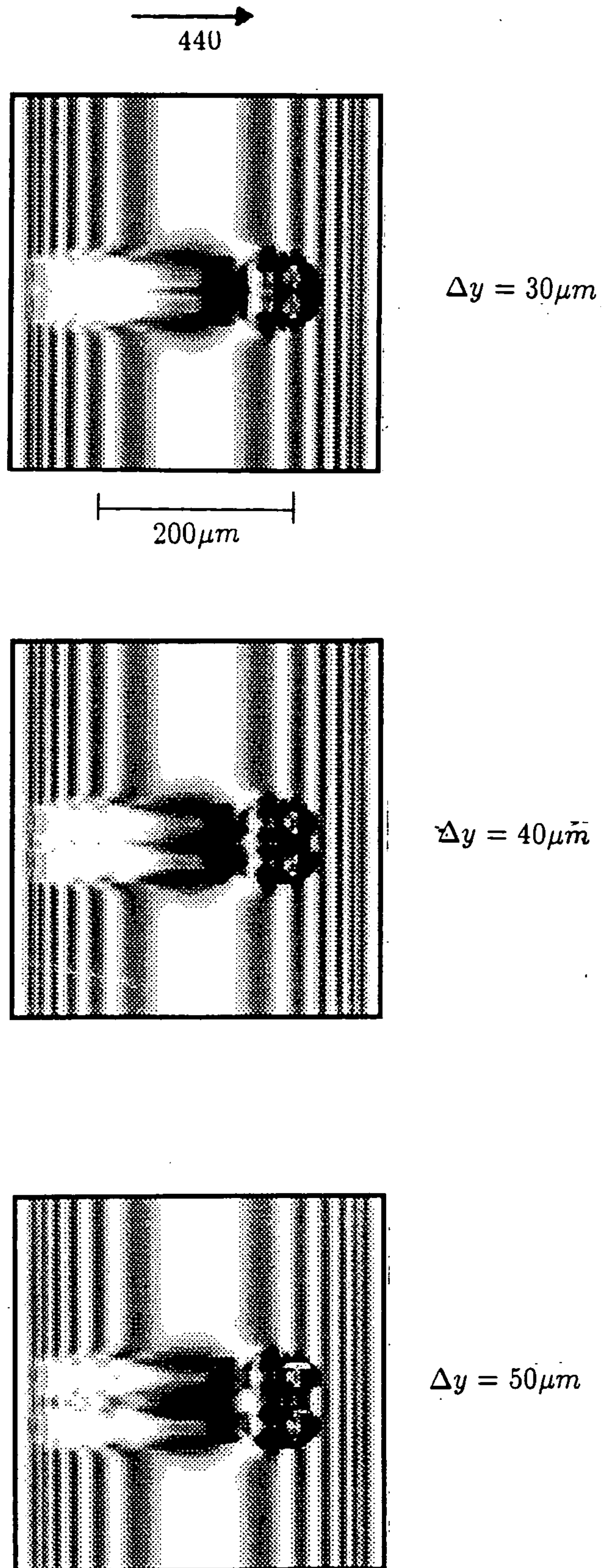

Fig. 4.25: Simulations for a pair of precipitates with different separation, Δy, in the experimental y-direction; deformation parameter, $C = 1 \times 10^{-19} m^3$ throughout.

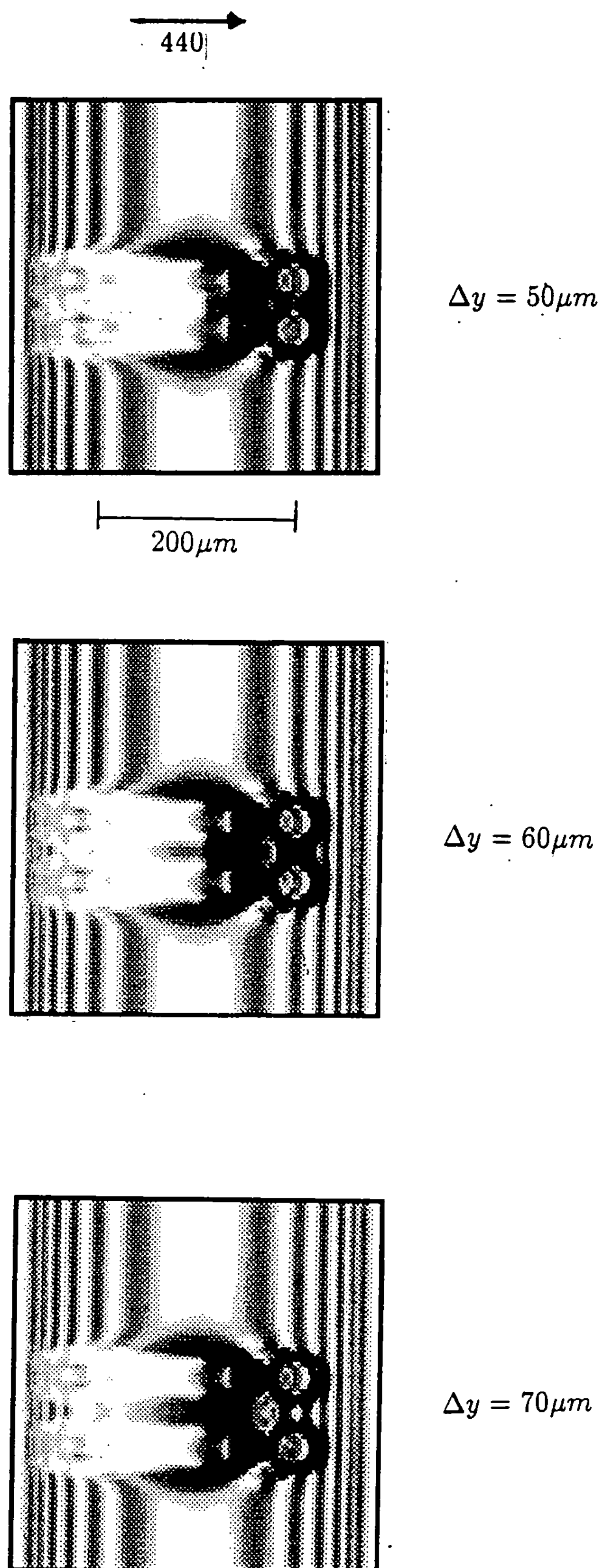

Fig. 4.26: Simulations for a pair of precipitates with different separation, Δy, in the experimental y-direction; deformation parameter, $C = 3 \times 10^{-19} m^3$ throughout.

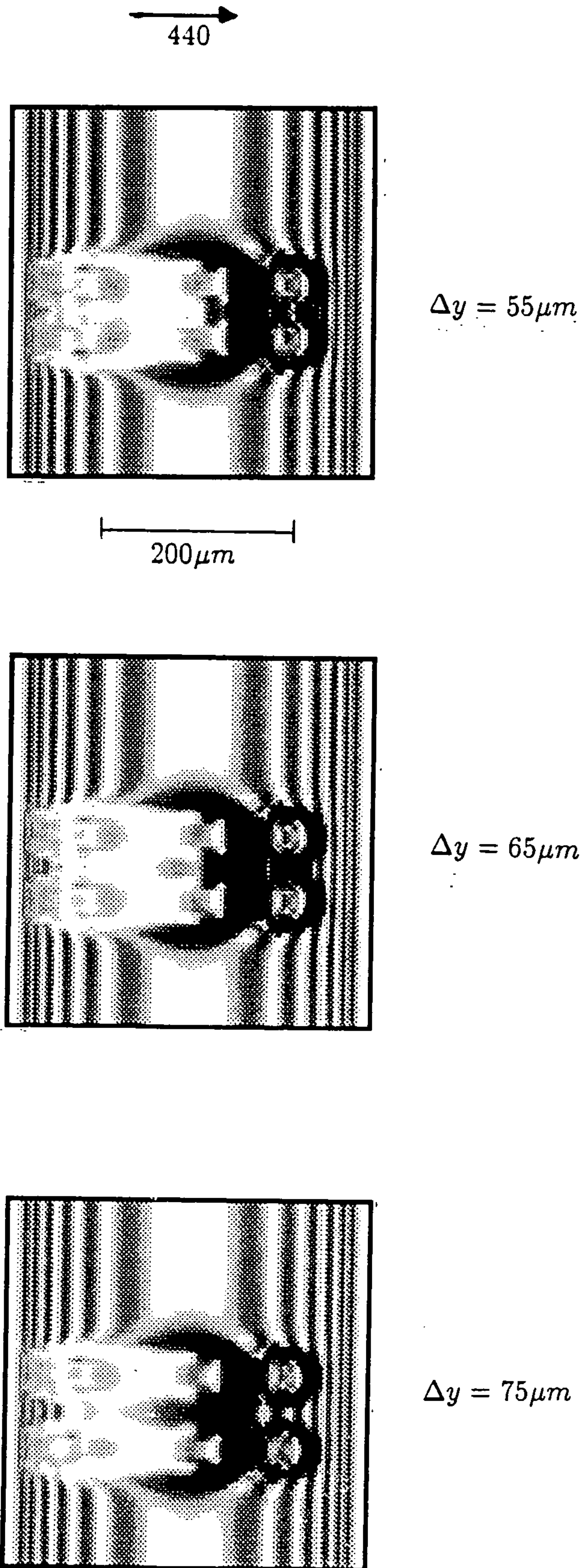

Fig. 4.27: Simulations for a pair of precipitates with different separation, Δy, in the experimental y-direction; deformation parameter, $C = 4 \times 10^{-19} m^3$ throughout.

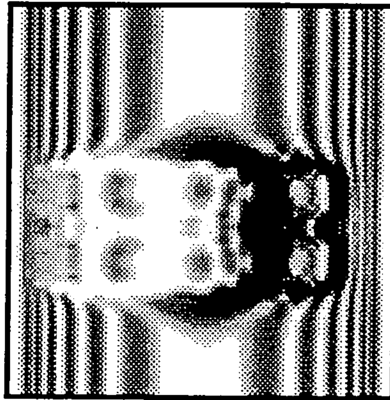

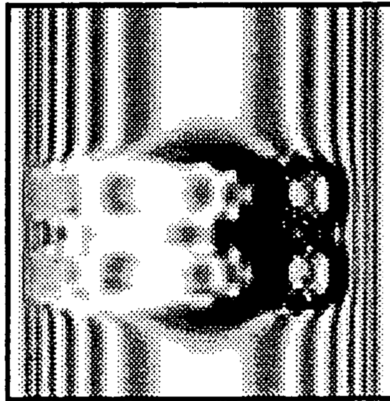

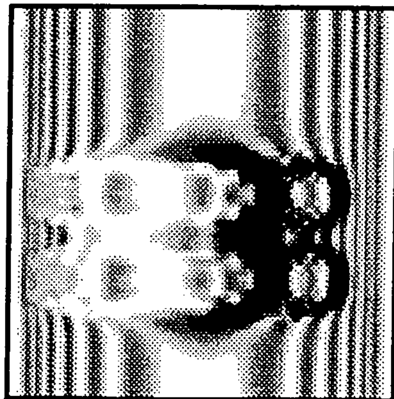

Fig. 4.28: Simulations for a pair of precipitates with different separation, Δy, in the experimental y-direction; deformation parameter, $C = 6 \times 10^{-19} m^3$ throughout.

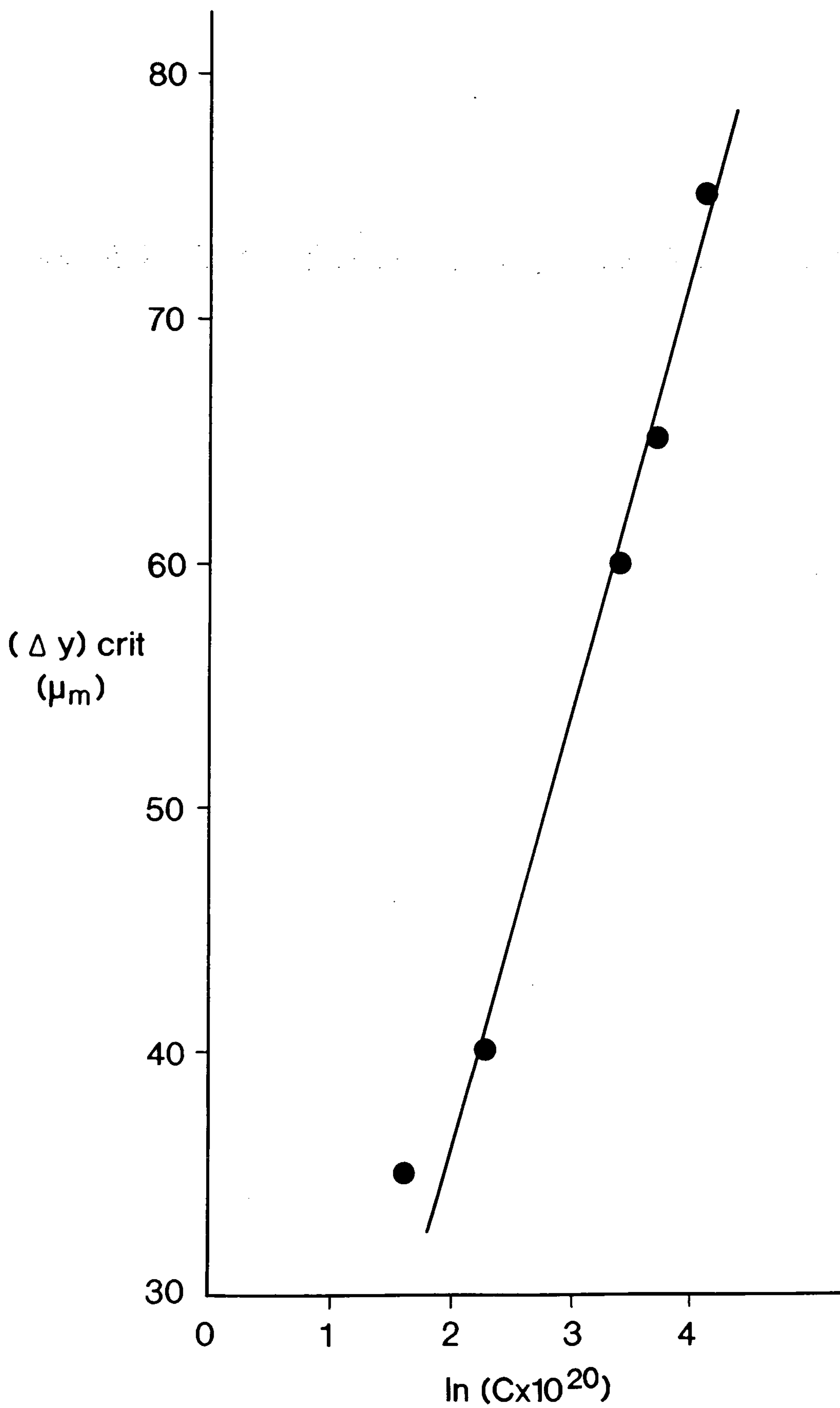

Fig. 4.29: Critical separation, Δy_{crit}, for two precipitates to be just resolved, as a function of deformation parameter, C, where C is measured in m^3.

$(\Delta y)_{crit}, (\mu m)$	$C, (\times 10^{20})$	$ln(C \times 10^{20})$
35	5	1.61
40	10	2.30
60	30	3.40
65	40	3.69
75	60	4.09

Table 4.4: Minimum separation, $(\Delta y)_{crit}$, for two precipitates to be just distinguishable as a function of deformation parameter, C.

where A is a constant.

Hence, the results of this work are in agreement with those of Green et al. [101]. In physical terms, this means that increasing the deformation parameter, C, by equal increments results in decreasing corresponding increments in image height, h.

4.8 General Discussion and Industrial Implications

The integration program $GENERAL.P$ (APPENDIX A) has been used in conjunction with the strain code $DIFFPOINT$ (APPENDIX B) for a precipitate to obtain excellent matching with experimental section topographs of oxygen precipitates in MCZ Si. The results are displayed in Figs. 4.9 and 4.10. Matching was possible in all cases studied, except for one precipitate, Fig. 4.11, which had grown so large following an 800°C anneal for 18 hours that its strain field was no longer spherically symmetric. The enhanced growth of this precipitate relative to others corresponding to the same annealing temperature and time may be attributable to impurities in the Si. It has been shown that carbon [82] and boron [83] impurities in Si can significantly enhance the precipitation of oxygen. Apart from the result of Fig. 4.11, striking uniformity of precipitate sizes was found for equivalent samples annealed at the same temperature and for the same duration. This is in agreement with the results of Green et al. [101], and it is proposed that the vast majority of precipitates are nucleated at approximately the same time, subsequently growing at the same rate.

Comparison of simulations with experimental images in Figs. 4.9 and 4.10 enabled the deformation parameter, C, to be determined as a function of annealing temperature, T. The results are displayed in Table 4.1. A linear relation was found between C and lnT, indicating that the precipitate volume increases at a decreasing rate with T. Fig. 4.13 shows a plot of $\ln C$ vs. $1/T$, for the spherical oxygen precipitates studied in this work. The non-linearity of the curve indicates that the spherical precipitates studied here do not follow the same growth equation, (4.1), as the square-plate oxygen precipitates studied by Wada et al. [90,91].

The successful matching of simulation with experiment in Figs. 4.9 and 4.10

indicates that the spherically symmetric strain relation of equation (4.3) provides an excellent model of the strain distribution due to real oxygen precipitates in Si. The low density of precipitates seen in the topographs pays tribute to the efficiency of the MCZ method in producing Si crystals of high quality. Furthermore, a clear industrial role is defined for X-ray section topography simulation. Given that individual precipitates can be imaged by the experimental technique, the simulation technique can be used to assign values to the deformation parameter and the precipitate depth in the crystal. These two quantities have a direct effect on the quality of wafers for use in device manufacture. First of all, the deformation parameter is an indication of the strain associated with a precipitate, and hence its potential to generate harmful process-induced defects. Also, the depth of precipitates is important, since oxygen precipitates in the active device region significantly reduce the electrical performance, whilst precipitates in the bulk enhance device yield through intrinsic gettering.

In section 4.4, it was shown that the effect of surface relaxation is enhanced with increasing deformation parameter, C. A study was made of the critical depth, z_{crit}, at which the effect of surface relaxation becomes negligible, as a function of C. The results are displayed in Table 4.3 and are plotted in Fig. 4.19. It was found that z_{crit} increases linearly with lnC. If the simulation technique is to be assigned an industrial role, then it is important that surface relaxation be incorporated into the simulation code, in the manner of section 4.4. This is especially true for near-surface studies. Otherwise, the reliability of the data derived from comparison of simulation with experiment is seriously questionable.

In section 4.6, simulations were performed for a CZ Si crystal with an oxygen precipitate density of $10^8 cm^{-3}$, consistent with the results of Wada et al. [90], with denuded zones of $30\mu m$ depth at top and bottom. The width of the perfect crystal part of the images, Fig. 4.23, was used to calculate the denuded zone depth with good accuracy, based only on a knowledge of the reflection indices, surface normal and crystal thickness. For a C-value of $2\times10^{-22}m^3$, the precipitates just ceased to be individually discernible, Fig. 4.23. This is in stark contrast to Figs. 4.9 and 4.10 for MCZ Si, where individual precipitates are very well resolved for C-values up to $7\times10^{-19}m^3$. This comparison serves to illustrate the comparatively high quality of Si grown by the MCZ method.

In section 4.7, the resolvability of precipitate pairs with respect to mutual displacement in the experimental y-direction was examined as a function of C. The results are displayed in Table 4.4 and are plotted in Fig. 4.29. The critical separation, $(\Delta y)_{crit}$, for which precipitates were just resolved was found to increase linearly with lnC. This agrees well with the results of Green et al. [101], which showed that the image height, h, in the experimental y-direction increases linearly with lnC.

Chapter 5

Intrinsic Gettering of Transition Metal Impurities at Dislocations in Silicon

5.1 Background and Context

5.1.1 Introduction

During the mechanical and chemical processes involved in Si wafer manufacture, the wafer comes into contact with a number of transition metals and their chemical solutions. These metals are absorbed into the wafer surface as impurities. The diffusivity of transition metals in Si at typical thermal processing temperatures is very high, so that these contaminants quickly diffuse from the crystal surface into the bulk. The solubility differential between processing temperature and room temperature is extremely high for transition metals in Si, so that upon cooling they form precipitates throughout the crystal. The presence of transition metal precipitates in the active device layer of a Si wafer is highly detrimental to device performance. Consequently, modern semiconductor technologies have had to find a way of removing transition metals from the surface layers of Si wafers for use in device fabrication.

In 1964, Patel [116] observed dislocation loops in Si samples containing oxygen, grown in a quartz crucible, following heat treatment at 1000°C. Transmission electron micrographs showed that each dislocation loop was centred upon a dark, unresolved image feature. Patel suggested that these small, dark images corresponded to oxygen precipitates which had generated dislocation loops as a stress-relief mechanism, by the process of *prismatic punching*, predicted by Seitz [117] in 1950.

Work in the late 1960's [118,119] and early 1970's [120] showed that Cu impurities exhibit a strong tendency to precipitate at oxygen-related defects in Si. In 1976, Tan and Tice [121] carried out the first detailed experimental observation of the punching out of prismatic dislocation loops by oxygen precipitates in Si. They showed that the precipitates have a square-plate form and that the dislocation loops

are interstitial in nature, exerting a compressive stress on the surrounding lattice. In the same year, Maher et al. [122] showed that the oxygen precipitates range in size from a few hundred angstroms to a few tenths of a micron, and that the dislocation loops have a rhombus shape. Subsequently, Tice and Tan [123] used transmission electron microscopy (TEM) to show that dislocation loops punched out by oxygen precipitates in Si act as nucleation centres for the precipitation of Cu impurities.

Tan et al. [124] pointed out that due to outdiffusion of oxygen from the crystal surface layers, upon heating in a non-oxygen ambient, precipitate-dislocation complexes (PDC's) will form predominantly in the bulk, leaving a defect-free surface. Moreover, this allows the removal of transition metal impurities (notably Cu, Fe and Ni) from the crystal surface layer, which is then ideal for device fabrication. This takes place according to the *intrinsic gettering* (IG) mechanism outlined below:

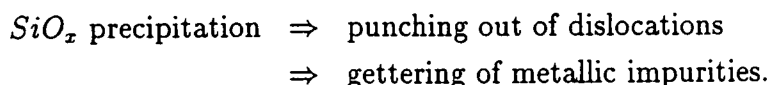

$$\begin{aligned} SiO_x \text{ precipitation } &\Rightarrow \text{ punching out of dislocations} \\ &\Rightarrow \text{ gettering of metallic impurities.} \end{aligned}$$

Gettering of metallic impurities takes place because the free energy of a precipitate-decorated dislocation is less than that of dispersed metal atoms plus an undecorated dislocation.

There are several alternative mechanisms by which intrinsic gettering can be accomplished. For example, Bai et al. [125] have shown that the defects generated in a thermally grown SiO_2/Si interface provide nucleation sites for the gettering of Cu impurities.

Consequently, the initial goal of removing transition metals from the surface layer of Si wafers is achieved using intrinsic gettering.

Precipitation of impurities at crystal defects is a process which is entirely internal, or *intrinsic*, to the Si wafer. Processes which achieve the same effect by externally imposed means are termed *extrinsic gettering.* The most common example is phosphorus-diffusion, used by Ourmazd and Schröter [126] for the gettering of Ni impurities in Si. The diffusion of phosphorus into the Si surface layer results in the formation of SiP particles, which promotes the emission of Si interstitials. Ni impurities combine with these interstitials to form an epitaxial layer of $NiSi_2$ on the Si surface. The process of IG has been thoroughly reviewed, both in general terms [127] and in terms of transition metal impurities [128].

A crucial feature of the IG process is the heat treatment used to activate it. A typical industrial thermal cycle is illustrated in Fig. 5.1, after Baginski and Monkowski [129]. The initial high temperature step causes outdiffusion of oxygen from the surface layer, leaving an oxygen-free denuded zone. The second step is a 600 - 800°C anneal to promote the generation of nucleation sites for oxygen precipitation. Annealing at temperatures greater than 900°C causes dissolution of these nucleation sites. The final, 1000°C step is used to promote growth of oxygen precipitates from the nucleation centres of the previous step. Baginski and Monkowski [129] have shown that oxygen-related defects generated by the mechanism of Fig. 5.1 allow the gettering of gold impurities.

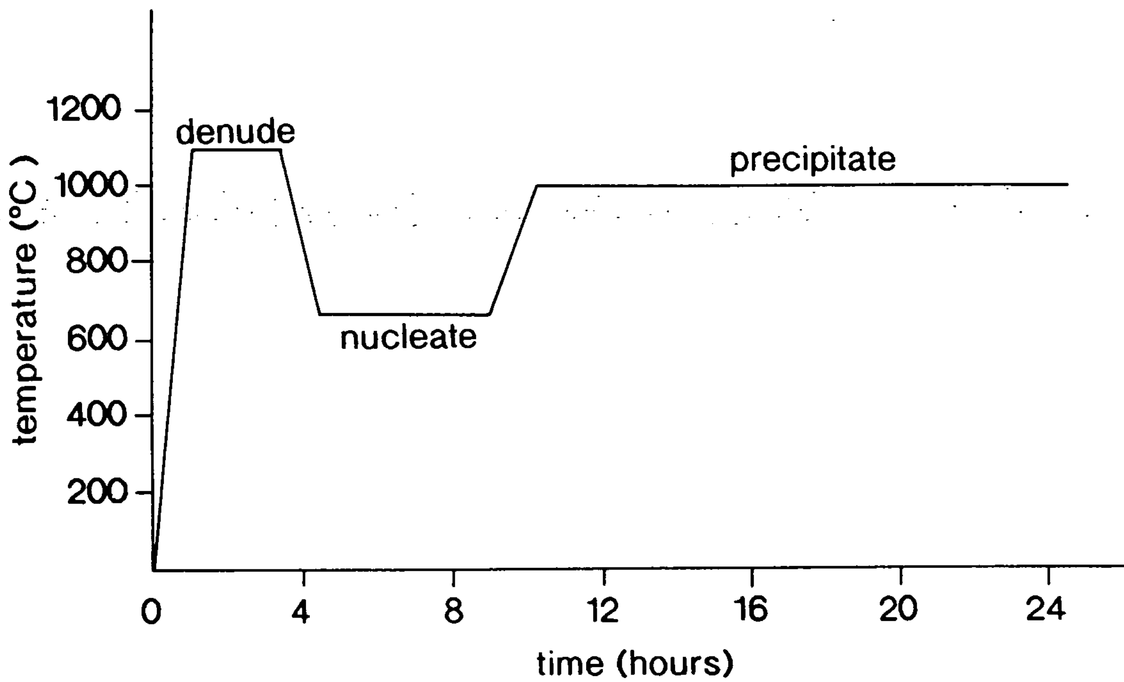

Fig. 5.1: Typical thermal cycle used to activate intrinsic gettering, (after Baginski and Monkowski).

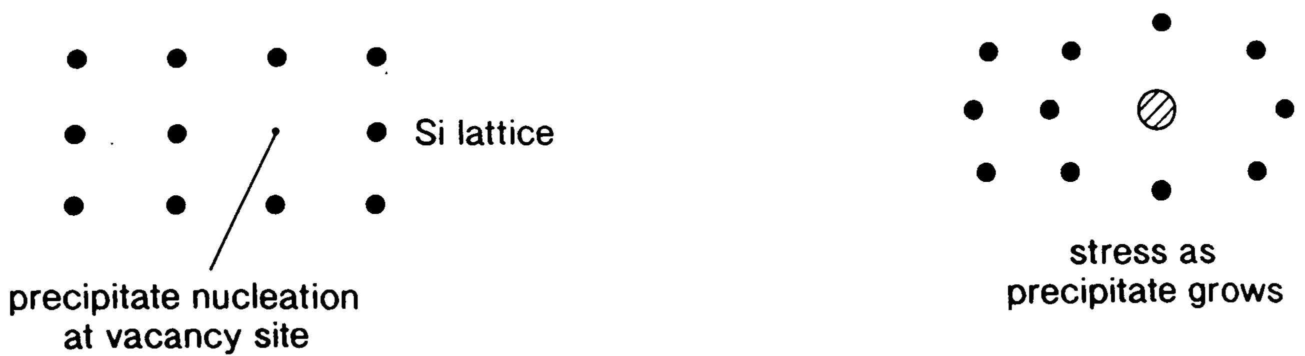

Fig. 5.2: Illustration of the model of Rivaud et al. (see text) for the nucleation and growth of oxygen precipitates in silicon.

Rivaud et al. [130] have undertaken studies to understand more precisely the nucleation of oxygen precipitates within the Si matrix. Their model is illustrated in Fig. 5.2. Oxygen atoms are trapped in lattice vacancy sites, forming precipitate nucleation centres. These nuclei grow with subsequent heat treatment, to form fundamental precipitates. Precipitates grow by reacting with neighbouring Si atoms and the resulting precipitate exhibits a 120% volume increase relative to the matrix. This dilation induces a stress in the adjacent Si lattice planes, which is relieved by the punching out of prismatic dislocations.

As well as the previously mentioned transition metals, studies have shown that Cr [131] and Fe [132] impurities are very efficiently gettered by oxygen-related defects in Si. The latter work showed that the concentration of interstitial Fe decreases with annealing time as a result of gettering.

The relative gettering efficiency for different transition metals has been investigated by Falster and Bergholz [39], using the *haze method*, illustrated in Fig. 5.3. A Si wafer containing oxygen-related defects was rubbed with five parallel wires of Ni, Pd, Fe, Cu and Co, in two orthogonal directions, Fig. 5.3(a). A heat treatment of 1200°C for 30 seconds was imposed, sufficient to saturate the sample thickness locally with each transition metal. Certain metals tend to precipitate at the wafer surface, following cooling from high temperatures. Regions of the wafer surface diffused with such precipitates exhibit *haze* when viewed in bright, collimated light. Hence, the amount of haze visible for each metal after the heat treatment of the sample in Fig. 5.3 is an indication of the relative gettering efficiency. The results are illustrated schematically in Fig. 5.3(b). Cu and Ni were found to be the easiest to getter, whilst Co and Pd showed progressively decreasing gettering efficiency. This is technologically very useful, since Cu and Ni are two of the most common contaminants. In addition, this result justifies the use of the Pd-test as a standard means of determining gettering efficiency. The gettering efficiency of Fe could not be determined by this method, since Fe does not precipitate appreciably at the wafer surface. However, Fe gettering efficiency has been determined by a more quantitative method [133], in which deep level transient spectroscopy (DLTS) was used to measure Fe concentration. In addition to the above results, a general trend was observed [39,133] for decreasing gettering efficiency with increased heating time. This was attributed to disruption of the defect structure during extended processing.

Another work [134], has shown that antimony doping of a Si wafer inhibits the formation of oxygen precipitates and hence reduces gettering efficiency. This undesirable effect was ameliorated to some extent by postannealing the processed wafer for a period of up to 48 hours. In general, the size and density of bulk defects was found to increase with postannealing time and with increasing wafer resistivity (decreased doping).

In addition to the gettering properties of oxygen-related defects, it has been shown [135,136] that SiO_x gettering centres inhibit the motion of dislocations. This is a useful means of preventing slip during wafer heat treatment.

The importance of IG within semiconductor technology can be illustrated by two examples. Tan et al. [124] have shown that current leakage from devices is substantially reduced when oxygen-related gettering centres are present in the crystal

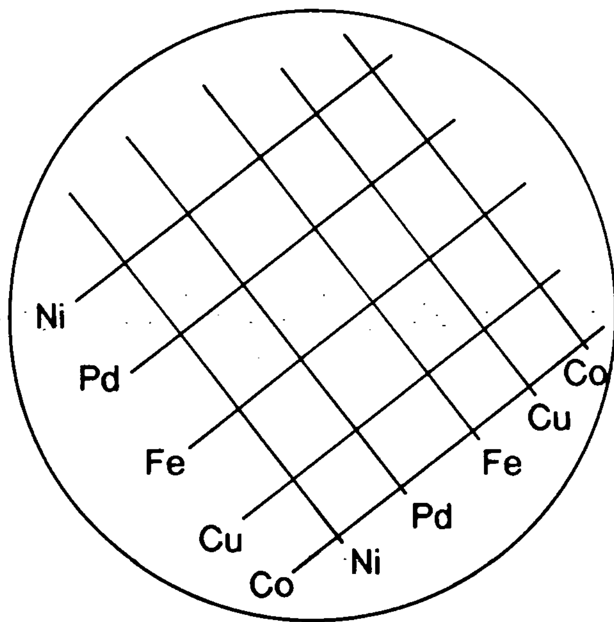

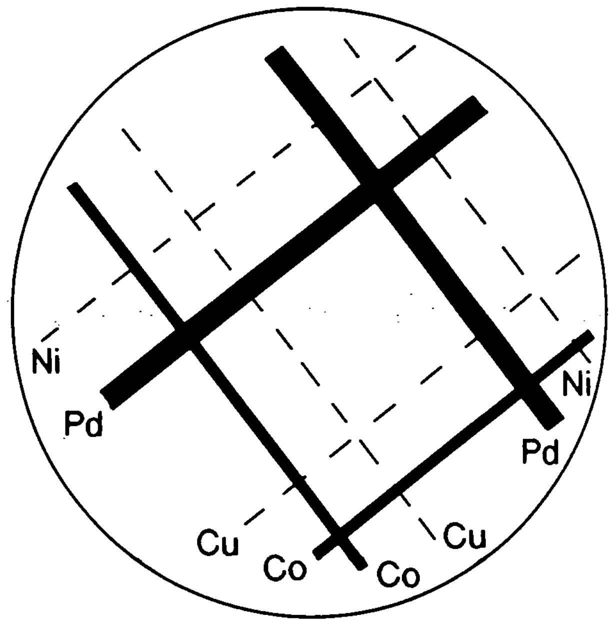

Fig. 5.3: Illustration of Falster and Bergholz's experiment for determining relative gettering efficiency by the haze method.

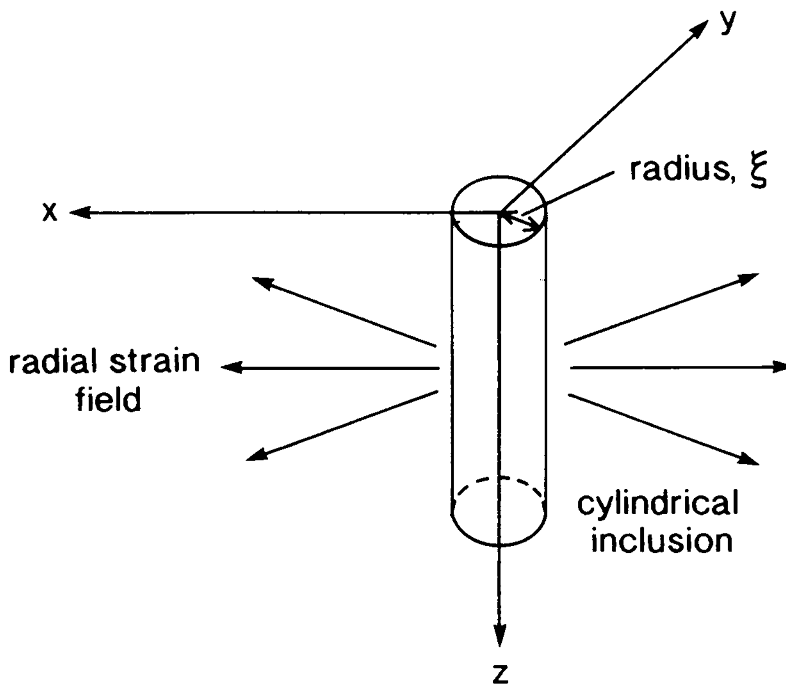

Fig. 5.4: Tanner's cylindrical inclusion model.

bulk. They showed that IG can be used in this way to increase device yield by a factor of five. In addition, Yue and Ruiz [137] showed that the storage time of a MOS capacitor is maximised when SiO_2 PDC's are present at least $25\mu m$ below the wafer surface.

Bourret et al. [138] have shown that edge dislocations in CZ Si act as sites for the nucleation of oxygen precipitates. They showed that oxygen precipitates form a cylindrical distribution along the dislocation core. More recently, Kidd et al. [139] have observed dislocations decorated with arsenic precipitates in In-doped $GaAs$ samples. Tanner [140] proposed that such precipitate distributions may be elastically modelled by an equivalent cylindrical inclusion, whose axis is collinear with the associated dislocation.

5.1.2 Statement of Approach

The purpose of the current work is to use the cylindrical inclusion model [140] to investigate the elastic properties of dislocations decorated with transition metal precipitates, resulting from the IG process. Also, it is of considerable importance to determine whether or not X-ray topography has the sensitivity to detect precipitate decoration, and to find out if the decorated dislocation shows significantly different contrast from the bare dislocation. Although much of the analysis of IG has been done using TEM, because of its high spatial resolution, X-ray topography is the ideal tool for the current task, because of its high sensitivity to lattice strain. Hence, the investigation has been done theoretically, by incorporating the appropriate strain equations [140] into the X-ray topography simulation program of the previous chapter.

The current author has developed code to calculate the strain due to a cylindrical inclusion, section 5.2, and due to a cylindrical distribution of precipitates, section 5.4. The precipitate distribution strain may be added to the strain due to the corresponding dislocation, according to linear elasticity theory, in order to obtain the strain due to the decorated dislocation. Analogously, the cylindrical inclusion strain may be added to the dislocation strain to provide an alternative elastic model of the decorated dislocation. In section 5.5, section topograph simulations of decorated dislocations were generated, using both the precipitate distribution model and the equivalent cylindrical inclusion. Comparison of corresponding images has been used to investigate the variation in cylindrical inclusion strain with precipitate strain.

5.2 Development of the Strain Code for a Cylindrical Inclusion

5.2.1 Strain Equations for a Cylindrical Inclusion

Kramer and Bauer [141] showed that a fluxoid (magnetic flux line) in a superconducting medium can be elastically modelled by an elastic cylindrical inclusion. They

derived the associated stress components in polar coordinates. Ivanov et al. [142] subsequently expressed the same equations in Cartesian coordinates.

Following on from this, Tanner [140] expressed the strain components due to a cylindrical inclusion lying along the z-axis of a Cartesian system, whose origin is at the defect line, Fig. 5.4, as:

$$e_{xx} = A\xi^2 \frac{x^2 - y^2}{(x^2 + y^2)^2} = -e_{yy},$$

$$e_{xy} = A\xi^2 \frac{2xy}{(x^2 + y^2)^2} = e_{yx}, \tag{5.1}$$

with all other components zero.

The quantity A in (5.1) is given by:

$$A = -\varepsilon(1 + \nu)/3(1 - \nu), \tag{5.2}$$

where the *lattice mismatch parameter*, ε, is the relative volume change between inclusion and matrix, and ν is Poisson's ratio.

The term ξ in (5.1) is the radius of the cylindrical inclusion.

5.2.2 Transformation of Coordinates from Experimental System to Inclusion System

In general, the decorated dislocation will lie skew relative to the experimental x, y, z-axes. In order to obtain the Cartesian system of the inclusion, it is necessary to perform two rotations of the x, y, z-axes, illustrated in Fig. 5.5. First of all, the x, z-axes are rotated by an angle ψ about the y-axis, Fig. 5.5(a), to generate the a, b, c-axes. Then, the b, c-axes are rotated by an angle ϵ about the a-axis, Fig. 5.5(b), to generate the s, t, u-axes. Suitable choice of the angles ψ and ϵ allows the u-axis to be oriented along any possible direction in three dimensional space. The u-axis is then taken as the axis of the cylindrical inclusion, so that equations (5.1) can be re-written:

$$e_{ss} = A\xi^2 \frac{s^2 - t^2}{(s^2 + t^2)^2} = -e_{tt},$$

$$e_{st} = A\xi^2 \frac{2st}{(s^2 + t^2)^2} = e_{ts}. \tag{5.3}$$

Points in the integration network of the simulation program are expressed in (x, y, z) coordinates. Hence, if s, t, u can be expressed in terms of x, y, z, the strain components (5.3) due to the inclusion can be found at all points in the integration network.

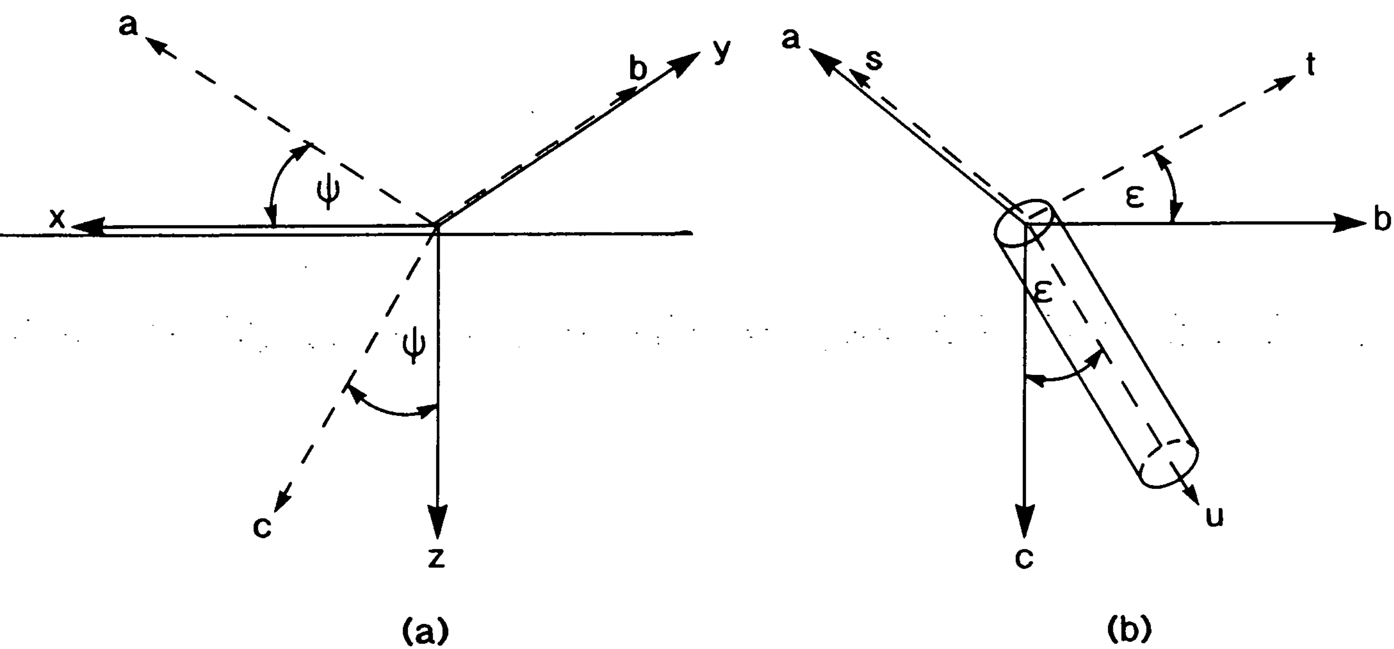

Fig. 5.5: Transformation of the x, y, z-axes into the a, b, c-axes, (a), and transformation of the a, b, c-axes into the s, t, u-axes, (b).

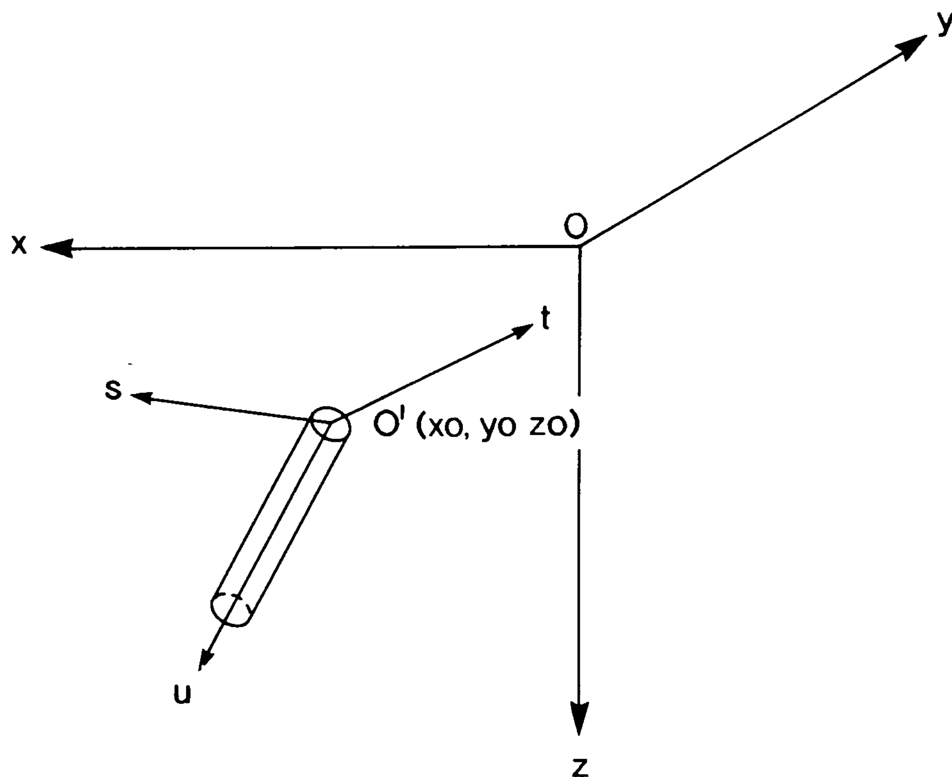

Fig. 5.6: Definition of the origin of the inclusion relative to the experimental x, y, z-axes.

From Fig. 5.5(b):

$$\begin{aligned} s &= a, \\ t &= b\cos\epsilon - c\sin\epsilon, \\ u &= b\sin\epsilon + c\cos\epsilon. \end{aligned} \tag{5.4}$$

Expressing equations (5.4) in matrix form:

$$\begin{pmatrix} s \\ t \\ u \end{pmatrix} = \begin{pmatrix} 1 & 0 & 0 \\ 0 & \cos\epsilon & -\sin\epsilon \\ 0 & \sin\epsilon & \cos\epsilon \end{pmatrix} \begin{pmatrix} a \\ b \\ c \end{pmatrix}. \tag{5.5}$$

From Fig. 5.5(a):

$$\begin{aligned} a &= x\cos\psi - z\sin\psi, \\ b &= y, \\ c &= x\sin\psi + z\cos\psi. \end{aligned} \tag{5.6}$$

Expressing equations (5.6) in matrix form:

$$\begin{pmatrix} a \\ b \\ c \end{pmatrix} = \begin{pmatrix} \cos\psi & 0 & -\sin\psi \\ 0 & 1 & 0 \\ \sin\psi & 0 & \cos\psi \end{pmatrix} \begin{pmatrix} x \\ y \\ z \end{pmatrix}. \tag{5.7}$$

From (5.5) and (5.7), the matrix **T** for transforming (x, y, z) coordinates into (s, t, u) coordinates is given as:

$$\mathbf{T} = \begin{pmatrix} 1 & 0 & 0 \\ 0 & \cos\epsilon & -\sin\epsilon \\ 0 & \sin\epsilon & \cos\epsilon \end{pmatrix} \begin{pmatrix} \cos\psi & 0 & -\sin\psi \\ 0 & 1 & 0 \\ \sin\psi & 0 & \cos\psi \end{pmatrix},$$

$$\text{so that, } \mathbf{T} = \begin{pmatrix} \cos\psi & 0 & -\sin\psi \\ -\sin\psi\sin\epsilon & \cos\epsilon & -\cos\psi\sin\epsilon \\ \sin\psi\cos\epsilon & \sin\epsilon & \cos\psi\cos\epsilon \end{pmatrix}. \tag{5.8}$$

Of course, the origin, O', of the inclusion will not necessarily be coincident with the origin, O, of the experimental axes. Let the coordinates of the inclusion origin be at the point $(x0, y0, z0)$ in x, y, z-space, Fig. 5.6. The point so defined is the origin of the s, t, u-axes, Fig. 5.6.

Then the transformation from (x, y, z) to (s, t, u) coordinates becomes:

$$\begin{pmatrix} s \\ t \\ u \end{pmatrix} = \begin{pmatrix} \cos\psi & 0 & -\sin\psi \\ -\sin\psi\sin\epsilon & \cos\epsilon & -\cos\psi\sin\epsilon \\ \sin\psi\cos\epsilon & \sin\epsilon & \cos\psi\cos\epsilon \end{pmatrix} \begin{pmatrix} x - x0 \\ y - y0 \\ z - z0 \end{pmatrix},$$

or, in explicit form:

$$\begin{aligned} s &= \cos\psi(x - x0) - \sin\psi(z - z0), \\ t &= -\sin\psi\sin\epsilon(x - x0) + \cos\epsilon(y - y0) \\ &\quad - \cos\psi\sin\epsilon(z - z0), \\ u &= \sin\psi\cos\epsilon(x - x0) + \sin\epsilon(y - y0) \\ &\quad + \cos\psi\cos\epsilon(z - z0). \end{aligned} \tag{5.9}$$

5.2.3 Derivation of Takagi's Differential Expression

In section 4.2, it was shown how the program *GENERAL.P* (APPENDIX A), together with the procedures *POINTDEF* and *DIFFPOINT* (APPENDIX B), could be used to integrate Takagi's equations, (2.55), using equations (3.8) and (3.9). The term *dsh*, calculated for a precipitate in *DIFFPOINT*, represents the differential expression $\frac{\partial}{\partial S_h}[\underline{h}.\underline{u}(\underline{r})]$ of equation (2.43), which is required in the numerical integration of Takagi's equations using (3.8) and (3.9). What is required now is a new procedure to calculate the term *dsh* for the strain field due to a cylindrical inclusion. In addition, a new procedure analogous to *POINTDEF* is needed to read in the inclusion parameters. These new procedures may then be used in conjunction with *GENERAL.P* to simulate X-ray topographs.

Expressing the quantity *dsh* from the previous chapter in a manner analogous to that of equation (4.4):

$$\begin{aligned} dsh &= \frac{\partial}{\partial S_h}[\underline{h}.\underline{u}(\underline{r})], \\ &= shs\frac{\partial}{\partial s}[h_s u_s + h_t u_t + h_u u_u] + sht\frac{\partial}{\partial t}[h_s u_s + h_t u_t + h_u u_u] \\ &\quad + shu\frac{\partial}{\partial u}[h_s u_s + h_t u_t + h_u u_u], \end{aligned} \tag{5.10}$$

where h represents the reciprocal lattice vector.

Recalling that $e_{pq} = \partial u_p/\partial q$, then from equations (5.3), expression (5.10) becomes:

$$dsh = shs(h_s e_{ss} + h_t e_{ts}) + sht(h_s e_{st} + h_t e_{tt}), \tag{5.11}$$

where the strain components, e_{pq}, are given by (5.3).

The next step is to derive expressions for h_s, h_t, shs and sht.

*** Finding h_s and h_t :**

The diffraction vector $\underline{h}$ has components in the experimental coordinate system (x, y, z) of $h[1]$, $h[2]$ and $h[3]$. These components are worked out automatically in procedure *POINTDEF* from the reflection indices $rf[1,2,3]$ and the surface normal components $rn[1,2,3]$. The same mechanism must be incorporated into the cylindrical analogue of *POINTDEF*. h_s and h_t are obtained by resolving $\underline{h}$ along the $\underline{s}$ and $\underline{t}$-directions.

It is necessary to express $\hat{\underline{s}}$ and $\hat{\underline{t}}$ as vectors in the x, y, z-system.

From Fig. 5.5:

$$\begin{aligned} \hat{\underline{s}} &= \hat{\underline{a}}, \\ &= (\cos\psi, 0, -\sin\psi). \end{aligned} \tag{5.12}$$

Let $\hat{\underline{t}} = (t_1, t_2, t_3)$.

Then, from Fig. 5.5:

$$\hat{\underline{t}}.\hat{\underline{y}} = \cos\epsilon,$$

$$\begin{aligned} \text{i.e., } (t_1, t_2, t_3).(0,1,0) &= \cos\epsilon, \\ \text{so that } t_2 &= \cos\epsilon. \end{aligned} \tag{5.13}$$

$$\text{Clearly, } \underline{\hat{s}}.\underline{\hat{t}} = 0.$$

$$\begin{aligned} \text{Then, } t_1 \cos\psi - t_3 \sin\psi &= 0, \\ \text{so that } t_1 &= t_3 \sin\psi / \cos\psi. \end{aligned} \tag{5.14}$$

$$\text{Also, } t_1^2 + t_2^2 + t_3^2 = 1.$$

Hence, using (5.13) and (5.14):

$$\begin{aligned} t_3^2 \tan^2\psi + \cos^2\epsilon + t_3^2 &= 1, \\ \text{so that } t_3 &= \pm \sin\epsilon \cos\psi. \end{aligned}$$

The negative solution is taken, since the z-component of $\underline{\hat{t}}$ must be negative, from the geometry of Fig. 5.5.

$$\text{Hence, } t_3 = -\sin\epsilon\ \cos\psi. \tag{5.15}$$

Combining (5.14) and (5.15):

$$t_1 = -\sin\epsilon \sin\psi. \tag{5.16}$$

Now combining (5.13), (5.15) and (5.16):

$$\underline{\hat{t}} = (-\sin\epsilon \sin\psi, \cos\epsilon, -\sin\epsilon \cos\psi). \tag{5.17}$$

So, using equations (5.12) and (5.17):

$$\begin{aligned} h_s &= \underline{h}.\underline{\hat{s}}, \\ &= h[1]\cos\psi - h[3]\sin\psi; \end{aligned} \tag{5.18}$$

$$\begin{aligned} h_t &= \underline{h}.\underline{\hat{t}}, \\ &= -h[1]\sin\epsilon\sin\psi + h[2]\cos\epsilon - h[3]\sin\epsilon\cos\psi. \end{aligned} \tag{5.19}$$

*** Finding *shs* and *sht* :**

In procedure *SETUP* within *GENERAL.P* (APPENDIX A), the variables $shx1$ and $shx3$, representing shx and shz, respectively, are defined:

$$\begin{aligned} shx1 &= -\sin(dir), \\ \text{and } shx3 &= \cos(dir). \end{aligned}$$

Referring to Fig. 5.7, it is then seen that:

$$\begin{aligned} shx &= \underline{\hat{S}_h}.\underline{\hat{x}}, \\ \text{and } shz &= \underline{\hat{S}_h}.\underline{\hat{z}}, \\ \text{where } \underline{\hat{S}_h} &= (-\sin(dir), 0, \cos(dir)). \end{aligned} \tag{5.20}$$

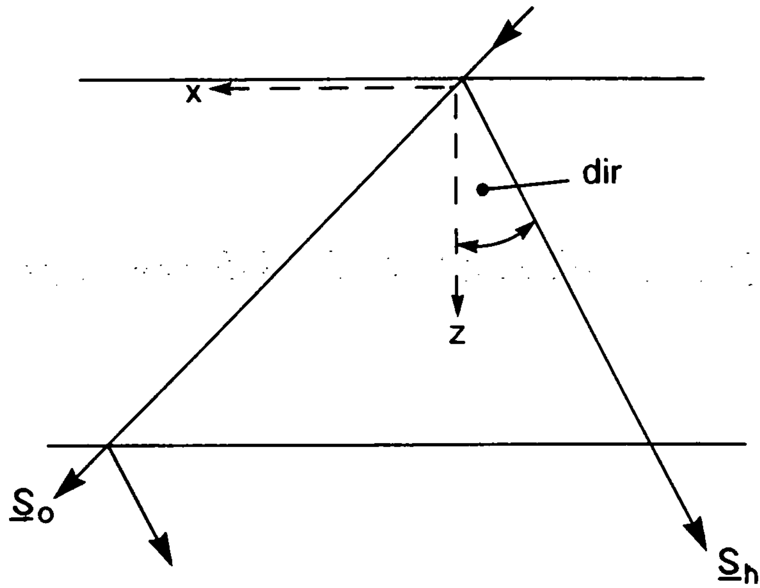

Fig. 5.7: Definition of the angle *dir* in terms of the diffraction geometry.

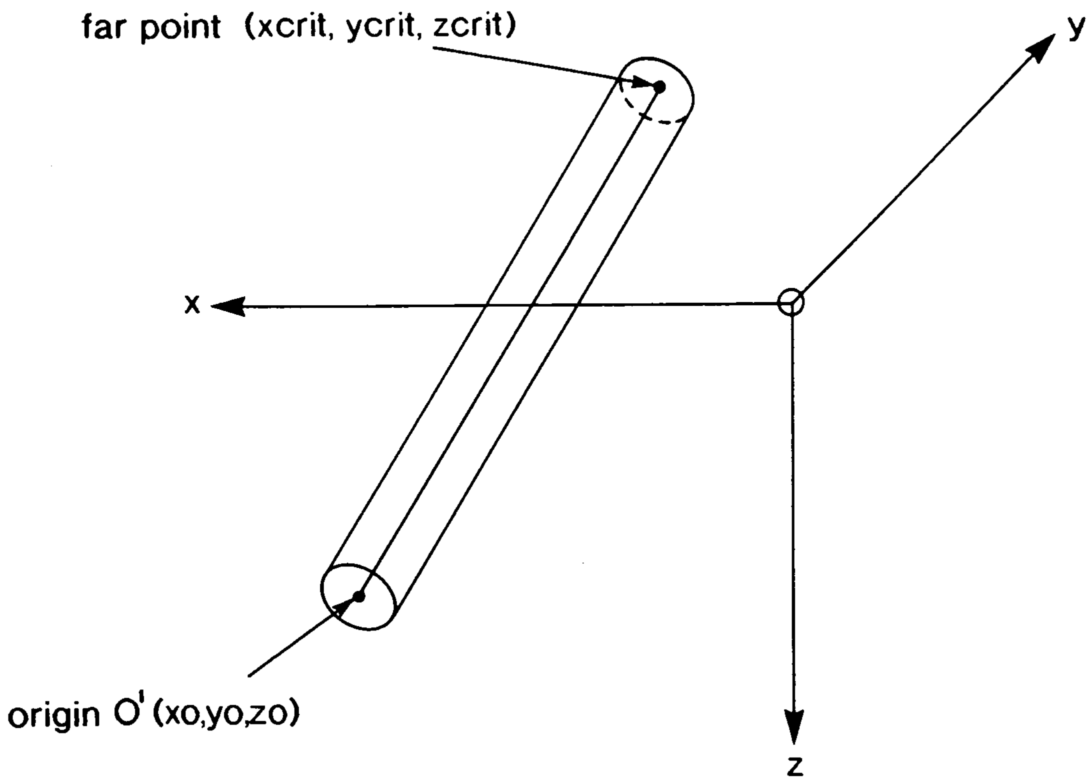

Fig. 5.8: Boundary coordinates of the cylindrical inclusion axis.

Similarly,

$$shs = \underline{\hat{s}}.\underline{\hat{S}_h}, \quad (5.21)$$
$$\text{and } sht = \underline{\hat{t}}.\underline{\hat{S}_h}. \quad (5.22)$$

Using (5.12) and (5.20), (5.21) becomes:

$$shs = -\cos\psi\sin(dir) - \sin\psi\cos(dir). \quad (5.23)$$

Using (5.17) and (5.20), (5.22) becomes:

$$sht = \sin\psi\sin\epsilon\sin(dir) - \cos\psi\sin\epsilon\cos(dir). \quad (5.24)$$

Hence, equations (5.18), (5.19), (5.23) and (5.24) give, respectively, h_s, h_t, shs and sht. These expressions can be incorporated into equation (5.11) to give dsh at all points in the integration network.

5.2.4 Derivation of Inclusion Orientation

The dislocation code *DISLOC.P* (APPENDIX D1) automatically calculates and displays the components of the dislocation orientation vector in experimental space. Later, it will be necessary to align the cylindrical u-axis with the dislocation line, by suitable choice of angles ψ and ϵ. Hence, it is necessary to express the components of vector $\underline{\hat{u}}$ in terms of ψ and ϵ.

From Fig. 5.5(a):

$$\underline{\hat{c}} = (\sin\psi, 0, \cos\psi), \quad (5.25)$$

in the x, y, z experimental system.

Using Fig. 5.5(b):

$$\underline{\hat{c}}.\underline{\hat{u}} = \cos\epsilon, \quad (5.26)$$
$$\underline{\hat{s}}.\underline{\hat{u}} = 0, \quad (5.27)$$
$$\underline{\hat{t}}.\underline{\hat{u}} = 0. \quad (5.28)$$

$$\text{Let } \underline{\hat{u}} = (u_1, u_2, u_3). \quad (5.29)$$

Using (5.25) and (5.29) in (5.26) gives:

$$u_1\sin\psi + u_3\cos\psi = \cos\epsilon. \quad (5.30)$$

Using (5.12) and (5.29) in (5.27) gives:

$$u_1\cos\psi - u_3\sin\psi = 0. \quad (5.31)$$

Finally, using (5.17) and (5.29) in (5.28) gives:

$$-u_1\sin\epsilon\sin\psi + u_2\cos\epsilon - u_3\sin\epsilon\cos\psi = 0. \quad (5.32)$$

From (5.30):

$$u_1 = \frac{\cos\epsilon - u_3\cos\psi}{\sin\psi}.$$

Substituting for u_1 in (5.31) then gives:

$$\begin{aligned}(\cos\epsilon - u_3\cos\psi)\frac{\cos\psi}{\sin\psi} - u_3\sin\psi &= 0, \\ \text{so that } u_3 &= \cos\epsilon\cos\psi. \end{aligned} \tag{5.33}$$

Substituting (5.33) into (5.31) gives:

$$\begin{aligned} u_1 &= \cos\epsilon\cos\psi\frac{\sin\psi}{\cos\psi}, \\ &= \cos\epsilon\sin\psi. \end{aligned} \tag{5.34}$$

Substituting for u_1 and u_3 into (5.32) gives:

$$\begin{aligned} u_2\cos\epsilon &= \cos\epsilon\sin\psi\sin\epsilon\sin\psi + \cos\epsilon\cos\psi\sin\epsilon\cos\psi, \\ \text{so that } u_2 &= \sin\epsilon. \end{aligned} \tag{5.35}$$

Combining (5.33), (5.34) and (5.35) gives:

$$\underline{\hat{u}} = (\cos\epsilon\sin\psi, \sin\epsilon, \cos\epsilon\cos\psi). \tag{5.36}$$

Using (5.36), the orientation of the cylinder axis in experimental space can be specified using the angles ψ and ϵ.

5.2.5 Boundary Conditions of the Inclusion

Suppose the origin $(x0, y0, z0)$ of the inclusion lies at that point on the cylindrical axis which is closest to the plane in which y is zero. Let the coordinates in experimental space of the opposite end of the cylinder axis be $(xcrit, ycrit, zcrit)$, Fig. 5.8.

Then, using (5.36):

$$zcrit - z0 = K\cos\epsilon\cos\psi, \tag{5.37}$$

where K is a constant.

$$\text{Then, } K = (zcrit - z0)/(\cos\epsilon\cos\psi). \tag{5.38}$$

Using (5.36) again:

$$\begin{aligned} ycrit - y0 &= K\sin\epsilon, \\ \text{so that } ycrit &= K\sin\epsilon + y0. \end{aligned} \tag{5.39}$$

$$\begin{aligned} \text{Similarly, } xcrit - x0 &= K\cos\epsilon\sin\psi, \\ \text{so that } xcrit &= K\cos\epsilon\sin\psi + x0. \end{aligned} \tag{5.40}$$

Consequently, given $(x0, y0, z0)$ and $zcrit$, equation (5.38) can be used to work out the value of K, which may then be used to work out $xcrit$ and $ycrit$ from (5.40) and (5.39), respectively.

The values calculated above can now be used to define the limits on u over which the strain field extends. From Fig. 5.9, remembering that the strain field has no u-component and neglecting end effects, it is clear that:

$$\begin{aligned} \text{if u} < 0\text{, then } dsh &= 0, \\ \text{if u} > \text{ucrit, then } dsh &= 0, \end{aligned}$$

and if $0 \leq u \leq ucrit$ then dsh will be given by equation (5.11).

From equations (5.9):

$$\begin{aligned} ucrit &= \sin\psi\cos\epsilon(xcrit - x0) + \sin\epsilon(ycrit - y0) \\ &\quad + \cos\psi\cos\epsilon(zcrit - z0). \end{aligned} \tag{5.41}$$

One problem emerges, in the fact that $zcrit = z0$ for an inclusion in an $x - y$ plane. In this case, the constant K of equation (5.38) cannot be used to obtain $xcrit$ and $ycrit$. The problem is solved by specifying the length l of the inclusion, to provide an alternative means of obtaining $xcrit$ and $ycrit$. Consider Fig. 5.10:

$$xcrit = x0 + l\cos\epsilon, \tag{5.42}$$

$$\text{and } ycrit = y0 + l\sin\epsilon. \tag{5.43}$$

It will be noted that if either ψ or ϵ is equal to 90° or 270°, then the term K will be undefined. The remedy is to test both ψ and ϵ to see if any of the four conditions above is true, and, if so, to reduce the unallowed value of ψ or ϵ by 2°. This removes the infinity, without significantly altering the orientation.

5.2.6 Lattice Mismatch Parameter

In the strain equations (5.3), the term A is defined by equation (5.2) in terms of the *lattice mismatch parameter*, ε. This parameter is defined [140] as the relative volume change between the inclusion and the surrounding matrix.

Hence,

$$\varepsilon = (V_i - V_b)/V_b, \tag{5.44}$$

$$\begin{aligned} \text{where } V_i &= \text{volume of unit cell in inclusion,} \\ \text{and } V_b &= \text{volume of unit cell in surrounding matrix.} \end{aligned}$$

The condition $V_i > V_b$ ($\varepsilon > 1$) implies an inclusion which places the surrounding matrix in compression, whilst $V_i < V_b$ ($\varepsilon < 1$) implies an inclusion which is being compressed.

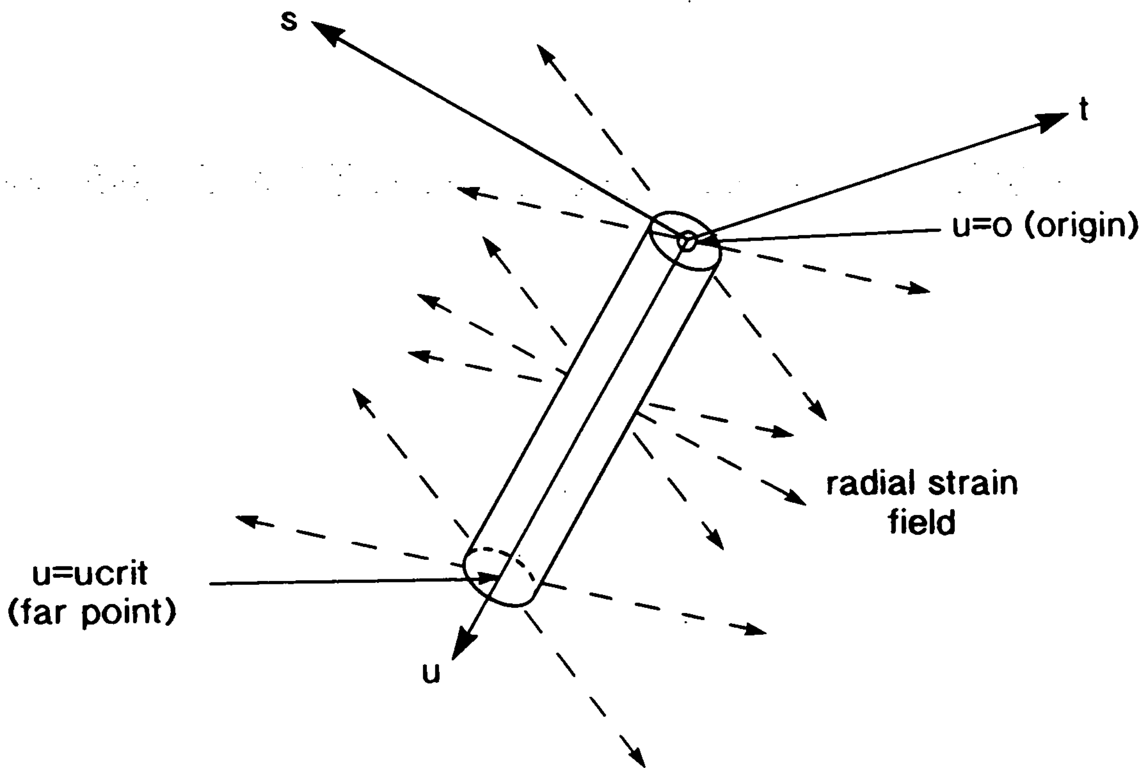

Fig. 5.9: Limits on the variable u defining the extent of the inclusion strain field.

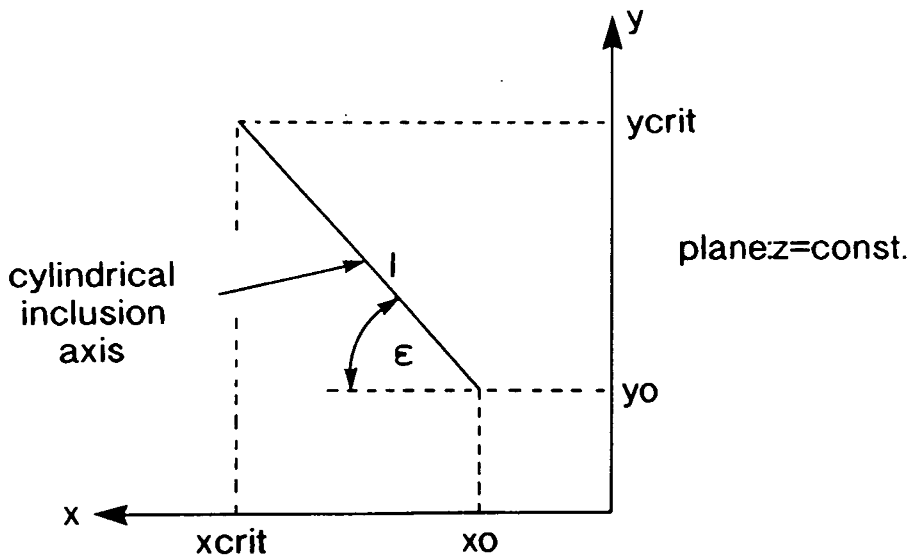

Fig. 5.10: Special case of an inclusion lying in a plane given by $z = const.$

5.2.7 Expressing the Equations in Computer Code

The equations of the preceding sections have been combined to form the *Pascal* procedure $DIFFCYL$ (APPENDIX E), whose purpose is to calculate the quantity dsh using equation (5.11). The associated procedure $CYLDEF$ (APPENDIX E) reads in the cylindrical inclusion parameters. All the parameters have the same names as in the preceding sections, except that the lattice mismatch parameter, ε, becomes $vfrac$, the inclusion length, l, becomes $clength$, the term K of equation (5.38) becomes $cylinc$, the term A of equation (5.3) becomes $acyl$ and the coordinates of the inclusion origin become $(xcyl0, ycyl0, zcyl0)$. This is done, in each case, to avoid ambiguity with other terms.

Line A of $DIFFCYL$ defines the value of $acyl$ using equation (5.2). Section α applies the 90° and 270° tests for the angles ψ and ϵ. Line B works out the value of $cylinc$ using equation (5.38). Section β works out the values of $xcrit$ and $ycrit$ using equations (5.39), (5.40), (5.42) and (5.43). These values are then used in section γ to work out $ucrit$, by equation (5.41). The code starting at line C applies the conditions on u limiting the extent of the strain field, and works out an expression for dsh from equation (5.11), using equations (5.3), (5.18), (5.19), (5.23) and (5.24). The final result is fed back to the simulation program $GENERAL.P$, when $DIFFCYL$ is called, to complete the process.

A typical input data file to be read by $CYLDEF$ is shown in APPENDIX H4. The procedure to calculate dsh for a dislocation is $DIFFDISL$ (APPENDIX D1) and the associated procedure to read in the dislocation parameters is $DISLOCN$ (APPENDIX D1). A procedure $DISLCALC.P$ (APPENDIX D2) is used to calculate the elastic parameters of the dislocation. All the dislocation procedures are due to Green. A typical data file to be read by $DISLOCN$ is shown in APPENDIX H3. In order to simulate for the combined strain field due to a dislocation and cylindrical inclusion, the inclusion-specific parameters of the inclusion input file are added to the end of the dislocation input file.

5.3 Comparison Between Corresponding Dislocation and Cylindrical Inclusion Images

5.3.1 Preliminary Comments

Using the code developed in the previous section, images have been simulated for a dislocation and the corresponding cylindrical inclusion. This has been done for edge, 60° and screw dislocations, using three different reflection geometries. It is useful for the subsequent work to compare the image structures due to the two defect types. In all the simulations of the current chapter, MoK_{α_1} radiation was assumed as the source X-radiation. Surface relaxation has not been taken into account, since dislocation gettering sites are located in the crystal bulk.

From equations (5.3) and (5.2) it is seen that the strain magnitude of the cylindrical inclusion, $A\xi^2$, depends on the lattice mismatch parameter, ε, and the inclusion

radius, ξ. This strain magnitude was varied by choosing a physically realistic value of ε, and hence A, as constant and allowing ξ to vary. Rivaud et al. [130] have shown that the increase in volume of SiO_x precipitates relative to the Si matrix is 120% . The volume increase for transition metals may be even higher, for example Cu_3Si precipitates are known [128] to exhibit a high crystallographic misfit. It is important to remember that the cylindrical inclusion is an elastic model and not a real, physical object. The physically meaningful quantity is the strain magnitude, $A\xi^2$, so that an arbitrary choice of A can be made and the resulting value of $A\xi^2$ is then determined by ξ. Bearing these points in mind, the ratio V_i/V_b in equation (5.44) was taken as 155% . Then, from equation (5.44), the lattice mismatch parameter,

$$\begin{aligned}\varepsilon &= (V_i - V_b)/V_b, \\ &= 0.55.\end{aligned}$$

Hence, from equation (5.2), taking Poisson's ratio, ν, for Si to be 0.28 [143], it is found that:

$$A = -0.33.$$

This value of A was used consistently in the generation of all cylindrical inclusion images, so that adjustment of ξ allowed the inclusion strain magnitude to be varied.

The results for the three different reflections are now presented. In each case, a (001) oriented, $500\mu m$ thick crystal was assumed. All the simulations were performed with a resolution equivalent to that characteristic of experimental section topography.

5.3.2 $\bar{1}31$ Reflection

In this case, the diffraction vector, $\underline{h}$, lies along the $[\bar{1}31]$ crystallographic direction, and a dislocation orientation, $\underline{l}$, was chosen in the $[0\bar{1}1]$ direction, since this gave the most characteristic image. The reflection geometry is shown in APPENDIX I3. Keeping the dislocation orientation fixed, the Burgers vector, $\underline{b}$, was chosen so that:

$$\begin{aligned}\underline{h}.\underline{b} &\neq 0, \text{ for image contrast,} \\ \underline{b}.\underline{l} &= 0, \text{ for an edge dislocation,} \\ \underline{b}.\underline{l} &= \frac{1}{2}, \text{ for a } 60^\circ \text{ dislocation,} \\ \text{and, } \underline{b}.\underline{l} &= 1, \text{ for a screw dislocation.}\end{aligned} \tag{5.45}$$

A set of $\frac{1}{2}[110]$ type Burgers vectors to satisfy (5.45) is then given as:

$$\begin{aligned}\text{edge dislocation : } \underline{b} &= \frac{1}{2}[011] \\ 60^\circ \text{ dislocation : } \underline{b} &= \frac{1}{2}[\bar{1}01] \\ \text{screw dislocation : } \underline{b} &= \frac{1}{2}[0\bar{1}1].\end{aligned}$$

The procedure *DISLOCN* (APPENDIX D1) calculated the dislocation orientation to be (-0.671, 0.224, 0.707) in experimental space. Hence, using equation (5.36):

$$\begin{aligned} \psi &= 316.5°, \\ \text{and } \epsilon &= 12.9°, \end{aligned}$$

for the cylindrical inclusion.

Upon specification of the defect axis origin, the procedure *DISLOCN* also calculates the coordinates $(xcrit, ycrit, zcrit)$ of the far point, Fig. 5.8. These values allow $ucrit$, Fig. 5.9, to be determined, using equations (5.41). For this and the following two reflections, the origin of the defect axis was chosen to give the richest possible image structure, to facilitate comparison.

The results are shown in Fig. 5.11, in which inclusions characterised by ξ-values of 0.08, 0.05 and 0.02μm are compared with the corresponding edge, 60° and screw dislocations. The input data file for the edge dislocation is shown in APPENDIX H3 and for the cylindrical inclusion with a ξ-value of 0.08μm in APPENDIX H4. First of all, it is clear that the dislocation and inclusion images are very similar in general form. This might be considered a potential difficulty, since it is important in the current chapter to identify and parameterise the structural differences between images due to bare and decorated dislocations. However, it will be shown in the following sections that such parameterisation can be achieved and used to analyse the strain contribution due to the gettered precipitates.

From Fig. 5.11, it is seen that the direct and intermediary images due to the edge dislocation are more extensive than those due to the 60° dislocation, which are in turn more extensive than the direct and intermediary images due to the screw dislocation. The variation in direct image size indicates a variation in the size of the highly distorted, strongly diffracting region immediately around the dislocation. An analogous variation in image sizes is manifest in the cylindrical inclusion images, as the ξ-value, and hence strain magnitude, is reduced from 0.08μm to 0.02μm. Suppose the cylindrical inclusion were superimposed upon the dislocation, to model a decorated dislocation. For a ξ-value of 0.08μm the inclusion strain would dominate the dislocation strain, whilst for a value of 0.02μm the reverse would be true. Apart from the above differences, the three dislocation images are quite similar, and it is suggested that any result for a decorated edge dislocation will also be true for decorated 60° and screw dislocations. The accuracy of this assertion is confirmed later by the results of section 5.5.3.

5.3.3 $\bar{4}40$ Reflection

In this case, the diffraction vector, $\underline{h}$, lies along the $[\bar{4}40]$ direction, and a dislocation orientation, $\underline{l}$, along the [011] direction was chosen. The reflection geometry is shown in APPENDIX I2. Keeping the dislocation orientation fixed and using conditions

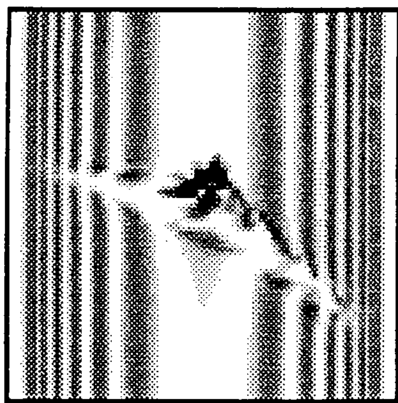

edge dislocation

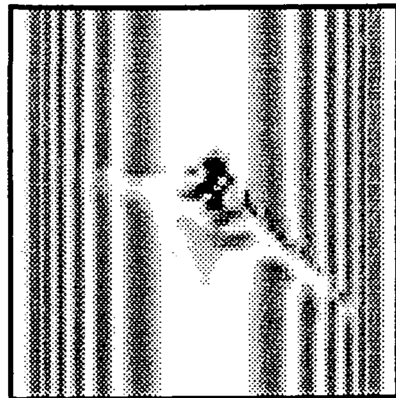

60° dislocation

100μm

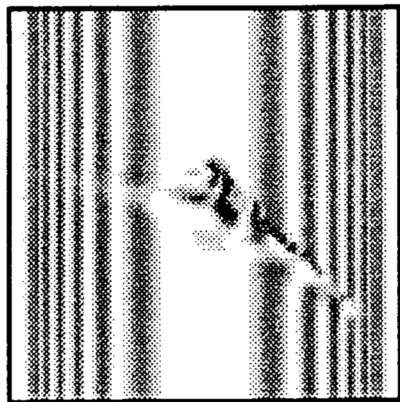

screw dislocation

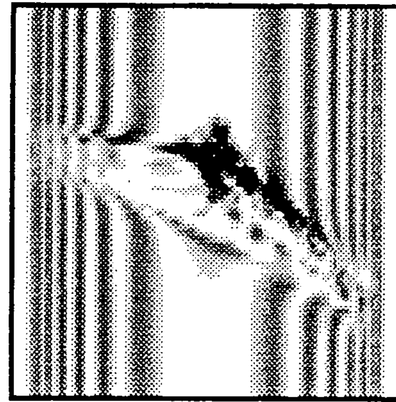

$\xi = 0.08\mu m$

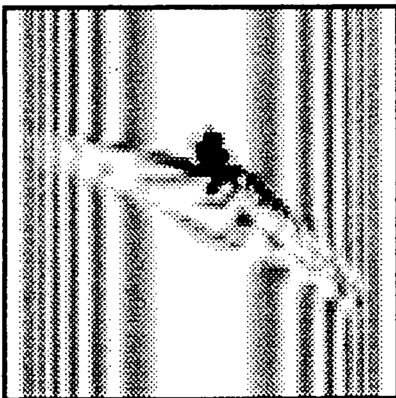

$\xi = 0.05\mu m$

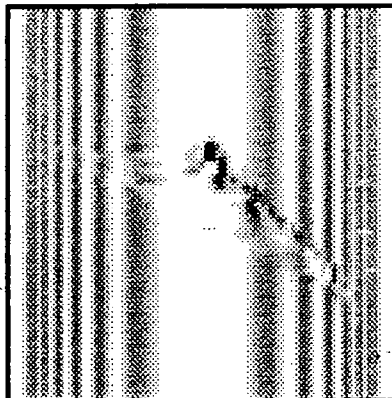

$\xi = 0.02\mu m$

Fig. 5.11: Comparison of edge, 60° and screw dislocation images with pure cylindrical inclusion images characterised by three different values of ξ; $\bar{1}31$ reflection.

(5.45), it is found that:

$$\begin{aligned}\text{edge dislocation}: \underline{b} &= \frac{1}{2}[0\bar{1}1] \\ 60^\circ \text{ dislocation}: \underline{b} &= \frac{1}{2}[101] \\ \text{screw dislocation}: \underline{b} &= \frac{1}{2}[011].\end{aligned}$$

The procedure *DISLOCN* (APPENDIX D1) calculated the dislocation orientation to be (-0.5, 0.5, -0.707) in experimental space.

Hence, using equation (5.36):

$$\begin{aligned}\psi &= 215.3^\circ, \\ \text{and } \epsilon &= 30.0^\circ,\end{aligned}$$

for the cylindrical inclusion.

The results are shown in Fig. 5.12. In this case, the variation between dislocation images is less marked. The small variations can be attributed to the changes in strain distribution resulting from adjustment of the Burgers vector orientation. Again, it is seen that an inclusion with a ξ-value of $0.08\mu m$ would tend to dominate the partner dislocation, whilst reducing the ξ-value to $0.02\mu m$ results in a reversal of this trend.

5.3.4 $3\bar{3}\bar{3}$ Reflection

In this case, the diffraction vector, $\underline{h}$, lies along the $[3\bar{3}\bar{3}]$ direction, and a dislocation orientation, $\underline{l}$, along the [101] direction was chosen. The reflection geometry is shown in APPENDIX I4. Keeping the dislocation orientation fixed and using conditions (5.45):

$$\begin{aligned}\text{edge dislocation}: \underline{b} &= \frac{1}{2}[\bar{1}01] \\ 60^\circ \text{ dislocation}: \underline{b} &= \frac{1}{2}[011].\end{aligned}$$

For this reflection and orientation, it is not possible to find a Burgers vector to satisfy conditions (5.45) simultaneously for a screw dislocation. In this case, any Burgers vector, $\underline{b}$, to satisfy the relation

$$\underline{b}.\underline{l} = 1,$$

will automatically give rise to the result

$$\underline{h}.\underline{b} = 0,$$

so that there is no contrast due to this particular dislocation. Simulations have been performed to confirm that this is indeed the case.

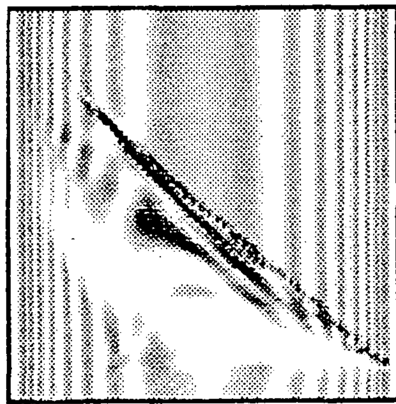

edge dislocation

200μm

60° dislocation

screw dislocation

$\xi = 0.08\mu m$

$\bar{4}40$

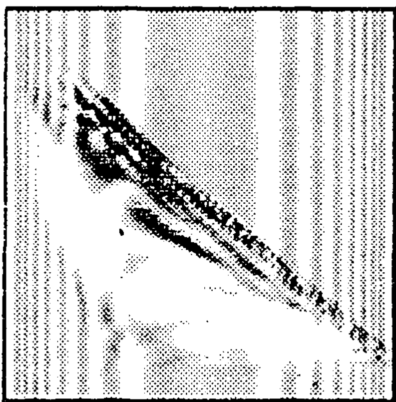

$\xi = 0.05\mu m$

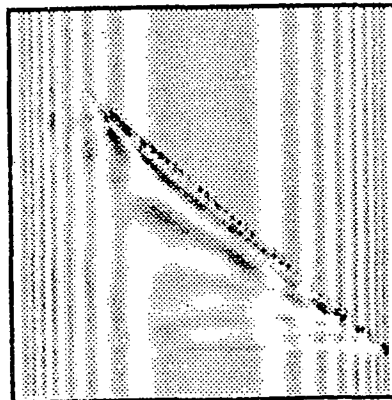

$\xi = 0.02\mu m$

Fig. 5.12: Comparison of edge, 60° and screw dislocation images with pure cylindrical inclusion images characterised by three different values of ξ; $\bar{4}40$ reflection.

The dislocation orientation in experimental space, calculated by *DISLOCN* (APPENDIX D1), was (0.5, 0.5, 0.707).

Hence, using equations (5.36):

$$\begin{aligned} \psi &= 35.3^\circ, \\ \text{and } \epsilon &= 30.0^\circ, \end{aligned}$$

for the cylindrical inclusion.

The results are shown in Fig. 5.13, where both dislocation images show a magnificent set of intermediary fringes. The differences in the intermediary fringe patterns of the edge and 60° dislocation images provide a very good illustration of the phase- (and hence srain-) dependence of the intermediary image.

Again, the variation of ξ has a marked effect on the strength of the cylindrical inclusion image. In particular, the size of the direct image varies strikingly across the range of ξ from $0.08\mu m$ to $0.02\mu m$.

Although the overall form of the dislocation and cylindrical inclusion images is very similar, the well-formed dislocation intermediary fringes do not appear in the cylindrical inclusion simulations. In addition, increasing the ξ-value to $0.08\mu m$ seems to wash out the intermediary pattern.

5.4 Development of the Strain Code for a Cylindrical Distribution of Precipitates

5.4.1 Statement of Problem

In order to investigate the applicability of the cylindrical inclusion model, it is necessary to compare the image due to a dislocation/cylindrical inclusion complex with that due to a dislocation surrounded by a cylindrical distribution of precipitates. To simulate for the latter case, a method has been devised to construct an imaginary cylindrical box, whose axis is collinear with the dislocation, and *sprinkle* precipitates at random throughout the box. In reality, the precipitate density will vary with radial displacement from the dislocation core. However, the homogeneous distribution implicit in the model above is satisfactory to a good approximation, since the radius of the cylindrical distribution is typically only a few angstroms. A spherically symmetric strain field, characterised by the deformation parameter C of Chapter 4, was attributed to each precipitate. The deformation parameter is proportional to the volume of a coherent spherical precipitate. In fact, it is known [128] that Co and Ni in Si can form disc- or plate-shaped metal disilcide precipitates. However, it has already been pointed out, in the previous chapter, that the the volume of a spherical precipitate is often very similar to the volume of an equivalent precipitate of a different form. In addition, when the precipitates are sufficiently close packed, their strain components cancel in all except the radial directions, and the spherical precipitate model is acceptable.

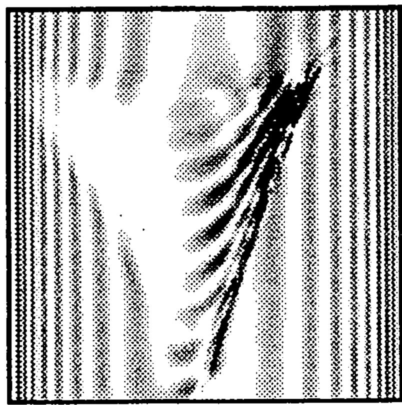

edge dislocation

200μm

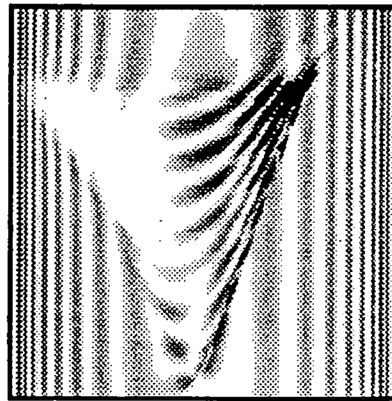

60° dislocation

$\xi = 0.08\mu m$

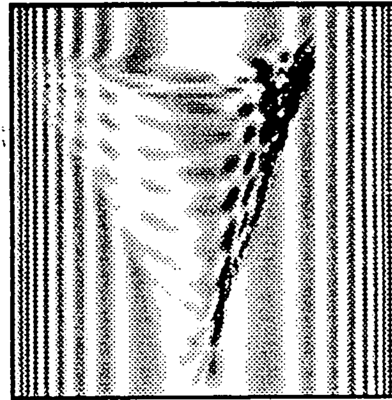

$\xi = 0.05\mu m$

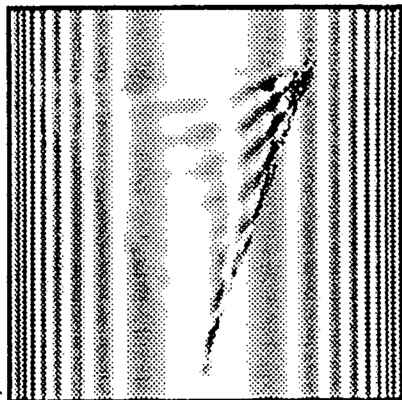

$\xi = 0.02\mu m$

Fig. 5.13: Comparison of edge and 60° dislocation images with pure cylindrical inclusion images characterised by three different values of ξ; $3\overline{3}\overline{3}$ reflection.

Let R^* be a random number between 0 and 1, and θ_{rnd} be a random angle between 0 and 2π radians. Let the axis of the cylindrical box be the u-axis of Fig. 5.5. Then the cylindrical coordinates (r, θ, u) of any precipitate are given by:

$$\begin{aligned} r &= r_{max}.R^*, \\ \theta &= 2\pi.R^*, \\ u &= ucrit.R^*, \\ \text{where } r_{max} &= \text{radius of cylindrical box.} \end{aligned}$$

Hence, the Cartesian coordinates of a general precipitate are:

$$\begin{aligned} s &= r.\cos(\theta_{rnd}), \\ t &= r.\sin(\theta_{rnd}), \\ u &= ucrit.R^*. \end{aligned} \tag{5.46}$$

The (s, t, u) coordinates so defined must then be converted to (x, y, z), to be consistent with the integration procedure of $GENERAL.P$ (APPENDIX A).

5.4.2 Derivation of the Transformation Equations

From Figs. 5.5(a) and 5.6:

$$\begin{pmatrix} x - x0 \\ y - y0 \\ z - z0 \end{pmatrix} = \begin{pmatrix} \cos\psi & 0 & \sin\psi \\ 0 & 1 & 0 \\ -\sin\psi & 0 & \cos\psi \end{pmatrix} \begin{pmatrix} a \\ b \\ c \end{pmatrix}. \tag{5.47}$$

Also, from Figs. 5.5(b) and 5.6:

$$\begin{pmatrix} a \\ b \\ c \end{pmatrix} = \begin{pmatrix} 1 & 0 & 0 \\ 0 & \cos\epsilon & \sin\epsilon \\ 0 & -\sin\epsilon & \cos\epsilon \end{pmatrix} \begin{pmatrix} s \\ t \\ u \end{pmatrix}. \tag{5.48}$$

Combining equations (5.47) and (5.48):

$$\begin{pmatrix} x - x0 \\ y - y0 \\ z - z0 \end{pmatrix} = \begin{pmatrix} \cos\psi & -\sin\psi\sin\epsilon & \sin\psi\cos\epsilon \\ 0 & \cos\epsilon & \sin\epsilon \\ -\sin\psi & -\cos\psi\sin\epsilon & \cos\psi\cos\epsilon \end{pmatrix} \begin{pmatrix} s \\ t \\ u \end{pmatrix}.$$

Expressing these equations explicitly:

$$\begin{aligned} x &= s\cos\psi - t\sin\psi\sin\epsilon + u\sin\psi\cos\epsilon \\ &\quad +x0, \\ y &= t\cos\epsilon + u\sin\epsilon + y0, \\ \text{and } z &= -s\sin\psi - t\cos\psi\sin\epsilon + u\cos\psi\cos\epsilon \\ &\quad +z0. \end{aligned} \tag{5.49}$$

5.4.3 Construction of the Strain Code

The acquisition of (s, t, u) coordinates based on equations (5.46) and the subsequent transfer to (x, y, z) coordinates, equations (5.49), is achieved using the procedure $BOXDEF$ (APPENDIX F).

In section α of $BOXDEF$, the defect parameters are read in. The variable C represents the precipitate deformation parameter of Chapter 4, whilst $ptlim$ is the total number of precipitates. The other variables have been defined in previous sections, and specify the orientation, position and size of the cylindrical box.

Before carrying on with this discussion, it is important to comment on the choice of values of the terms $ptlim$ and r_{max}. Work by Kidd et al. [139] showed that the number of arsenic precipitates gettered by an $840\mu m$ length of dislocation in In-doped $GaAs$ varied from 44 without annealing up to 55 for a 6 hour anneal at 1000°C. For the present work, a characteristic number of precipitates along the dislocation above was taken to be 50. Hence, the value of $ptlim$ used in the simulations here was chosen, in each case, to give a number of precipitates per unit length of dislocation consistent with Kidd's results. The precise effect of precipitate density is investigated in section 5.6. Kidd et al. [139] showed in the same work that gettered precipitates were localised to the dislocation core. Maroudas and Brown [136] have taken the dislocation core radius to be equal to the lattice parameter of the host crystal. Hence, in this investigation, the value of precipitate distribution radius, r_{max}, has been taken as $5\AA$, consistent with Si.

In section β, the value of $ucrit$ is calculated in exactly the same way as in $DIFFCYL$ (APPENDIX E). In section γ, the s, t, u coordinates of each precipitate are calculated from (5.46), where the variables $random(0)$ and $thetrnd$ represent R^* and θ_{rnd}, respectively. Each coordinate variable s, t, u, x, y and z is allocated a one-dimensional array with $ptlim$ elements. Every time a coordinate value is calculated, it is fed to an element in the appropriate array. The variable $ptno$ is the precipitate ordinal number.

The value of dsh for each precipitate is calculated in $DIFFBOX$ (APPENDIX F) which is exactly the same as $DIFFPOINT$ (APPENDIX B). The total value of dsh due to all precipitates is calculated in section ϕ of $GENERAL.P$ (APPENDIX A), which calls upon $DIFFBOX$.

5.5 Variation of Cylindrical Inclusion Strain as a Function of Precipitate Strain

5.5.1 Statement of Approach

What is proposed is essentially a calibration of the strain magnitude, $A\xi^2$, of the cylindrical inclusion model in terms of the deformation parameter, C, of the real, physical precipitates decorating a dislocation. The units of $A\xi^2$ are m^2 and those of C are m^3. Using the simulation technique, the inclusion model can be turned into

$C,(\times 10^{22}m^3)$	$\xi,(\times 10^2\mu m)$	$\mid A\xi^2 \mid,(\times 10^{17}m^2)$	$\mid A\xi^2 \mid /C,(\times 10^{-5}m^{-1})$
1	1.0	3.3	3.3
2	1.5	7.4	3.7
5	2.0	13.2	2.6
20	4.0	52.8	2.6
40	6.0	118.8	3.0

Table 5.1: $\mid A\xi^2 \mid$ vs. C for $\bar{1}31$ reflection.

$C,(\times 10^{22}m^3)$	$\xi,(\times 10^2\mu m)$	$\mid A\xi^2 \mid,(\times 10^{17}m^2)$	$\mid A\xi^2 \mid /C,(\times 10^{-5}m^{-1})$
2	1.0	3.3	1.7
5	1.5	7.4	1.5
10	2.0	13.2	1.3
20	3.0	29.7	1.5
50	5.0	82.5	1.7

Table 5.2: $\mid A\xi^2 \mid$ vs. C for $\bar{4}40$ reflection.

a practical tool for defect parameterisation. The three reflections and dislocation orientations of section 5.3 are used again here.

Matching pairs of simulations, corresponding to the cylindrical inclusion model and the precipitate distribution model are obtained. Hence, it is possible to obtain the variation of $A\xi^2$ with C.

5.5.2 Edge Dislocation Results

Simulations for bare and decorated edge dislocations in the $\bar{1}31$ reflection are shown in Fig. 5.14 for the precipitate distribution model and in Fig. 5.15 for the cylindrical inclusion model. The input data file for a dislocation with precipitate distribution is shown in APPENDIX H5 and for a dislocation associated with a cylindrical inclusion in APPENDIX H6. Good one-to-one matching was obtained between Figs. 5.14(b)-(e) and Figs. 5.15(b)-(e), respectively, and the results are summarised in Table 5.1. Note that $A\xi^2$ is a negative quantity, since $A < 0$ for an inclusion which places the surrounding lattice under compression. This sign convention is taken as understood, and it is the magnitude $\mid A\xi^2 \mid$ that is presented in Table 5.1.

Analogous sets of simulations for the $\bar{4}40$ reflection are given in Fig. 5.16 for the preciptate distribution model and in Fig. 5.17 for the cylindrical inclusion model. Again, good matching was obtained between Figs. 5.16(b)-(e) and Figs. 5.17(b)-(e), respectively, and the results are summarised in Table 5.2.

In addition, sets of simulations for the $3\bar{3}\bar{3}$ reflection are shown in Fig. 5.18 for the precipitate distribution model and in Fig. 5.19 for the cylindrical inclusion

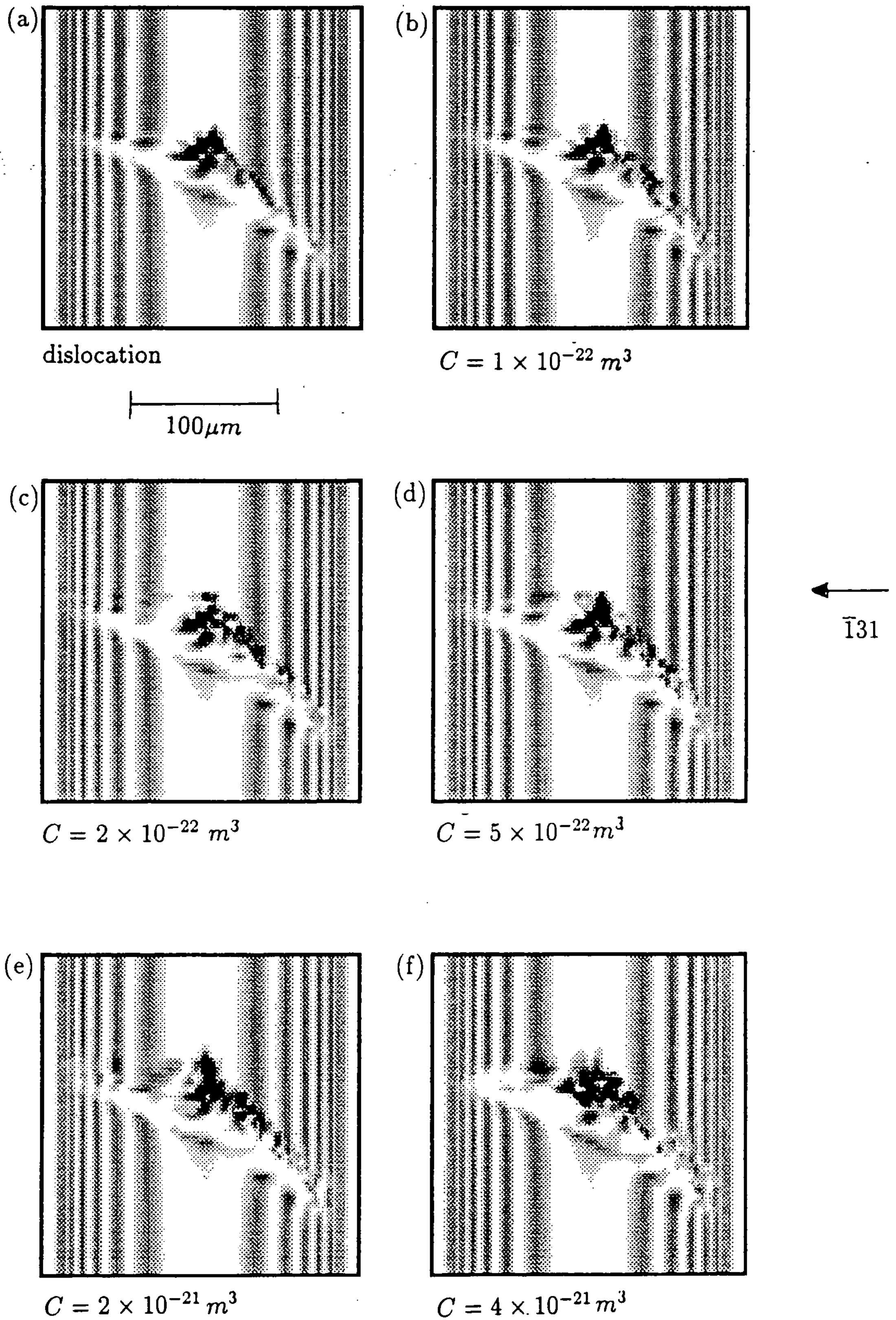

Fig. 5.14: Simulations for bare and decorated dislocations in the $\bar{1}31$ reflection, where the C-values of precipitate decoration are indicated.

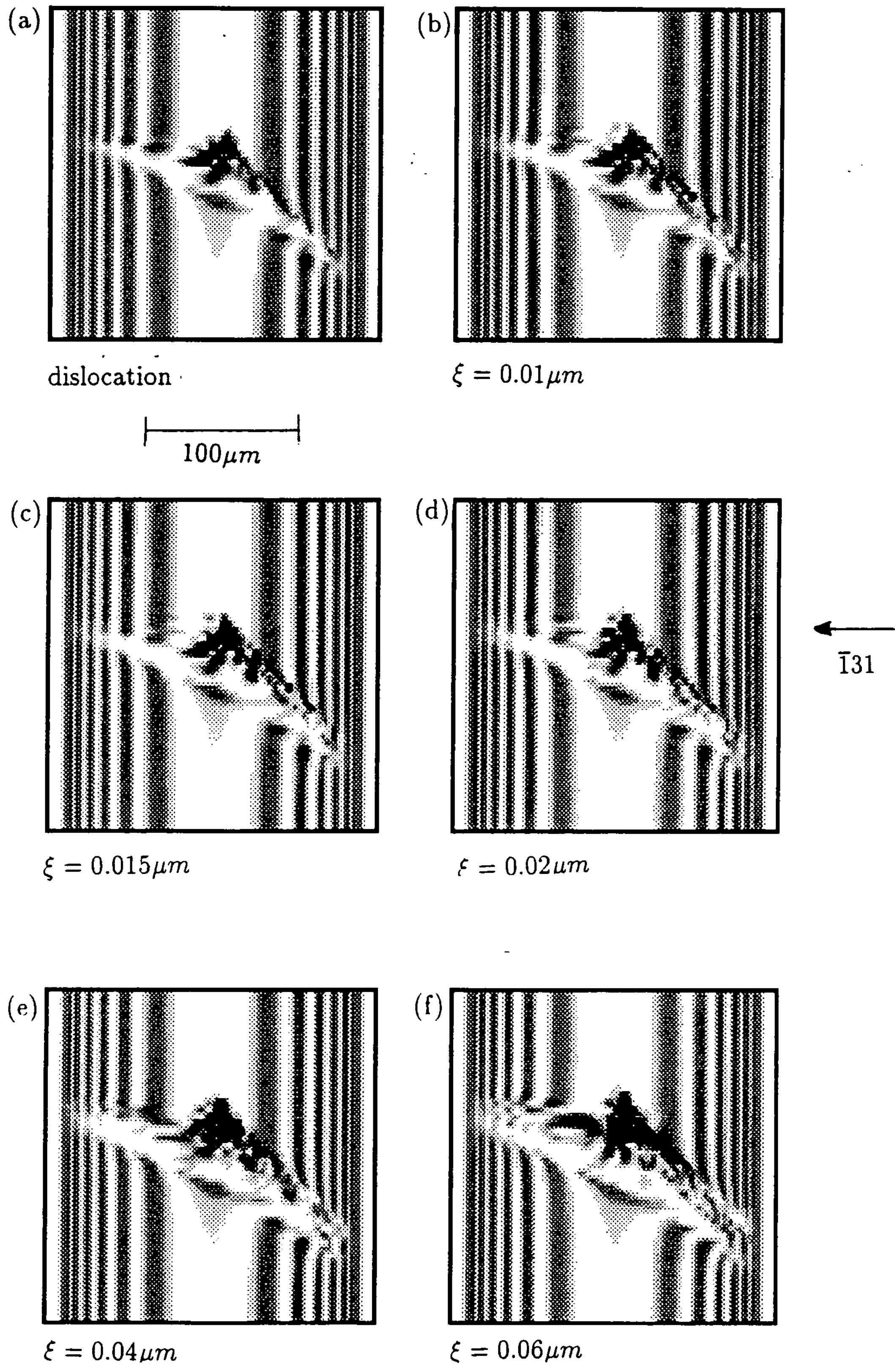

Fig. 5.15: Simulations using the equivalent cylindrical inclusion to model the precipitate distribution results of Fig. 5.14, for the ξ-values indicated.

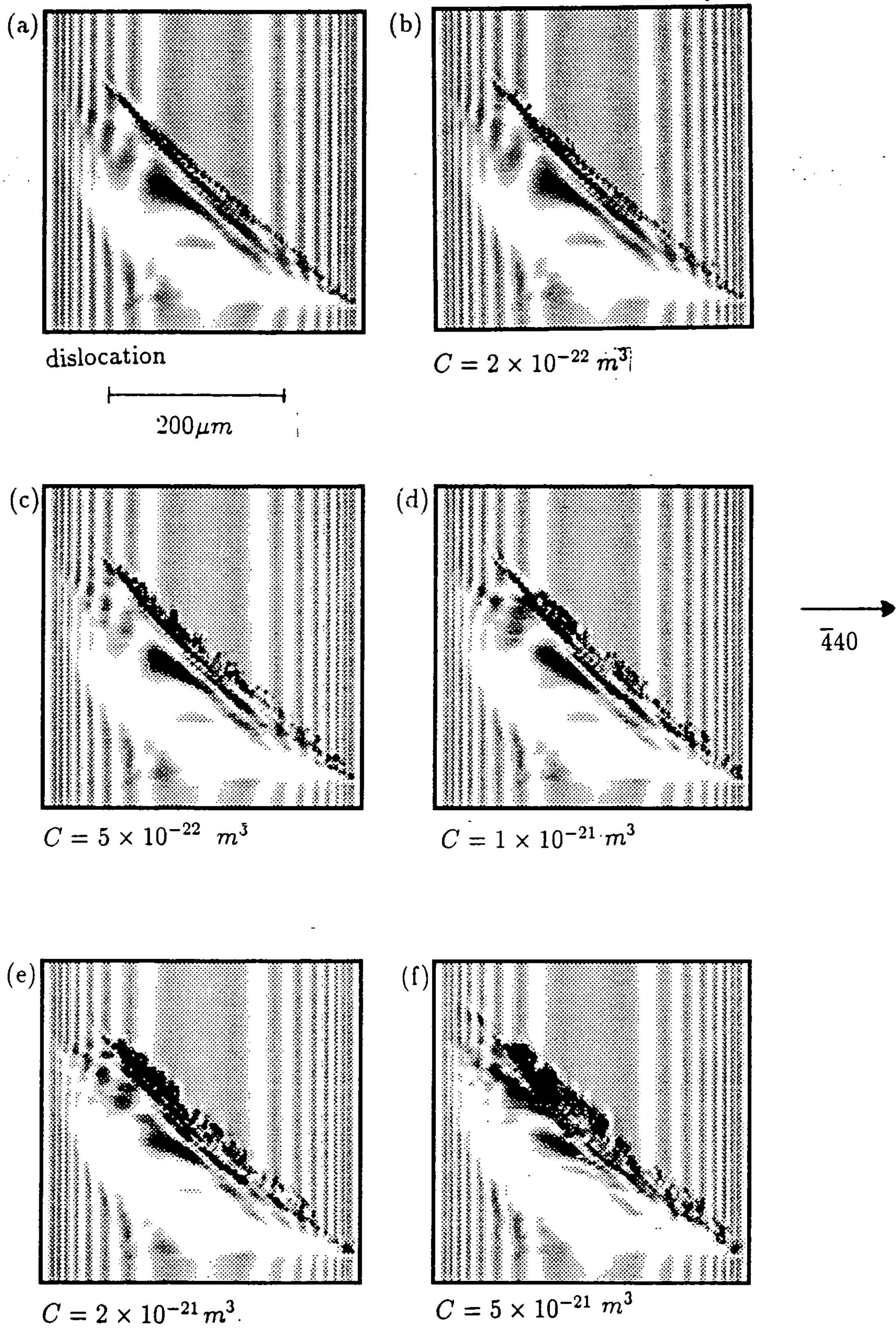

Fig. 5.16: Simulations for bare and decorated dislocations in the $\bar{4}40$ reflection, where the C-values of precipitate decoration are indicated.

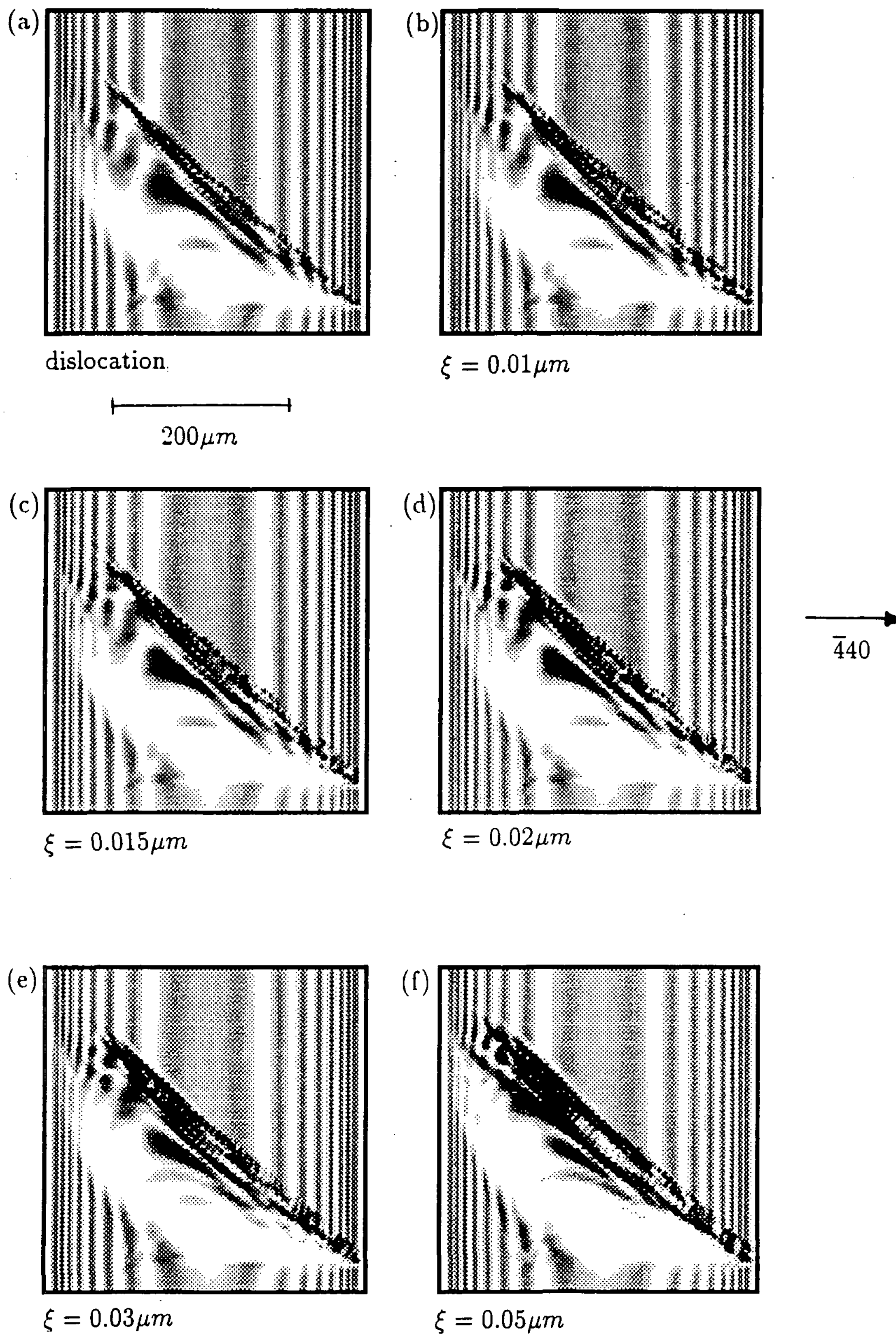

Fig. 5.17: Simulations using the equivalent cylindrical inclusion to model the precipitate distribution results of Fig. 5.16, for the ξ-values indicated.

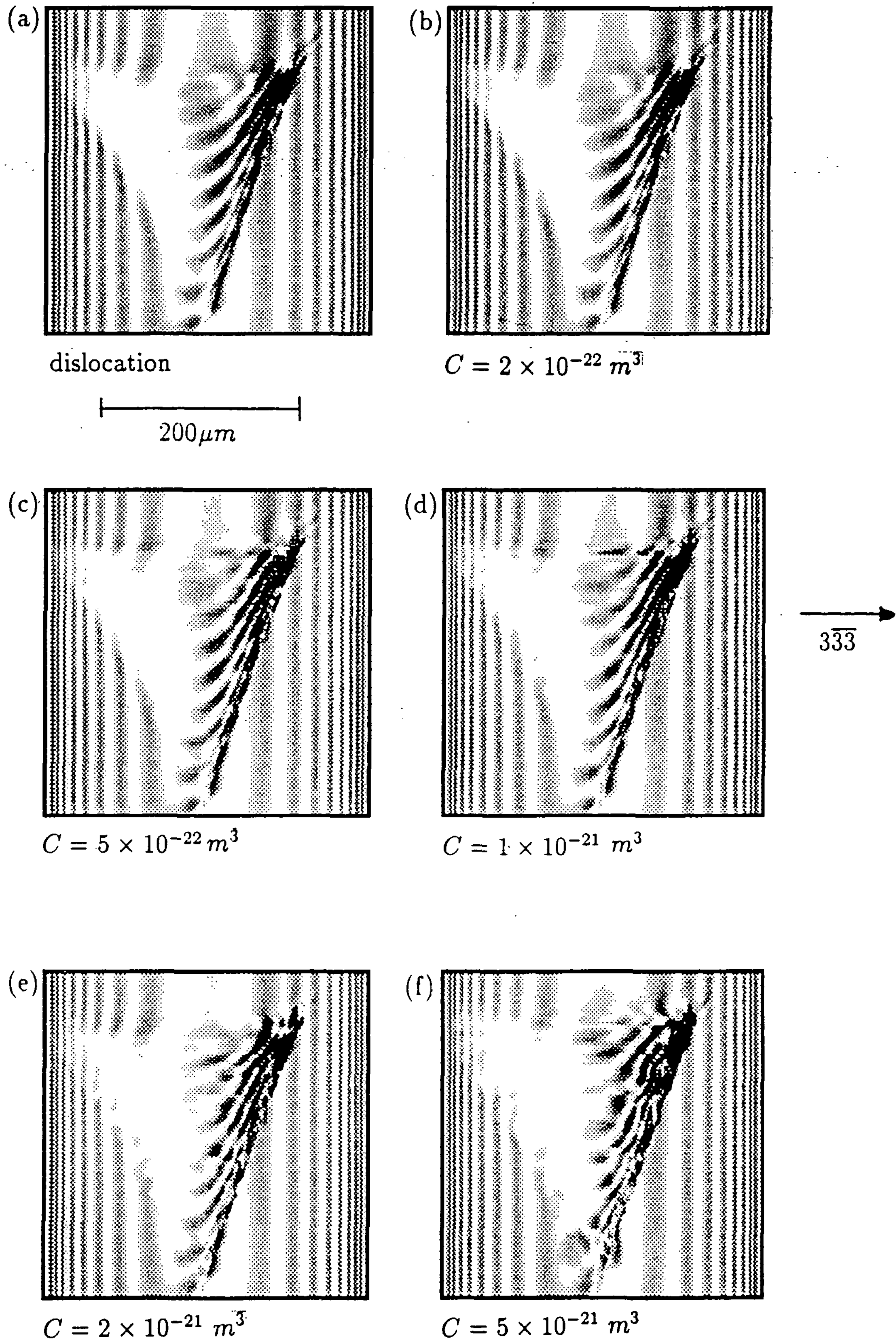

Fig. 5.18: Simulations for bare and decorated dislocations in the $3\overline{3}\overline{3}$ reflection, where the C-values of precipitate decoration are indicated.

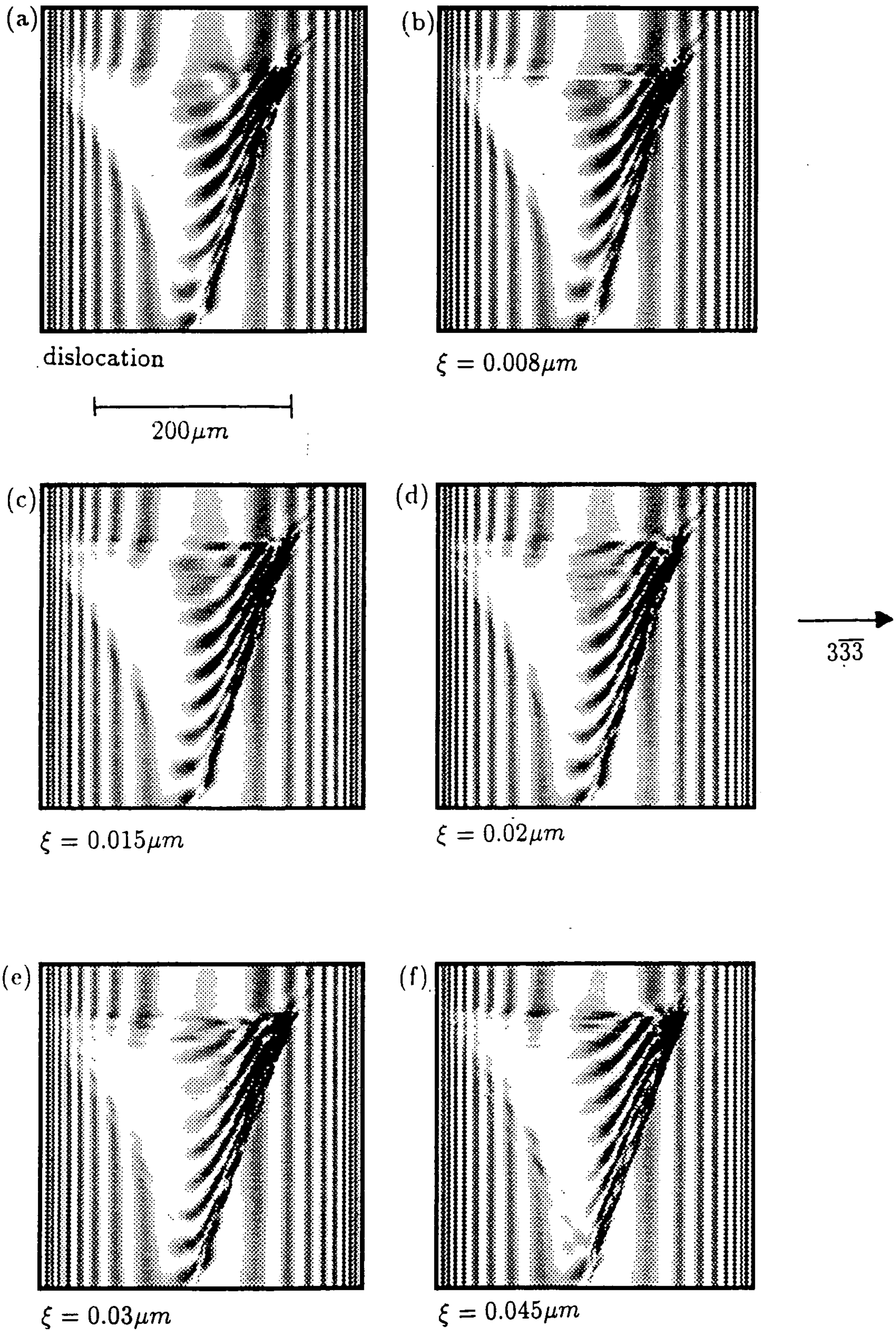

Fig. 5.19: Simulations using the equivalent cylindrical inclusion to model the precipitate distribution results of Fig. 5.18, for the ξ-values indicated.

$C,(\times 10^{22}m^3)$	$\xi,(\times 10^2\mu m)$	$\mid A\xi^2 \mid,(\times 10^{17}m^2)$	$\mid A\xi^2 \mid /C,(\times 10^{-5}m^{-1})$
2	0.8	2.1	1.1
5	1.5	7.4	1.5
10	2.0	13.2	1.3
20	3.0	29.7	1.5
50	4.5	66.8	1.3

Table 5.3: $\mid A\xi^2 \mid$ vs. C for $3\bar{3}\bar{3}$ reflection.

model. Consistently good matching was obtained between Figs. 5.18(b)-(e) and Figs. 5.19(b)-(e), respectively, and the results are summarised in Table 5.3.

For all three reflections, the lowest C, ξ-values correspond to the situation where the precipitate decoration just ceases to be distinguishable from the dislocation. In all cases, the critical value of C for distinguishability was between 1 and $2 \times 10^{-22}m^3$. It is interesting to compare this with the much higher values of C ($\sim 10^{-19}m^3$) for the oxygen precipitates of the previous chapter. This indicates a usefully high visibility of precipitate decoration at edge dislocations. This has important technological implications, which will be discussed in section 5.10.

As the strain associated with the decoration in the $\bar{1}31$ reflection was increased, the size of the direct image also increased and the disruption to the Pendellösung pattern became more pronounced, a characteristic and very useful indication of strain magnitude. The increase in direct image size with increasing strain is also noticeable in the $\bar{4}40$ and $3\bar{3}\bar{3}$ reflections.

For high strains, the precipitate distribution in the $\bar{4}40$ reflection (Fig. 5.16) exhibits a *lumpiness*, which is absent in the corresponding cylindrical inclusion images (Fig. 5.17). The reason for this is that the precipitate distribution represents a number of discrete strain centres, whilst the cylindrical inclusion is homogeneous. In the $3\bar{3}\bar{3}$ reflection, the beautifully formed intermediary fringes due to the cylindrical inclusion (Fig. 5.19) become distorted at high strains in the precipitate distribution model (Fig. 5.18). This effect can also be attributed to the discrete nature of the precipitate distribution strain field.

The data in Tables 5.1, 5.2 and 5.3 was used to plot graphs of $\mid A\xi^2 \mid$ vs. C for the three different reflections. The three graphs were drawn separately to aid clarity, and are shown in Figs. 5.20, 5.21 and 5.22. The striking feature in each case is the linearity of the relationship between $\mid A\xi^2 \mid$ and C. However, the gradients of the straight lines, displayed in Table 5.4, are all different.

The reason for the variation in gradient of the three straight lines will be explained in section 5.5.4. The important point is that the strain magnitude of the cylindrical inclusion, $\mid A\xi^2 \mid$, is directly proportional to the deformation parameter, C, and that the constant of proportionality depends on the reflection.

At this stage it is worthwhile to point out that the computational time required to generate a simulation using the cylindrical inclusion model was significantly less

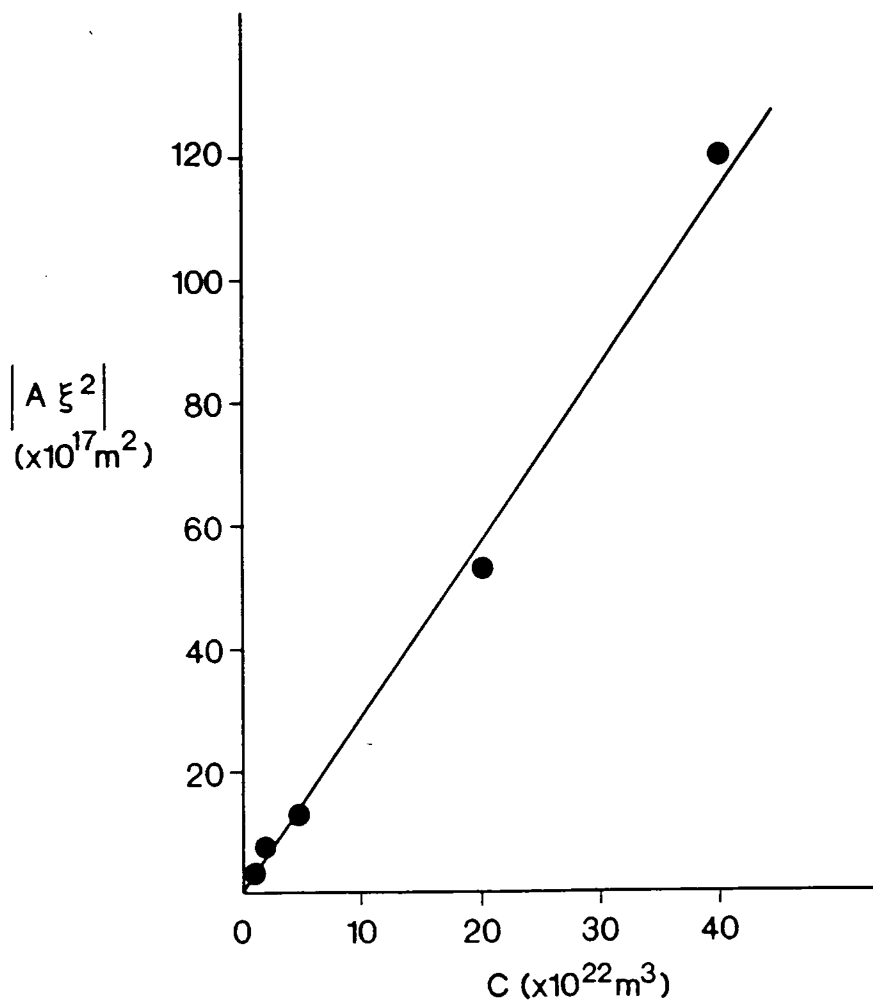

Fig. 5.20: Variation of cylindrical inclusion strain magnitude, $\mid A\xi^2 \mid$, with deformation parameter, C, associated with precipitate decoration, for the $\bar{1}31$ reflection.

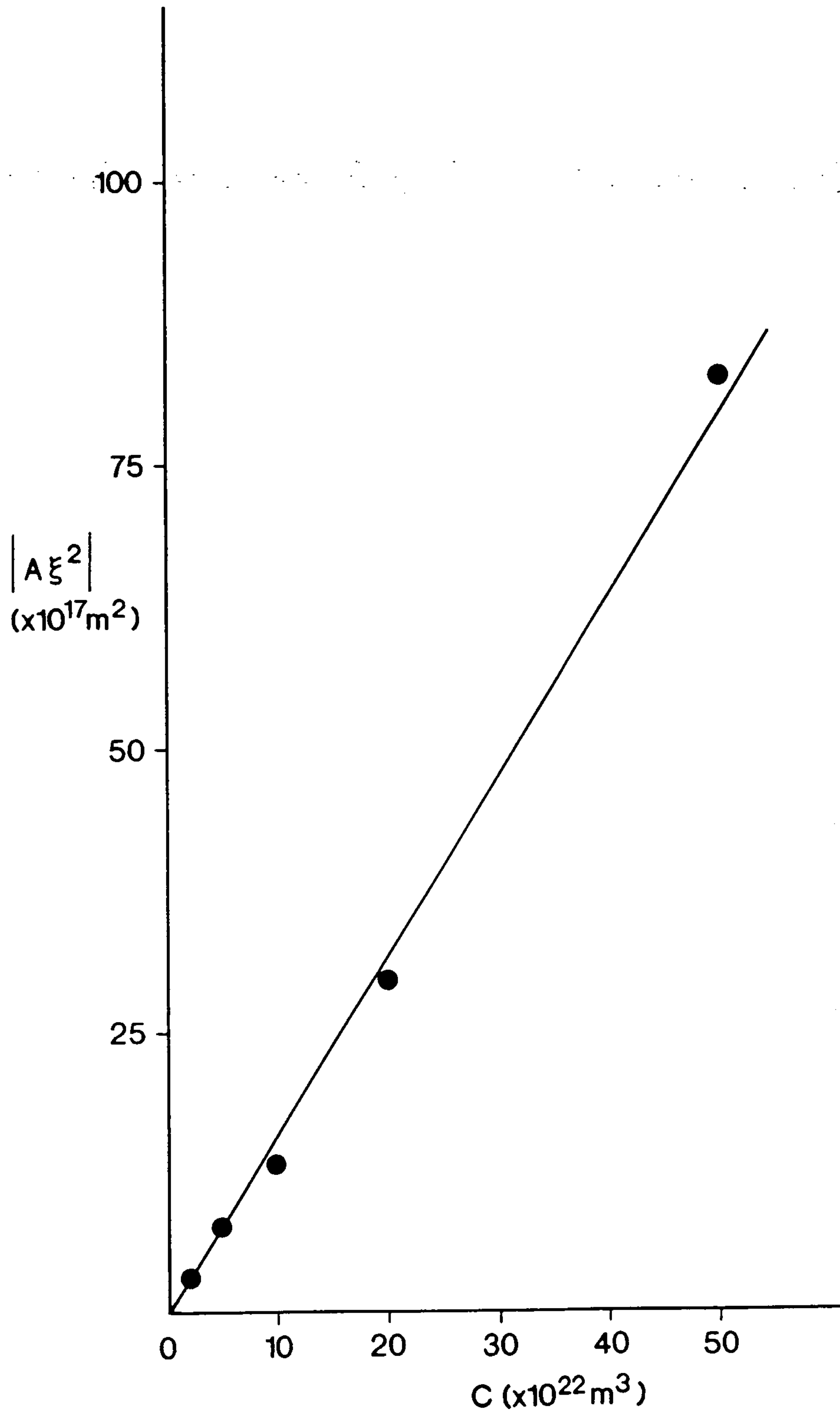

Fig. 5.21: Variation of cylindrical inclusion strain magnitude, $| A\xi^2 |$, with deformation parameter, C, associated with precipitate decoration, for the $\bar{4}40$ reflection.

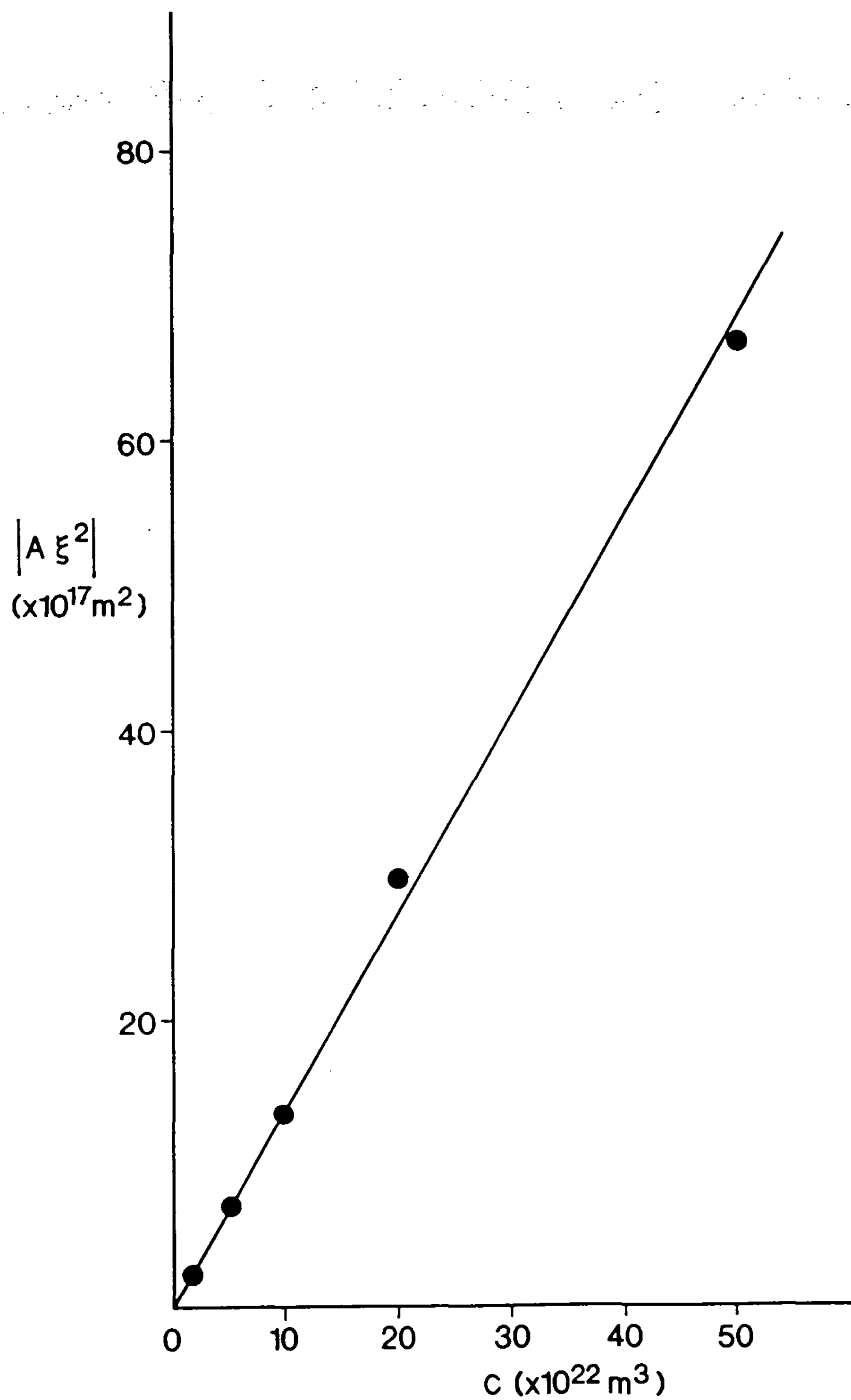

Fig. 5.22: Variation of cylindrical inclusion strain magnitude, $\mid A\xi^2 \mid$, with deformation parameter, C, associated with precipitate decoration, for the $3\overline{3}\overline{3}$ reflection.

Reflection	$\mid \underline{h} \mid$	$\mid A\xi^2 \mid vs.C\ gradient, (\times 10^{-5} m^{-1})$
$\bar{1}31$	3.32	2.88
$\bar{4}40$	5.66	1.60
$33\bar{3}$	5.20	1.40

Table 5.4: Gradient of $\mid A\xi^2 \mid$ vs. C curve for different reflections.

than was possible with the precipitate distribution model. This is a clear advantage of the inclusion model, in terms of its possible technological use, in conjunction with experimental topography, to parameterise the strains associated with dislocations decorated with transition metal impurities. This process would be exactly analogous to the matching of simulation with experiment for the single precipitates studied in Chapter 4.

5.5.3 60° and Screw Dislocation Results

In section 5.3.2 the comment was made that the three dislocation images of Fig. 5.11 are quite similar in form. Hence, it was suggested that any result for a decorated edge dislocation will also be true for decorated 60° and screw dislocations. The accuracy of this assertion is now tested.

Simulations for bare and decorated 60° dislocations in the $\bar{1}31$ reflection are shown in Fig. 5.23 for the precipitate distribution model and in Fig. 5.24 for the cylindrical inclusion model. Good one-to-one matching was obtained between the images of Figs. 5.23(b)-(e) and Figs. 5.24(b)-(e), respectively, for the same C, ξ-value pairs as for the edge dislocation (Figs. 5.14 and 5.15).

The same process was repeated for screw dislocations, again using the $\bar{1}31$ reflection. The results are shown in Fig. 5.25 for the precipitate distribution model and in Fig. 5.26 for the cylindrical inclusion model. Good matching was again obtained for the same pairs of C, ξ-values as for the edge dislocation.

The conclusion here is that the variation in inclusion strain magnitude, $\mid A\xi^2 \mid$, with precipitate strain magnitude, C, is the same for edge, 60° and screw dislocations. Moreover, the dislocation images in the $\bar{1}31$ reflection showed greater variation than in the other two reflections. On the basis of these results, it may be concluded that any result for a decorated edge dislocation, in any of the reflections used in this chapter, is also true for the corresponding decorated 60° and screw dislocations. Henceforth, results will only be taken for edge dislocations.

5.5.4 Discussion

An explanation is now offered for the variation of the $\mid A\xi^2 \mid$ vs. C curves with different reflections, pointed out in section 5.5.2.

$\bar{1}31$

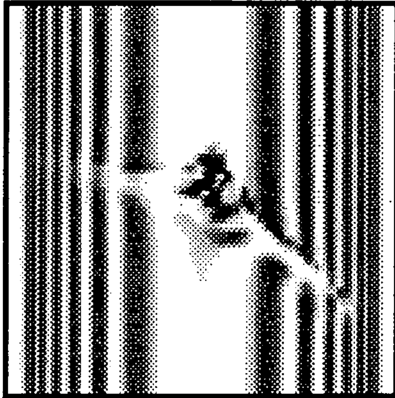

(a) 60° dislocation

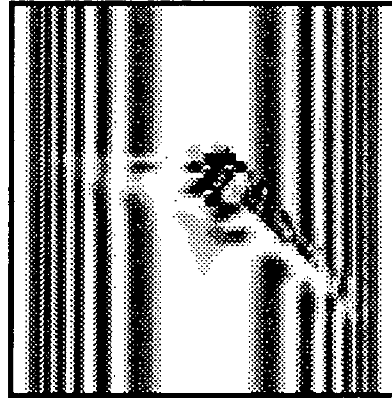

(b) $C = 1 \times 10^{-22} m^3$

100μm

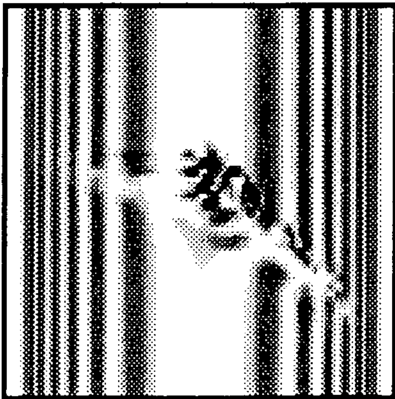

(c) $C = 2 \times 10^{-22}\ m^3$

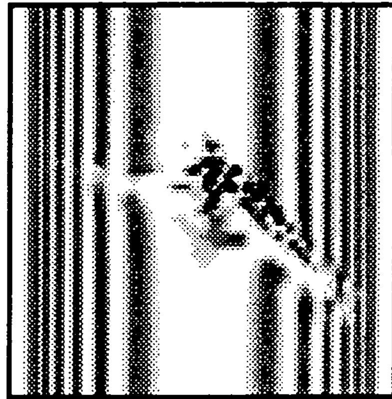

(d) $C = 5 \times 10^{-22} m^3$

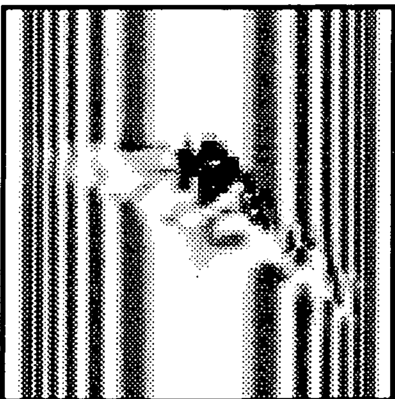

(e) $C = 2 \times 10^{-21} m^3$

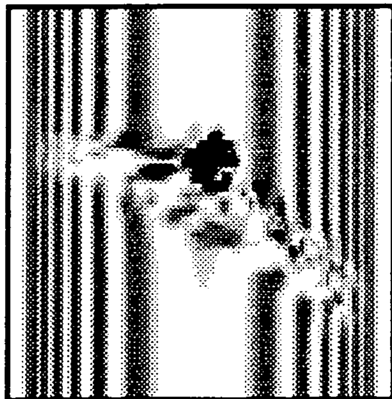

(f) $C = 4 \times 10^{-21} m^3$

Fig. 5.23: Simulations for bare and decorated 60° dislocations in the $\bar{1}31$ reflection, where the C-values of precipitate decoration are indicated.

$\overline{1}31$

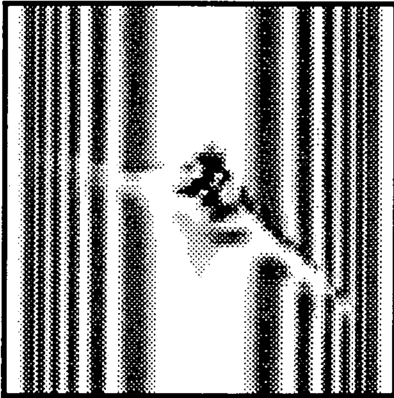
(a) 60° dislocation

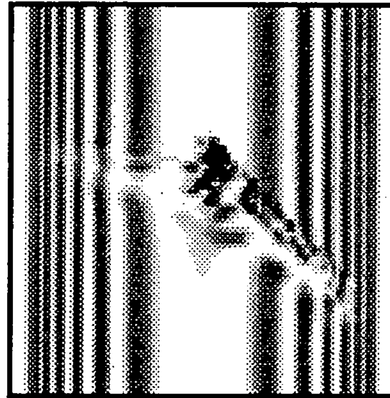
(b) $\xi = 0.01\mu m$

100μm

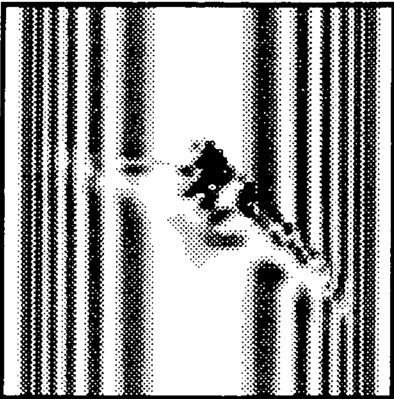
(c) $\xi = 0.015\mu m$

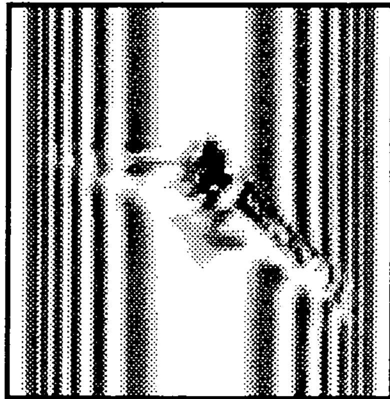
(d) $\xi = 0.02\mu m$

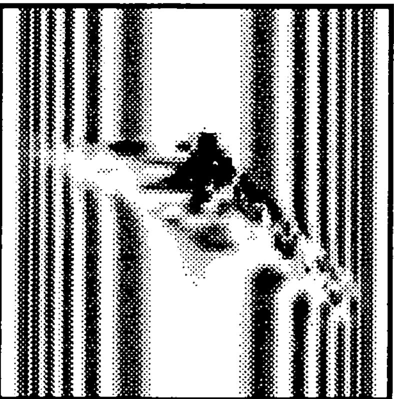
(e) $\xi = 0.04\mu m$

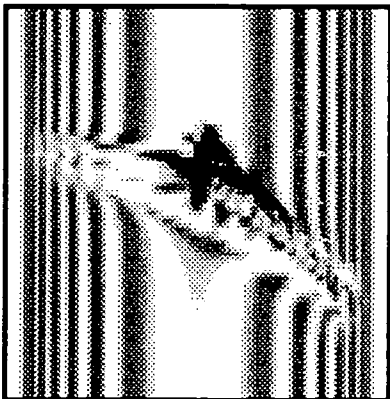
(f) $\xi = 0.06\mu m$

Fig. 5.24: Simulations using the equivalent cylindrical inclusion to model the results of Fig. 5.23, for the ξ-values indicated.

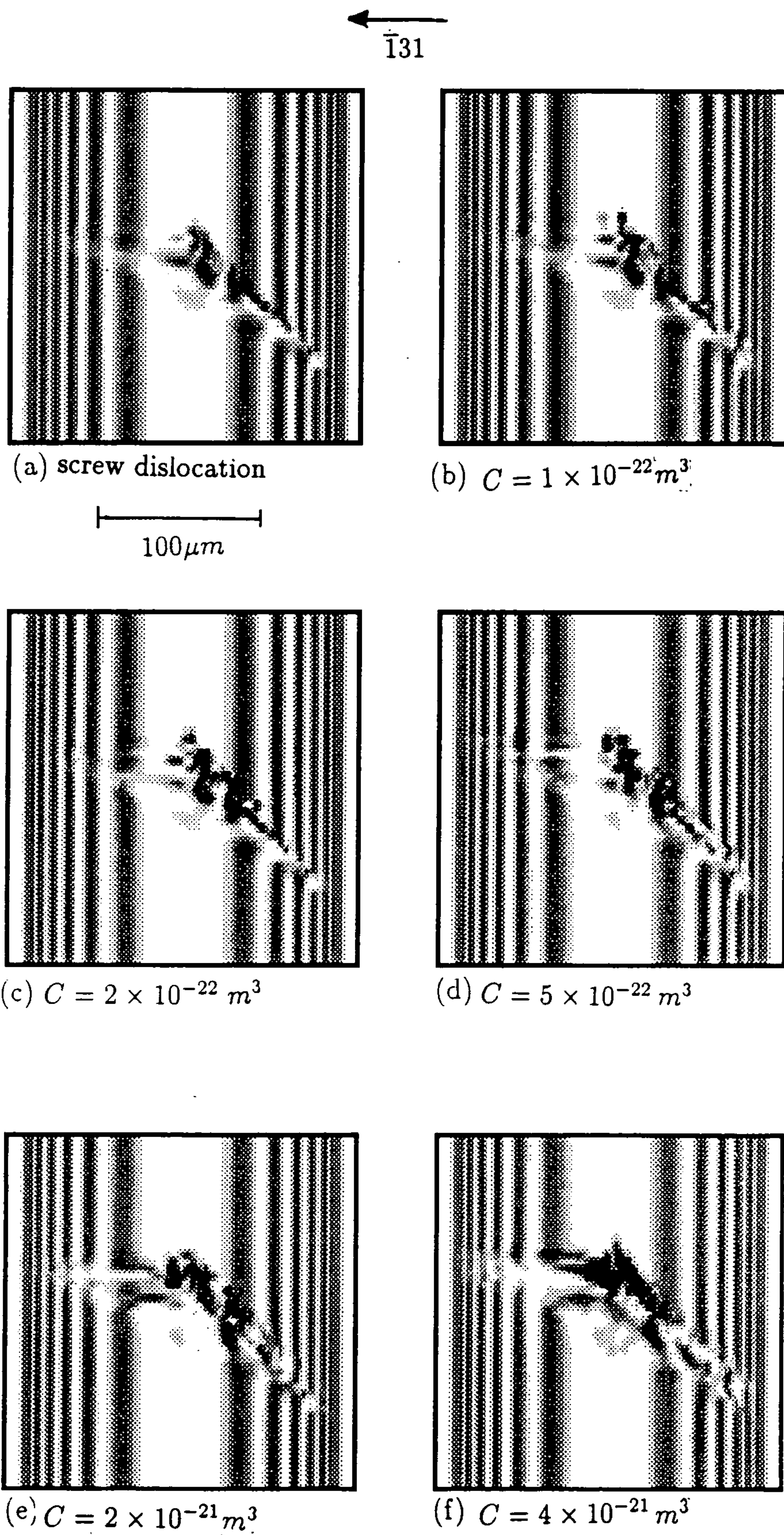

Fig. 5.25: Simulations for bare and decorated screw dislocations in the $\bar{1}31$ reflection, where the C-values of precipitate decoration are indicated.

$\overline{1}31$

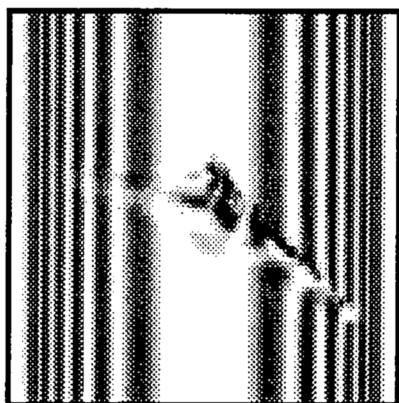

(a) screw dislocation

100μm

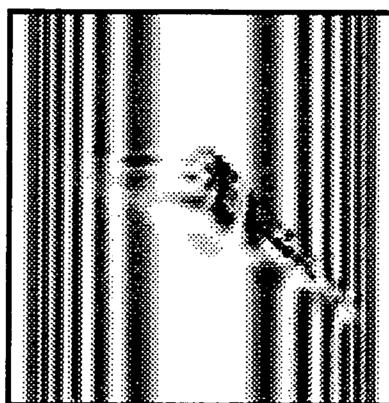

(b) $\xi = 0.01\mu m$

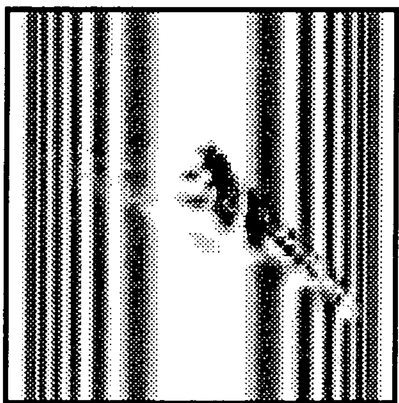

(c) $\xi = 0.015\mu m$

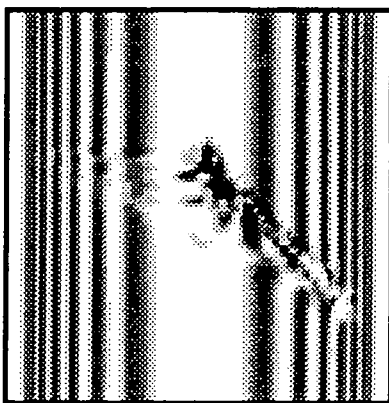

(d) $\xi = 0.02\mu m$

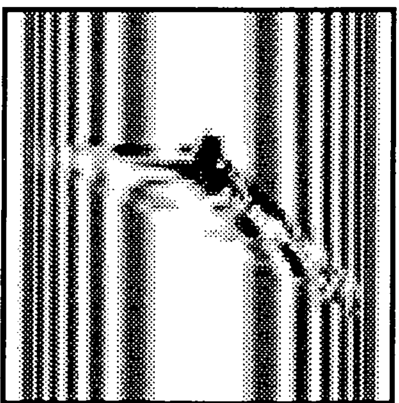

(e) $\xi = 0.04\mu m$

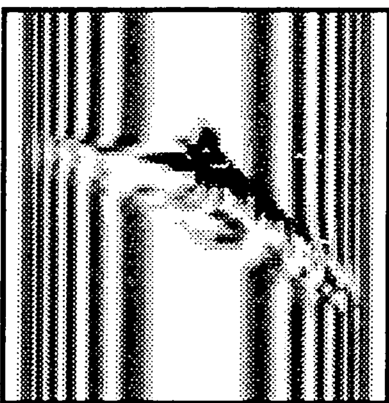

(f) $\xi = 0.06\mu m$

Fig. 5.26: Simulations using the equivalent cylindrical inclusion to model the results of Fig. 5.25, for the ξ-values indicated.

Consider the cylindrical inclusion of Fig. 5.27. Let the cylindrical coordinates of a general point, P, relative to the inclusion axis be (r, θ, u).

Then:

$$s = r\cos\theta, \tag{5.50}$$
$$\text{and } t = r\sin\theta. \tag{5.51}$$

Hence, the strain equations (5.3) become:

$$\begin{aligned} e_{ss} &= \frac{\partial u_s}{\partial s} = A\xi^2\frac{(\cos^2\theta - sin^2\theta)}{r^2}, \\ &= -e_{tt}, \\ &= \frac{\partial u_t}{\partial t}, \end{aligned} \tag{5.52}$$

and

$$\begin{aligned} e_{st} &= \frac{\partial u_s}{\partial t} = A\xi^2\frac{2\cos\theta\sin\theta}{r^2}, \\ &= e_{ts}, \\ &= \frac{\partial u_t}{\partial s}. \end{aligned} \tag{5.53}$$

Using (5.52) and (5.53) in conjunction with Fig. 5.27:

$$\begin{aligned} \frac{\partial u_r}{\partial r} &= e_{rr}, \\ &= \frac{\partial u_s}{\partial r}\cos\theta + \frac{\partial u_t}{\partial r}\sin\theta, \\ &= \cos\theta\left(\frac{\partial u_s}{\partial s}\frac{\partial s}{\partial r} + \frac{\partial u_s}{\partial t}\frac{\partial t}{\partial r}\right) \\ &\quad + \sin\theta\left(\frac{\partial u_t}{\partial s}\frac{\partial s}{\partial r} + \frac{\partial u_t}{\partial t}\frac{\partial t}{\partial r}\right). \end{aligned}$$

Hence,

$$e_{rr} = \cos\theta(e_{ss}\cos\theta + e_{st}\sin\theta) + \sin\theta(e_{ts}\cos\theta + e_{tt}\sin\theta).$$

Substituting for e_{ss}, e_{tt}, e_{st} and e_{ts} from (5.52) and (5.53) gives:

$$\begin{aligned} e_{rr} &= \frac{A\xi^2}{r^2}\left[\cos^2\theta(\cos^2\theta - \sin^2\theta) - \sin^2\theta(\cos^2\theta - \sin^2\theta) + 4\sin^2\theta\cos^2\theta\right], \\ &= \frac{A\xi^2}{r^2}(\cos^2\theta + \sin^2\theta)^2, \\ \text{so that } e_{rr} &= \frac{A\xi^2}{r^2}. \end{aligned} \tag{5.54}$$

The radial strain component, e_{rr}, for a cylindrical inclusion is given by (5.54), where $\mid A\xi^2 \mid$ is the strain magnitude. The fact that A is equal to -0.33 in the previous simulations indicates that the strain induced displacement, u_r, reduces

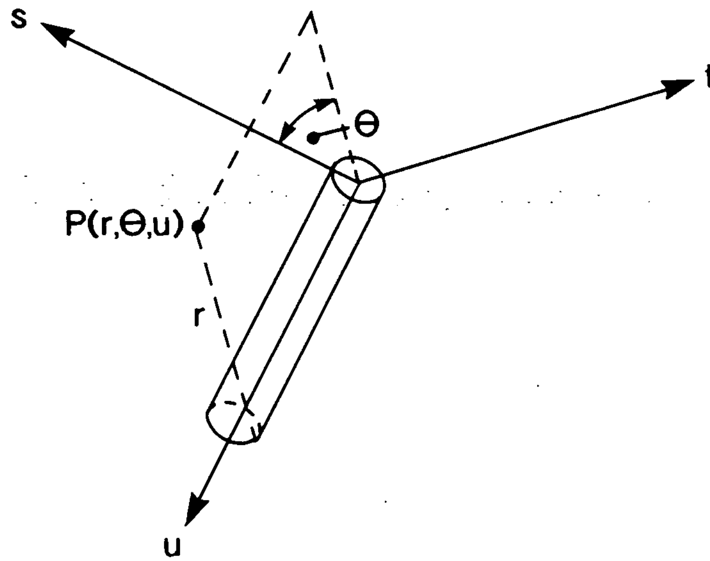

Fig. 5.27: Cylindrical polar coordinates based on the inclusion.

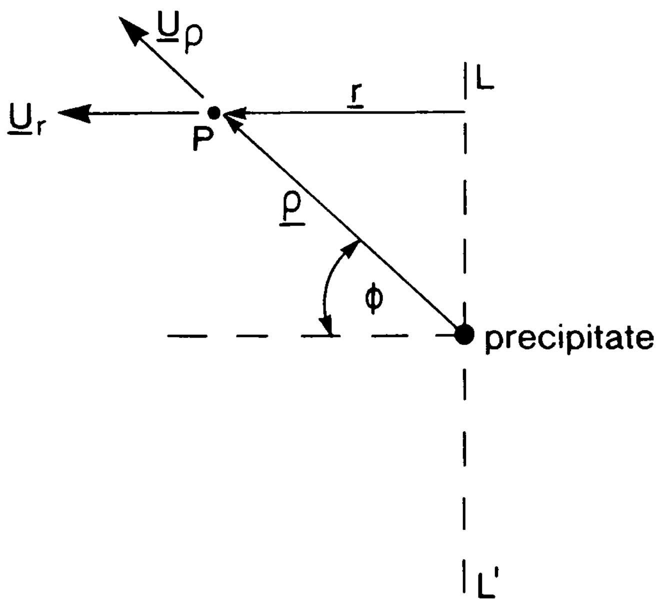

Fig. 5.28: Strain field due to a distribution of precipitates along a straight line.

with radial displacement, r, as required. Now consider the spherical precipitate of Fig. 5.28, where ρ and r are the spherical and cylindrical radial coordinates, respectively.

The strain field due to the precipitate is given by:

$$\underline{u_\rho} = \frac{C}{\rho^2}\underline{\hat{\rho}}. \tag{5.55}$$

$$\begin{aligned} \text{Now, } u_r &= u_\rho \cos\phi. \\ \text{But, } r &= \rho\cos\phi, \\ \text{so that } u_r &= \frac{C}{r^2}\cos^3\phi, \end{aligned}$$

using (5.55).

$$\text{Then, } \frac{\partial u_r}{\partial r} = e_{rr} = -\frac{2C}{r^3}\cos^3\phi. \tag{5.56}$$

Suppose the line LL' delineates a precipitate distribution. The total radial strain component, $[e_{rr}]_{tot}$, at some specific radius r, due to an infinitely close-packed distribution of point spherical strain centres is then given by:

$$\begin{aligned} [e_{rr}]_{tot} &= \int_{-\frac{\pi}{2}}^{\frac{\pi}{2}} -\frac{2C}{r^3}\cos^3\phi d\phi, \\ &= -\frac{4C}{r^3}\int_0^{\frac{\pi}{2}} \cos\phi(1-\sin^2\phi)d\phi, \\ &= -\frac{4C}{r^3}\left[\sin\phi - \frac{1}{3}\sin^3\phi\right]_0^{\frac{\pi}{2}}, \\ \text{so that } [e_{rr}]_{tot} &= -\frac{8C}{3r^3}. \end{aligned} \tag{5.57}$$

$C > 0$, so that u_r reduces with radial displacement, r, away from the axis LL', as required.

From (5.54) and (5.57), the ratio of radial strain components of the inclusion and the precipitate distribution is:

$$\begin{aligned} [e_{rr}]_{cyl} / [e_{rr}]_{pr} &= Br, \\ \text{where } B &= -\frac{3A\xi^2}{8C}, \end{aligned} \tag{5.58}$$

and is a positive constant, since $A < 0$.

Equation (5.58) means that the radial displacement component, u_r, and hence the lattice distortion, decreases at a faster rate for the cylindrical inclusion than for the precipitate distribution, with increasing radial displacement, r. Hence, the volume of strongly diffracting crystal surrounding a precipitate distribution is inherently larger than the diffracting volume associated with the equivalent cylindrical inclusion.

Work by Miltat and Bowen [144] has shown that the diffracting volume around a dislocation depends on the reflection. They pointed out that the diffracting volume decreases with increasing diffraction vector magnitude, $| \underline{h} |$, and so is greatest for low order reflections.

Figs. 5.14 and 5.18 demonstrate that this effect also applies to the precipitate decoration around a dislocation. In the $\bar{1}31$ reflection of Fig. 5.14, a value of C of $2 \times 10^{-22}m^3$ is sufficient to show a marked difference between the decorated and undecorated dislocation images. However, in the $3\bar{3}\bar{3}$ reflection of Fig. 5.18, decoration with precipitates with a C-value of $1 \times 10^{-21}m^3$ makes very little difference to the bare dislocation image. Diffraction is clearly enhanced in the $\bar{1}31$ reflection, analogous to the results of Miltat and Bowen [144], outlined above. Hence, the same effect of decreasing diffracting volume with increasing order of reflection applies to the decorated dislocation itself.

Hence, it is possible to explain the difference in gradients of the $| A\xi^2 |$ vs. C curves of section 5.5.2 for different reflections. In low order reflections, the dislocation-precipitate strain, characterised by the parameter C, gives rise to enhanced diffraction because of the comparatively large diffracting volume. From equation (5.58), the diffracting volume of the cylindrical inclusion model is inherently smaller than that of the precipitate distribution model. Consequently, it is necessary for the cylindrical inclusion strain magnitude, $| A\xi^2 |$, to increase more rapidly relative to C for low order reflections, in order to obtain matching between simulations generated by the two defect models.

The explanation outlined above is borne out, within appropriate error limitations, by the results of Table 5.4. The $| A\xi^2 |$ vs. C gradient for the $\bar{1}31$ reflection ($| \underline{h} |= 3.32$) is $2.88 \times 10^5m^{-1}$. For the other two reflections, the values of $| \underline{h} |$ are higher and both quite similar, whilst the $| A\xi^2 |$ vs. C gradients are both around $1.5 \times 10^5m^{-1}$.

5.6 Variation of Strain with Precipitate Density

The precipitate line density has so far been taken as $6.03 \times 10^4m^{-1}$ of dislocation, consistent with the observations of Kidd et al. [139] mentioned in section 5.4.3. The purpose of the present section is to investigate the variation in strain of a decorated dislocation with precipitate line density, ρ_p.

Three values of ρ_p were taken, four times less, three times greater and six times greater, respectively, than the value of $6.03 \times 10^4m^{-1}$ used to generate the images of Fig. 5.14. Matching of the resulting images with the corresponding cylindrical inclusion simulations is shown in APPENDIX J, and the results are displayed in Table 5.5, Table 5.6 and Table 5.7.

It is interesting to note that for the lowest precipitate density, it was not possible to obtain matching for the images with C equal to 1 and $2 \times 10^{-22}m^3$, since the decorated dislocation was then indistinguishable from its undecorated counterpart. The results of Tables 5.5, 5.6 and 5.7, together with Table 5.1 for the original value of ρ_p, are plotted on the same graph in Fig. 5.29. Linear variation of $| A\xi^2 |$ with

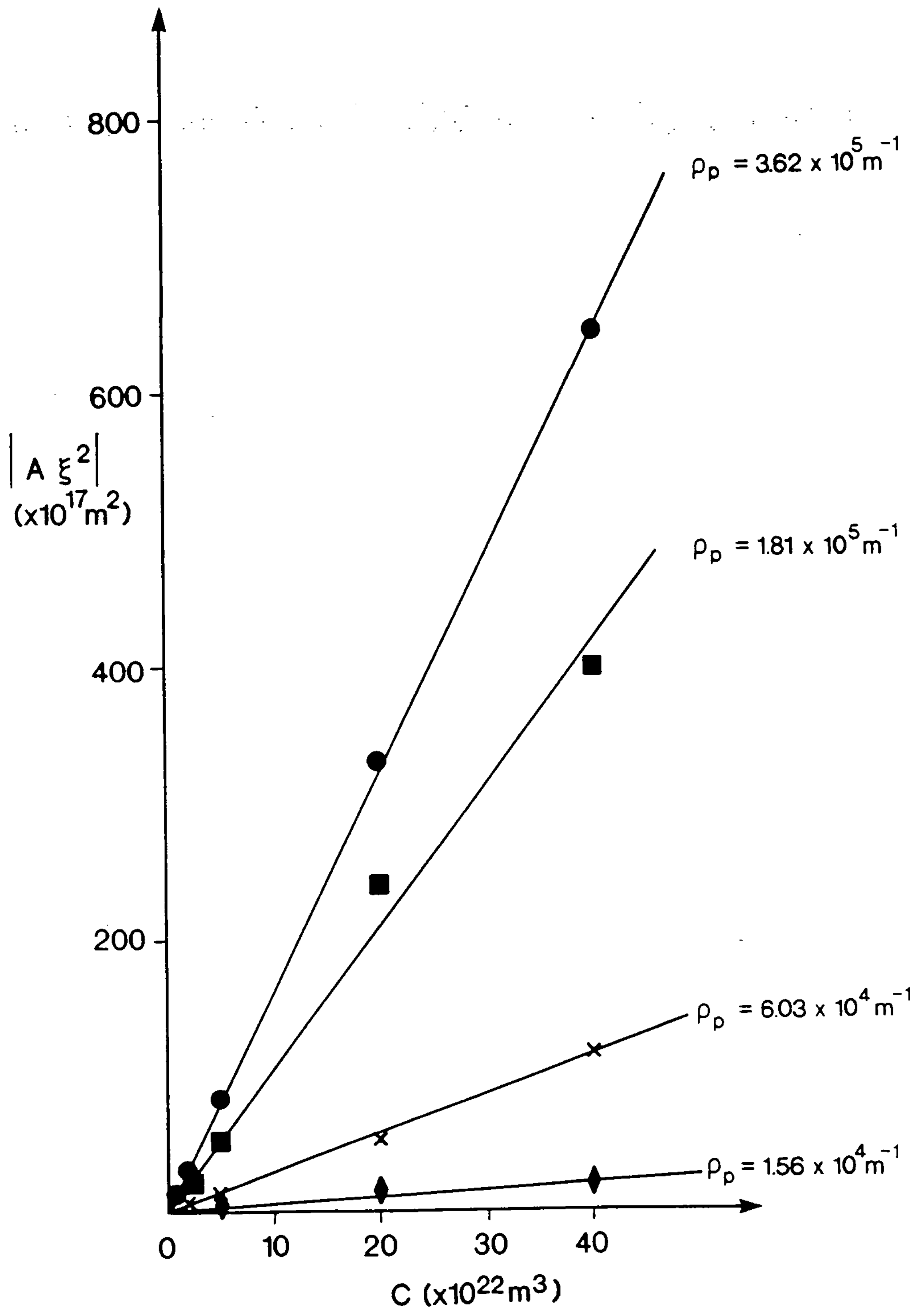

Fig. 5.29: Inclusion strain magnitude, $| A\xi^2 |$, vs. deformation parameter, C, for different values of precipitate line density, ρ_p, using the $\bar{1}31$ reflection.

$C, (\times 10^{22} m^3)$	$\xi, (\times 10^2 \mu m)$	$\mid A\xi^2 \mid, (\times 10^{17} m^2)$	$\mid A\xi^2 \mid /C, (\times 10^{-4} m^{-1})$
1			
2			
5	1.0	3.3	6.6
20	2.0	13.2	6.6
40	2.5	20.6	5.2

Table 5.5: $\mid A\xi^2 \mid$ vs. C for precipitate density, ρ_p, of $1.56\times10^4 m^{-1}$ in $\bar{1}31$ reflection.

$C, (\times 10^{22} m^3)$	$\xi, (\times 10^2 \mu m)$	$\mid A\xi^2 \mid, (\times 10^{17} m^2)$	$\mid A\xi^2 \mid /C, (\times 10^{-5} m^{-1})$
1	1.5	7.4	7.4
2	2.5	20.6	10.3
5	4.0	52.8	10.6
20	8.5	238.4	11.9
40	11.0	399.9	10.0

Table 5.6: $\mid A\xi^2 \mid$ vs. C for precipitate density, ρ_p, of $1.81\times10^5 m^{-1}$ in $\bar{1}31$ reflection.

$C, (\times 10^{22} m^3)$	$\xi, (\times 10^2 \mu m)$	$\mid A\xi^2 \mid, (\times 10^{17} m^2)$	$\mid A\xi^2 \mid /C, (\times 10^{-6} m^{-1})$
1	2.0	13.2	1.3
2	3.0	29.7	1.5
5	5.0	82.5	1.7
20	10.0	330.0	1.7
40	14.0	646.8	1.6

Table 5.7: $\mid A\xi^2 \mid$ vs. C for precipitate density, ρ_p, of $3.62\times10^5 m^{-1}$ in $\bar{1}31$ reflection.

$\delta, (\times 10^{-4} m^{-1})$	$\rho_p, (\times 10^{-4} m^{-1}$ of dislocation)
5.6	1.6
28.8	6.0
105.0	18.1
162.0	36.2

Table 5.8: Gradient, δ, of $\mid A\xi^2 \mid$ vs. C curve as a function of precipitate density, ρ_p.

$r_{max}, (\times 10^{10} m)$	$\pi r_{max}^2, (\times 10^{19} m^2)$	$\xi, (\times 10^6 m)$	$\pi \xi^2, (\times 10^{15} m^2)$
5.0	7.9	0.04	5.0
7.5	17.7	0.06	11.3
10.0	31.4	0.08	20.1
12.5	49.1	0.095	28.4
15.0	70.7	0.115	41.5

Table 5.9: Cross-sectional area, $\pi\xi^2$, of equivalent cylindrical inclusion as a function of cross-sectional area, πr_{max}^2, of precipitate distribution.

C is again found, and the gradient, δ, of the $\mid A\xi^2 \mid$ vs. C curve increases with ρ_p. Corresponding values of δ and ρ_p are displayed in Table 5.8.

The variation of δ with ρ_p is plotted in Fig. 5.30, and it is found that δ varies linearly with ρ_p, with gradient equal to 4.97. Hence, the value of $A\xi^2$ required to match a specific value of C can be found for all possible precipitate densities, ρ_p, for the $\bar{1}31$ reflection.

5.7 Variation of Strain with Radius of Precipitate Distribution

Tanner [140] has commented that the impurity cloud around a dislocation can be of significant magnitude. It is of interest, then, to investigate the variation in image when the radius, r_{max}, of the precipitate distribution is increased from the value of $5\mathring{A}$ used in the previous sections.

Figs. 5.31(a)-(e) show simulations for a dislocation decorated with a cylindrical distribution of precipitates of radius $5\mathring{A}$, $7.5\mathring{A}$, $10\mathring{A}$, $12.5\mathring{A}$ and $15\mathring{A}$, respectively. The $\bar{1}31$ reflection was used, C was set to $4 \times 10^{-21} m^3$ throughout and the volume number density of precipitates was kept fixed at the value used in section 5.5. Figs. 5.32(a)-(e) show the dislocation-inclusion images matching the dislocation-precipitate images of Figs. 5.31(a)-(e), respectively, and the results are displayed in Table 5.9.

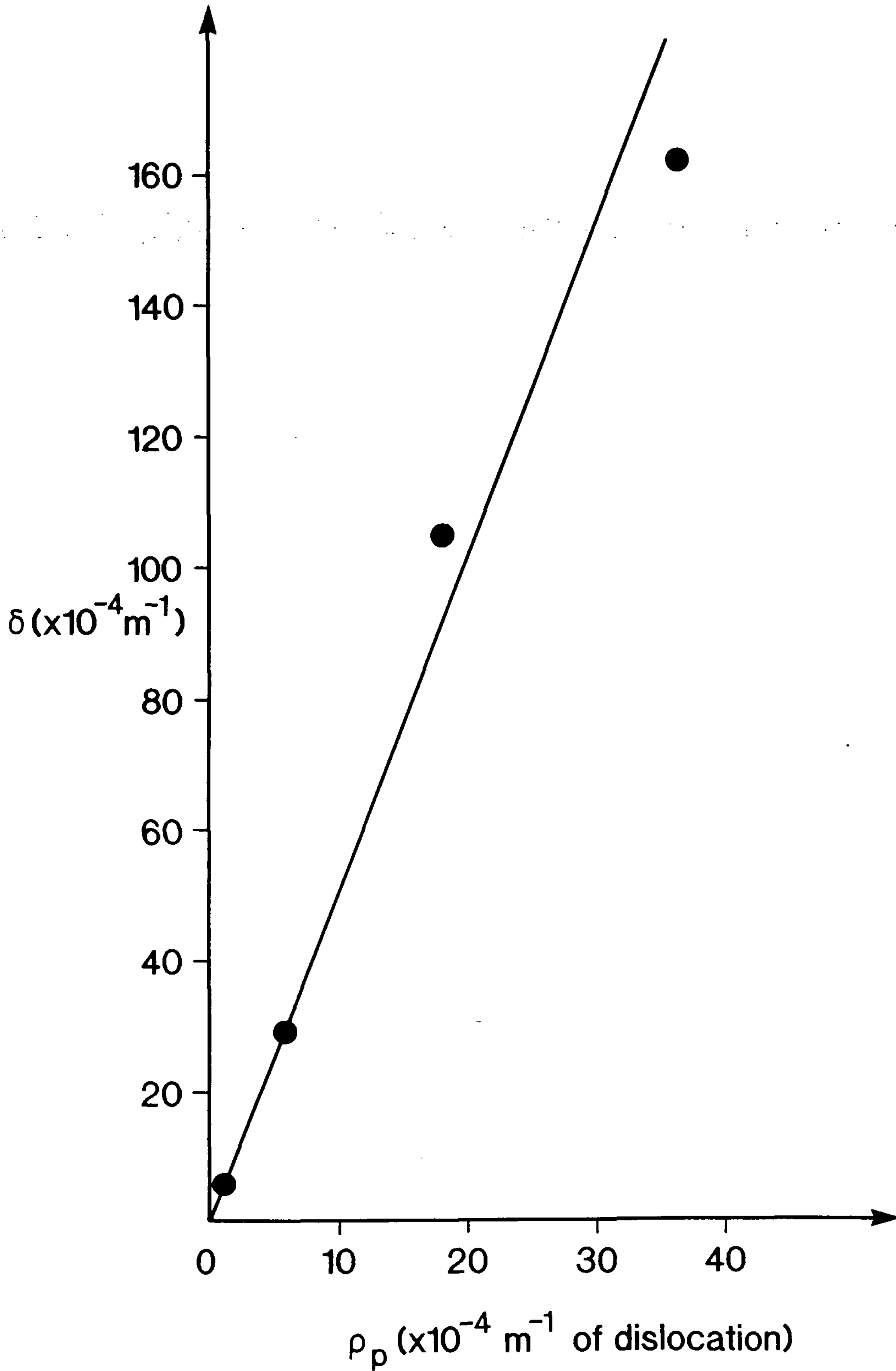

Fig. 5.30: Variation in the gradient, δ, of the $\mid A\xi^2 \mid$ vs. C curves for different values of precipitate line density, ρ_p.

$\bar{1}31$

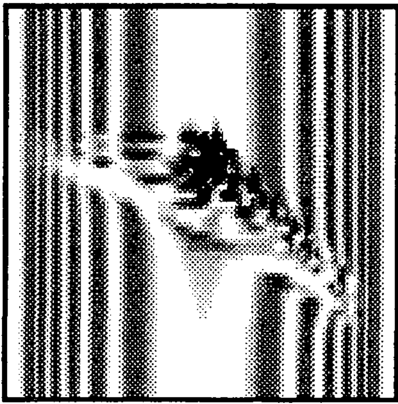

(a) radius = 5Å

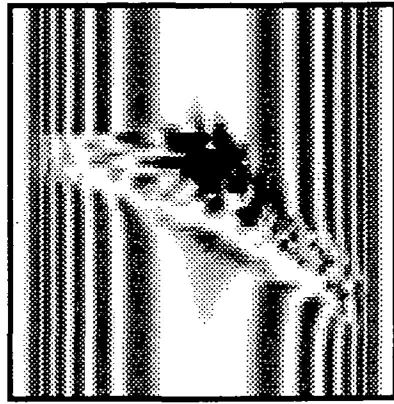

(b) radius = 7.5Å

100μm

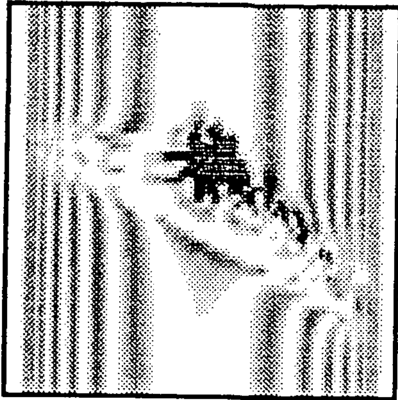

(c) radius = 10Å

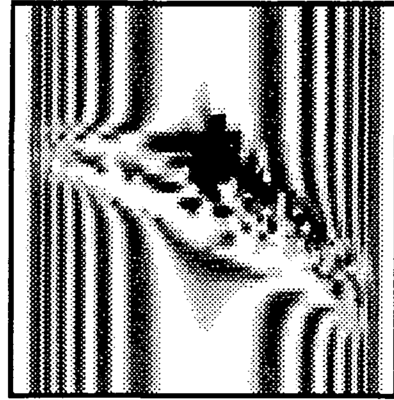

(d) radius = 12.5Å

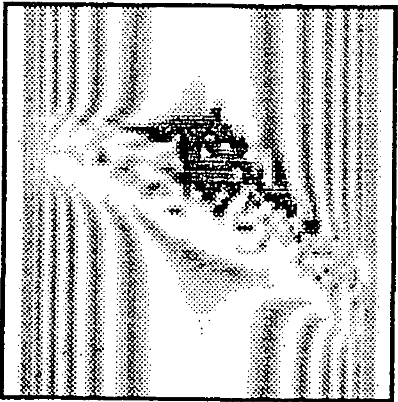

(e) radius = 15Å

Fig. 5.31: Simulations for a dislocation decorated with a cylindrical distribution of precipitates, for several values of distribution radius. C was taken as $4\times10^{-21}m^3$ and the $\bar{1}31$ reflection was assumed.

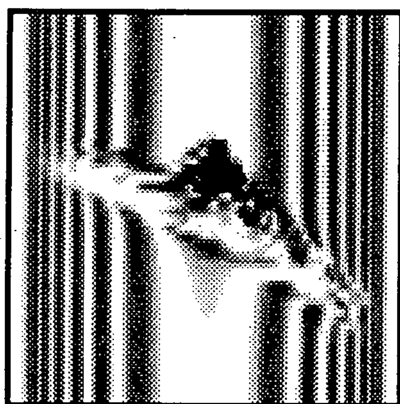
(a) $\xi = 0.04\mu m$

100μm

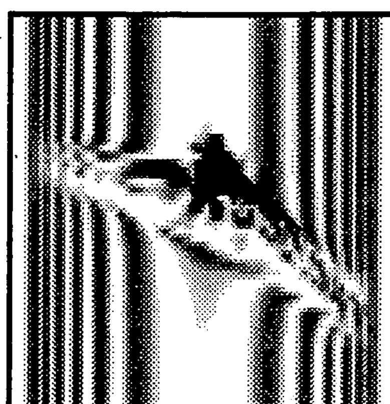
(b) $\xi = 0.06\mu m$

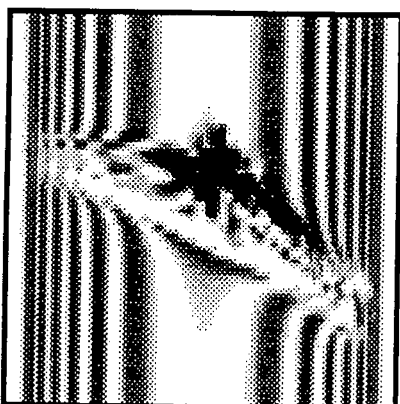
(c) $\xi = 0.08\mu m$

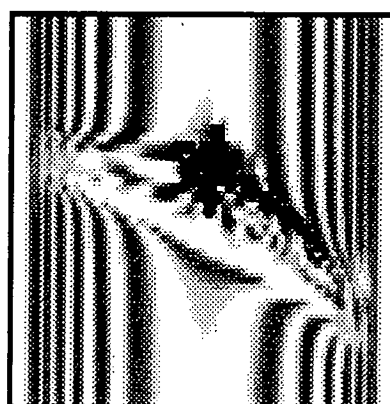
(d) $\xi = 0.095\mu m$

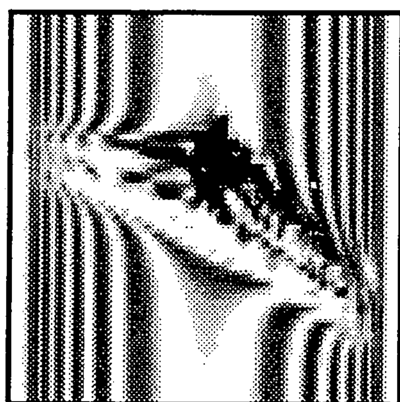
(e) $\xi = 0.115\mu m$

Fig. 5.32: Simulations using the equivalent cylindrical inclusion to model the results of Fig. 5.31, for the ξ-values indicated.

The cross-sectional area, $\pi\xi^2$, of the cylindrical inclusion is plotted as a function of the cross-sectional area, πr^2_{max}, of the precipitate distribution, in Fig. 5.33. From the graph, it is seen that the cross-sectional area of the inclusion must increase linearly with the cross-sectional area of the precipitate distribution, in order to obtain matching between the respective images. Of course, the magnitude, $| A\xi^2 |$, of the inclusion strain field is directly proportional to its cross-sectional area. Hence, it can be concluded that the strain magnitude of the equivalent cylindrical inclusion increases linearly with the cross-section of the precipitate distribution, with all other parameters constant.

5.8 Reversal of the Strain Associated with a Cylindrical Inclusion

It is of interest to see how the image due to a cylindrical inclusion changes upon reversal of the associated strain. In physical terms, the inclusion of the previous sections, which compresses the surrounding lattice, is replaced by an inclusion which is compressed by the lattice.

The new strain field was obtained by the simple expedient of reversing the sign of the lattice mismatch parameter, ε. In the input data file, the value of the term $vfrac$, representing ϵ, was changed from 0.4 to -0.4. Hence, the value of the term A of equations (5.2) and (5.3) changed from -0.33 to 0.33.

Fig. 5.34 compares simulations generated using the original and reversed strain fields, in the $3\bar{3}\bar{3}$ reflection of section 5.5.5. Each pair of simulations corresponds to a specific value of ξ. Simulation pairs with ξ equal to $0.08\mu m$ and $0.02\mu m$ show a noticeable difference, but the pair with ξ equal to $0.05\mu m$ show very little difference, and would effectively be indistinguishable in experimental topography. It is noticeable that the only variation in image structure is in the intermediary fringes. This is not surprising, since the intermediary image is an interference effect and is highly sensitive to small changes in lattice strain. Moreover, the interference character of intermediary image formation provides the explanation as to why some ξ-values induce a divergence between corresponding image pairs, whilst others do not. The volume of the strongly diffracting region around the inclusion depends on the magnitude and not on the sign of the strain field. This is why the direct images are almost identical in corresponding image pairs.

This study was undertaken using the $3\bar{3}\bar{3}$ reflection and geometry of section 5.3.4 simply because the associated intermediary fringe structure was particularly characteristic. However, the same comments made above apply equally well to the $\bar{1}31$ and $\bar{4}40$ reflection cases of sections 5.3.2 and 5.3.3, respectively.

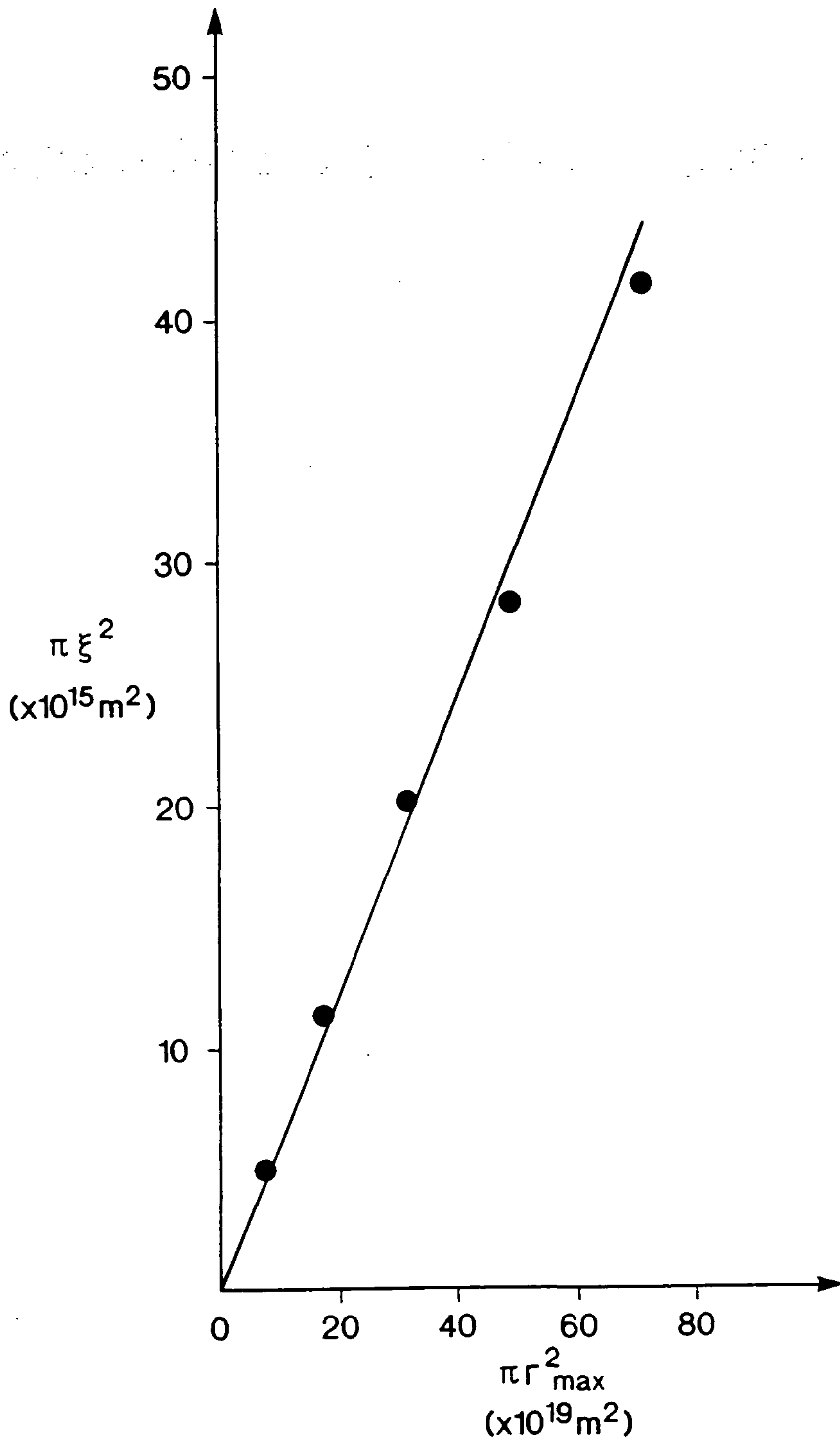

Fig. 5.33: Cross-sectional area, $\pi\xi^2$, of equivalent cylindrical inclusion as a function of cross-sectional area, πr^2_{max}, of precipitate distribution.

$3\bar{3}\bar{3}$

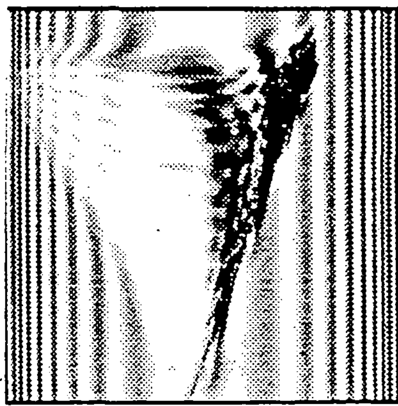

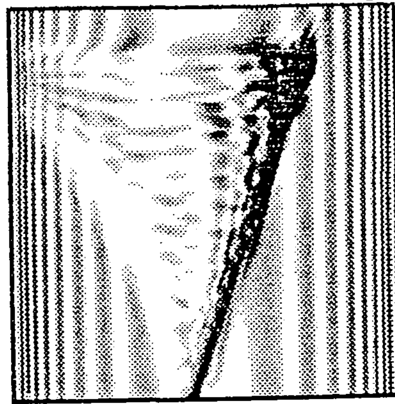

$\xi = 0.08\mu m$

$200\mu m$

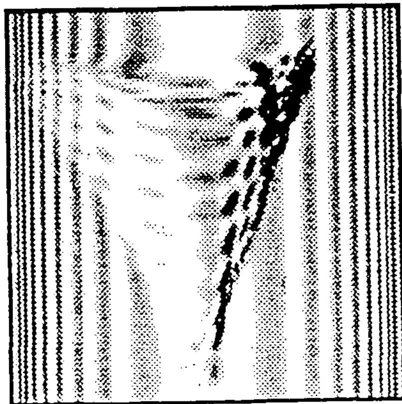

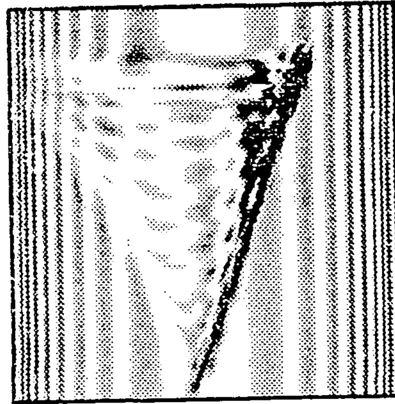

$\xi = 0.05\mu m$

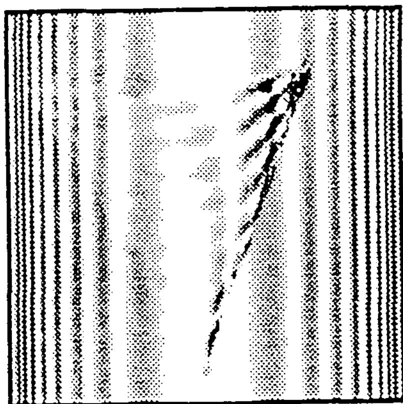

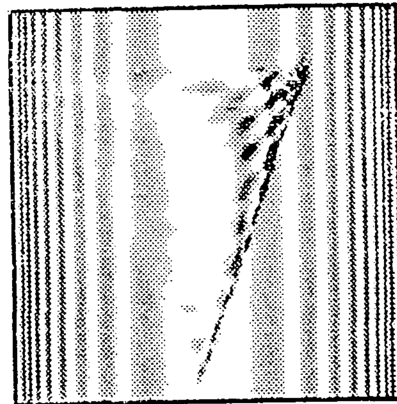

$\xi = 0.02\mu m$

original strain field

reversed strain field

Fig. 5.34: Comparison of simulations generated using the standard and reversed cylindrical inclusion strain fields, for the ξ-values indicated.

5.9 Resolvability of Two Decorated Dislocations as a Function of Strain

5.9.1 Introduction

Bourret et al. [138] have studied oxygen precipitation in dislocation-rich CZ Si samples with dislocation density $\sim 10^5 cm^{-2}$. A question may be posed as to the degree of distinguishability of such dislocations, in experimental topography, after decoration with transition metal precipitates. In particular, it is of interest to know how the distinguishability changes with increased strain associated with the decorated dislocations.

This question has been addressed in the current section, using the dislocation-inclusion model to represent a decorated dislocation. The $\bar{1}31$ geometry and defect orientation of section 5.3.2 have been used throughout, and a mutual displacement in the experimental y-direction was assigned to the decorated dislocations. Simulations were performed by calling the procedure $DIFFCYL$ (APPENDIX E) a second time in the integration procedure of $GENERAL.P$ (APPENDIX A), and incorporating the y-displacement in the second execution of $DIFFCYL$. The values of dsh from the two executions of $DIFFCYL$ were added, and the total was fed into the integration procedure.

The dislocation density of $10^5 cm^{-2}$ quoted by Bourret et al. [138] corresponds to a perpendicular separation of adjacent dislocations of approximately $32 \mu m$.

5.9.2 Results

In the present work, the dislocations were assumed to be mutually perpendicular, and the perpendicular separation of adjacent dislocations was assigned the variable κ. The following derivation illustrates how to convert from y-displacement, Δy, to κ.

From section 5.3.2, the dislocation orientation is given as:

$$\hat{\underline{u}} = (-0.671, 0.224, 0.707).$$

Let the vector $\underline{\kappa}$ be perpendicular to $\hat{\underline{u}}$. Since the mutual displacement of the dislocations is in the y-direction, geometrical considerations imply that the x-component of $\underline{\kappa}$ must be zero.

Hence,

$$\hat{\underline{\kappa}} = \alpha(0, 0.707, -0.224),$$

where α is a normalisation factor and is equal to 1.35.

Consequently,

$$\begin{aligned} \kappa &= \mid \underline{\kappa} \mid, \\ &= \alpha \Delta y (0, 0.707, -0.224).(0, 1, 0), \\ \text{so that } \kappa &= 0.95 \Delta y. \end{aligned} \tag{5.59}$$

$\Delta y, (\mu m)$	$\kappa, (\mu m)$	$\xi_{crit}, (\mu m)$	$C_{crit}, (\times 10^{21} m^3)$	$ln(C_{crit} \times 10^{21})$
20	19.0			
30	28.5	0.05	2.9	1.06
40	38.0	0.09	9.3	2.23
50	47.5	0.12	16.5	2.80
60	57.0	0.14	22.5	3.11
70	66.5	0.16	29.3	3.38
80	76.0	0.20	45.8	3.82

Table 5.10: Variation of critical deformation parameter, C_{crit}, with perpendicular separation, κ, of adjacent decorated dislocations.

For several values of Δy from $20\mu m$ to $80\mu m$, series of simulations were obtained to find the critical value, ξ_{crit}, of ξ for which two decorated dislocations are just resolved. The simulations are shown in APPENDIX K and the corresponding results are displayed in Table 5.10.

Relation (5.59) above was used to convert Δy to κ and the graph of Fig. 5.20 was used to convert ξ_{crit} to the corresponding C_{crit}, assuming a precipitate density of $6.03\times10^4 m^{-1}$ of dislocation. Table 5.10 includes entries for a term C^*_{crit}, equal to 10^{21} times the value of C_{crit}. The results are plotted in Fig. 5.35 which shows a linear relationship between $ln(C^*_{crit})$ and κ, for values of κ greater than about $45\mu m$. This variation will be discussed in section 5.9.3, below. An equivalent graph for any other value of precipitate density, ρ_p, could easily be drawn by re-calculating the values of C_{crit} from the original ξ_{crit}, using the graph of Fig. 5.30 relating δ and ρ_p. It was noted that the bare dislocation images were not distinguishable for values of κ below $28.5\mu m$. This represents a natural absolute limit on distinguishability, since the resolution of the simulations in this chapter is equivalent to that of experimental topography.

5.9.3 Discussion

The results of this section have been confined to one reflection and one dislocation orientation only. However, several significant and useful results have been obtained. For the $\bar{1}31$ reflection and defect orientation of section 5.3.2, it has been shown that adjacent dislocations are distinguishable down to a perpendicular separation, κ, of $28.5\mu m$. For this value of κ, the dislocations remained resolved when decorated with precipitates of C-value up to $2.9\times10^{-21}m^3$. Upon reduction of κ to $19.5\mu m$, even bare dislocations were no longer resolvable. The result outlined above is of considerable technological relevance. The critical κ-value of $28.5\mu m$ corresponds to a dislocation density of $1.2\times10^5 cm^{-2}$, of the same order of magnitude as that quoted by Bourret et al. [138] for dislocation-rich CZ Si samples. The important conclusion is that experimental topography should be capable of resolving dislocations with decoration of C-value up to $2.9\times10^{-21}m^3$ even in the case of samples with very high

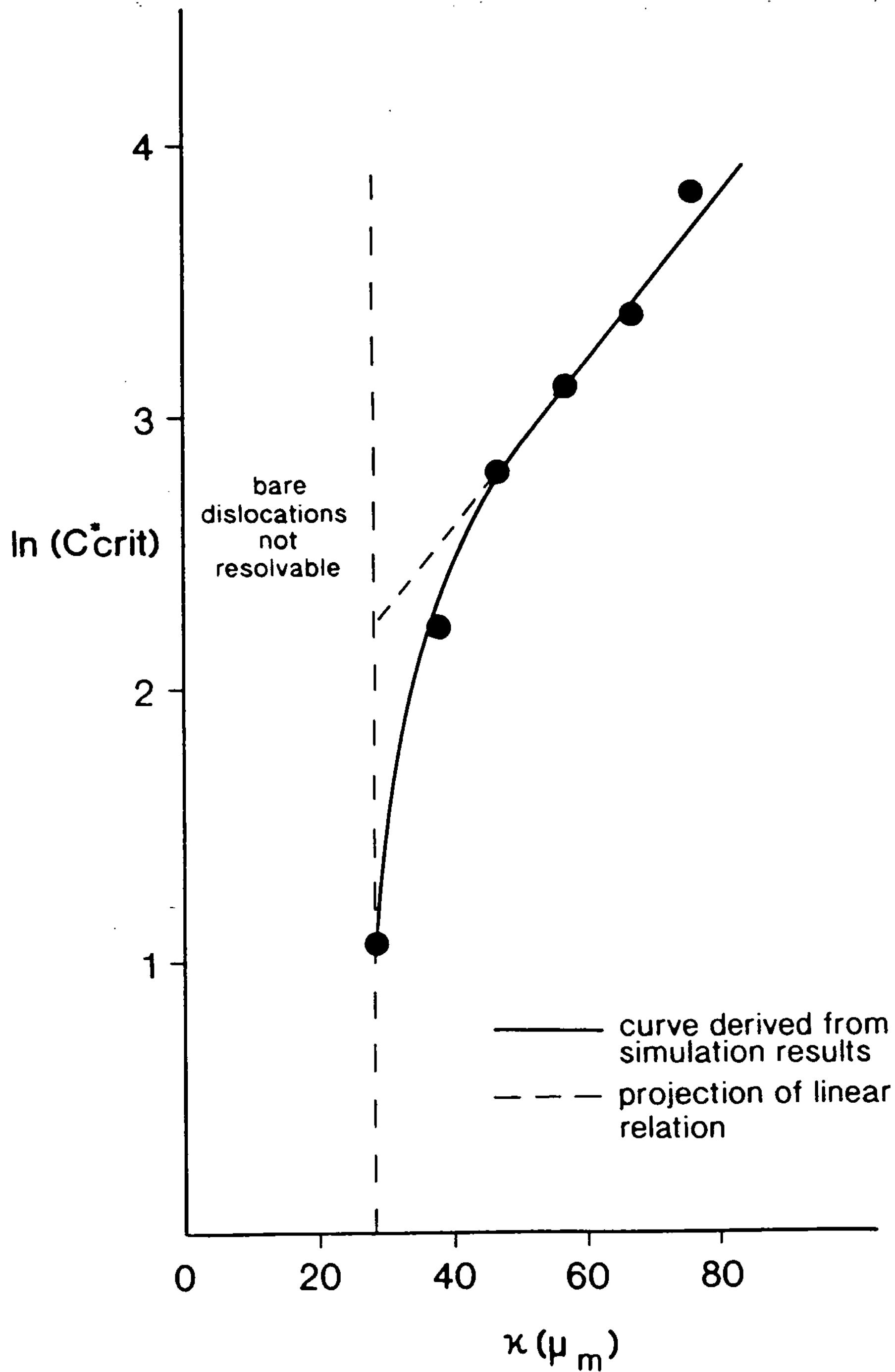

Fig. 5.35: Variation of $ln(C_{crit} \times 10^{21})$ with perpendicular separation, κ, of decorated dislocations, where C_{crit}, measured in m^3, is the critical value of deformation parameter for which adjacent decorated dislocations are just resolved.

dislocation density.

The comments above define a role for X-ray section topography as a test of gettering efficiency. Suppose test dislocations in the crystal bulk are imaged by section topography prior to a gettering treatment. A topograph of the same dislocation distribution after the treatment will show a contribution to the original dislocation images due to the strain induced by precipitate decoration. The extent of this contribution, parameterised in the previous sections of this chapter, is then an indication of the gettering efficiency of the dislocation distribution.

The linear variation of $ln(C^*_{crit})$ with κ, for κ greater than about $45\mu m$, in the previous section is analogous to a result pointed out by Green et al. [101] for the case of a single precipitate. They showed that the image height, h, in a plane perpendicular to the plane of incidence increases linearly with lnC, where C is the precipitate deformation parameter. Assuming that this linear relation carries through to the decorated dislocation case, it is to be expected that the quantity Δy, and hence κ, increases linearly with $ln(C^*_{crit})$, for decorated dislocations to be resolvable. This linearity breaks down for values of κ less than about $45\mu m$, because of the increasingly significant strain contribution due to the dislocations themselves.

5.10 General Discussion and Industrial Implications

The Cylindrical Inclusion model of Tanner [140] has been shown to be an accurate means of simulating section topographs due to dislocations decorated with precipitates. The computation time to simulate using this model compares very favourably with that for the corresponding precipitate distribution model. All the simulations of this chapter were taken with a resolution equivalent to experimental topography, so that any predictions made can be genuinely considered to apply to the experimental technique.

In section 5.5, MoK_{α_1} radiation in three different reflections was used to generate images with characteristic structure, from which definite results could be derived. In this section, the precipitate line density was taken as $6.03\times10^4 m^{-1}$ of dislocation, after Kidd et al. [139], and the radius of the precipitate distribution was assumed to be $5\mathring{A}$. It was shown that precipitate decoration with C-value as low as $1\times10^{-22}m^3$ could be distinguished from the host dislocation. Clearly, this represents a very small strain magnitude in comparison with the C-values of $\sim 10^{-19}m^3$ found for oxygen precipitates in Chapter 4. This indicates a very high visibility of precipitate decoration in X-ray section topography, and identifies a clear technological role for topography in the detection and characterisation of precipitate gettering at dislocations in Si crystals.

Investigations showed convergence of the results for edge, 60° and screw dislocations. It is concluded that, for the reflections studied here, any result for a decorated edge dislocation will also be true for the corresponding decorated 60° and screw dislocations.

Linear variation of the inclusion strain magnitude, $| A\xi^2 |$, with precipitate strain magnitude, C, was obtained for the $\bar{1}31$, $\bar{4}40$ and $3\bar{3}\bar{3}$ reflections, and section 5.5.4 explains why the gradients of the corresponding straight lines, Figs. 5.20, 5.21 and 5.22 are different. This is a combination of the different radial variation in displacement field, $\underline{u}(\underline{r})$, for the two defect types, and the difference in the diffracting volume activated by different reflections. It was found that the gradient of the $| A\xi^2 |$ vs. C curve is highest for low-order reflections. This result for a decorated dislocation has been shown to be in agreement with an analogous result of Miltat and Bowen [144] for a bare dislocation, which identifies an increase in diffracting volume with decreasing diffraction vector magnitude.

In section 5.6, the gradient, δ, of the $| A\xi^2 |$ vs. C curve was shown to increase linearly with precipitate line density, ρ_p. The graph of δ vs. ρ_p in Fig. 5.30 can be used to obtain the $| A\xi^2 |$ vs. C relation for any precipitate density in the $\bar{1}31$ reflection.

The results of section 5.7 show that for precipitate distributions of varying radius, the cross-sectional area of the equivalent cylindrical inclusion must increase linearly as the cross-section of the precipitate distribution, in order to obtain matching of simulation pairs. This linear relation is plotted in Fig. 5.33.

It has been shown [139] that TEM can be used to determine both the precipitate density, ρ_p, and distribution radius, r_{max}, of a precipitate decorated dislocation. Having established values of ρ_p and πr_{max}^2 as initial conditions, the linear relations of sections 5.5, 5.6 and 5.7 can be used to specify the C-value associated with the precipitate decoration. The physical meaning of this is defined with reference to the C-values obtained for oxygen precipitates in Chapter 4, by matching of simulation with experiment.

The results of section 5.9 indicate that for the $\bar{1}31$ reflection and dislocation geometry studied, the minimum perpendicular separation, κ, of adjacent dislocations for resolvability is $28.5\mu m$. For this value of κ, adjacent decorated dislocations are resolved for C-values up to $2.9\times10^{-21}m^3$. This result is technologically very important, since it means that decorated dislocations in dislocation-rich CZ Si, as used by Bourret et al. [138], are resolvable by experimental X-ray section topography. The critical value, C_{crit}, of C for resolvability was determined as a function of κ, and a linear relation was found, Fig. 5.35, between $ln(C_{crit} \times 10^{21})$ and κ, for κ-values less than about $45\mu m$. This relation is explained by extension of a result due to Green et al. [101], which defines a linear relation between $ln(C)$ and the height, h, of the image due to a single precipitate. The linearity between $ln(C_{crit} \times 10^{21})$ and κ in Fig. 5.35 breaks down for κ less than about $45\mu m$ because of the increasingly significant strain contribution due to the dislocations themselves.

Use of section topography as a test of gettering efficiency has been proposed. Topographs of dislocations taken before and after gettering will show an expansion and change in strucure of the corresponding dislocation images, due to decoration with transition metal precipitates. The extent of this change in the dislocation images, parameterised in the preceding sections, can then be used as a test of gettering efficiency.

X-ray section topography has received little attention in the gettering literature, on account of the superior spatial resolution of TEM. However, the results of the current work define a specific role for section topography, via experiment in conjunction with simulation, in the parameterisation of strain effects due to precipitate decorated dislocations.

Chapter 6

Investigation of Device-Induced Strain in Silicon Substrates

6.1 Background and Context

6.1.1 Technological Motivation

Diffusion of impurities into selective areas of Si wafers, to fabricate devices, induces strain in the Si lattice. When the impurity concentration is sufficiently high, misfit dislocations are generated in the region of high strain, to reduce the total elastic energy. These process-induced defects can have a very detrimental effect on device performance. Consequently, the measurement and control of device-induced strains is of considerable technological importance.

Thermal oxidation of a Si wafer is an integral part of device fabrication technology. Formation of a layer of SiO_2 on the Si surface takes place when the Si substrate is heated in oxygen at processing temperatures typically around 1000°C. The thermal expansion coefficients of Si and SiO_2 differ considerably:

$$\begin{aligned} \alpha_{Si} &= 3.0 - 4.5 \times 10^{-6} K^{-1}, \\ \text{and } \alpha_{SiO_2} &= 5.0 \times 10^{-7} K^{-1}. \end{aligned}$$

This means that, upon cooling the wafer to room temperature, the oxide film contracts less than the underlying substrate, giving rise to equal and opposite strains in the film and substrate. If the film has been partially etched away, then the strain is especially high near the film edge, with the possibility of dislocation propagation as in the device case of the previous paragraph. In fact, the case of a device formed on the Si substrate by diffusion or ion-implantation is elastically analogous to the case of an oxide film, and this similarity will be commented upon later.

The growth of a silicon-nitride (Si_3N_4) film on a Si substrate has become a standard industrial technique for protecting the active device region from oxidation [145], but there have been reports [146] of dislocations at the edges of nitride films. This is because a Si_3N_4 film grown by *chemical-vapour-deposition* (CVD) induces a very high compressive stress ($\sim 1 \times 10^7 Nm^{-2}$) in the Si lattice. This is of the

same order of magnitude as the macroscopic yield stress of Si, ($1.5\times10^7 Nm^{-2}$ at 1050°C; $1.1\times10^7 Nm^{-2}$ at 1100°C). In general, however, the effect of this high stress is suppressed by the fact that the Si lattice is much thicker ($\sim$ 1000 times) than the Si_3N_4 film. In fact, Tamura and Sunami [147] have shown that dislocation propagation does not take place provided the film thickness does not exceed $300nm$.

Upon annealing in oxygen, the Si_3N_4 surface gradually becomes coated with a film of SiO_2, according to the reaction:

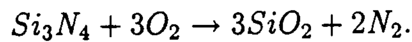

$$Si_3N_4 + 3O_2 \rightarrow 3SiO_2 + 2N_2.$$

It is interesting to note that the thicknesses of oxide films formed in wet oxygen are significantly higher than those formed in dry oxygen.

The thermal expansion coefficient of Si_3N_4 ($\alpha_N = 2.5 - 3.8 \times 10^{-6} K^{-1}$) is very similar to that of the Si substrate, so that differential contraction again occurs and the SiO_2 film induces a strain in the substrate via the Si_3N_4 layer. Again, it is technologically very important to monitor and control these strains, since the defects which they induce are highly detrimental to device yield. Fabian [145] has commented that X-ray topography, with its inherent sensitivity to lattice strain, is well suited to this task.

6.1.2 Blech and Meieran's Strain Equations

It has been known for many years that X-ray topographs show enhanced darkening [148] and characteristic fringe phenomena [149] associated with diffraction from thin film boundaries on single crystal substrates. In 1967, Blech and Meieran [143] developed a model to describe the strain induced in the Si substrate by a thin, discontinuous surface film. The substrate was assumed to be semi-infinite and elastically isotropic.

Blech and Meieran's model is illustrated in Fig. 6.1. Let the force per unit length along each edge be S, in opposite directions for the two edges. The force exerted on the substrate by a length dy of film is Sdy. Consider the stress-induced displacement components u_0, v_0, w_0 in the experimental x_0, y_0, z_0-directions, at a general point, P, with polar coordinates (r, ϕ) relative to the film edge EE'. For an infinite strip, v_0 is equal to zero from symmetry considerations. A symmetric reflection was assumed, for which the Bragg planes are parallel to the plane $x = 0$, so that the w_0 component can be neglected.

Assuming the separation, l, of the film edges to be very large, the treatment can be restricted to the edge EE' alone. On the basis of this assumption, Blech and Meieran's equations can be written:

$$\begin{aligned} \partial u_0/\partial z_0 &= -\frac{2S\cos\phi}{r}\left[(AB - C) + 2A\sin^2\phi\right], \\ \partial u_0/\partial x_0 &= -\frac{2S\sin\phi}{r}\left[(AB - C) - 2A\cos^2\phi\right], \end{aligned} \qquad (6.1)$$

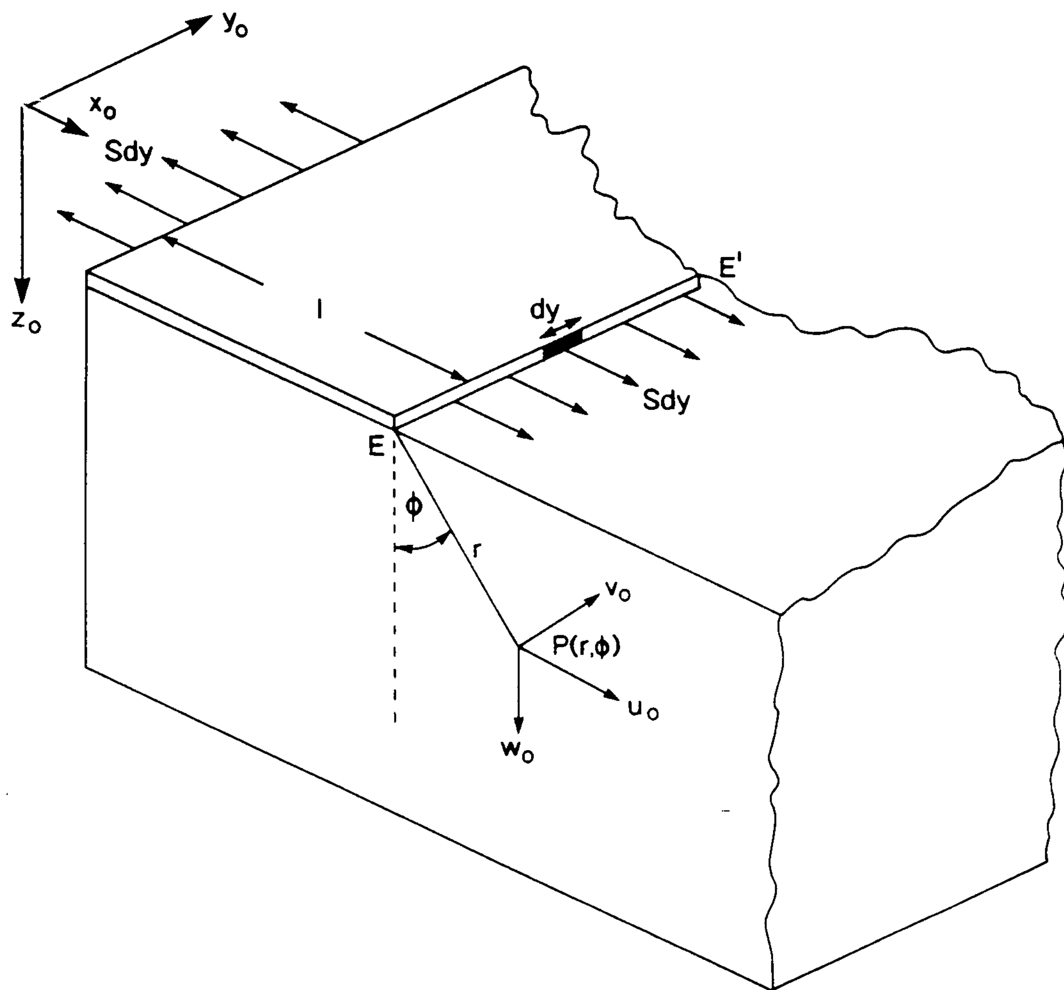

Fig. 6.1: Blech and Meieran's strain model for a thin film deposited on a substrate.

$$\begin{aligned} \text{where } A &= (1+\nu)/2\pi E, \\ B &= 3-4\nu, \\ C &= (1+\nu)(1-2\nu)/2\pi E, \end{aligned}$$

and ν, E are Poisson's ratio and Young's modulus, respectively.

In the late 1960's and early 1970's, Patel and Kato [150,151,152] developed Blech and Meieran's model on the basis of Kato's eikonal theory, in order to investigate fringe phenomena in X-ray section topographs due to oxide edges on Si substrates. The crystal/film geometry and reflection geometry assumed by Kato and Patel are indicated in Figs. 6.2(a) and (b), respectively. The film edge is now inclined so that the surface normal to the edge makes an angle δ with the experimental x-axis.

From Fig. 6.1,

$$\begin{aligned} x_0 &= r\sin\phi, \\ \text{and } z_0 &= r\cos\phi. \end{aligned}$$

Hence, equations (6.1) can be re-written:

$$\begin{aligned} \partial u_0/\partial z_0 &= 4AS\left[\frac{C-AB}{2A}\frac{z}{r^2} - \frac{zx_0^2}{r^4}\right], \\ \partial u_0/\partial x_0 &= 4AS\left[\frac{C-AB}{2A}\frac{x_0}{r^2} + \frac{x_0 z^2}{r^4}\right]. \end{aligned} \tag{6.2}$$

The displacement component u_0 was directed along the x_0-direction. Now consider the stress-induced displacement u, directed along the x-axis of Fig. 6.2(a).

Clearly,

$$x_0 = x\cos\delta + y\sin\delta, \tag{6.3}$$

$$\text{and } u = u_0\cos\delta. \tag{6.4}$$

From equation (6.4):

$$\frac{\partial u}{\partial z} = \cos\delta\frac{\partial u_0}{\partial z_0}.$$

From equations (6.3) and (6.4):

$$\begin{aligned} \frac{\partial u}{\partial x} &= \cos\delta\frac{\partial u_0}{\partial x_0}\frac{\partial x_0}{\partial x}, \\ &= \cos^2\delta\frac{\partial u_0}{\partial x_0}. \end{aligned}$$

Hence, using equations (6.2), we obtain:

$$\partial u/\partial x = 4AS\cos^2\delta\left[\frac{C-AB}{2A}\frac{x_0}{r^2} + \frac{x_0 z^2}{r^4}\right],$$

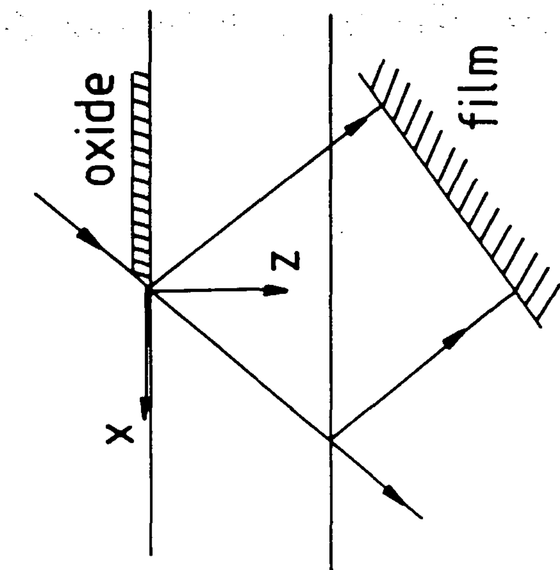

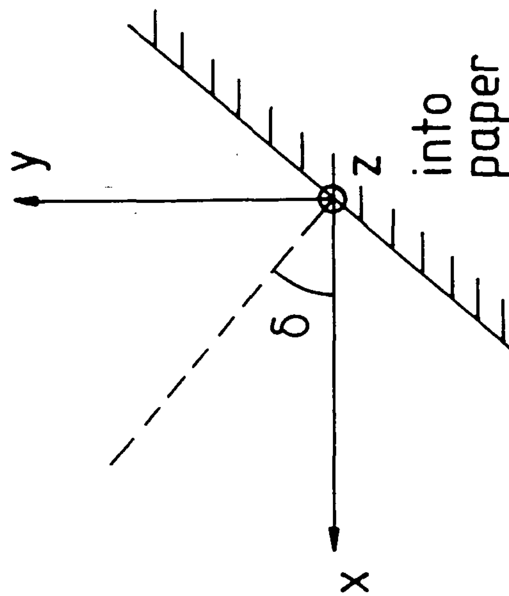

Fig. 6.2: Crystal/film geometry (a) and reflection geometry (b) assumed by Kato and Patel.

$$\begin{aligned}
\partial u/\partial z &= 4AS\cos\delta\left[\frac{C-AB}{2A}\frac{z}{r^2}-\frac{zx_0^2}{r^4}\right], \qquad (6.5)\\
\text{where } r^2 &= x_0^2+z^2,\\
\frac{AB-C}{2A} &= 1-\nu = 0.72, \text{ for } Si,\\
4AS &= 2(1+\nu)(S/\pi E),\\
&= 2.56S/\pi E,
\end{aligned}$$

and x_0 is given by equation (6.3).

The stress-induced displacement, u, is directed along the experimental x-axis. The reason why the y-component of the original displacement, u_0, has been neglected will be explained in section 6.2.1. Equations (6.5) represent Kato and Patel's formulation [152] of the strain equations of Blech and Meieran [143].

Patel and Kato [153] applied their formulation of the theory to predict the positions of the extra hook-shaped Pendellösung fringes observed previously by other workers [149] in experimental topographs. The predictions of their theory agreed well with the positions as measured from experimental topographs. In a related work, Ando et al. [154] used the same theory to predict the intensity contours in experimental topographs. Good agreement was obtained, except for those parts of the crystal corresponding to the highly distorted region in the immediate vicinity of the oxide-edge. It is seen from the equations (6.5) that at the edge itself r is equal to zero and there is a singularity in the strain field. This represents a flaw in Blech and Meieran's strain model, and explains why good matching was not possible for regions close to the oxide film discontinuity. Even disregarding the singularity, the eikonal theory ceases to be valid in regions of highly distorted crystal. Consequently, Ando et al. [154] introduced an exponentially varying strain-relaxation term to reduce the strain magnitude locally in the vicinity of the edge. In this way, matching was possible, but the authors did not offer a definitive theoretical justification for their strain-relaxation term.

An alternative means of avoiding the singularity of equations (6.5) was proposed by Filscher [155], involving the removal, in the calculation, of a thin lamina containing the film edge. This sort of approach has been criticised by Petrashen and Shulpina [156] as being inconsistent from a physical point of view. They referred to work by Petrashen [66] which indicated that the required accuracy could be obtained by using Takagi's equations, (2.55), rather than Kato's eikonal theory. Takagi's equations have the advantage over eikonal theory in that they are valid even for highly distorted crystal. Noting the similarity between the strain fields due to oxide- and device-edges, Petrashen and Shulpina [156] used Takagi's equations in conjunction with the unmodified Blech and Meieran equations to simulate successfully X-ray section topographs of edge regions of heavy boron doping on Si substrates.

Blech and Meieran's equations assume that the force exerted on the substrate is concentrated at the edge itself. In reality, this force will be distributed across a region of the substrate. However, Hu [157] has pointed out that, provided the

elastic modulus of the substrate is greater than that of the film, more than seven-eighths of the total film force is located within a distance of one film thickness from the film edge. Young's modulus for Si is known [158] to be $1.7\times10^{11} Nm^{-2}$, and for α-quartz [159] to be $1.05\times10^{10} Nm^{-2}$ along the crystallographic c-axis, at room temperature. Taking Young's modulus for the SiO_2 film to be similar to that for quartz, it is seen from Hu's result, above, that Blech and Meieran's assumption of an edge-concentrated force is well-founded.

Blech and Meieran's theory assumed that the stress-induced displacement in the experimental z-direction, Fig. 6.2, could be neglected. Hence, their treatment of stresses was two-dimensional in nature. Isomae [160] has extended the Blech and Meieran model to accommodate stress-induced displacement in all three experimental coordinate directions. However, he found that the stress distribution resulting from the three-dimensional analysis was very similar to that of Blech and Meieran's model, except in the vicinity of a corner where two edges of a rectangular film met.

More recently, Epelboin [161] has simulated the experimental section topographs due to Patel and Kato [153] by numerical integration of Takagi's equations. He used an unpublished expression for the lattice displacement, due to S. Mader, which contained an additional term to that derived by Blech and Meieran. Based on the elastic theory of Timoshenko and Goodier [162], the model included a moment, in addition to the force, concentrated at the oxide edge. However, a large number of simulations with a wide range of deformation parameters showed that the effect of this term was negligible, and below the resolution of experimental topography. Hence the strain model used by Epelboin was essentially that of Blech and Meieran.

For high values of edge-induced strain, Epelboin observed additional fringes in the central part of the simulated images. He attributed these to interference between wavefields created close to the surface, but noted that such fringes had never been observed experimentally. In order to fit the experimental data, he was forced to propose that the strain at real film edges is reduced, by lack of adhesion or relaxation during cooling, to a level at which the additional fringes are not seen. There is no physical explanation for such an assumption, and it is very unsatisfactory. Earlier work by Petrashen and Shulpina [156] strongly suggests that the unmodified strain equations of Blech and Meieran can be used to obtain satisfactory simulation of section topographs. This approach has been adopted here, in order to re-examine the image structure in section topographs of oxide film edges.

6.2 Transformation of the Strain Equations into Computer Code

The purpose of the current section is to construct a procedure analogous to procedure *DIFFPOINT* (APPENDIX B) to calculate the quantity *dsh* from the strain equations (6.1) for an oxide film.

6.2.1 Extension of Kato and Patel's Treatment

In Blech and Meieran's model [143], the surface film was taken to be very wide, so that the treatment was effectively restricted to a single edge. Hence, the equations (6.5) of Kato and Patel's formulation [152] refer to an isolated left-hand edge, Fig. 6.2.

In the current work, it is necessary to consider films whose widths are of the order of microns. Hence, the strain contibution due to both edges must be taken into account.

In section 6.1.1, it was pointed out that when a SiO_2/Si wafer cools from processing temperature, the oxide layer contracts less than the underlying substrate. Hence, at working temperatures, the film exerts a tensile stress on the substrate. From careful consideration of the geometry of Fig. 6.2 and the associated equations (6.5), it is then seen that the term S, representing force per unit length along the edge, must take positive values. Blech and Meieran [143] have shown that the region of heavy distortion due to edge-induced stress is localised to the immediate vicinity of the edge. They found that the elastic response of the Si lattice relaxes the lattice planes to their undeformed configuration within a distance of a few tens of angstroms from the edge itself.

In equations (6.5), the term x_0 represents the perpendicular distance of a general point, P, from the left-hand edge of Fig. 6.3. Let the perpendicular distance of P from the right-hand edge of the film be χ_0, Fig. 6.3. In order to apply equations (6.5) consistently to the two edges, it is seen that the sign of χ_0 must be reversed relative to x_0. In Kato and Patel's formulation [152], the sign convention, embodied in equation (6.3), is given as:

$$\begin{aligned} x_0 &> 0 \text{ on L. H. S. of L. H. edge,} \\ x_0 &= 0 \text{ at L. H. edge,} \\ x_0 &< 0 \text{ on R. H. S. of L. H. edge.} \end{aligned}$$

For consistency, it is then necessary to adopt the convention:

$$\begin{aligned} \chi_0 &< 0 \text{ on L. H. S. of R. H. edge,} \\ \chi_0 &= 0 \text{ at R. H. edge,} \\ \chi_0 &> 0 \text{ on R. H. S. of R. H. edge.} \end{aligned}$$

The conditions above are mutually satisfied by setting:

$$\chi_0 = -(x_0 + H\cos\delta), \tag{6.6}$$

where H is the separation of the device edges in the experimental x-direction.

Clearly, the strain induced in the substrate by the two edges is of opposite sign. Hence, mirror symmetry means that one may simply reverse the sign of $(\partial u/\partial x)_{R.H.}$ relative to $(\partial u/\partial x)_{L.H.}$, also replacing x_0 by χ_0.

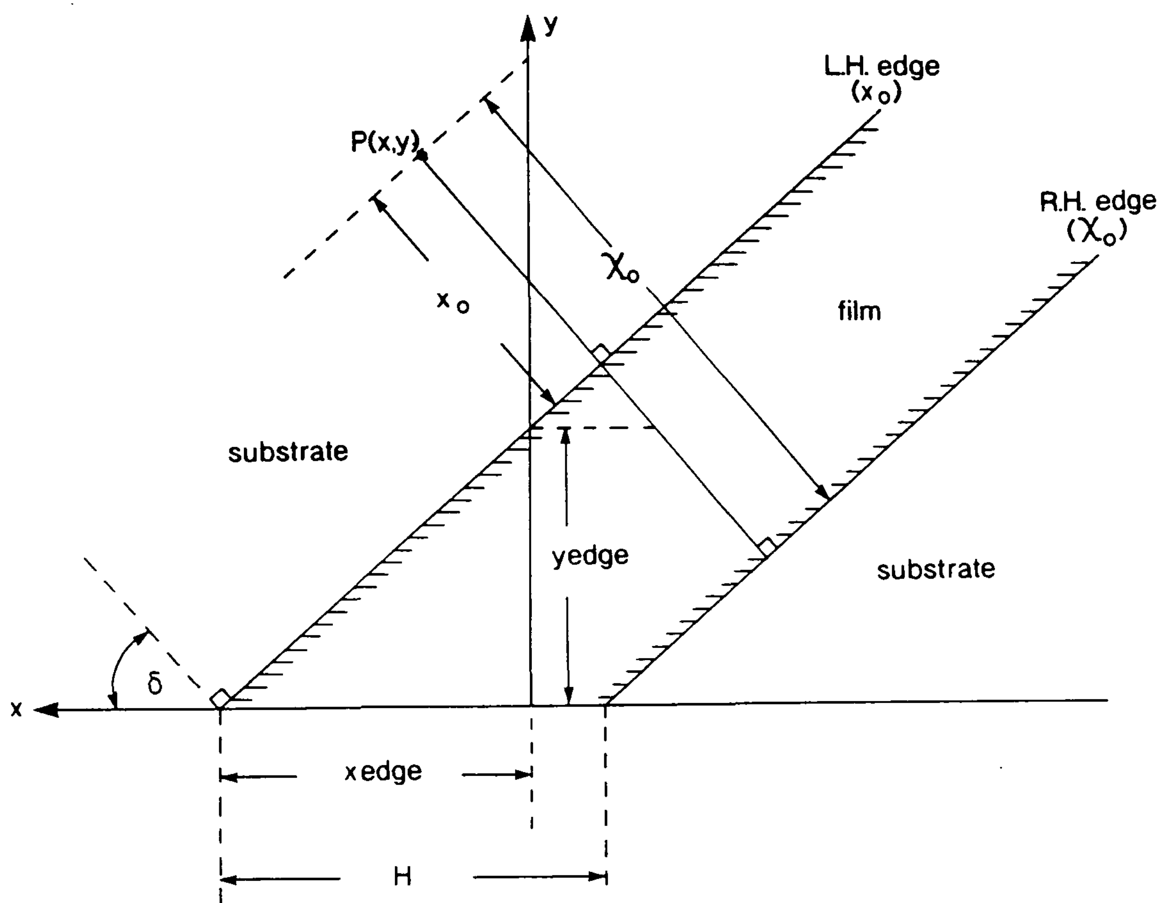

Fig. 6.3: Geometry of a film on a silicon substrate.

Hence, the total x-component of strain becomes:

$$(\partial u/\partial x)_{tot} = \tau \cos^2 \delta \left[0.72\left(\frac{\chi_0}{\chi_0^2+z^2} - \frac{x_0}{x_0^2+z^2}\right) + z^2\left(\frac{x_0}{(x_0^2+z^2)^2} - \frac{\chi_0}{(\chi_0^2+z^2)^2}\right)\right], \tag{6.7}$$

where $\tau = 2.56(S/\pi E)$.

The z-components of strain are combined in an analogous manner, so that:

$$(\partial u/\partial z)_{tot} = \tau \cos \delta \left[0.72z\left(\frac{1}{\chi_0^2+z^2} - \frac{1}{x_0^2+z^2}\right) + z\left(\frac{\chi_o^2}{(\chi_0^2+z^2)^2} - \frac{x_0^2}{(x_0^2+z^2)^2}\right)\right]. \tag{6.8}$$

Recalling equation (4.4),

$$\begin{aligned} dsh &= \frac{\partial}{\partial S_h}\left[\underline{h}.\underline{u}(\underline{r})\right], \\ &= shx\frac{\partial}{\partial x}\left[h_x u_x + h_y u_y + h_z u_z\right] \\ &\quad + shy\frac{\partial}{\partial y}\left[h_x u_x + h_y u_y + h_z u_z\right] \\ &\quad + shz\frac{\partial}{\partial z}\left[h_x u_x + h_y u_y + h_z u_z\right]. \end{aligned} \tag{6.9}$$

Now, each plane of incidence is parallel to the plane $y = 0$. Hence, the diffraction vector, $\underline{h}$, has no y-component, so that h_y is equal to zero. Consequently, any stress-induced displacement in the y-direction of Fig. 6.3 will not make any contribution to the value of dsh, given by equation (6.9). This is why displacements in the y-direction were not considered in the derivation of equations (6.5). In addition, the vector $\underline{S_h}$, defined in Fig. 5.7, has no component in the y-direction. Hence, the direction cosine, shy, of the angle between the $\underline{S_h}$ and y-directions is also equal to zero. Here, Blech and Meieran's convention that the vertical component of displacement, u_z, is zero is retained.

Hence, retaining only the non-vanishing terms, equation (6.9) becomes:

$$dsh = shx.h_x\frac{\partial u}{\partial x} + shz.h_x\frac{\partial u}{\partial z}, \tag{6.10}$$

where $\partial u/\partial x$ and $\partial u/\partial z$ are given by equations (6.7) and (6.8), respectively.

Hence, dsh is defined by equation (6.10), in conjunction with (6.7) and (6.8), and the sign convention of equation (6.6).

6.2.2 Development of the Strain Code

The Pascal procedure *DIFFSTRIP* (APPENDIX G) has been constructed to implement equation (6.10). The perpendicular distances x_0 and χ_0 are calculated in section α, taking into account the sign convention implicit in equation (6.6). The

term τ of equations (6.7) and (6.8), which is defined after equation (6.7), is calculated in line A. Here, the force per unit length, S, and Young's modulus, E, are represented by the terms $flnth$ and *ymod*, respectively. Also, the separation, H, of the film edges in the x-direction, used to calculate χ_0 from equation (6.6), is represented by the variable *horiz*. In section β, the terms $\partial u/\partial x$ and $\partial u/\partial z$ are calculated according to equations (6.7) and (6.8), and are represented by the variables ddx and ddz, respectively. Finally, dsh is evaluated in line B, according to equation (6.10).

The associated procedure to read in the film parameters is $STRIPDEF$ (APPENDIX G). Lengths and angles are input in microns and degrees, respectively, and subsequently converted into metres and radians. The term *zdispl* represents the z-coordinate of the film, and is needed to specify whether the film is on the entrance or exit surface. The terms $xedge$, $yedge$ and *zdispl* specify the orientation and position of the film relative to the Borrmann fan. These terms modify the x, y, z arguments of $DIFFSTRIP$ when it is called in section χ of the integration procedure of $GENERAL.P$ (APPENDIX A). It is important that the singularity of the strain field should never coincide with a node of the integration network. This is in fact prevented from happening by the manner in which the integration procedure of $GENERAL.P$ works. For each plane of incidence, the single node at the apex of the Borrmann fan is automatically assigned values of wave amplitudes, based on the boundary conditions calculated in the integration procedure of $GENERAL.P$. Clearly, since the device-edge occurs at the crystal surface, the possibility of a node being located at the singularity is then removed. The code has been configured so that the position and orientation of the film on the substrate surface are specified by either $xedge$ or $yedge$, the unused term being set to zero. In some cases it is more convenient to use $xedge$, whilst in other cases vice-versa. Substrate curvature can be incorporated into the model by adding the radius of curvature to the input data file, following the film-specific parameters. The radius of curvature is then read by procedure $CURVEDEF$ (APPENDIX C), and fed into $DIFFCURVE$ (APPENDIX C) to calculate the contribution to dsh made by substrate curvature. The total value of dsh is then calculated in $GENERAL.P$ assuming linear elasticity theory. APPENDIX H7 shows a typical input data file to be read by $STRIPDEF$.

Hence, a method has been devised to combine the strain equations (6.7) and (6.8) with numerical integration of Takagi's equations, to simulate X-ray section topographs due to surface films on Si substrates.

6.3 Simulation of Experimental Images due to Oxide Film Edges

6.3.1 Introduction

In order to test the reliability of the strain code derived in the previous section, procedure $DIFFSTRIP$ (APPENDIX G) was used in conjunction with $GENERAL.P$ (APPENDIX A) to simulate some of the section topographs obtained experimentally

by Ando et al. [154]. They studied a (001) oriented Si single crystal of thickness 1.33mm, using $AgK_{\alpha 1}$ radiation in the 220 reflection, illustrated in APPENDIX I5. The surface of the substrate was thermally oxidised and the resulting oxide film was etched away except for a square island, Fig. 6.4. Initially, section topographs were taken at approximately position D, Fig. 6.4, where the orientation of the diffracting planes is indicated by the line AA'. Section topographs taken for a number of film/substrate geometries showed characteristic hook-shaped fringes in the regions associated with the film edge. In a previous work [153], Patel and Kato found a direct proportionality between the force, S, per unit length along the edge and the film thickness, t. This relationship is illustrated in Fig. 6.5. For the experimental case described by Fig. 6.4, the film thickness was 5,100$\AA$ and the associated S-value was $200Nm^{-1}$.

6.3.2 Results

Ando et al. [154] obtained section topographs for the S-value quoted above and for the film/substrate geometry of Fig. 6.2, with values of δ of 30° and 60°. The values of S, δ and the film and crystal dimensions quoted by Ando et al. [154] for their experiment, were fed into the simulation program of section 6.2, and the resulting simulations are compared with the topographs of Ando et al. in Fig. 6.6. Figs. 6.6(a) and (b) correspond to the $\delta = 30°$ and 60° cases, respectively.

In generating the simulations of Fig. 6.6, the substrate was assumed to be bent, with a uniform radius of curvature of 20m, consistent with experimental measurements [163] of industrially processed wafers. Clearly, this assumption is simplistic, since the film only covers part of the substrate, however the approximation is good in the region of interest, close to the film edge. Fig. 6.4 is drawn to scale from the original due to Patel and Kato [153]. The separation, H, in the x-direction of opposite edges is 3.3mm and the topographs were taken so that essentially only one edge was imaged. The value of *yedge* was selected so as to give a centralised image with respect to the simulation frame and, of course, *zdispl* was set to zero for the entrance surface. The horizontal integration step, *horiz*, was set to $0.29\mu m$.

Very good agreement was obtained between simulation and experiment, both in the shape and position of direct and dynamical images and also of the Pendellösung fringes. These are extremely sensitive to the phase changes induced by the strain at the film boundary and, as Patel and Kato pointed out [153], provide a sensitive test of the model. The value of the force, S, per unit length at the film edge of $200Nm^{-1}$ used in the simulations of Fig. 6.6 is exactly that used by Ando et al. [154] in their eikonal model fits to experimental data. On the basis of these results, it may be concluded that Blech and Meieran's equations [143] can be used satisfactorily for simulations based on Takagi's theory of diffraction in distorted crystals.

There is no trace in the simulations of Figs. 6.6(a) and (b) of the additional fringes reported by Epelboin [161]. However, Epelboin commented that the visibility and extent of the additional fringes depends on the value of force per unit length, S, along the edge. For the value of S equal to $200Nm^{-1}$ used in the simulations of Fig. 6.6, Epelboin found that the additional fringes were only just visible. The

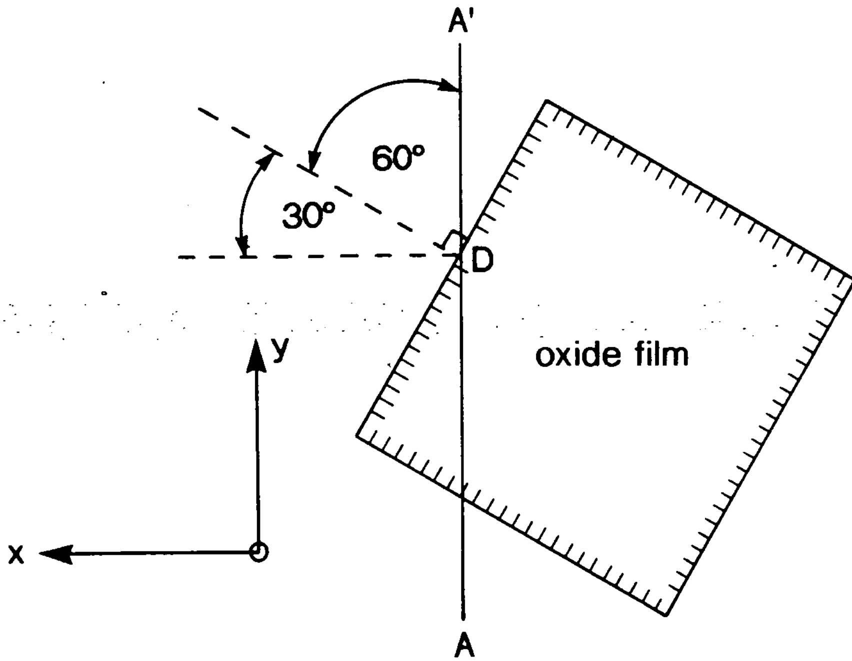

Fig. 6.4: Film/substrate geometry of Ando et al.

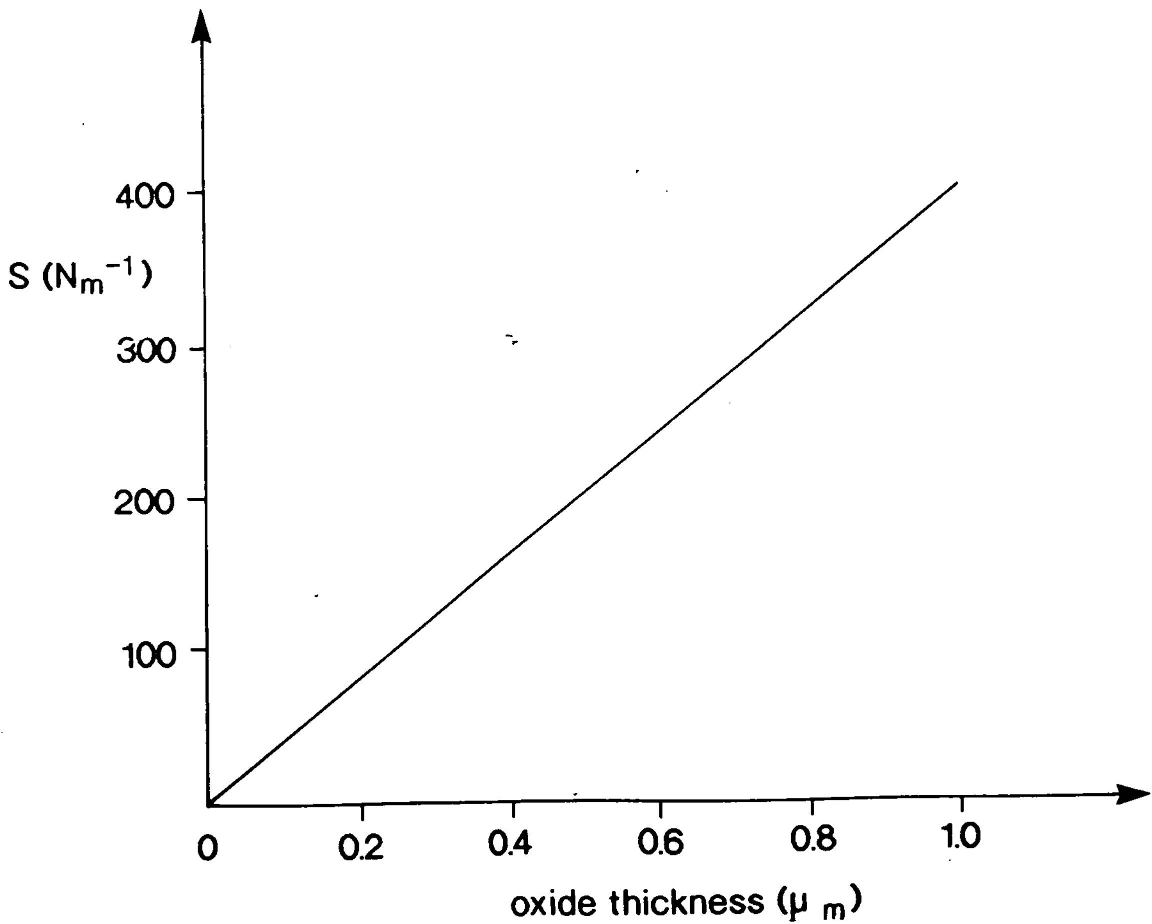

Fig. 6.5: Force per unit length, S, as a function of oxide film thickness, (after Patel and Kato).

220

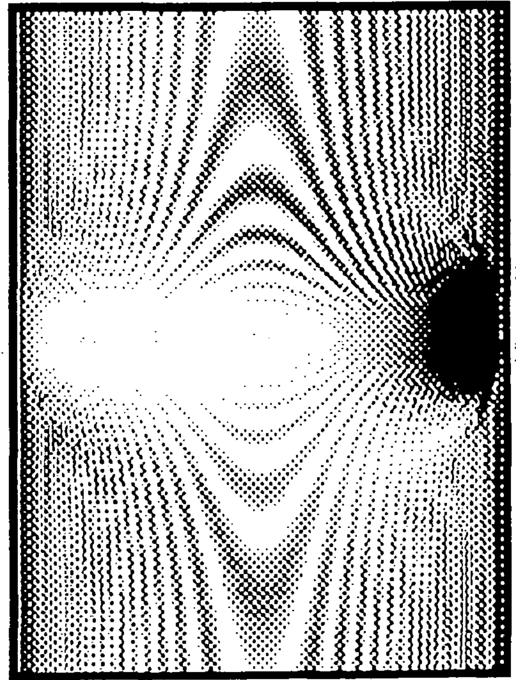

(a) 30°

200μm

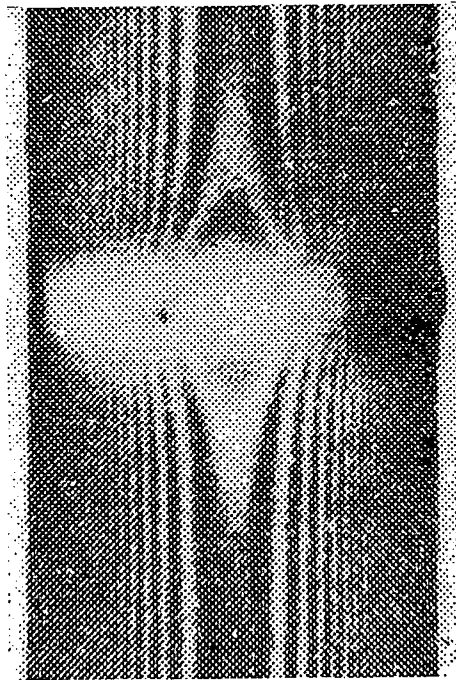

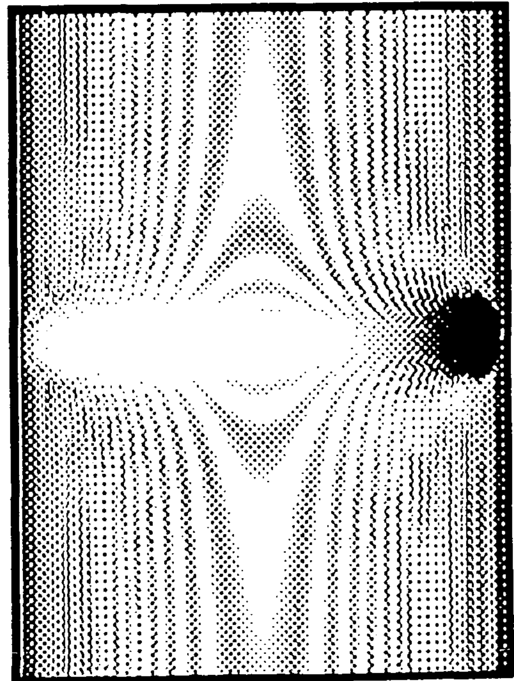

(b) 60°

experiment

simulation

Fig. 6.6: Simulation vs. experimental section topographs of an oxide film on a silicon substrate for two values of the orientation, δ, of the film edge normal to the experimental x-axis. Topographs obtained by Ando et al., for a (001) oriented, 1330μm thick silicon substrate, imaged in the 220 reflection with AgK_{α_1} radiation.

positions and form of the extra fringes found by Epelboin are indicated schematically in Fig. 6.7. The simulation of Fig. 6.6(a), for $\delta = 30°$, was repeated for a much higher S-value of $800Nm^{-1}$, and the resulting simulation is shown in Fig. 6.8(a). The horizontal and vertical integration steps of Fig. 6.8(a) were taken as $2\mu m$ and $0.59\mu m$, respectively. It is immediately obvious that the hook-shaped fringes are closer together and narrower, resulting from the increased strain at the film edge. Also, the additional fringes are just discernible, in the form and positions predicted by Epelboin [161], Fig. 6.7. Retaining the same value of S equal to $800Nm^{-1}$, the vertical and horizontal integration steps were reduced to $1\mu m$ and $0.29\mu m$, respectively. The resulting simulation is shown in Fig. 6.8(b). One set of additional fringes is visible at the left-hand edge of the image frame, in approximately the position predicted by Epelboin, shown in Fig. 6.7. However, the overall visibility of these fringes is not significantly enhanced by decreasing the horizontal integration step from $0.59\mu m$ to $0.29\mu m$. This will be discussed shortly. From Fig. 6.8, it is seen that reduction in the integration step results in a decrease in the spacing of adjacent hook-shaped interference fringes. The edge-induced strain giving rise to the fringes in Fig. 6.8 is exceptionally high ($S = 800Nm^{-1}$), resulting in extremely rapid spatial variation of the wave amplitudes in the crystal. The results suggest that in order to accommodate this very rapid variation, the horizontal integration step should be reduced to a value considerably lower than $0.59\mu m$, used in Fig. 6.8(a). However, the fact remains that for the physically realistic S-value of $200Nm^{-1}$, excellent matching was obtained between the fringes in experimental and simulated images, without recourse to an ultra-fine integration net. Furthermore, the results of section 6.4.3 indicate that for physically realistic edge-induced strains, the image structure in simulations shows a convergence with decreasing integration step, which is already established for the step sizes used in Fig. 6.8.

6.3.3 Discussion

The strain code *DIFFSTRIP* and the integration code *GENERAL.P* have been used to simulate section topographs due to oxide films on Si single crystals. Particularly pleasing is the good matching between the position and form of the Pendellösung fringes of the experimental and simulated images. These fringes are particularly sensitive to the phase changes induced by the strain at the film edge. In addition, the value of force per unit length, S, of $200Nm^{-1}$ used in the simulations here is exactly that used by Ando et al. [154] in their eikonal model fits to the experimental data.

The additional fringes of Epelboin have been found in the simulations here, in the positions and form predicted by Epelboin [161], but only for very high strains ($S \sim 800Nm^{-1}$) and for a fine integration step ($TRANSV \leq 0.59\mu m$). Epelboin commented that the additional fringes were only just visible for S equal to $200Nm^{-1}$ and were much more clearly defined for S equal to $400Nm^{-1}$. Epelboin proposed a strain-relaxation mechanism to explain the absence of these additional fringes in experimental section topographs. However, the results of this work suggest that the S-values used by Epelboin to generate his simulations were too high. Excellent matching of simulations with experimental images in Fig. 6.6 was possible for an

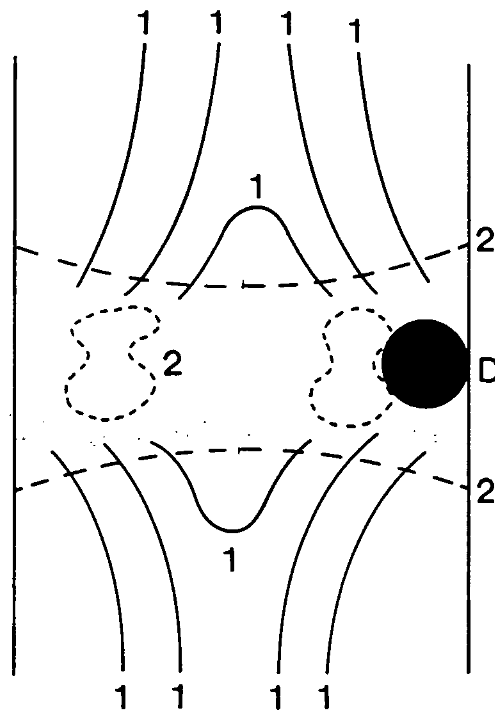

Fig. 6.7: Schematic representation of the positions of the extra fringes visible in the simulations of Epelboin, for very high values of edge strain, (after Epelboin).
D : direct image.
1 : fringes corresponding to interference between curved wavefields.
2 : extra fringes corresponding to interference between newly created wavefields.

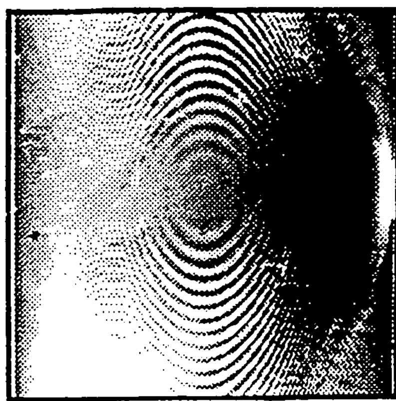

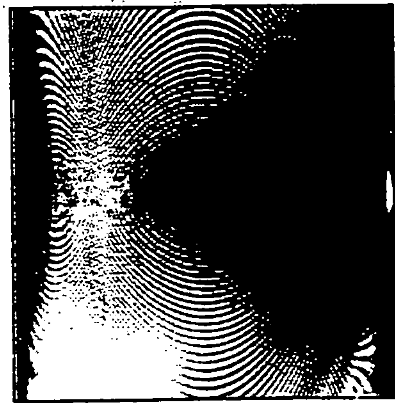

220

(a) $TRANSV = 0.59\mu m$ (b) $TRANSV = 0.29\mu m$

$100\mu m$

Fig. 6.8: Simulations for high film edge strain ($S = 800Nm^{-1}$), for horizontal integration step, $HORIZ$, equal to $0.59\mu m$ and $0.29\mu m$, showing the extra fringes reported by Epelboin.

S-value of $200Nm^{-1}$, in agreement with the results of Ando et al. [154], without any need for artificial strain relaxation at the film edge.

All of the simulations in Figs. 6.6 and 6.8 were generated assuming a photographic resolution of 1 - $2\mu m$, consistent with experimental topography. The visibility of the additional fringes did not increase appreciably as a result of decreasing the horizontal integration step from $0.59\mu m$ to $0.29\mu m$. The fact that the additional fringes of Epelboin have not been reported in experimental topographs may be due to statistical noise reducing the visibility of the fringes, or the absence of experiments on films sufficiently thick to show such an effect clearly.

6.4 Simulation of Images due to a Device on a Silicon Substrate

6.4.1 Introduction

The contrast of diffused device structures on a Si substrate has recently been investigated by Loxley [163]. He examined the contrast in X-ray section topographs, taken with MoK_{α_1} radiation in the $\bar{4}40$ reflection, associated with $50\mu m$ wide devices on the exit surface of a $500\mu m$ thick, (001) oriented Si wafer. The reflection geometry is illustrated in APPENDIX I2. In particular, he studied the effect on image structure of device position relative to the Borrmann fan base.

6.4.2 Results

Loxley recorded topographs for four device positions relative to the Borrmann fan base, illustrated schematically in Fig. 6.9. The corresponding experimental images, and their simulations, are also shown in Fig. 6.9. The simulations were generated using the experimental parameters stated above. The terms δ, $horiz$ and $zdispl$ were assigned values of 0°, $50\mu m$ and $500\mu m$ respectively. The value of $xedge$ was adjusted to alter the position of the device relative to the Borrmann fan base. The characteristics of the experimental and simulated images are in good agreement for a value of S equal to $30Nm^{-1}$. It is interesting to compare this with the S-value of $35Nm^{-1}$ used by Petrashen and Shulpina [156] to obtain experiment-simulation matching for devices constructed by boron doping of Si.

As the device moves into the direct beam, Fig. 6.9(b), from a point just outside the Borrmann fan, Fig. 6.9(a), the direct image width increases to a maximum. When the device lies inside the Borrmann fan, its outer edge just touching the direct beam, Fig. 6.9(c), the direct image extends to roughly the same distance from the edge of the section as in (b), but contrast is now absent at the extreme left-hand edge. When the device lies inside the Borrmann fan, far from the direct beam, Fig. 6.9(d), there is no longer any clear direct image. This is because the effective misorientation in the direct beam path is so small that X-rays outside the dynamical diffraction range, which form the direct image, are not diffracted.

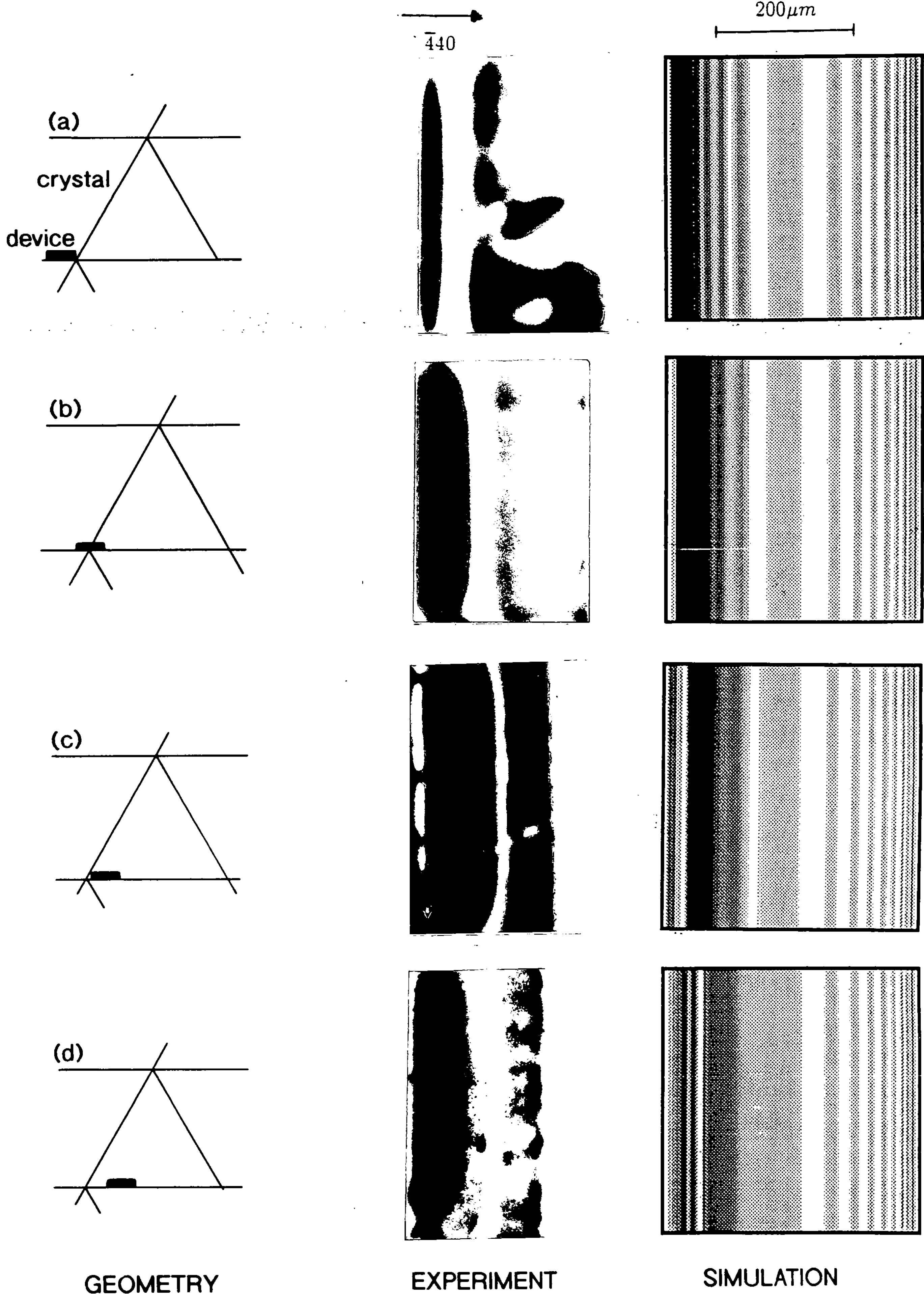

Fig. 6.9: Simulation of experimental section topographs obtained by Loxley for several different positions of device on the exit surface relative to the Borrmann fan base. Topographs were taken using MoK_{α_1} radiation in the $\bar{4}40$ reflection.

6.4.3 Convergence Criteria

In the work above, and in the investigations of the following sections, conclusions are drawn from the relative sizes and positions of direct images in simulations. Epelboin [58,59] has commented that a varying step algorithm (V. S. A.) must be used in order to accurately simulate direct images in X-ray topographs. The reason for this is that the integration step in a V. S. A. is chosen throughout the Borrmann fan to suit the local variation in wave amplitudes. However, if the integration step in a constant step algorithm (C. S. A.) is made sufficiently small, then the same accuracy should be attainable. The only drawback is then the correspondingly increased computation time of the C. S. A. Of course, the integration program $GENERAL.P$ (APPENDIX A), used in this thesis, is based on a C. S. A. Consequently, it is important to verify the convergence of the results for direct image widths and positions with decreasing integration step size. The vertical and horizontal steps, $ELEM$ and $TRANSV$, used to generate the simulations of Fig. 6.9 were $3.0\mu m$ and $2.39\mu m$, respectively. Fig. 6.10 shows repetitions of Fig. 6.9(a) with all parameters the same except for the integration step, $ELEM$, which was allowed to decrease from the original value of $3\mu m$ to a value of $0.5\mu m$. The overall image structure remains almost identical, and the direct image width as measured on the simulation is 10mm in each case. Hence, the results indicate a convergence of direct image width, which is already established at the value of $ELEM$ of $3\mu m$ used in the simulations of Fig. 6.9. In addition to the above observations, it is interesting to note the extra detail at the edges of the simulations of Fig. 6.10 with increasing resolution. Enhanced resolution allows the simulation program to follow more effectively the rapid spatial variation in the wavefields close to the Borrmann fan edges.

It is known that the size of the direct image of a defect depends on the photographic response of the recording film. The response is characterised by the density of grey levels, D, and the illumination, E, defined by:

$$\begin{aligned} E &= It, \\ \text{where } I &= \text{intensity of source radiation,} \\ \text{and } t &= \text{exposure time.} \end{aligned}$$

The relation between D and E is effectively linear, except at saturation where the D vs. E curve flattens out, as expected. Various D vs. E dependences have been proposed, and the linear relation between D and E quoted above has been adopted in the current work. For each simulation, the gradient of the D vs. E curve is calculated by the photo-representation program, according to the properties of the commonly used Ilford L4 Nuclear Emulsion. However, the direct image derives precisely from the non-linear D vs. E domain at saturation. An important question is then defined as to the reliability of the results of Fig. 6.9 with respect to variation in photographic response. The reliability can be tested by taking several values of D for the same E-value and determining whether or not the conclusions from the resulting simulations agree. This test has been arranged by the simple expedient of altering the *conversion gradient* of the assumed linear relation between D and E, in order to obtain several grey densities for the same illumination. In Fig. 6.10, the

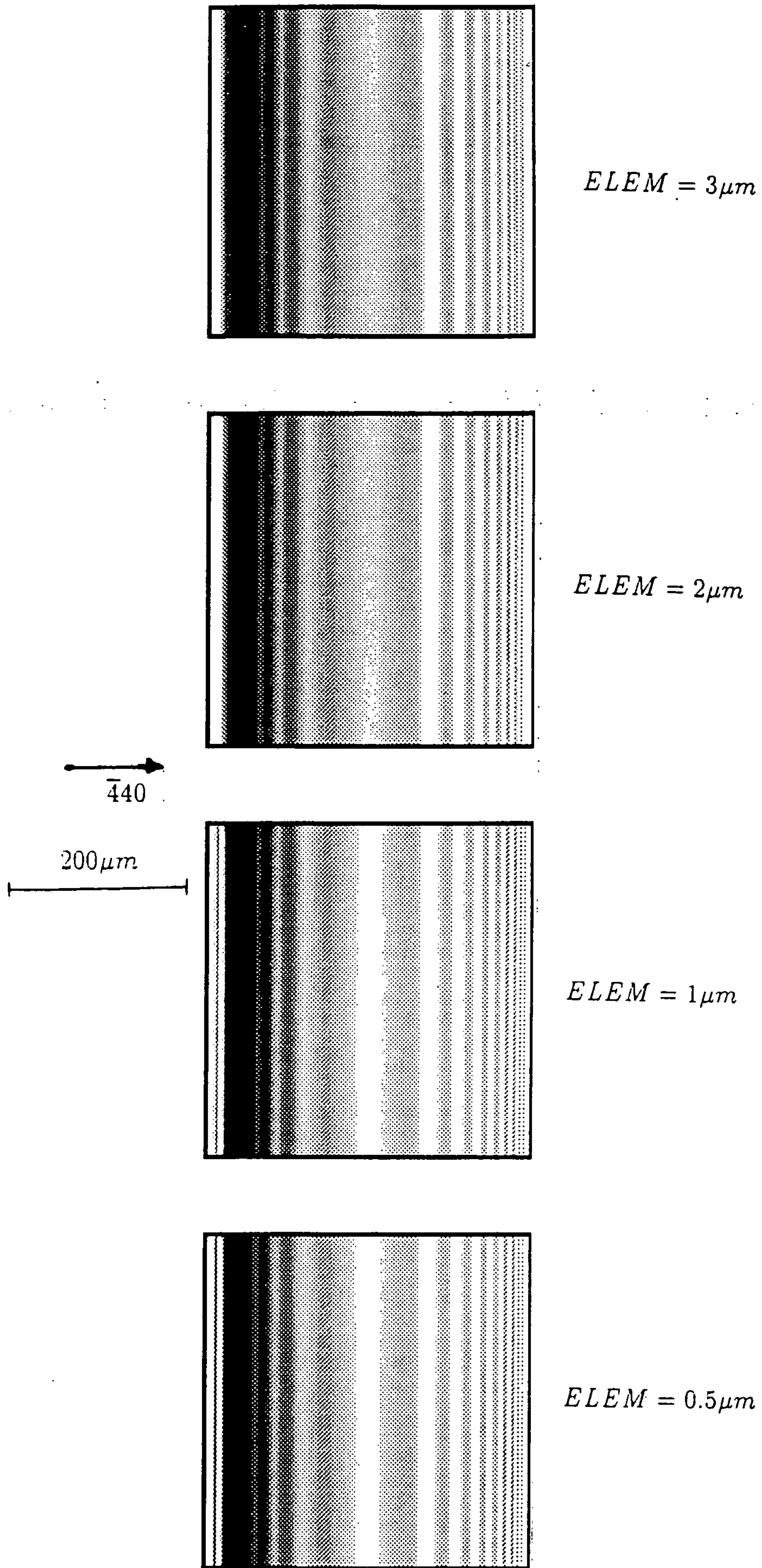

Fig. 6.10: Repetition of the simulation of Fig. 6.9(a), for decreasing vertical integration step, $ELEM$.

Conversion gradient	Δ_{conv}, (mm on simulation)
0.3	7
0.5	10
1.0	14

Table 6.1: Convergence values of direct image width, Δ_{conv}, for different photographic responses.

conversion gradient took the default value of 0.51. The results of the first part of the test are illustrated in Fig. 6.11 for the same resolutions as in Fig. 6.10, but for two different conversion gradients. For each value of conversion gradient, convergence of the direct image width, Δ, was observed to have taken place already at the value of $ELEM$ equal to $3\mu m$, although the absolute values of Δ were different for each photographic response. The convergence values of Δ from Figs. 6.10 and 6.11 are displayed in Table 6.1. The important conclusion here is that the step size at which convergence occurs is independent of photographic response, despite the difference in absolute values of direct image width.

The second part of the photographic test involves repeating the simulations of Fig. 6.9(a)-(d) for different conversion gradients. Fig. 6.12 shows repetitions of Figs. 6.9(a)-(d) with gradients 0.4 and 0.7, to compare with the default value used in Fig. 6.9. For a gradient of 0.4, the direct image is noticeably fainter than previously, but it is seen that all the comments made in section 6.4.2 concerning the relative widths and positions of direct images are still applicable. The images for a conversion gradient of 0.7 show much heavier contrast, indicating a high level of saturation, but the same comments as above still apply.

The important conclusion here is that the trend for relative sizes and positions of direct images is independent of photographic response. This has been demonstrated for a wide range of responses, right up to heavy saturation of the recording film.

6.4.4 Conclusions

In section 6.4.2, the strain code of $DIFFSTRIP$ (APPENDIX G) together with the integration program $GENERAL.P$ (APPENDIX A) were used to simulate the experimental results of Loxley [163] for diffused device regions on the exit surface of a Si crystal. The same relative trends in direct image widths and positions were observed in both experiment and simulation. In addition, the S-value of $30Nm^{-1}$ for best matching was very similar to the value of $35Nm^{-1}$ found by Petrashen and Shulpina [156] for similar studies of boron diffused device regions on Si. One must not pay too much attention to this similarity, since device-induced strain is influenced by several different physical factors, but as an order of magnitude comparison it is interesting.

The work of the following sections will be concerned with relative sizes and positions of direct images, rather than absolute values of these quantities. The results

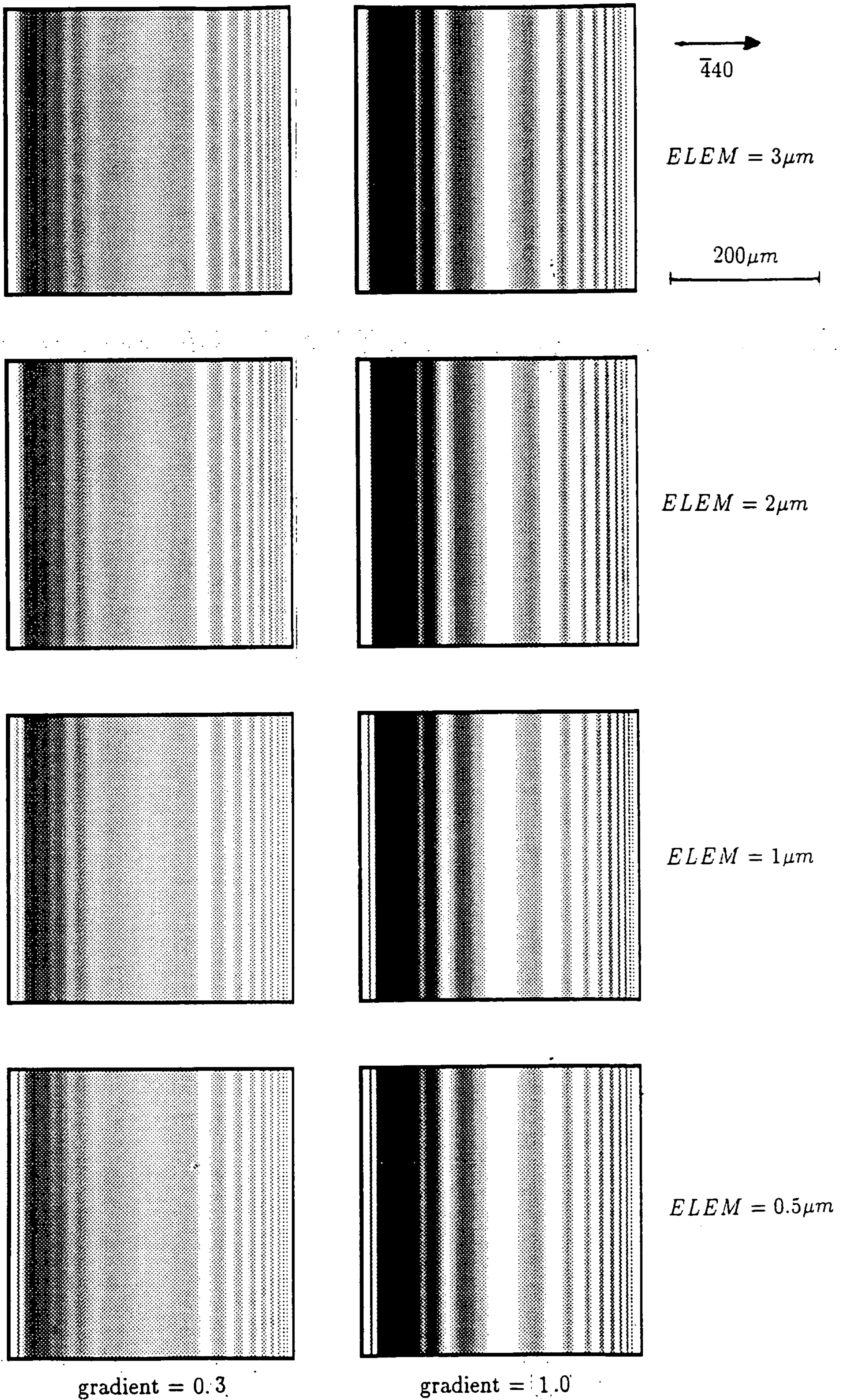

Fig. 6.11: Repetition of the simulations of Fig. 6.10, for two different photographic responses, characterised by the conversion gradient used to convert from X-ray illumination into grey density on the film.

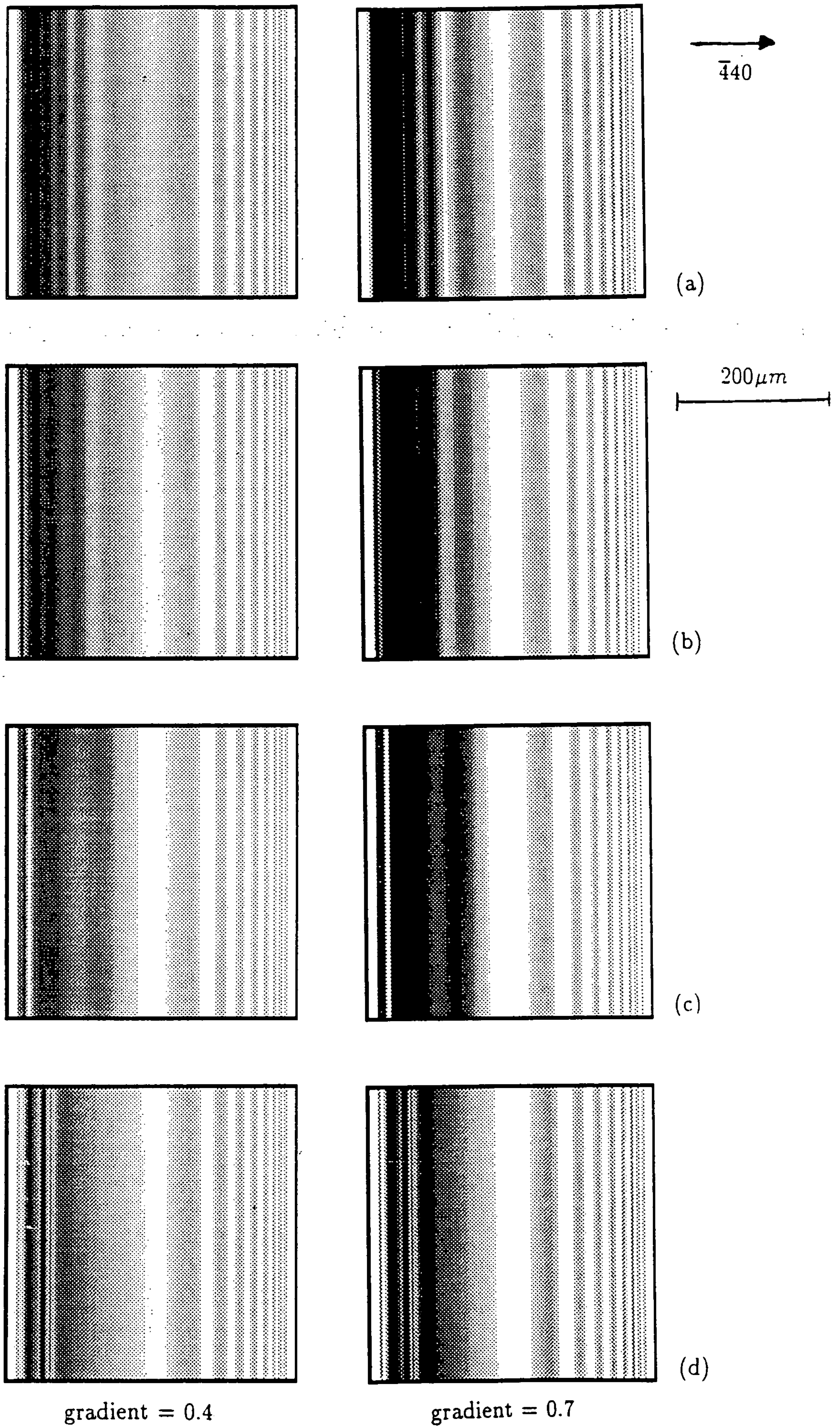

Fig. 6.12: Repetition of the simulations of Figs. 6.9(a)-(d), for two different photographic responses, characterised by their conversion gradients.

of section 6.4.3 indicate that trends in these relative quantities are independent of horizontal integration step below $2.39\mu m$, and of the photographic response of the recording film. The latter conclusion was found to be true across a wide range of photo-responses, right up to heavy saturation of the recording film.

6.5 Image Structure for Devices on the Entrance and Exit Surfaces

6.5.1 Statement of Method

Having established the reliability of the integration code, *GENERAL.P*, and the photo-response code, these have been used to study the variation in image structure with device position.

Consider Fig. 6.13, which shows six possible positions of device on the entrance and exit surfaces. The device edges were taken to be perpendicular to the planes of incidence, so that δ was set to zero. The device width and crystal thickness were taken to be $50\mu m$ and $500\mu m$, respectively. Simulations were performed, for each of the positions (a)-(f) in Fig. 6.13, and the correspondng images are presented in Figs. 6.14(a)-(f), respectively. AgK_{α_1} radiation was assumed, in the 220 reflection, and the edge-induced strain was characterised by an S-value of $200Nm^{-1}$. The vertical and horizontal integration steps were $5\mu m$ and $1.5\mu m$, respectively. The corresponding perfect crystal simulation is shown at the bottom of Fig. 6.14.

6.5.2 Position (a)

The crystal distortion is strongest immediately to the left of the left-hand edge of the device, so that strong diffraction occurs from a region around the top vertex of th Borrmann fan. This is why the direct image is seen at the extreme right-hand side of the simulation.

6.5.3 Position (b)

The strain effect of the left-hand edge is predominantly outside the Borrmann fan. The strain induced by the right-hand edge is localised to the left-hand central section of the lower part of the fan, with comparatively little distortion at the bottom left-hand corner. For this reason, the direct image is quite narrow and there is a region of lighter contrast at the extreme left-hand edge of the simulation frame.

6.5.4 Position (c)

Neither edge of the device is as close to the direct beam as the left-hand edge was in position (a). Hence, the distortion in the apex of the Borrmann fan is less

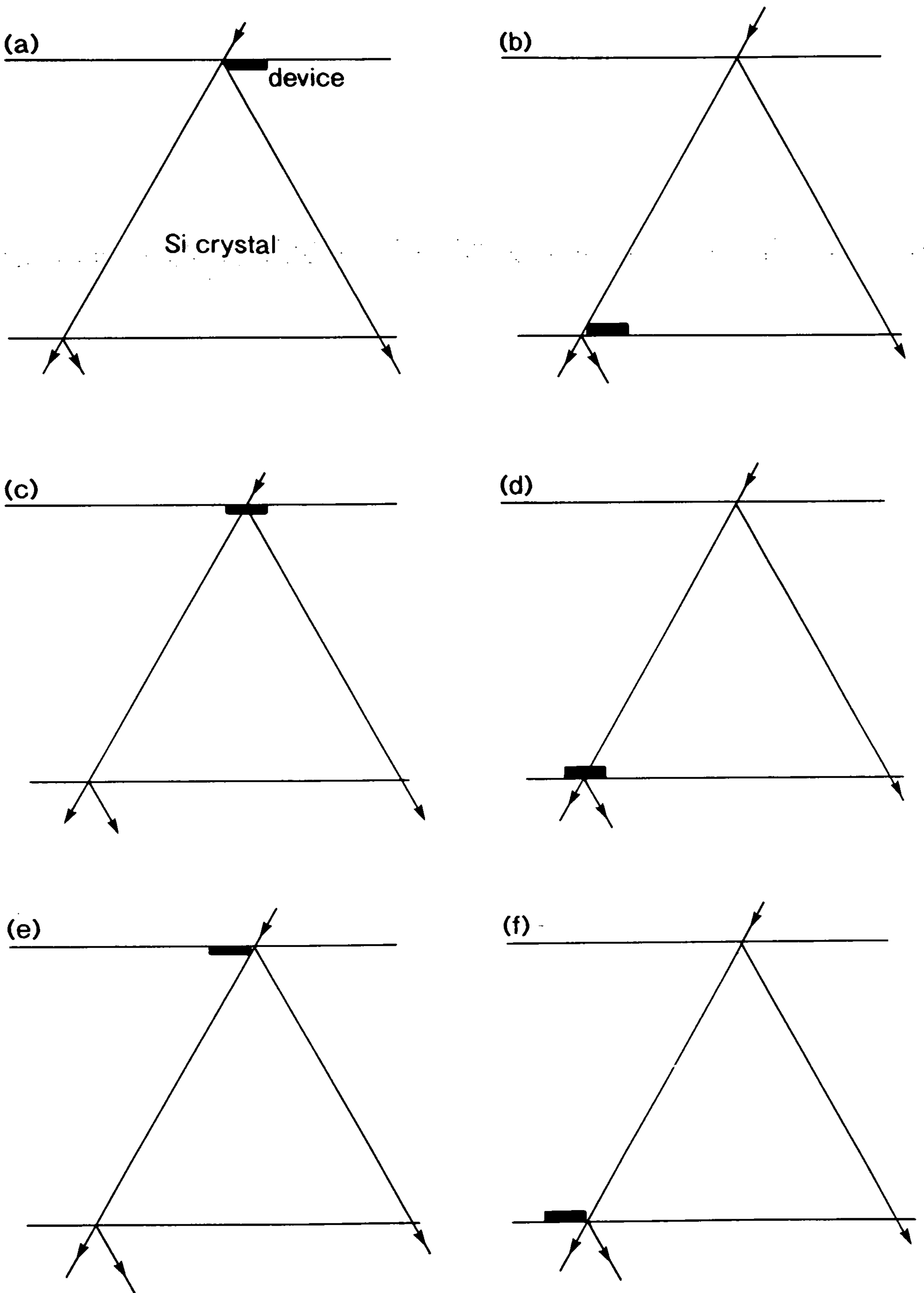

Fig. 6.13: Six possible positions of device on the entrance and exit surfaces.

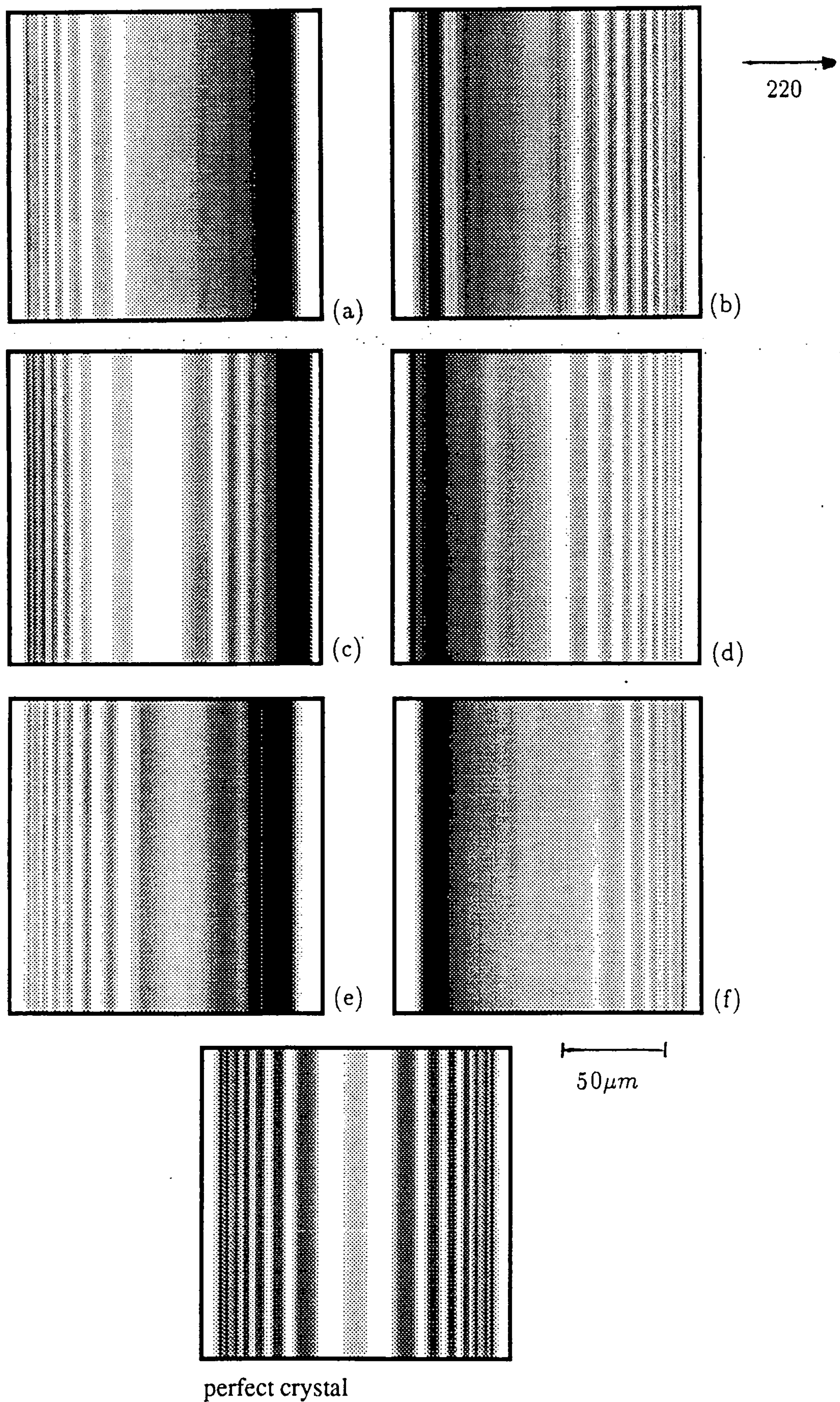

Fig. 6.14: Simulations corresponding to the positions of device illustrated schematically in Figs. 6.13(a)-(f), respectively. The device width and crystal thickness were set to $50\mu m$ and $500\mu m$, respectively, and AgK_{α_1} radiation in the 220 reflection was assumed.

pronounced and less extensive than in case (a). This is the reason why the direct image is narrower, and the rest of the Borrmann fan is less influenced by strain-induced diffraction, than in case (a).

6.5.5 Position (d)

The situation is similar to case (b), since the right-hand edge induces the distortion giving rise to the direct image. However, in this case, the right-hand edge is closer to the direct beam than in case (b), and the direct image is correspondingly wider, whilst the rest of the Borrmann fan is less affected by strain-induced diffraction, than in case (b). In addition, the heavy distortion is closer to the bottom left corner of the fan than in case (b), so that the area of comparatively light contrast at the left-hand edge of the simulation is narrower than in case (b).

6.5.6 Position (e)

The situation is physically similar to case (a), although it is now the right-hand edge which induces strain around the top vertex of the Borrmann fan, resulting in a direct image localised to the extreme right-hand side of the simulation frame.

6.5.7 Position (f)

The distortion is confined to the bottom left corner of the Borrmann fan, so that the direct image is localised to the left-hand edge of the image frame. From simulations (b), (d) and (f), it is noticeable how the influence of strain-induced diffraction within the whole Borrmann fan reduces progressively as the right-hand edge is shifted, relatively, towards the periphery of the fan.

6.6 Distinguishability of Devices in X-ray Section Topography

6.6.1 Introduction

Unlike extensive oxide films, which can be considered semi-infinite, most devices are comparable in size to the X-ray extinction distance and the base width of the Borrmann fan. Current semiconductor technology requires the production of devices of the order of $1\mu m$ in size [164]. The edges of a device induce opposite strains in the underlying substrate, so that for a narrow device the total strain tends to zero. Hence, the possibility exists that the region of distortion due to a narrow device is so small that its presence is not manifested on X-ray topographs. The purpose of the current section is to examine the size of device at which this cancelling effect becomes significant, and to determine how the distinguishability of a device depends on its associated strain.

6.6.2 Results

Fig. 6.15(a) shows a device of width H in the experimental x-direction equal to $150\mu m$, where the inclination δ is equal to 60°. The corresponding simulated X-ray section topograph, taken assuming AgK_{α_1} radiation in the 220 reflection, with a source slit width of $5\mu m$, is shown in Fig. 6.15(b). The value of force per unit length, S, along the edge was taken as $200Nm^{-1}$.

Two distinct images are visible in Fig. 6.15(b), corresponding to the two edges of the device. There is a partial reversal of contrast, black to white, between parts of the images, resulting from the opposite directions of strain at the two edges.

The perpendicular separation, W, of the device edges is, of course, the real device width, and is given by:

$$\begin{aligned} W &= H\cos\delta, \\ &= H/2, \end{aligned}$$

for the geometry of Fig. 6.15(a). Fig. 6.16 shows a series of simulations for an S-value of $500Nm^{-1}$, over a range of values of W much smaller than that used in Fig. 6.15. For a device width, W, of $3\mu m$, the image shows two clearly identifiable contributions, equivalent to the images of Fig. 6.15(b). However, upon reducing the device width further, these two edge contributions become successively less distinguishable. It is seen that for a device width, W, less than about $1\mu m$, the image due to the device is effectively indistinguishable from the Pendellösung fringes. Hence, the minimum device width for distinguishability is $1\mu m$ for an S-value of $500Nm^{-1}$.

The resolution of the photo-response program was equivalent to the best attainable resolution in experimental topography. In addition, the simulations of Fig. 6.16 were generated using a horizontal integration step, $TRANSV$, of $0.88\mu m$. It is important that the value of $TRANSV$ be less than the minimum H-value in the investigation. Otherwise, the true strain profile is not revealed by the simulation technique and a false value of minimum detectable device width is obtained.

Fig. 6.17 shows simulations corresponding to the geometry and S-value used in Fig. 6.16, for device width, W, equal to $0.5\mu m$, but for decreasing horizontal integration step, $TRANSV$. It is clear that decreasing the value of $TRANSV$ from $0.88\mu m$ to $0.29\mu m$ makes very little difference to the resulting image. The convergence of image structure is established already for the value of horizontal integration step of $0.88\mu m$ used in Fig. 6.16.

Sets of simulations similar to the one shown in Fig. 6.16, but for different values of force per unit length, S, are shown in APPENDIX L. In each case, a minimum value, W_{min}, of device width for distinguishability was found. The results are summarised in Table 6.2. It was noted that the value of δ equal to 60° consistently gave the most clearly identifiable images, no other orientation giving a lower limit on detectability.

The variation of W_{min} with S is plotted in Fig. 6.18. The minimum detectable device size falls as the lattice deformation within the device, characterised by the parameter S, increases. The dependence of W_{min} on S is asymptotic at values of S greater than about $300Nm^{-1}$, in the particular axperimental conditions chosen.

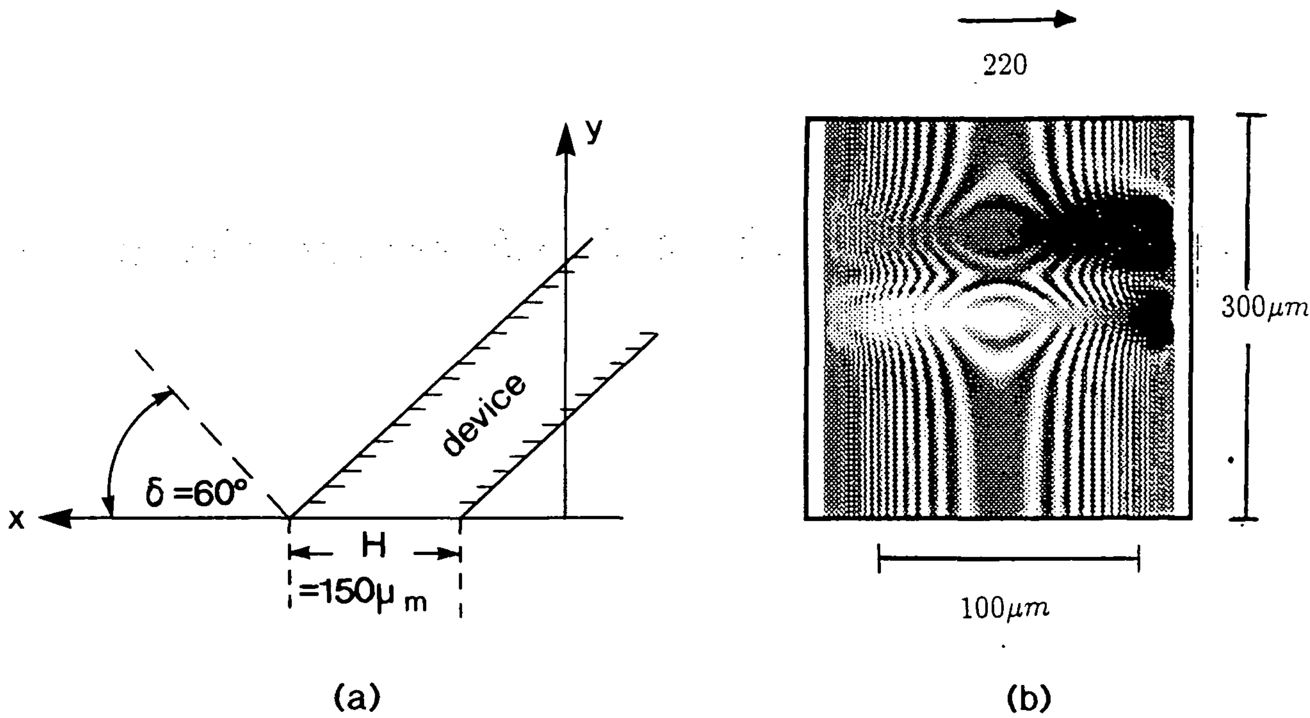

Fig. 6.15: Experimental geometry (a) and simulation (b) for a wide device inclined to the x, y-axes at an angle $\delta = 60°$.

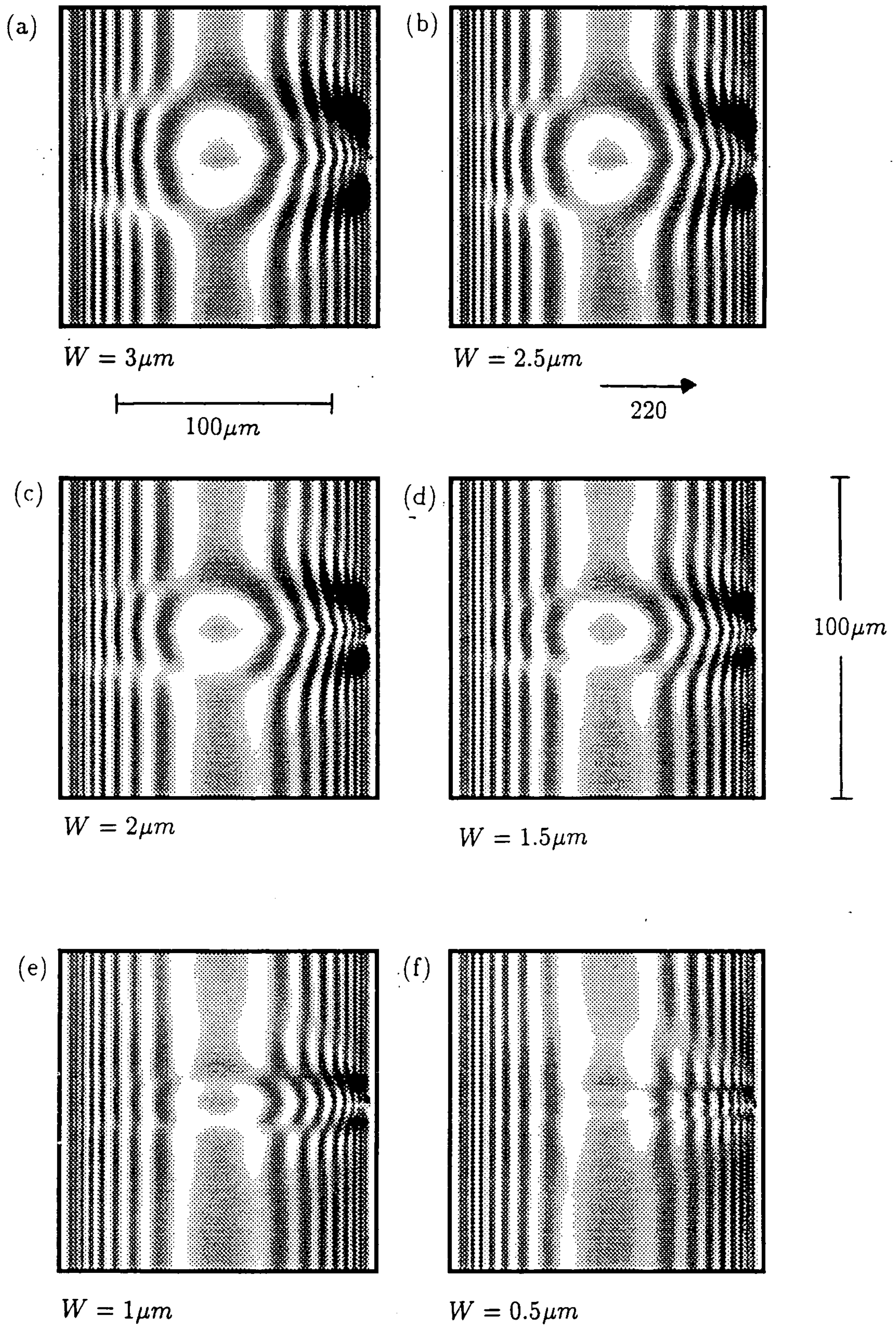

Fig. 6.16: Simulations corresponding to the geometry of Fig. 6.15(a), but for smaller device widths. Here, W is the perpendicular separation of the opposite edges of the device.

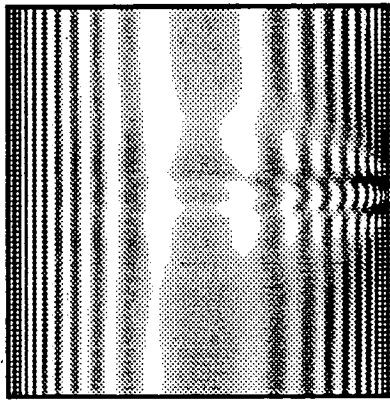

220

$TRANSV = 0.88\mu m$

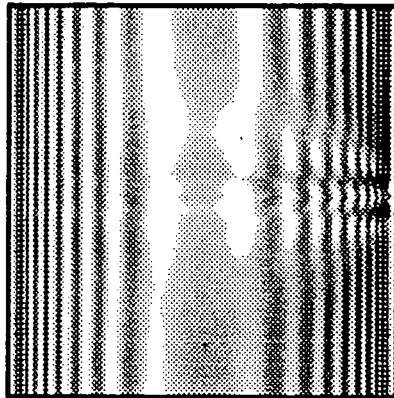

$100\mu m$

$TRANSV = 0.59\mu m$

$100\mu m$

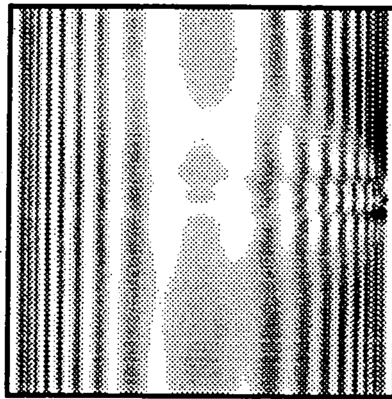

$TRANSV = 0.29\mu m$

Fig. 6.17: Repetition of the simulation of Fig. 6.16(f) for decreasing horizontal integration step, $HORIZ$.

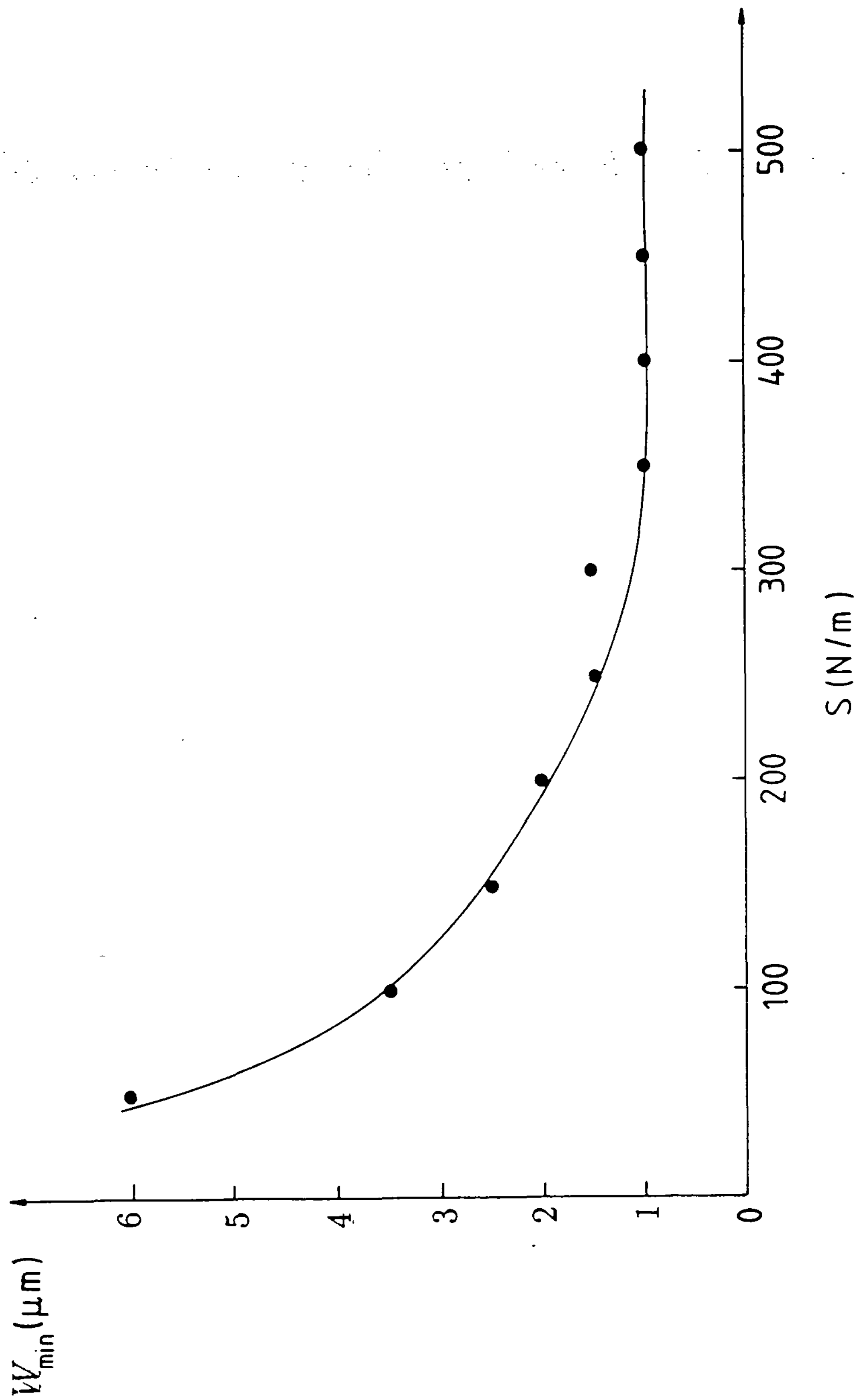

Fig. 6.18: Variation of the minimum device width, W_{min}, for detectability in section topography as a function of force, S, per unit length of device edge.

Force per unit length, $S(Nm^{-1})$	$H_{min}, (\mu m)$	$W_{min}, (\mu m)$
50	12	6.0
100	7	3.5
150	5	2.5
200	4	2.0
250	3	1.5
300	3	1.5
350	2	1.0
400	2	1.0
450	2	1.0
500	2	1.0

Table 6.2: Minimum detectable device width, W_{min}, as a function of device strain.

6.6.3 Discussion

The convergence test of Fig. 6.17 has been used to show that the images of Fig. 6.16 are independent of horizontal integration step, below the value of $0.88\mu m$ used in Fig. 6.16.

The results of Fig. 6.18 indicate that, for the experimental conditions chosen, the minimum detectable device width in section topography is $1\mu m$. However, for S-values characteristic of real solid-state devices (typically $< 100Nm^{-1}$) the minimum detectable device width is greater than $3.5\mu m$, from Fig. 6.18. Consequently, it is clear that the limit on detectable device width, for real devices, is above the limits set by the geometric and other practical constraints of experimental topography. This means that the devices referred to by Dellow et al. [164] would not be visualised on a section topograph. Transmission electron microscopy (TEM) would allow the visualisation of these small-scale devices, but would not provide information on device-induced strain. This will be discussed further in section 6.8.

6.7 Variation in Lattice Distortion with Device-Induced Strain

6.7.1 Introduction

It has already been pointed out that the two edges of a device induce equal and opposite strains in the underlying substrate. For successively narrower devices, the cancelling of the strains due to opposite edges becomes more and more significant. Hence, by using sufficiently narrow devices, it should be possible to minimise the magnitude and extent of device-induced distortion in the substrate. The technological relevance of this is well-defined. Reduction of device-induced distortion inhibits the propagation of misfit dislocations, which in turn increases device yield. The

purpose of the current section is to investigate these effects on a semi-quantitative basis, using the simulation method of the preceding sections.

6.7.2 Results

In the section topograph of a device-edge region, the width of the direct image gives an indication of the size of the heavily distorted *diffracting volume* of crystal in the immediate vicinity of the edge. It is expected that increasing the force per unit length, S, along the edge will increase the size of the distortion and hence the width of the direct image. It is of interest to see how this result is affected by reducing the device width, H.

In section 6.4.3, it was shown that the current simulation process does not allow absolute values of physical quantities to be obtained by measurement of the direct image in simulations. However, it was also found that information can be extracted from the relative sizes of the simulated direct images. In this section, the variation in direct image width, Δ, has been interpreted in terms of the variation in diffracting volume with the parameters S and H.

Consider the device/substrate geometry of Fig. 6.19. The device is located just outside the Borrmann fan, with its right-hand edge just touching the direct beam. The distortion induced in the Si lattice by the two edges is illustrated schematically by the equal effective misorientation contours of Fig. 6.19. Simulations corresponding to this system have been generated assuming an $800\mu m$ thick, (001) oriented Si substrate, imaged in the $\bar{4}40$ reflection, using $MoK_{\alpha 1}$ radiation. The Bragg angle for this case is equal to 21.68°, and the inclination, δ, of the device relative to the experimental x, y-axes was taken as zero. Four sets of simulations have been taken, for devices of width given by H equal to ∞, $50\mu m$, $10\mu m$ and $2\mu m$. The $H = \infty$ case corresponds to an isolated right-hand edge, and was achieved by setting the variable *horiz* to $100{,}000\mu m$ in the input data file. Each set of simulations was taken for S-values of 20, 50, 100, 200, 300 and $400Nm^{-1}$. The four sets of simulations are displayed in Figs. 6.20, 6.21, 6.22 and 6.23. In each case, the direct image is the black band at the left-hand edge of the image frame. The fact that a direct image is visible at all for the $2\mu m$ wide device, for low values of S, might at first seem to contradict the results of Fig. 6.18 for device detectability. However, this is not the case. By simple inspection of the images of Figs. 6.20 - 6.23, it is not possible to attribute these images unambiguously to a device edge, since any line defect would give a similar image structure. The work of section 6.6 was concerned with specific identification of a device by its associated section topograph, and so the results of Fig. 6.18 stand. The widths of the direct images of Figs. 6.20 - 6.23 were measured using a $1mm$ graduated rule. Now, from the geometry of Fig. 6.19, the width of the topograph is $591\mu m$. Also, the simulation frame width is equal to $51mm$. Hence, $1mm$ on the simulation corresponds to $11.6\mu m$ on the topograph. In this way, it was possible to convert the direct image width, Δ, as measured on each simulation, into a corresponding value in μm on the topograph. No physical significance is attached to these absolute values, for reasons already explained, but rather to the relative values within each set. The error bars in Figs. 6.20 - 6.23 reflect the fact that the

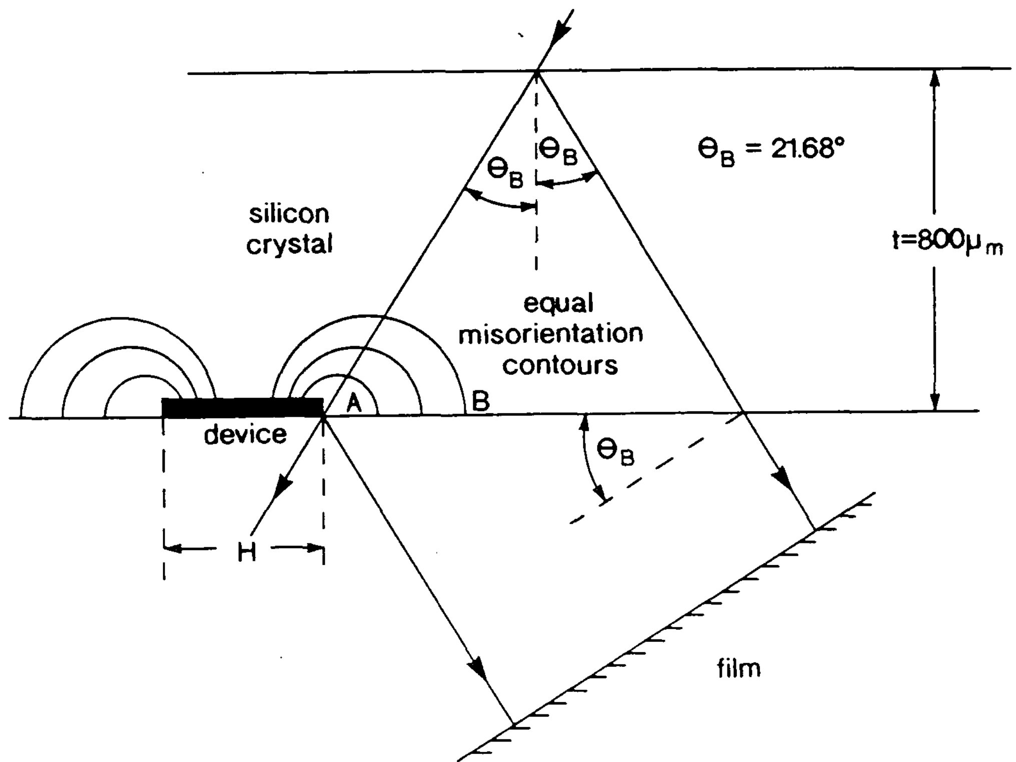

Fig. 6.19: Device/substrate geometry for analytical investigation of device-induced distortion. A (001) oriented, $800\mu m$ thick silicon wafer was assumed, and the $\bar{4}40$ reflection was taken.

$\bar{4}40$

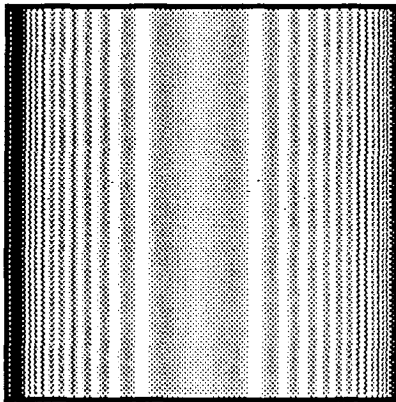

S = 20N/m

300μm

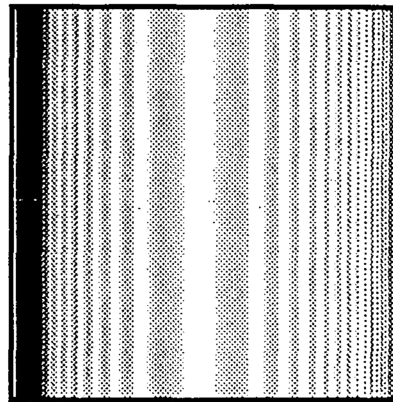

S = 50N/m

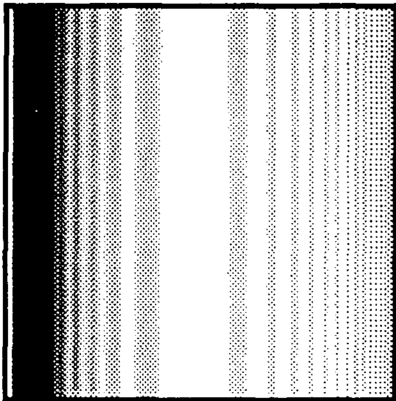

S = 100N/m

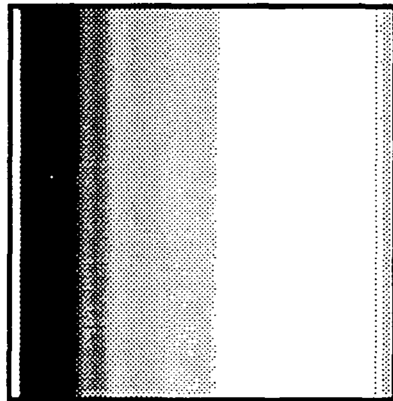

S = 200N/m

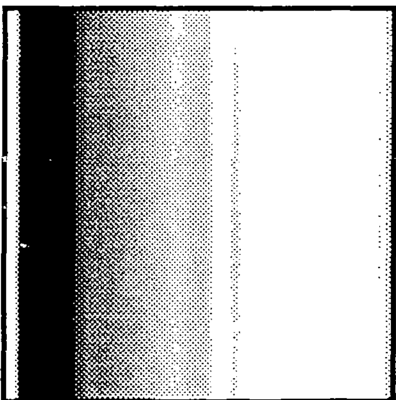

S = 300N/m

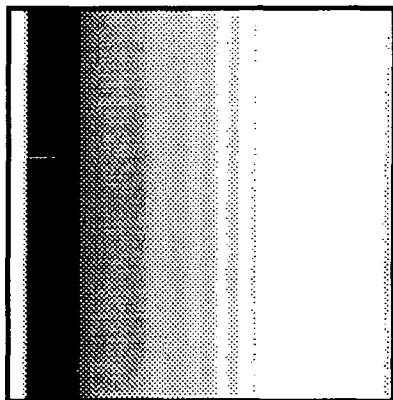

S = 400N/m

Fig. 6.20: Simulations for the system illustrated in Fig. 6.19, for several values of force, S, per unit length of device edge, for an isolated right-hand edge.

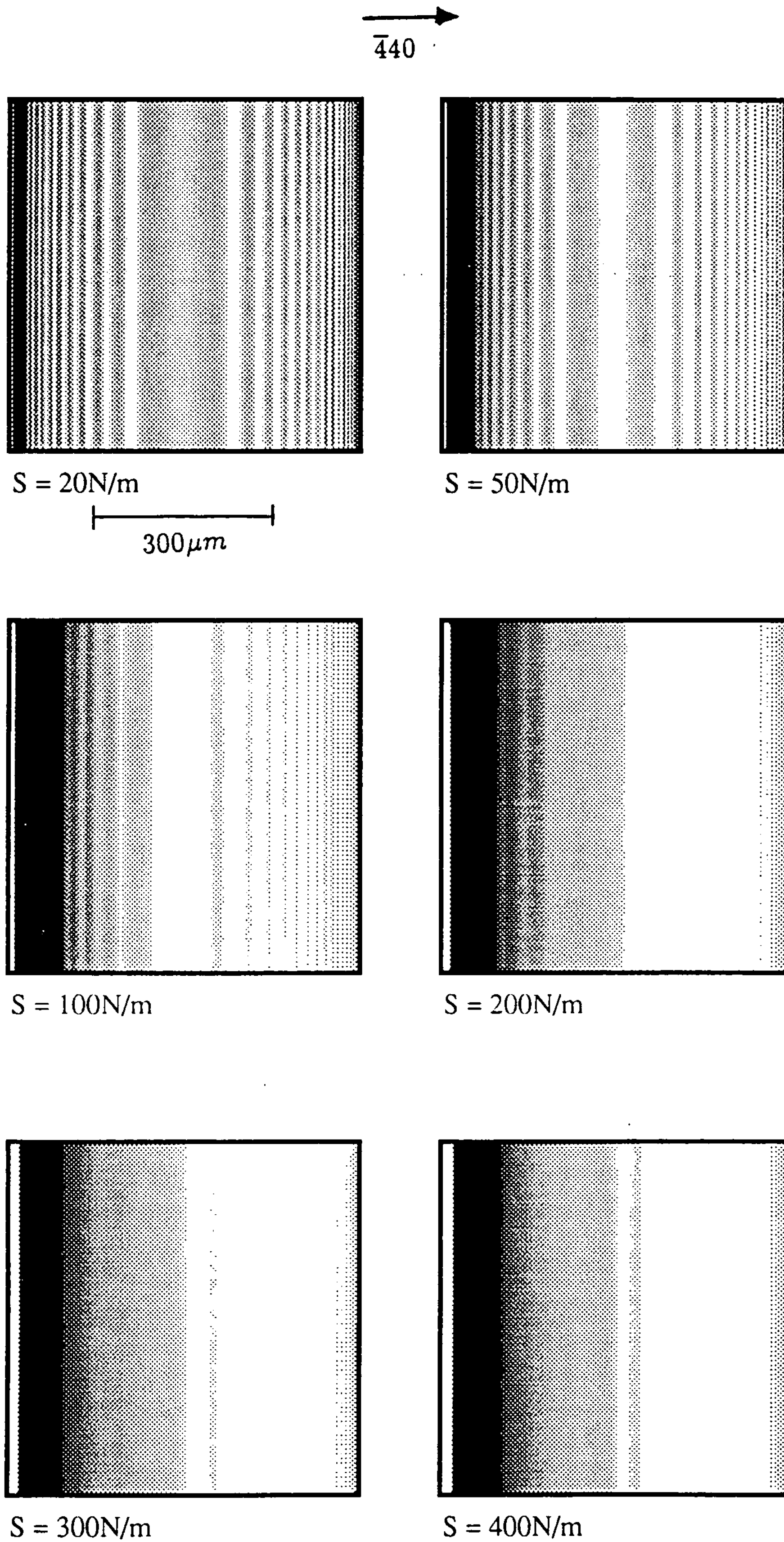

Fig. 6.21: Simulations for the system illustrated in Fig. 6.19, for several values of force, S, per unit length of device edge, for a device of width, H, equal to $50\mu m$.

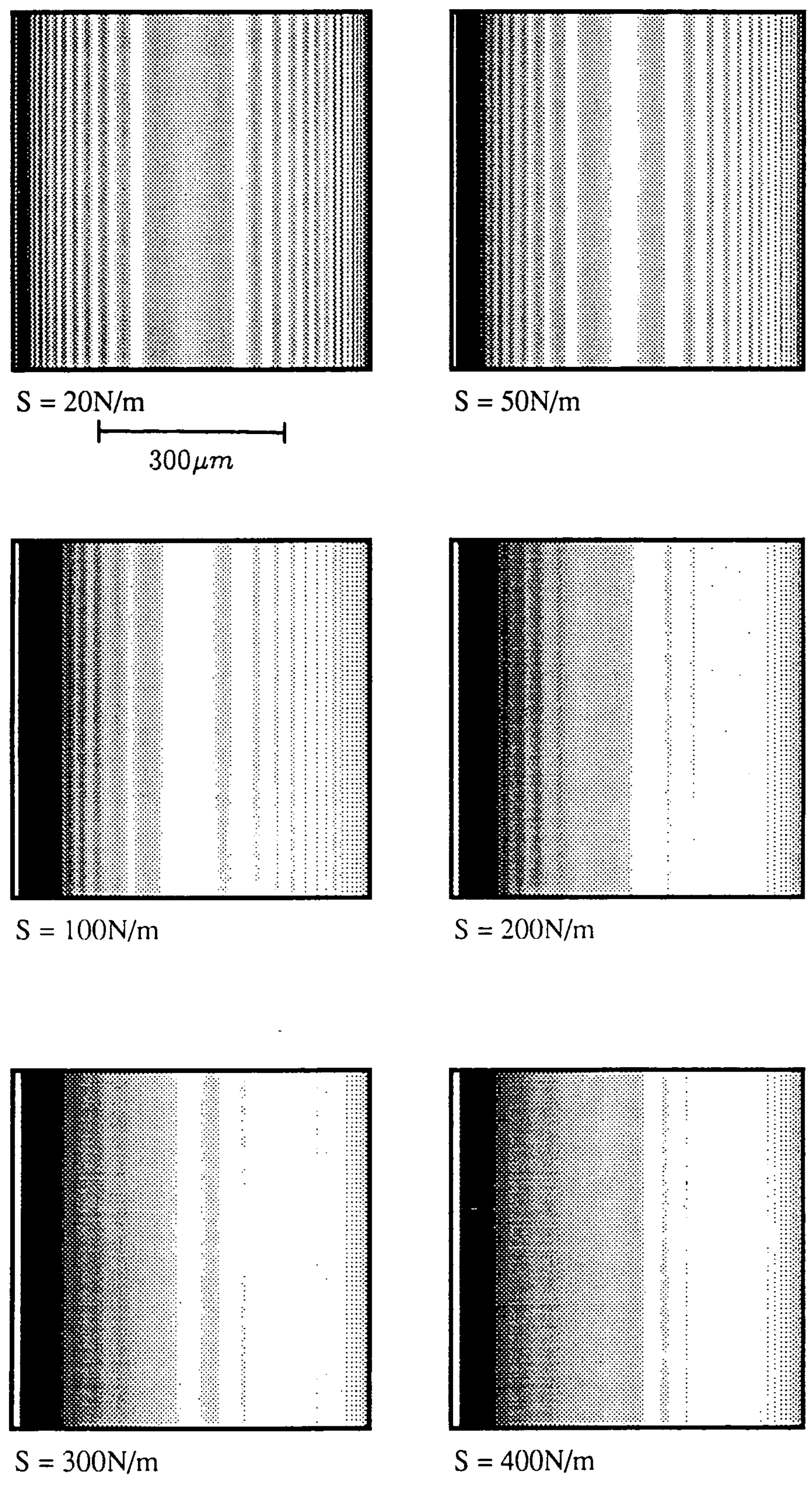

Fig. 6.22: Simulations for the system illustrated in Fig. 6.19, for several values of force, S, per unit length of device edge, for a device of width, H, equal to $10\mu m$.

$[\bar{4}40]$

S = 20N/m

S = 50N/m

$300\mu m$

S = 100N/m

S = 200N/m

S = 300N/m

S = 400N/m

Fig. 6.23: Simulations for the system illustrated in Fig. 6.19, for several values of force, S, per unit length of device edge, for a device of width, H, equal to $2\mu m$.

Δ,(mm on sim.)	Δ,(μm on top.)	$S,(Nm^{-1})$	lnS
2.0	23	20	3.00
4.0	46	50	3.91
6.0	70	100	4.61
9.0	104	200	5.30
9.5	110	300	5.70
10.0	116	400	5.99

Table 6.3: Direct image width, Δ vs. lnS for device width, $H = \infty$.

Δ,(mm on sim.)	Δ,(μm on top.)	$S,(Nm^{-1})$	lnS
2.5	29	20	3.00
4.5	52	50	3.91
8.0	93	100	4.61
8.5	99	200	5.30
8.5	99	300	5.70
9.0	104	400	5.99

Table 6.4: Direct image width, Δ vs. lnS for device width, $H = 50\mu m$.

measurements with the rule were accurate to $\pm 0.5mm$. The results of Figs. 6.20, 6.21, 6.22 and 6.23 are summarised in Tables 6.3, 6.4, 6.5 and 6.6, respectively.

The results embodied in Tables 6.3 - 6.6 are plotted in Fig. 6.24, which shows the relative variation in direct image width, Δ, with lnS, for an isolated right-hand edge and for three different widths of device.

A clear trend is observed from Fig. 6.24. The relationship between Δ and lnS is effectively linear over the range studied, for the isolated right-hand edge. This is a reflection of the fact that as the distorted region expands, further expansion becomes increasingly difficult, due to the non-linear increase in elastic potential energy of the system. Also, as the region A, Fig. 6.19, expands under device-induced strain, the

Δ,(mm on sim.)	Δ,(μm on top.)	$S,(Nm^{-1})$	lnS
2.0	23	20	3.00
4.0	46	50	3.91
5.0	58	100	4.61
6.5	75	200	5.30
7.0	81	300	5.70
6.5	75	400	5.99

Table 6.5: Direct image width, Δ vs. lnS for device width, $H = 10\mu m$.

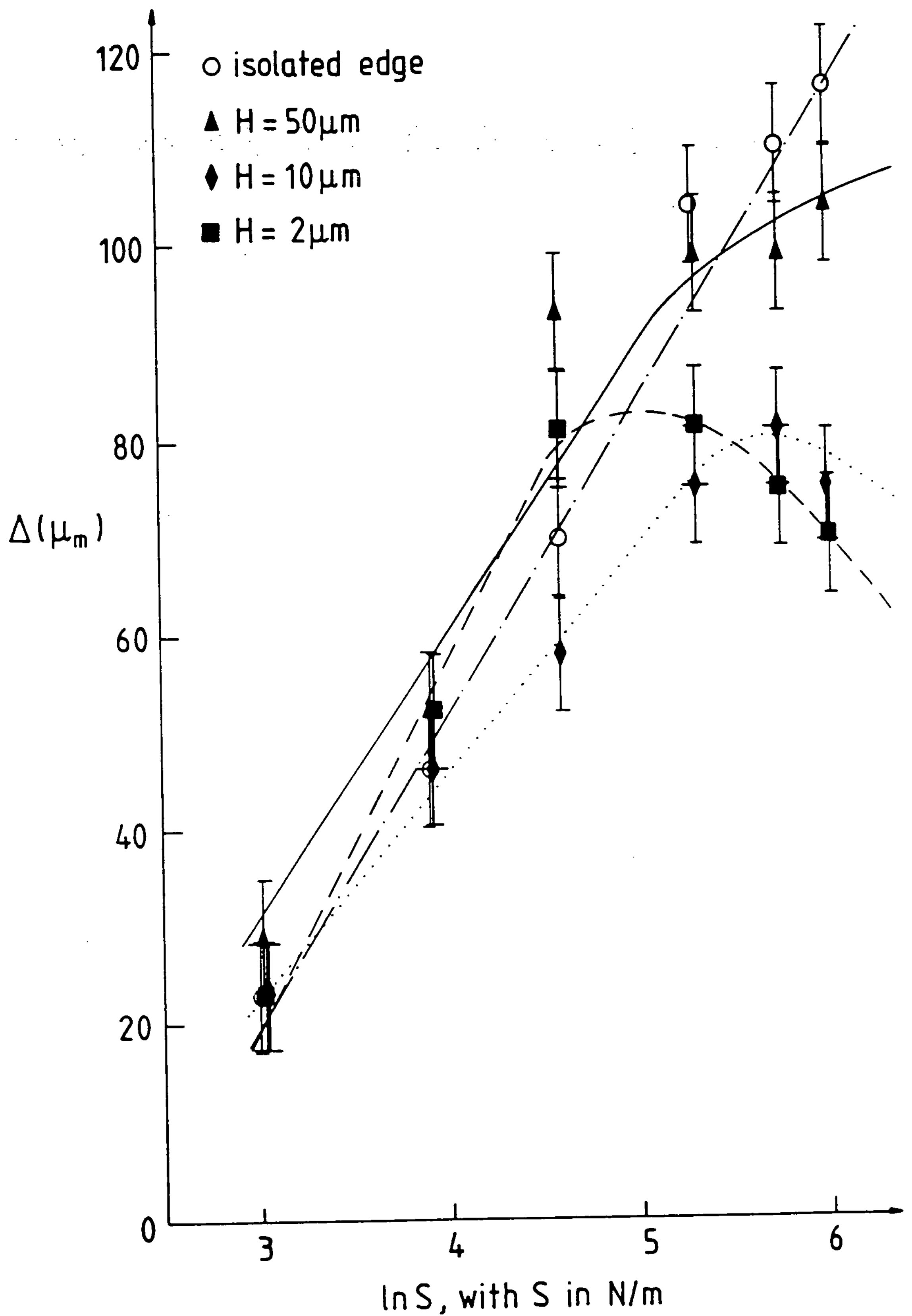

Fig. 6.24: Relative variation in direct image width, Δ, as a function of *lnS*, where *S* is the force per unit length of device edge, for devices of different width.

Δ,(mm on sim.)	Δ,(μm on top.)	$S,(Nm^{-1})$	lnS
2.0	23	20	3.00
4.5	52	50	3.91
7.0	81	100	4.61
7.0	81	200	5.30
6.5	75	300	5.70
6.0	70	400	5.99

Table 6.6: Direct image width, Δ vs. lnS for device width, $H = 2\mu m$.

Device width, $H(\mu m)$	Critical S-value, $S_{crit}(Nm^{-1})$
10	300
2	150

Table 6.7: Critical S-value for maximum device-induced distortion as a function of device width, H.

region B, Fig. 6.19, is compressed, so exerting an increasingly high restoring force on the atoms of region A.

From Fig.6.24, the linear relation between Δ and lnS begins to flatten out for devices of finite width, as the strain effect of the left-hand edge begins to counteract the effect of the right-hand edge. For the cases of H equal to $10\mu m$ and $2\mu m$, there is a critical S-value for which the device-induced distortion reaches a maximum, before starting to decrease. From Fig. 6.24, this critical value of S reduces with device width, since the device-edge strain fields overlap more readily for narrower devices. Table 6.7 contains a summary of the critical S-values for which the turning points in distortion occur, for device-widths given by H equal to $10\mu m$ and $2\mu m$.

To further emphasize the cancelling of strains due to the two edges, simulations were obtained in the $H = 2\mu m$ case for S-values up to $800Nm^{-1}$. The extra simulations are shown in Fig. 6.25 and the complete set of results, including Table 6.6, is displayed in Table 6.8.

A new graph for the $H = 2\mu m$ case was drawn from the results of Table 6.8, and is shown in Fig. 6.26. The trend is clear. Beyond a critical S-value of $150Nm^{-1}$, the direct image width, Δ, decreases roughly linearly with lnS, as the total distortion due to the device also decreases. As an example, when the force per unit length, S, is $800Nm^{-1}$, the total distortion is the same as when S is approximately equal to $70Nm^{-1}$.

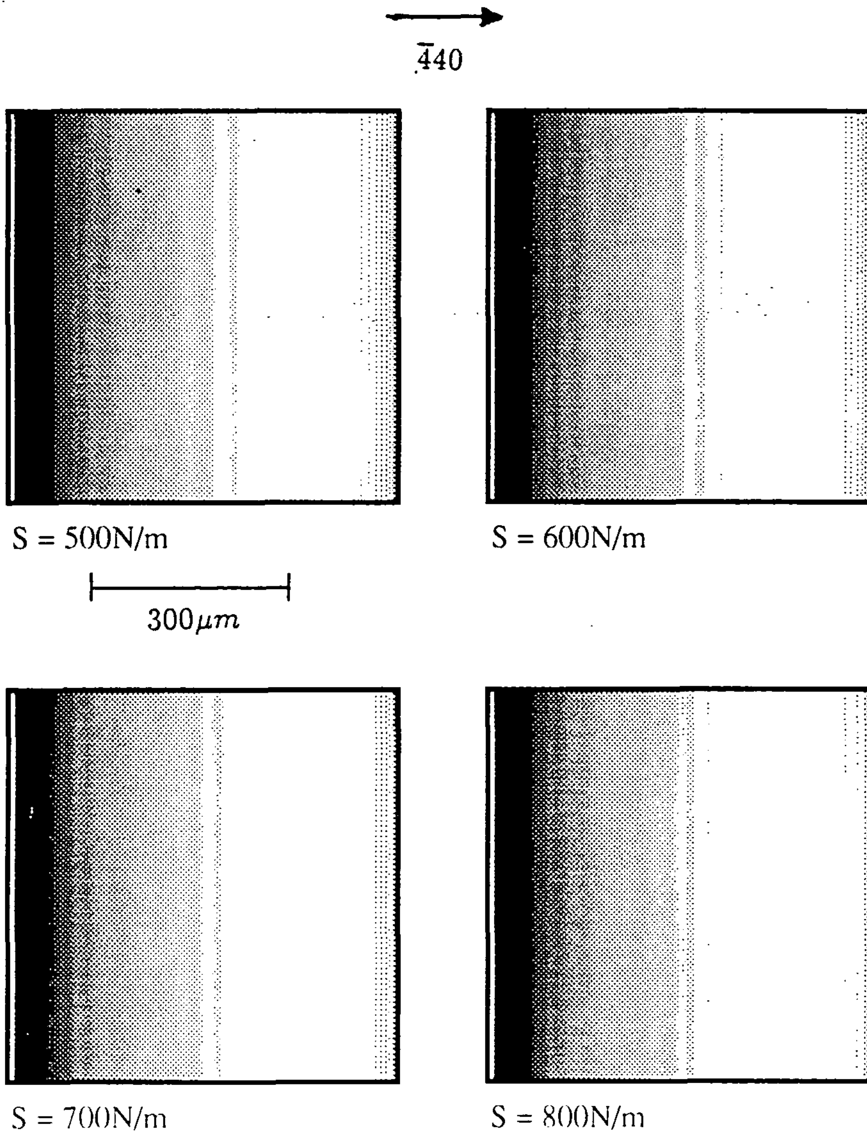

Fig. 6.25: Simulations for the system illustrated in Fig. 6.19, for several values of force, S, per unit length of device edge, for a device of width, H, equal to $2\mu m$.

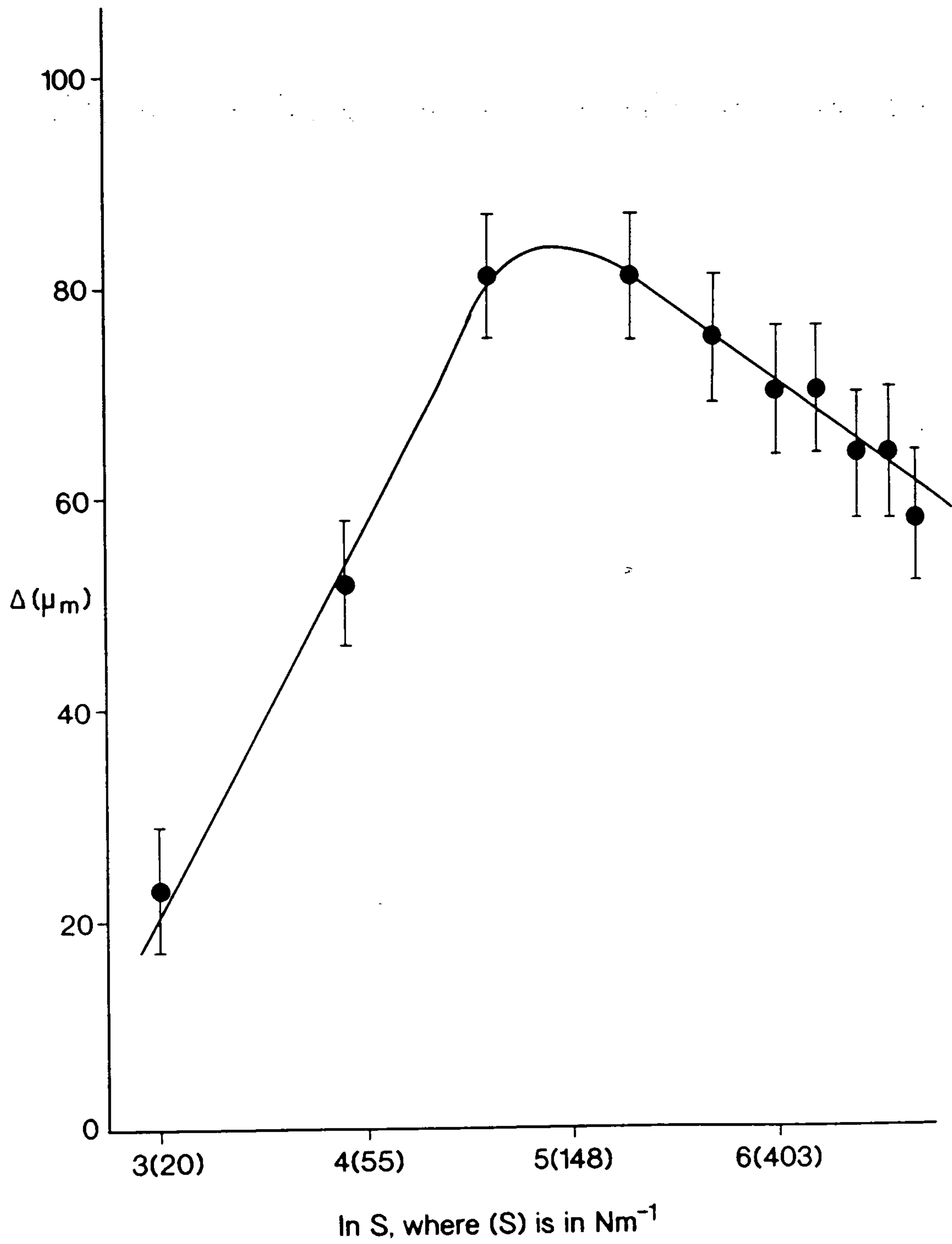

Fig. 6.26: Variation of direct image width, Δ, with lnS, where S is the force per unit length of device edge, for device width $H = 2\mu m$; complete data set.

Δ,(mm on sim.)	Δ,(μm on top.)	$S, (Nm^{-1})$	lnS
2.0	23	20	3.00
4.5	52	50	3.91
7.0	81	100	4.61
7.0	81	200	5.30
6.5	75	300	5.70
6.0	70	400	5.99
6.0	70	500	6.21
5.5	64	600	6.40
5.5	64	700	6.55
5.0	58	800	6.68

Table 6.8: Direct image width, Δ vs. lnS for device width, $H = 2\mu m$; complete data set.

6.7.3 Increase in Substrate Lattice Parameter with Device-Induced Strain

The results of section 6.7.2 illustrate qualitatively the variation in lattice distortion with device-induced strain. What is proposed now is a more quantitative analysis of this distortion, in terms of the variation in substrate lattice parameter.

Consider a device whose position relative to the Borrmann fan is given by Fig. 6.19. The device/substrate geometry in the exit surface is shown in Fig. 6.27. First of all, consider the device width, H, to be very large. Then, taking δ equal to zero and applying Kato and Patel's equations, (6.5), to the right-hand edge alone:

$$\begin{aligned} \left(\frac{\partial u}{\partial x'}\right)_{R.H.} &= \frac{2.56}{\pi E} S \left[\frac{x_0 z^2}{r^4} - 0.72 \frac{x_0}{r^2}\right], \\ \left(\frac{\partial u}{\partial z'}\right)_{R.H.} &= \frac{2.56}{\pi E} S \left[-\frac{z x_0^2}{r^4} - 0.72 \frac{z}{r^2}\right]. \end{aligned} \tag{6.11}$$

Let us restrict our attention to the lattice distortion at the exit surface ($z' = 0$). Then, from (6.11):

$$\left(\frac{\partial u}{\partial x'}\right)_{R.H.} = \frac{2.56}{\pi E} S \left(-\frac{0.72}{x'}\right). \tag{6.12}$$

In order to obtain the corresponding strain component due to the left-hand edge, it is simply necessary to reverse the sign of the expression on the right-hand side of (6.12) and to replace x' by $x' + H$, so that:

$$\left(\frac{\partial u}{\partial x'}\right)_{L.H.} = -\frac{2.56}{\pi E} S \left(-\frac{0.72}{x' + H}\right). \tag{6.13}$$

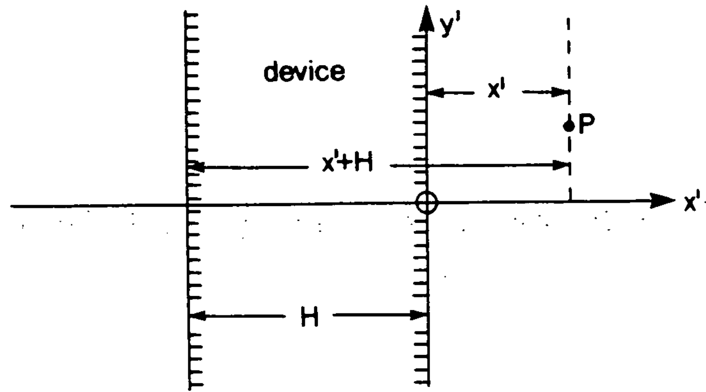

Fig. 6.27: Device/substrate geometry within the exit surface.

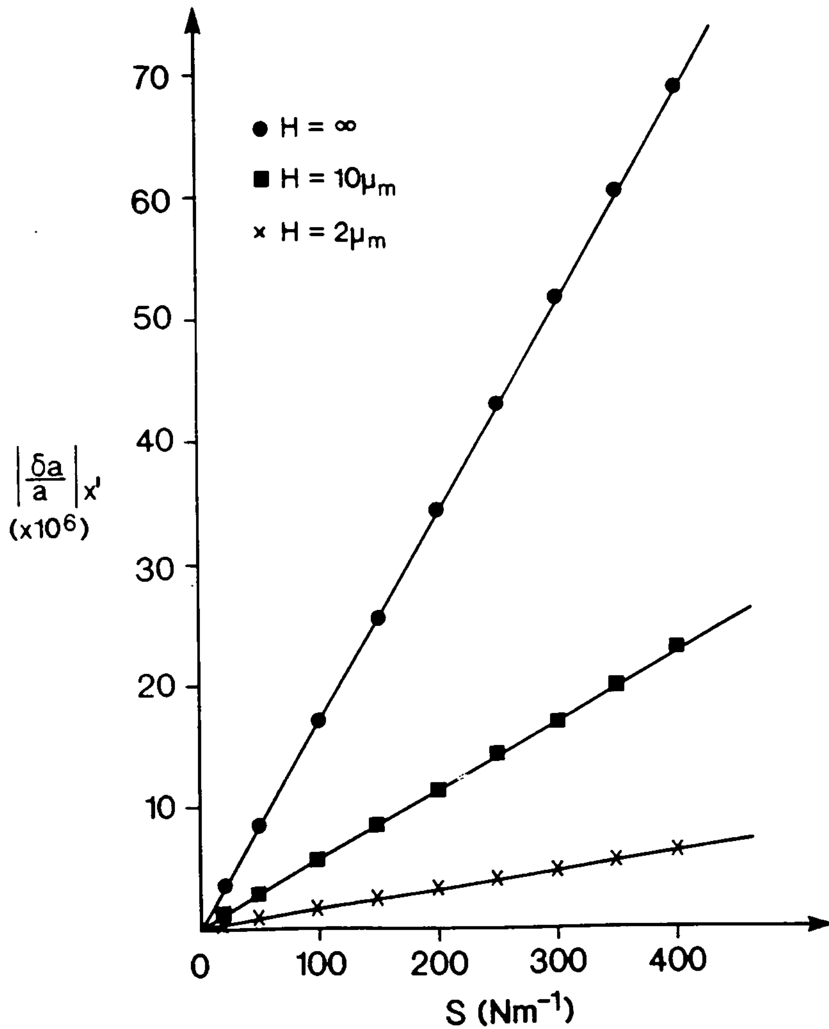

Fig. 6.28: Variation of fractional increase, $| \frac{\delta a}{a} |$, in lattice parameter at a point distant $20\mu m$ from the right-hand edge of Fig. 6.27, with force, S, per unit length of device edge, for devices of different width, H.

From (6.12) and (6.13), the total strain at a general point is given by:

$$\frac{\partial u}{\partial x'} = -\frac{2.56}{\pi E} S \left(\frac{0.72}{x'} - \frac{0.72}{x' + H} \right). \tag{6.14}$$

The quntity $\partial u / \partial x'$ is the pure translational strain in the x'-direction and is equal to the fractional increase in lattice parameter, $\left[\frac{\delta a}{a}\right]_{x'}$, in the x'-direction.

The negative sign on the left-hand side of (6.14) merely signifies that the lattice distortion decreases with increasing x'. Hence, the fractional increase in lattice parameter in the x'-direction, due to device-induced strain, is given by:

$$\begin{aligned} \mid \delta a/a \mid_{x'} &= \Omega S \left(\frac{1}{x'} - \frac{1}{x' + H} \right), \qquad (6.15) \\ \text{where } \Omega &= \frac{1.84}{\pi E}, \text{ and is a constant.} \end{aligned}$$

Two points immediately follow from equation (6.15). As the device width, H, tends to zero, the fractional increase in lattice parameter also tends to zero. In addition, for a very wide device, equation (6.15) becomes:

$$\mid \delta a/a \mid_{x'} = \Omega S / x'.$$

Hence, for a wide device (i.e. considering only the right-hand edge of Fig. 6.27) the fractional increase in lattice parameter at any point P, perpendicular distance x' from the device-edge, is proportional to the force per unit length, S, along the edge and inversely proportional to x'.

Unfortunately, it is impossible to determine $\mid \frac{\delta a}{a} \mid_{x'}$ at the edge itself, since x' is then zero and the right-hand side of equation (6.15) is undefined. The strain-relaxation terms introduced by Ando et al. [154] and Epelboin [161] do not have any theoretical basis, and so it is impossible to use them here to obtain the true strain at the device-edge. However, Ando et al. [154] artificially relaxed the strain over a distance of $20\mu m$ from the edge, in order to obtain good matching between their theory and experiment. Hence, it is safe to say that Blech and Meieran's equations truly reflect the strain-distribution at distances greater than $20\mu m$ from the device-edge.

Consider the test point, P^*, at x' equal to $20\mu m$ relative to the right-hand edge of Fig. 6.27, on the exit surface. Table 6.9 shows the fractional increase in lattice parameter at point P^*, for the isolated right-hand edge and for devices of width, H, equal to $10\mu m$ and $2\mu m$.

The values of $\mid \frac{\delta a}{a} \mid_{x'}$ shown in Table 6.9 were calculated from equation (6.15). The variation in $\mid \frac{\delta a}{a} \mid_{x'}$ at point P^* with S is plotted for the $H = \infty, 10\mu m$ and $2\mu m$ cases in Fig. 6.28. The variation is linear in each case, with decreasing gradient for decreasing device width. This indicates the increasing extent to which the left-hand edge compensates for the strain induced by the right-hand edge, Fig. 6.19, with decreasing device width. This is manifest on a larger scale by the reduction in the heavily distorted diffracting volume beyond a certain value of S, illustrated for the $H = 10\mu m$ and $2\mu m$ devices in Fig. 6.24.

S, (Nm^{-1})	$\mid \frac{\delta a}{a} \mid_{x'}, (\times 10^6)$; $H = \infty$	$\mid \frac{\delta a}{a} \mid_{x'}, (\times 10^6)$; $H = 10\mu m$	$\mid \frac{\delta a}{a} \mid_{x'}, (\times 10^6)$; $H = 2\mu m$
20	3.4	1.1	0.3
50	8.4	2.9	0.8
100	17.2	5.7	1.6
150	25.8	8.6	2.3
200	34.5	11.5	3.1
250	43.1	14.4	3.9
300	51.7	17.2	4.7
350	60.3	20.1	5.5
400	68.9	23.0	6.3

Table 6.9: Fractional increase in lattice parameter, at a fixed point, as a function of force, S, per unit length of device edge, for devices of different widths

$x', (\mu m)$	$\mid \frac{\delta a}{a} \mid_{x'}, (\times 10^8); H = \infty$	$\mid \frac{\delta a}{a} \mid_{x'}, (\times 10^8); H = 10\mu m$	$\mid \frac{\delta a}{a} \mid_{x'}, (\times 10^8); H = 2\mu m$
20	516.8	172.3	47.0
30	344.5	86.1	21.5
40	258.4	51.7	12.3
50	206.7	34.5	8.0
60	172.3	24.6	5.6
80	129.2	14.4	3.2
100	103.4	9.4	2.0

Table 6.10: Variation of fractional increase in lattice parameter with displacement, x', away from the right-hand edge of Fig. 6.27, for different device widths, H.

Now consider the variation in $\mid \frac{\delta a}{a} \mid_{x'}$ with x' away from the right-hand edge of Fig. 6.27. Matching of simulations with Loxley's experimental results, Fig. 6.9, was possible for a device-induced strain characterised by an S-value of $30Nm^{-1}$. Taking this value of S, the results of Table 6.10 were calculated, using equation (6.15).

The results are plotted in Fig. 6.29, for the cases of H equal to ∞, $10\mu m$ and $2\mu m$. It is immediately obvious that the fractional increase in lattice parameter at any point reduces with decreasing device width, H. In addition, it is seen that the narrower the device, the faster the relative fall-off in $\mid \frac{\delta a}{a} \mid_{x'}$ with x'. This provides some quantitative insight into the process by which the maxima of the Δ vs. lnS curves of Fig. 6.24 shift to the left for decreasing device width.

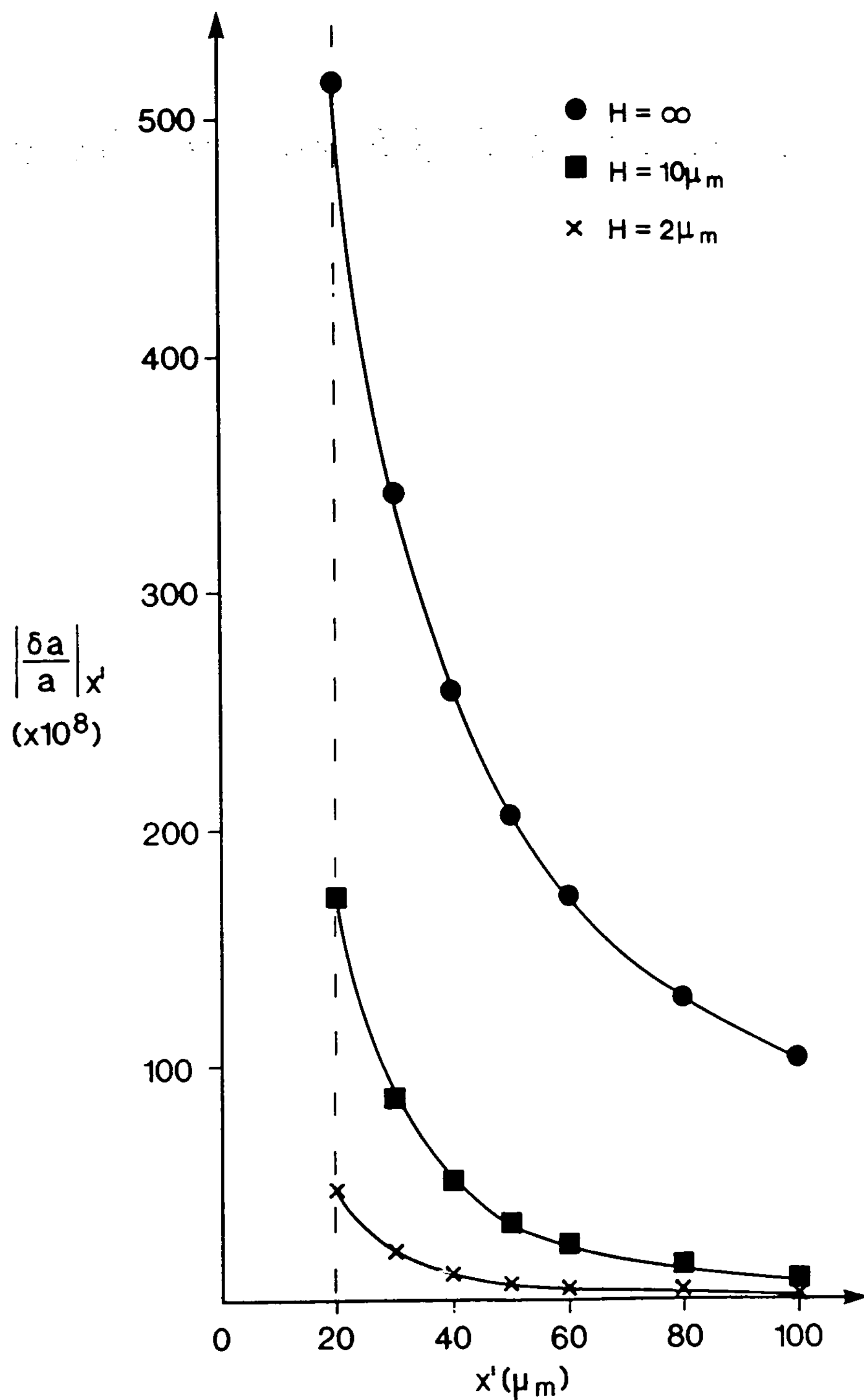

Fig. 6.29: Variation in fractional increase, $| \frac{\delta a}{a} |_{x'}$, in lattice parameter with displacement, x', away from the right-hand edge of Fig. 6.27, for different values of device width, H.

6.8 General Discussion and Industrial Implications

The strain code $DIFFSTRIP$ (APPENDIX G) has been used in conjunction with the integration program $GENERAL.P$ (APPENDIX A) to simulate experimental section topographs due to oxide film edges, section 6.3, and devices, section 6.4, on Si substrates. In each case, good matching was obtained between simulated and experimental images. The additional fringes found by Epelboin [161] for very high oxide film strains have also been observed here. It was found that the visibility of the fringes was not appreciably enhanced by doubling the resolution of the integration network. Consequently, it is suggested that statistical noise in the photographic process tends to suppress the visibility of these extra fringes.

The simulation code was used to simulate the relative variation in position and width of direct images in experimental topographs due to Loxley [163], for different positions of device relative to the Borrmann fan base. In section 6.4.3, it was shown that absolute values of the size of the distortion induced by a device cannot be determined by measurement of the direct image width on a simulation. However, the relative variation in distortion can be obtained as a function of force per unit length, S, along the device edge, and device width, H. In section 6.5, a study was made of the effect on image structure of device position on the entrance and exit surfaces. It was found that the proximity of a device edge to the direct beam, especially for a device on the entrance surface, strongly affects the strain-induced diffraction throughout the Borrmann fan. This is manifest by the extent of the disruption to the Pendellösung fringes.

In section 6.6, simulations were undertaken to determine the minimum device width detectable by section topography. Simulations were obtained for several S-values (APPENDIX L) to determine the minimum detectable device width, W_{min}, in each case. It was noted that a value of δ equal to 60° consistently gave the most clearly identifiable images, no other orientation giving a lower limit on detectability. The results, summarised in Table 6.2, are displayed in Fig. 6.18. With increasing S, the minimum detectable device width decreased asymptotically to a limit of $1\mu m$. However, for S-values characteristic of real devices (S < $100Nm^{-1}$) the minimum detectable device width was at least $3.5\mu m$. For a typical S-value of $35Nm^{-1}$, determined by Petrashen and Shulpina [156] for a device built by boron ion-implantation on Si, the minimum detectable device width, W_{min}, given by Fig. 6.18, is over $6\mu m$. For device sizes characteristic of those used in current industrial processes, it is clear that X-ray topography cannot be used to image the strains at devices.

In section 6.7, the effect of the cancelling of strains due to opposite device edges was investigated by considering the device/crystal geometry of Fig. 6.19. Relative changes in the direct image width, Δ, allowed conclusions to be drawn concerning the effect of the parameters H and S on the total distortion induced by the device.

It was found that the variation of Δ with lnS was effectively linear for a very wide device. However, for narrower devices ($H < 10\mu m$) the Δ vs. lnS curve flattens out and reaches a maximum, beyond which Δ decreases with increasing

S, Fig. 6.24. This result is attributed to the increased effect of strain cancellation between the two edges with decreasing H and increasing S. The value of S to induce the maximum distortion decreases with decreasing device width, Table 6.7, due to the increased ease with which edge strains may cancel for narrower devices.

A brief analysis of the effect of H and S on the variation in lattice parameter, a, is given in section 6.7.3. Of course, Blech and Meieran's equations cease to be physically realistic in the region of the singularity at the edge itself. However, at a test point $20\mu m$ distant from the edge, Table 6.9 gives the fractional increase in lattice parameter as a function of S, for different device widths. The results are plotted in Fig. 6.28, illustrating that the fractional increase, $\mid \frac{\delta a}{a} \mid$, in lattice parameter is directly proportional to S, with increasing gradient for increasing device width, H. The results of Table 6.10, plotted in Fig. 6.29, show that the narrower the device, the faster the fall-off in $\mid \frac{\delta a}{a} \mid$ with increasing displacement, x', away from the right-hand edge of Fig. 6.27. These results contribute to the conclusion that lattice distortion, and hence detrimental defect propagation, is inhibited by manufacturing devices as narrow as possible.

Chapter 7

Conclusions

The aim of this work has been to study the strains associated with process-induced defects in Si single crystals, using simulation of X-ray section topographs.

Section topographs due to oxygen precipitates in MCZ Si samples treated at different annealing temperatures, T, have been simulated, Figs. 4.9 and 4.10. A linear relation was found between the deformation parameter, C, representing the precipitate strain magnitude, and lnT. This indicates that the precipitate volume increases at a decreasing rate with T. The curve of lnC vs. $1/T$, Fig. 4.13, based on the results of Figs. 4.9 and 4.10, did not show the inverse proportionality expected from the equation of growth, (4.10), for square-plate precipitates. Consequently, it is concluded that the growth equation (4.1) is not applicable to the spherical oxygen precipitates in MCZ Si studied here. Matching of simulation with experiment enabled values to be assigned to the deformation parameter, C, and the precipitate depth. These two quantities are of considerable importance on an industrial level. First of all, the deformation parameter denotes the ability of a precipitate to generate harmful strain-induced defects. In addition, precipitates in the active device layer significantly inhibit the electrical performance, whilst precipitates in the bulk enhance device yield through intrinsic gettering. Given the speed with which simulations can be generated on, for example, a SUN workstation, a potentially valuable role is defined for simulation, in conjunction with experiment, in wafer quality control.

Striking uniformity in the sizes of precipitates formed in equivalent samples was observed, consistent with the results of other workers. This was true except for one precipitate, Fig. 4.11, which had grown so large that its strain field was no longer spherically symmetric. It is known that carbon and boron impurities enhance the precipitation of oxygen in Si, and it is suggested that a localised concentration of such an impurity was responsible for the formation of this anomalous precipitate. It is proposed that, in general, the vast majority of precipitates which survive to maturity are nucleated at approximately the same time, subsequently growing at the same rate.

A study was made of the critical depth, z_{crit}, at which the effect of surface relaxation becomes negligible, for precipitate images. It was found that z_{crit} increases linearly with lnC, Fig. 4.19. Any industrial application of the simulation technique

should incorporate surface relaxation, to ensure that the correct values are assigned to physical parameters.

Simulations have been generated for a CZ Si crystal, containing an as-processed density of precipitates, with denuded zones at the top and bottom surfaces. The perfect crystal Pendellösung fringes at the extreme left of the image, characteristic of an exit surface denuded zone, were clearly seen, Fig. 4.23. The high density of precipitate images, unresolved for C-values greater than $2\times10^{-22}m^3$, is in stark contrast to the images of oxygen precipitates in MCZ Si, Figs. 4.9 and 4.10, which were well resolved for C-values up to $\sim 10^{-19}m^3$. This serves to illustrate the quality of MCZ Si relative to CZ Si.

The critical separation, $(\Delta y)_{crit}$, of two precipitates for their images to be just resolved was found to increase linearly with lnC, Fig. 4.29. This agrees with a result of other workers which showed that the precipitate image height increases linearly with lnC.

It is well known that oxygen precipitates in the bulk of a Si crystal can generate dislocations, which act as gettering sites for the removal of harmful transition metal impurities from the active device layer. A study has been made in the current work of the strain effects of these dislocation-precipitate complexes. The cylindrical inclusion model was used to represent the strain distribution associated with precipitate decoration.

First of all, it was found that section topography allows precipitate decoration to be distinguished from the associated dislocation for values of C as low as $1\times10^{-22}m^3$. Such a high degree of visibility is potentially very useful within the semiconductor technology. This result means that section topography simulation, in conjunction with experiment, could be used as a test of gettering efficiency and a means of parameterising the associated strains. Furthermore, simulations generated using the cylindrical inclusion model require a much smaller computation time than would be possible by considering a distribution of precipitates.

For three different reflections and dislocation orientations, the strain magnitude, $\mid A\xi^2 \mid$, associated with the cylindrical inclusion was found to increase linearly with precipitate deformation parameter, C. The gradient, δ, of the linear relation was found to be highest for low-order reflections, and an explanation has been offered for this. First of all, it is known that the diffracting volume around a dislocation increases with decreasing diffraction vector magnitude. The simulations of Figs. 5.14 - 5.19 show that the same result holds for the precipitate decoration and, by extension, for the decorated dislocation itself. In addition, equation (5.58) implies that the radial strain associated with the inclusion falls off with radial displacement more rapidly than the radial strain associated with the precipitate distribution. Hence, the diffracting volume associated with an equivalent cylindrical inclusion is inherently smaller than that of the precipitate disribution which it models. Combining the above results, it is seen that $\mid A\xi^2 \mid$ must increase more rapidly relative to C for low-order than for high-order reflections. This is the reason why the gradient, δ, was found to be greatest for low-order reflections.

Part of the motivation for the study of decorated dislocations has been the thor-

ough *calibration* of the cylindrical inclusion model, in preparation for its potential use as an industrial tool. Figs. 5.30 and 5.33 show, respectively, a linear increase in δ with precipitate line density, ρ_p, and a linear increase in inclusion cross-section with precipitate distribution cross-section. Figs. 5.30 and 5.33, in conjunction with Fig. 5.20, allow the application of the cylindrical inclusion model to any possible size of precipitate distribution, containing any possible size and density of precipitates, for the $\bar{1}31$ reflection studied. Work by other authors has shown that ρ_p and the precipitate distribution size can be determined accurately by TEM. With these values as initial conditions, the above simulation scheme in conjunction with experiment becomes a feasible possibility for parameterising decorated dislocation strain. This has potential industrial applications in the detection and control of harmful strain-induced defect propagation.

It has been shown that decorated dislocation pairs are resolvable by section topography for a perpendicular separation, κ, as low as $28.5\mu m$. For this value of κ, the decorated dislocations are resolved for C-values up to $2.9\times10^{-21}m^3$. The value of κ quoted above is characteristic of dislocation-rich CZ Si, so that even in this case, section topography can be used to identify individual decorated dislocations.

A study was made of the critical deformation parameter, C_{crit}, for adjacent decorated dislocations to be just resolved, as a function of κ. Above a value of κ equal to about $45\mu m$, the variation of $ln(C_{crit} \times 10^{21})$ with κ was linear, Fig. 5.35. This is an interesting extension of the single precipitate result, quoted previously, that the image height increases linearly with lnC. However, for κ-values below about $45\mu m$, the linearity breaks down, Fig. 5.35, as the strain contribution due to the dislocations becomes increasingly significant.

TEM has received considerable attention in the gettering literature, because of its excellent spatial resolution. However, the results of the current work indicate that X-ray section topography also has a useful and very specific part to play in terms of strain parameterisation.

The growth of an oxide layer, or the fabrication of a device by ion-implantation or diffusion, on a Si substrate has become a standard feature of semiconductor technology. The strains induced by these processes directly affect device quality, through strain-related defect propagation. Section topography is well suited to the analysis of these strains, and this has been accomplished in the current work by the simulation technique.

The well known hook-shaped fringes found in section topographs of oxide edge regions on Si substrates have been simulated, Fig. 6.6. Simulations by another worker have shown that for very high edge strains, an extra set of fringes should apppear. The fact that these extra fringes have never been observed experimentally was attributed to a relaxation mechanism present in real oxide layers. These extra fringes have been observed in the current work, for very high edge strains, but reduction of the horizontal integration step from $0.59\mu m$ to $0.29\mu m$, Fig. 6.8, did not appreciably enhance the visibility of the fringes. All the simulations were performed assuming a photographic resolution equivalent to experimental topography. Consequently, it is suggested that statistical limitations, and small oxide and device thickness, may be the reason why these fringes have not been observed

experimentally.

Section topographs of a device on the exit surface of a Si wafer, at various positions relative to the Borrmann fan base, have been simulated, Fig. 6.9. This work was extended to study the effect on image structure of device position on the entrance and exit surfaces. It was demonstrated that maximum disruption to the perfect crystal Pendellösung fringes occurred when the device was on the entrance surface, close to the direct beam.

Studies have been been undertaken to determine the minimum device width, W_{min}, detectable by X-ray section topography. W_{min} was determined as a function of the force per unit length, S, exerted on the substrate by the device edge, Fig. 6.18. W_{min} tends asymptotically to $1\mu m$ for high strains, but for strains characteristic of contemporary devices ($S < 100Nm^{-1}$) W_{min} is at least $3.5\mu m$. It is clear that the minimum detectable device width is above the limits set by the geometric and other constraints set by the experimental technique.

The effect of cancellation of the strains due to opposite device edges has been studied. The direct image width, Δ, in simulation gives an indication of the size of the distortion induced in the substrate by the device. For an isolated edge, the variation of Δ with lnS was roughly linear, Fig. 6.24. However, for device widths of $10\mu m$ and $2\mu m$, the curve flattens out, reaching a maximum beyond which Δ decreases with increasing S, Fig. 6.24. Furthermore, the S-value for the turning point in Δ decreases with decreasing device width, H. Clearly, a narrow device together with very high edge strain maximises the overlap between the opposing strains due to opposite device edges. This in turn minimises the total distortion in the substrate, reducing the possibility of undesirable defect propagation. To explain these effects on a microscopic level, an analysis was made of the effect of H and S on the variation in lattice parameter, a. The fractional increase in lattice parameter, $\mid \frac{\delta a}{a} \mid$, at a fixed distance from one edge of a device was found to increase linearly with S, with increasing gradient for increasing device width, H, Fig. 6.28. It was also shown, Fig. 6.29, that the narrower the device, the faster the relative fall-off in $\mid \frac{\delta a}{a} \mid$ with increasing displacement away from the right-hand edge of Fig. 6.27. The results of Figs. 6.28 and 6.29 confirm that strain-induced defect propagation may be minimised by manufacturing devices as narrow as possible.

Several areas of further research can be identified. In the current work, intrinsic gettering was investigated in terms of decorated dislocations. However, oxygen precipitates in Si often generate prismatic dislocation loops, as a stress relief mechanism. These dislocation loops act as very effective gettering sites for transition metal impurities, and are therefore worthy of attention. The strain equations describing a dislocation loop are very complicated, and the task of transforming them into computer code would be substantial. However, having accomplished this, it would be a simple matter to use linear elasticity within the simulation technique to obtain simulations of section topographs due to dislocation loops decorated with precipitate distributions. The technological value of this, as in the cases studied in the present work, is in the parameterisation of strain by the use of simulation in conjunction with experiment.

The *wafer bonding* technique, discussed in Chapter 1, for the production of *silicon*

on insulator (SOI) wafers, is a standard feature of semiconductor technology, on account of the perfection of the SOI layer. However, incomplete bonding of the base Si wafer and the SiO_2 surface of the bonded wafer results in the formation of voids. These voids render the SOI wafer useless for device preparation, since unbonded Si is unstable with thermal processing. It is known that X-ray section topography can be used to detect the presence of such voids, because of the strain which they exert on the surrounding Si lattice. It would be interesting and useful to develop the strain code to simulate for these defects, and to match with the corresponding experimental section topographs. In this way, it would be possible to gain a quantitative insight into the elastic effect of voids on the underlying Si lattice and, by inference, on the SOI layer.

The integration program used in this work was based on a constant step algorithm (C.S.A), so that measurement of direct image sizes could be used to highlight general trends, but not to assign absolute values. The reasons for this were discussed at length in Chapter 6. It would be a useful development of the current work to devise a varying step algorithm (V.S.A), so that direct image measurements, of the kind made in Chapter 6, could be used to assign absolute values to the size of the difracting volume induced by a defect. In addition, the computation time required to generate a simulation using a V.S.A. would be preferentially shorter than would be possible, for the same accuracy, with a C.S.A.

The integration program used throughout this work calculates the wave amplitudes at each point in successive planes of incidence throughout the Borrmann fan. Of course, the intensity at any point is simply the square of the amplitude of the wavefield at that point. Hence, it would be a simple matter to write the code to display the intensities of the refracted and diffracted wavefields at all points throughout a selected plane of incidence. In this way, it would be possible to observe directly the redistribution of energy around a crystal defect, and to understand more fully the structure of the resulting topographic image. Repeating the process for successive planes of incidence, it would then be possible to generate a three dimensional map of the energy distribution within the Borrmann fan.

Comparison of simulation with experiment, to obtain matching, has been performed by eye in this work. This is an acceptable option, since the human eye allows sensitive discrimination between levels of grey and relative deviations in image structure. However, a more objective method of comparison may be available by means of a computerised digitiser. The digitiser converts an image into an array of small dots, and associates a level of grey with each such point. Application of this process to an experimental image and a proposed simulation, in conjunction with a suitable statistical comparison of grey levels at all corresponding points, offers the possibility of greater reliability and accuracy in the allocation of values to physical parameters by the simulation technique.

The prospect of reduced computational time in generating simulations is always an attractive one, especially from the point of view of industrial application of the simulation technique. Parallel processing may have a useful contribution to make in this respect in the future. Each line in the integration network, parallel to a plane of incidence, may be calculated independently. Consequently, by using several PC's

in tandem, or even a transputer, the calculated intensity data may be acquired in a fraction of the time taken using a single machine.

Appendix A

A computer program called *GENERAL.P*, written in Pascal, is listed, to integrate Takagi's equations iteratively.

```
program general(input, output);

type carray=array[1..12] of real;

#include "globals.h"
#include "complex.h"
#include "disloc.h"
#include "point.h"
#include "curve.h"
#include "results.h"
#include "cylinder.h"
#include "strip.h"
#include "cylbox.h"

const pi=3.14159;
{      maxno=5000;
      resolution=125;
}


var io:integer;

    (*  Setup routine  *)
    defect_code:integer;
    lambda,theta,alpha,absorb,thickness,deltat,width,kappa:real;
    p,q,dir,alt,dv1,dv2,point_separation:real;
    beta,dielep,dieleq,qhio,qhip,qhim:complex;
    lmaxt:integer;

    patry,height,pzy,pas:real;
    ang,param,rn,rf:vector;


    (*  Integration routine  *)
    as,plane:integer;
    xd0,yd0,zd0,depth,dsh,total:real;            (*** 22/1/91 ajh ***)
    k:integer;
    rl:real;

    (*  Integration parameters  *)
    elem,transv,sq2:real;
    ap1,ap2,xdis,zdis,diz,dix:real;
    c,shx1,shx3:real;
    xc,yc,zc:larray;                             (*** 24/1/91 ajh ***)
    xcsingl,zcsingl:real;                        (*** 24/1/91 ajh ***)

    xcurve,radius:real;
    co3,co4,co5:vector;
    gd:vector;
    maxplane,lmin,limbe,lmax:integer;
    c1,c2,a,b,ab:complex;
    da:matrix;
    cn:carray;
    prno,prlim,iseed:integer;                             (*** DNZ ***)
    xmin,xmax,ymin,ymax,zmin,zmax:real;                   (*** DNZ ***)
    vfrac,xsi,psi,eps:real;                               (*** CYL ***)
    xcyl0,ycyl0,zcyl0,zcrit,clength:real;                 (*** CYL ***)
    flnth,ymod,delta,xedge,yedge,horiz,zdispl:real;  (** STRIP **)
    ptno,ptlim:integer;                                   (** CYLBOX **)
    rmax:real;                                            (** CYLBOX **)
    xbox,ybox,zbox:zarray;                                (** CYLBOX **)
    x,y,z:real;                                           (** CYLBOX **)
    totbox:real;                                          (** CYLBOX **)

    (*  Results parameters  *)
    data:text;
```

```
    mini,maxi:real;
    store1,store2:big;

    dislocation,precipitate,curvature,cylinder,strip,cylbox:boolean;
    perfect:boolean;
    factor,fen,fou,field,wl:real;
    i,limit,ip,kperfo,jj,ipll:integer;
    dum1,dum2,dum3,d,e,f:complex;
    phi:wave;
    reflex:barray;
{
procedure dislocn(var da:matrix;var xcsingl,zcsingl,dix,diz:real;
                var cn:carray;patry,q:real;a,ang,rn,rf:vector);external;
                                                        (*** 24/1/91 ajh ***)

procedure diffdisl(var dsh:real;x1,x2,ap1,ap2:real;co3,co4,co5:vector;
                 cn:carray);external;

procedure pointdef(var c:real;var prno,prlim:integer;iseed:integer;
                 var xmin,xmax,ymin,ymax,zmin,zmax:real;
                 var xc,yc,zc:larray;
                 var gd:vector;a,ang,rn,rf:vector);external;  (* RND *)

procedure diffpoint(var dsh:real;x,y,z,sh1,sh2,c:real;gd:vector);external;

procedure curvedef(var radius:real;var gd:vector;
                 a,ang,rn,rf:vector);external;

procedure diffcurve(var dsh:real;x,z,sh1,sh2,t,r:real;gd:vector);external;

procedure cyldef(var vfrac,xsi,psi,eps,xcyl0,ycyl0,zcyl0,zcrit,clength:real;
                var gd:vector;
                a,ang,rn,rf:vector);external;   (*** cyl ***)

procedure diffcyl(var dsh:real;x,y,z,xsi,psi,eps:real;gd:vector);external;
                                               (*** cyl ***)


procedure stripdef(var flnth,ymod,delta,xedge,yedge,horiz,zdispl:real;
                 var gd:vector;
                 a,ang,rn,rf:vector);external;   (*** 7/2/92 STRIP ***)


procedure diffstrip(var dsh:real;x,y,z,flnth,ymod,delta,horiz,shx,shz:real;
                  gd:vector);external;           (*** 7/2/92 STRIP ***)

procedure boxdef(var c:real;var ptno,ptlim,iseed:integer;var psi,eps:real;
               x,y,z:real;var xcyl0,ycyl0,zcyl0:real;
               var rmax,zcrit,clength:real;var xbox,ybox,zbox:zarray;
               var gd:vector;a,ang,rn,rf:vector);external;

procedure diffbox(var dsh:real;x,y,z,sh1,sh2,c:real;gd:vector);external;


procedure results(var jj:integer;maxplane:integer;var store1,store2:big;
                var data:text;
                var mini,maxi:real;reflex:barray;
                kperfo,limit,ip,io:integer);external;
}
procedure trap;
begin
end;
{
  procedure cmult(a,b:complex;var c:complex);external;
  procedure cadd(a,b:complex;var c:complex);external;
  procedure csub(a,b:complex;var c:complex);external;
```

```
  procedure cdiv(a,b:complex;var c:complex);external;
}
procedure integrate;

var dum1,dum2,dum3,d,e,f:complex;
    ks,as,l,k:integer;
    x,dc1,dc2,temp,y,z,xi,zd1,zd2,r1,aa:real;

begin           (* integration *)
    ip:=ip-1;
    temp:=0;
   (*core(plane);*)
   (*begin        *)
    if dislocation then begin
      aa:=yd0-plane;
      xd0:=xdis+aa*dix;
      zd0:=zdis+aa*diz;
      yd0:=2;
    end;
   (*end;         *)
      y:=plane*patry;  (* ???? - *)
    r1:=1;
    for k:=limbe to maxno-1 do begin  (* b.c.s at entrance surface *)
      phi[1,k].re:=field*r1;
      phi[1,k].im:=0;
      r1:=r1*fen;
      phi[2,k].re:=0;
      phi[2,k].im:=0;
    end;
    depth:=0;
    for l:=lmin to lmax do begin  (* loop for each layer *)
      depth:=depth+elem;
      xi:=-depth*sin(alpha)/cos(alpha)+sq2;
      limit:=maxno-1;
      phi[1,limit].re:=0;
      phi[1,limit].im:=0;
      phi[2,limit].re:=0;
      phi[2,limit].im:=0;
      as:=0;
      x:=xi;
      z:=depth-0.5*elem;
 if dislocation then begin
      zd1:=da[1,3]*(z-zd0);
      zd2:=da[2,3]*(z-zd0);
 end;
          for ks:=limit to maxno-1 do begin  (* loop for each node in a layer *)
            as:=as+1;
            x:=x-transv;
            if dislocation then begin
                 dc1:=da[1,1]*(x-xd0)+zd1;
                 dc2:=da[2,1]*(x-xd0)+zd2;
            end;
          if perfect then dsh:=0
          else begin
        if dislocation then  diffdisl(temp,dc1,dc2,ap1,ap2,co3,co4,co5,cn);
        if precipitate then begin              (***  DNZ  ajh ***)
           total:=0.0;
           for prno:=1 to prlim do begin
           diffpoint(dsh,x-xc[prno],y-yc[prno],z-zc[prno],shx1,shx3,c,gd);
           total:=total+dsh
                                end;
           dsh:=total;
           dsh:=q*pi*dsh;                                          section γ
           end else dsh:=0;
        if precipitate then temp:=dsh;
        if curvature then begin
```

```
                        diffcurve(dsh,x-xcurve,z,shxl,shx3,thickness,radius,gd);
                        dsh:=q*pi*dsh;
                        end else dsh:=0;
       if curvature then temp:=dsh;
       if cylbox then begin            (**** CYLBOX  ajh  **)
          totbox:=0;
          for ptno:=1 to ptlim do begin
          diffbox(dsh,x-xbox[ptno],y-ybox[ptno],z-zbox[ptno],shxl,shx3,c,gd);
          totbox:=totbox+dsh
                                      end;
          dsh:=totbox;
          dsh:=q*pi*dsh;
                    end
       else
                         dsh:=0;
       if cylinder then begin         (** CYLIND. INCLUSION ajh   **)
          diffcyl(dsh,x,y,z,xsi,psi,eps,gd);
          dsh:=q*pi*dsh
                         end else dsh:=0;
       if strip then begin                   (** OXIDE STRIP  ajh **)
          diffstrip(dsh,x-xedge,y-yedge,z-zdispl,flnth,ymod,delta,horiz,
                    shxl,shx3,gd);
             dsh:=q*pi*dsh
                    end;
       if precipitate then dsh:=dsh+temp;
       if dislocation then  dsh:=temp+dsh;
       if strip then dsh:=dsh+temp;
         end;
         dsh:=dsh+wl;
         cl.im:=dsh;
         c2.im:=-dsh;
         csub(cl,ab,d);

        cmult(a,phi[2,ks+1],duml);
        cadd(duml,phi[1,ks+1],e);
        cmult(b,phi[1,ks],duml);
        cmult(c2,phi[2,ks],dum2);
        cadd(duml,dum2,f);
        cmult(cl,e,duml);
        cmult(a,f,dum2);
        cadd(duml,dum2,dum3);
        cdiv(dum3,d,phi[1,ks]);
        cmult(b,e,duml);
        cadd(duml,f,dum2);
        cdiv(dum2,d,phi[2,ks]);
      end;  (* ks *)
    end;   (* l *)
 (* if plane=l then writeln('range on bottom ',(xi-transv-sq2)*le06:2:1,
                        ' ',(x-sq2)*le06:2:1);*)     (* 24/1/91 ajh *)
end;  (* integration *)


procedure display;
begin
  writeln;
  writeln('   SECTION TOPOGRAPH SIMULATION');
  writeln;
  writeln('wavelength ',lambda*le10:1:4,' Angstrom');
  writeln('bragg angle ',180*theta/pi:3:2,' degrees');
  writeln('psi zero ',180*alpha/pi:3:2,' degrees');  writeln;
(*writeln('mu ',absorb:1:4);
  writeln('beta ',beta.re,'  ',beta.im);
  writeln('chi h + ',qhip.re,'  ',qhip.im);
  writeln('chi h - ',qhim.re,'  ',qhim.im);
  writeln('chi o   ',qhio.re,'  ',qhip.im);      *)
```

section γ

section λ

section δ

section ϵ

```
  writeln('slab thickness ',elem*1e06:1:2,' micron');
  writeln('sample thickness ',thickness*1e06:1:1,' microns');  writeln;
  writeln('transverse step ',transv*1e06:1:2,' microns');
  writeln('transverse printed step ',point_separation*1e06:1:2,' microns');
  writeln;
  writeln('slit width ',width*1e06:1:1,' microns');  writeln;
(*writeln('a= ',param[1]:1:3,' 10(-4) microns');
  writeln('b= ',param[2]:1:3,' 10(-4) microns');
  writeln('c= ',param[3]:1:3,' 10(-4) microns');
  writeln('cos a= ',ang[1]:1:2,'  cos b= ',ang[2]:1:2,
          '  cos c= ',ang[3]:1:2);                          *)
  writeln('surface ',rn[1]:4:0,rn[2]:4:0,rn[3]:4:0);
  writeln('reflection ',rf[1]:4:0,rf[2]:4:0,rf[3]:4:0);  writeln;
  writeln('image height ',height*1e06:1:1,'  microns');
  writeln('image point separation ',patry/2*1e06:1:2,'  microns');  writeln;
  writeln(maxplane:5,' calculated planes of incidence');
end;

procedure setup;
var i:integer;
begin


  dislocation:=false;
  precipitate:=false;
  curvature:=false;
  cylinder:=false;
  strip:=false;
  cyibox:=false;
  read(defect_code);                              (* *)
  if defect_code=1 then  dislocation:=true;
  if defect_code=2 then  precipitate:=true;
  if defect_code=4 then  curvature:=true;
  if defect_code=5 then begin dislocation:=true;
                              curvature:=true; end;
  if defect_code=6 then begin precipitate:=true;
                              curvature:=true; end;
  if defect_code=7 then cylinder:=true;
  if defect_code=8 then begin
                         dislocation:=true;
                         cylinder:=true
                        end;
  if defect_code=9 then strip:=true;
  if defect_code=10 then begin
                         strip:=true;
                         curvature:=true; end;
  if defect_code=11 then cylbox:=true;
  if defect_code=12 then begin
                          dislocation:=true;
                          cylbox:=true
                         end;
 readln(defect_code); if defect_code=0 then perfect:=false else perfect:=true;
 (*rewrite(data,'FILE=output.dat');*)
 (*  rewrite(data,'unit=2');          15 Oct 87   *)
  rewrite(data,'output');
  readln(kperfo);  io:=0;
  readln(lambda,theta,alpha,absorb);
  readln(qhio.re);
  readln(qhim.re,qhim.im);
  readln(qhip.re,qhip.im);
  readln(elem,thickness,deltat,width);
  readln(param[1],param[2],param[3],ang[1],ang[2],ang[3]);
  readln(rn[1],rn[2],rn[3],rf[1],rf[2],rf[3]);
  readln(height,pzy);

 (************************************)
```

```
(*                                 *)
(*      Geometry constants         *)
(*                                 *)
(**********************************)

  kappa:=pi/lambda;
  dir:=(alpha+2*theta)*pi/180;
  alt:=(alpha+theta)*pi/180;
  alpha:=alpha*pi/180;
  theta:=theta*pi/180;

(**********************************)
(*     Integration parameters     *)
(**********************************)

  transv:=elem*((sin(dir)/cos(dir))-(sin(alpha)/cos(alpha)));
  sq2:=0.5*elem*sin(dir)/cos(dir);
  p:=elem/cos(alpha);
  q:=elem/cos(dir);
  dv1:=pi*p/(2*lambda);
  dv2:=pi*q/(2*lambda);
  beta.re:=-deltat*sin(2*theta)-0.5*qhio.re*(cos(dir)/cos(alpha)-1);  ]- section α
  beta.im:=0;                                                         ]
  c1.re:=1-kappa*q*beta.im;                                           ]
  c2.re:=1+kappa*q*beta.im;                                           ]- section β
  w1:=-kappa*q*beta.re;                                               ]
  dielep.re:=dv1*qhim.im;
  dielep.im:=-dv1*qhim.re;
  dieleq.re:=dv2*qhip.im;
  dieleq.im:=-dv2*qhip.re;
  a:=dielep;
  b:=dieleq;
  cmult(a,b,ab);

  point_separation:=transv*kperfo;
  patry:=point_separation*cos(dir)*2;        (* for next line *)

  maxplane:=trunc(height/patry+0.5);          (** 22 NOV. 1991   **)
  maxplane:=maxplane+1;                       (** 22 NOV. 1991   **)

  if dislocation then  dislocn(da,xdis,zdis,dix,diz,cn,patry,q,param,ang,rn,rf);
  if precipitate then  pointdef(c,prno,prlim,iseed,xmin,xmax,ymin,ymax,
                              zmin,zmax,xc,yc,zc,gd,param,ang,rn,rf);
  if curvature then  curvedef(radius,gd,param,ang,rn,rf);
  if cylinder then cyldef(vfrac,xsi,psi,eps,xcyl0,ycyl0,zcyl0,zcrit,clength,
                                                     gd,param,ang,rn,rf);
  if strip then stripdef(flnth,ymod,delta,xedge,yedge,horiz,zdispl,
                                                     gd,param,ang,rn,rf);
  if cylbox then boxdef(c,ptno,ptlim,iseed,psi,eps,x,y,z,xcyl0,ycyl0,zcyl0,rmax,

  if width>transv then xcurve:=-width/2 else xcurve:=0;


  fen:=exp(absorb*sin(alt)*transv/(2*cos(theta)));
  fou:=exp(-absorb*sin(alt)*transv/cos(theta));

(***************************************)
(*   Integration control parameters   *)
(***************************************)

 (**  maxplane:=trunc(height/patry+0.5);  22 NOV. 1991    **)
 (**  maxplane:=maxplane+1;                    "          **)

  lmaxt:=trunc(thickness/elem+0.5);
  if transv>width then width:=transv;
  lmin:=trunc(width/transv+1.5);
```

```
  if (lmaxt+lmin)>(maxno-1) then lmax:=maxno-2 else lmax:=lmaxt+lmin-1;
if io=0 then writeln('lmin = ',lmin,' lmax = ',lmax,' ',lmax-lmin+1,' layers');
  limbe:=maxno+1-lmin;

  field:=1/sqrt((lmin-1)*cos(alpha));

display;

for i:=1 to maxno do begin
  phi[1,i].re:=0;
  phi[1,i].im:=0;
  phi[2,i].re:=0;
  phi[2,i].im:=0;
end;
trap;

(***********************************)
(*     Diff (dsh)  parameters      *)
(***********************************)

   shx1:=-sin(dir);       (* 9/3/88  shx1:=abs(cos(dir));  *)
   shx3:=cos(dir);        (* 9/3/88  shx2:=-abs(sin(dir)); *)

if dislocation then begin
  for i:=1 to 3 do begin
    co3[i]:=cn[i]*(sqr(cn[i+6])+cn[i+9]);
    co4[i]:=2*cn[i+3]*cn[i+6];
    co5[i]:=sqr(cn[i+6])+cn[i+9];
  end;
  ap1:=da[1,3]*abs(cos(dir))-da[1,1]*abs(sin(dir));
  ap2:=da[2,3]*abs(cos(dir))-da[2,1]*abs(sin(dir));
end;
  yd0:=2;      (* *)
  ip:=2;
  if io=0 then writeln(maxplane,'planes of incidence');
  dsh:=0;
end;

(*****************************************)
(*             Main Program              *)
(*****************************************)

begin
  setup;

if dislocation then begin
  writeln('position of dislocation in first plane');
  writeln('x = ',xdis);
  writeln('z = ',zdis);
end;

plane_num := 0;

  for plane:=1 to maxplane do begin   (* loop for each plane of incidence *)
    integrate;
    factor:=exp(-absorb*depth/cos(alpha));

    jj:=kperfo;
    rl:=1;
    for k:=limit to 4999 do begin
      jj:=jj+1;
      reflex[jj]:=factor*rl*(sqr(phi[2,k].re)+sqr(phi[2,k].im));
      rl:=rl*fou;
    end;
```

```
    results(jj,maxplane,store1,store2,data,mini,maxi,reflex,kperfo,limit,ip,io);
    if perfect then perfect:=false;

  end; (*  plane  *)

if dislocation then begin
  writeln('position of dislocation in last plane');
  writeln('x = ',xd0);
  writeln('z = ',zd0);
end;

    jj:=kperfo;
    for k:=limit to 4999 do
       jj:=jj+1;

  results(jj,maxplane,store1,store2,data,mini,maxi,reflex,kperfo,limit,200,io);

  close(data);
end.
```

Appendix B

A procedure *POINT.P*, written in Pascal, is listed, and represents the strain code for a precipitate.

```
(**********************************************)
(*                                            *)
(*  1/12/86 Segment checked and comments added *)
(*  11/1/87 Altered for point defect          *)
(*  12/2/87 Diffpoint added                   *)
(*  9/3/88  db corrected and output added     *)
(*  9/3/88  diffpoint corrected               *)
(*                                            *)
(**********************************************)

#include "globals.h"
#include "algebra.h"
#include "crystal.h"
#include "point.h"

type ivector=array[1..3] of integer;

var prno,prlim:integer;                     (* 25/1/91 ajh *)
    xc,yc,zc:larray;                        (* 25/1/91 ajh *)
    iseed:integer;                          (* RANDOM ajh *)
    xbot,xtop,ybot,ytop,zbot,ztop:real;

procedure diffpoint(var dsh:real;x,y,z,shx,shz,c:real;gd:vector);

var rsqr,t1,t2,dhdx1,dhdx3:real;
begin
  rsqr:=sqr(x)+sqr(y)+sqr(z);
  t2:=gd[1]*x+gd[2]*y+gd[3]*z;
  t1:=sqrt(sqr(rsqr)*rsqr);
  dhdx1:=(gd[1]-3*x*t2/rsqr)/t1;
  dhdx3:=(gd[3]-3*z*t2/rsqr)/t1;   (*  9/3/88  *)
  dsh:=dhdx1*shx+dhdx3*shz;        (*  9/3/88  *)
  dsh:=c*dsh;
end;

procedure pointdef(var c:real;var prno,prlim:integer;iseed:integer;
                   var xmin,xmax,ymin,ymax,zmin,zmax:real;var xc,yc,zc:larray;
                   var gd:vector;a,ang,rn,rf:vector); (*** RANDOM ajh ***)


var v:vector;
    i,m,n:integer;
    sm,sn,sp:real;
    g,r,dr,db:matrix;
    np,nq:ivector;

begin
  np[1]:=2; np[2]:=3; np[3]:=1;
  nq[1]:=3; nq[2]:=1; nq[3]:=2;
  readln(prlim); ———————————————— (*** 23/1/91 ajh ***) ─┐
  readln(c);     ———————————————— (*** RANDOM ajh ***)  ─┘── section α
  readln(xmin,xmax);                (*** RANDOM ajh ***)
  readln(ymin,ymax);                (*** RANDOM ajh ***)
  readln(zmin,zmax);                (*** RANDOM ajh ***)
  iseed:=seed(wallclock);           (*** RANDOM ajh ***)  ─┐
  for prno:=1 to prlim do begin     (*** RANDOM ajh ***)   │
    xc[prno]:=(xmin+(xmax-xmin)*random(0))*1.0E-06;   (* RANDOM **)  │
    yc[prno]:=(ymin+(ymax-ymin)*random(0))*1.0E-06;   (* RANDOM **)  ├── section β
    zc[prno]:=(zmin+(zmax-zmin)*random(0))*1.0E-06    (* RANDOM **)  │
                        end;        (*** RANDOM ajh ***)  ─┘
(**********************************************)
(*                                            *)
(*   Calculate transformation matrices and    *)
(*    transform  rf recip to elasticity       *)
(*               rn recip to elasticity       *)
```

```
(*                                              *)
(************************************************)

  crystal(g,r,dr,a,ang);
  vecrot(v,r,rf);
  vecrot(rf,dr,v);
  vecrot(v,r,rn);
  vecrot(rn,dr,v);

(************************************************)
(*                                              *)
(*      Calculate transformation matrices       *)
(*        db  elasticity to experiment          *)
(*                                              *)
(************************************************)
(*                                              *)
(*     Experiment axes :                        *)
(*       -x  proj of diffraction vector on surf *)
(*        y  perpendicular to incidence plane   *)
(*        z  inward perpendicular to surface    *)
(*                                              *)
(************************************************)

  sm:=0; sn:=0; sp:=0;
  for i:=1 to 3 do begin
    sm:=sm+sqr(rn[i]);
    sn:=sn+rn[i]*rf[i];
  end;
  for i:=1 to 3 do begin
    db[3,i]:=rn[i]/sqrt(sm);
    db[1,i]:=rn[i]*sn/sm-rf[i];      (* 9/3/88  db[1,i]:=rf[i]-rn[i]*sn/sm;   *)
    sp:=sp+sqr(db[1,i]);
  end;
  sm:=0;
  sp:=sqrt(sp);
  for i:=1 to 3 do begin
    db[1,i]:=db[1,i]/sp;
  end;
  for i:=1 to 3 do begin
    m:=np[i];
    n:=nq[i];
    db[2,i]:=db[1,n]*db[3,m]-db[1,m]*db[3,n];
  end;

  vecrot(gd,db,rf);

  writeln;
  writeln('In experimental coordinates diffraction vector is');
  writeln(gd[1],'  ',gd[2],'  ',gd[3]);
  writeln;
  writeln('POINT DEFECT');
  writeln;                                               (* 25/1/91 ajh *)
  writeln('PRECIPITATE COORDS (microns) ARE : ');        (*     "       *)
    for prno:=1 to prlim do begin                        (*     "       *)
  writeln(xc[prno]*1E06,yc[prno]*1E06,zc[prno]*1E06);    (*     "       *)
    end;                                                 (*     "       *)
  writeln;                                               (*     "       *)
  writeln('Size parameter is ',c);
  writeln;
end;
```

Appendix C

A procedure *CURVE.P*, written in Pascal, is listed, and represents the strain code for a curved crystal.

```
(**********************************************)
(*                                            *)
(*  13/3/87 Segment written                   *)
(*  17/5/55 db matrix corrected               *)
(*                                            *)
(**********************************************)

#include "globals.h"
#include "algebra.h"
#include "crystal.h"
#include "curve.h"

type ivector=array[1..3] of integer;

procedure diffcurve(var dsh:real;x,z,sh1,sh2,t,r:real;gd:vector);

var v1,v2,theta,xbar,vbar,dhdx1,dhdx2:real;
begin
  v1:=z-t/2;
  v2:=r+z;
  theta:=arctan( x/( sqrt(1-sqr(x/v2))*v2 ) );
  xbar:=x/v2;
  vbar:=v1/v2;
  dhdx1:=( gd[1]*(1-xbar*(xbar-theta)) -
         gd[3]*(xbar*(1-sqr(xbar))+theta*(1-sqr(xbar))) )*vbar;
dhdx1:=dhdx1-gd[3]*xbar*(1-sqr(xbar));
  dhdx2:=theta*( gd[1]-gd[3]*(1-vbar)*xbar );
dhdx2:=dhdx2-gd[3]*v1*xbar;

(* theta:=x/(r+t/2);
   rr:=(r+z)/(r+t/2);
dhdx1:=gd[1]*rr*(cos(theta)-1) - gd[3]*rr*sin(theta);
dhdx2:=gd[1]*sin(theta) + gd[3]*(cos(theta)-1);           *)
  dsh:=dhdx1*sh1+dhdx2*sh2;
end;

procedure curvedef(var radius:real;var gd:vector;
                  a,ang,rn,rf:vector);
{
const np=ivector(2,3,1);
      nq=ivector(3,1,2);
}
var v:vector;
    i,m,n:integer;
    sm,sn,sp:real;
    g,r,dr,db:matrix;
    np,nq:ivector;

begin
  np[1]:=2; np[2]:=3; np[3]:=1;
  nq[1]:=3; nq[2]:=1; nq[3]:=2;
  readln(radius);
  write('Radius of curvature');
  writeln(radius:1.3,' metre');

(**********************************************)
(*                                            *)
(*   Calculate transformation matrices and    *)
(*    transform  rf recip to elasticity       *)
(*               rn recip to elasticity       *)
(*                                            *)
(**********************************************)

  crystal(g,r,dr,a,ang);
  vecrot(v,r,rf);
  vecrot(rf,dr,v);
```

```
  vecrot(v,r,rn);
  vecrot(rn,dr,v);

(**********************************************)
(*                                            *)
(*     Calculate transformation matrices      *)
(*       db  elasticity to experiment         *)
(*                                            *)
(**********************************************)
(*                                            *)
(*     Experiment axes :                      *)
(*       x                                    *)
(*       y  perpendicular to incidence plane  *)
(*       z  inward perpendicular to surface   *)
(*                                            *)
(**********************************************)

  sm:=0; sn:=0; sp:=0;
  for i:=1 to 3 do begin
    sm:=sm+sqr(rn[i]);
    sn:=sn+rn[i]*rf[i];
  end;
  for i:=1 to 3 do begin
    db[3,i]:=rn[i]/sqrt(sm);
    db[1,i]:=rn[i]*sn/sm-rf[i];    (* 17/5/88 db[1,i]:=rf[i]-rn[i]*sn/sm; *)
    sp:=sp+sqr(db[1,i]);
  end;
  writeln('db corrected');          (* 17/5/88 *)
  sm:=0;
  sp:=sqrt(sp);
  for i:=1 to 3 do begin
    db[1,i]:=db[1,i]/sp;
  end;
  for i:=1 to 3 do begin
    m:=np[i];
    n:=nq[i];
    db[2,i]:=db[1,n]*db[3,m]-db[1,m]*db[3,n];
  end;

  vecrot(gd,db,rf);

end;
```

Appendix D

A procedure *DISLOC.P*, written in Pascal, is listed in APPENDIX D1, and represents the strain code for a dislocation. The procedure *DISLCALC.P*, listed in APPENDIX D2, is used to calculate the elastic parameters of the dislocation.

APPENDIX D1

```
(*********************************************)
(*                                           *)
(*  1/12/86 Segment checked and comments added  *)
(*  12/2/87 Diffdisl procedure added          *)
(*  3/11/87 Disl altered to Recip. Lattice i/p  *)
(*  3/11/87 Corrected x direction in matrix db  *)
(*                                           *)
(*********************************************)

#include "globals.h"

type ivector=array[1..3] of integer;
     cmatrix=array[1..3,1..3] of complex;
     cvector=array[1..3] of complex;
     carray=array[1..12] of real;

#include "complex.h"
#include "crystal.h"
#include "algebra.h"
#include "dislcalc.h"
#include "disloc.h"

procedure diffdisl(var dsh:real;x1,x2,ap1,ap2:real;co3,co4,co5:vector;
                   cn:carray);

var x4,dh1x1,dh1x2:real;
    co1,co2:vector;
    i:integer;

begin
  if abs(x2)>=0.1E-10 then begin
    x4:=sqr(x2);
    dh1x1:=0;
    dh1x2:=0;
    for i:=1 to 3 do begin
      co1[i]:=x1-cn[i-6]*x2;
      co2[i]:=x2*co3[i];
(*    temp2:=cn[i]*x1;
      temp2:=temp2+cn[i-3]*x2;
      temp2:=temp2/ ( sqr(co1[i])+cn[i+9]*x4 );
      dh1x2:=dh1x2+temp2;
      temp1:=co4[i]*x2-co2[i];
      temp1:=temp1+cn[i+3]*x1;
      temp1:=temp1/( (sqr(co1[i])+cn[i+9]*x4)*co5[i] );
      dh1x1:=dh1x1+temp1;                                        *)
      dh1x2:=dh1x2+(cn[i]*x1+cn[i+3]*x2)/(sqr(co1[i])-cn[i+9]*x4);
      dh1x1:=dh1x1+(cn[i-3]*x1-co2[i]+co4[i]*x2)/
                   ((sqr(co1[i])+cn[i+9]*x4)*co5[i]);
    end;
    dsh:=dh1x1*ap1+dh1x2*ap2;
  end;
end;


procedure dislocn(var da:matrix;var xc,zc,dix,diz:real;
                 var cn:carray;patry,q:real;a,ang,rn,rf:vector);
{
const np=ivector(2,3,1);
      nq=ivector(3,1,2);
}
var b,disl,v,gd,bd:vector;
    i,j,k,l,m,n,mn:integer;
    sm,sn,sp:real;
    bt:array[1..21] of real;
    g,r,dr,db,dc,h:matrix;
```

```
    cc,c:tensor;
    d,p,su:cvector;
    el,em,a2,u,v2:cmatrix;
    np,nq:ivector;

procedure initialise;

begin
  np[1]:=2; np[2]:=3; np[3]:=1;
  nq[1]:=3; nq[2]:=1; nq[3]:=2;
  readln(b[1],b[2],b[3],disl[1],disl[2],disl[3]);
  writeln('Burgers vector = ',b[1]:1:3,'  ',b[2]:1:3,'  ',b[3]:1:3);
  writeln('dislocation orientation ',disl[1]:1:0,'  ',disl[2]:1:0,'  ',
                                                     disl[3]:1:0);
  readln(xc,zc);
  write('position of the core in the first plane ');
  writeln(xc:1:3,'  ',zc:1:3,' microns');
  writeln('elastic stiffnesses');
end;

begin
  initialise;

(**********************************************)
(*                                            *)
(*   Calculate transformation matrices and    *)
(*    transform  b  crystal to elasticity     *)
(*               rf recip to elasticity       *)
(*               rn recip to elasticity       *)
(*               disl recip to elasticity     *)
(*                                            *)
(**********************************************)

  crystal(g,r,dr,a,ang);
  vecrot(v,dr,b);
  b:=v;
  vecrot(v,r,rf);
  vecrot(rf,dr,v);
  vecrot(v,r,rn);
  vecrot(rn,dr,v);

  vecrot(v,r,disl);
  vecrot(disl,dr,v);

(**********************************************)
(*                                            *)
(*     Calculate transformation matrix        *)
(*       db  elasticity to experiment         *)
(*                                            *)
(**********************************************)
(*                                            *)
(*    Experiment axes :                       *)
(*       x  projection of opposite direction  *)
(*          to diffraction vector onto surface *)
(*       y  perpendicular to incidence plane  *)
(*       z  inward perpendicular to surface   *)
(*                                            *)
(**********************************************)

  sm:=0; sn:=0; sp:=0;
  for i:=1 to 3 do begin
    sm:=sm+sqr(rn[i]);
    sn:=sn+rn[i]*rf[i];
  end;
  for i:=1 to 3 do begin
    db[3,i]:=rn[i]/sqrt(sm);
```

```
    db[1,i]:=rn[i]*sn/sm-rf[i];     (* db[1,i]:=rf[i]-rn[i]*sn/sm;    *)
writeln(' NEW VERSION');
    sp:=sp+sqr(db[1,i]);
  end;
  sp:=sqrt(sp);
  for i:=1 to 3 do db[1,i]:=db[1,i]/sp;
  for i:=1 to 3 do begin
    m:=np[i];
    n:=nq[i];
    db[2,i]:=db[1,n]*db[3,m]-db[1,m]*db[3,n];
  end;

(***********************************************)
(*                                             *)
(*   Transform disl elasticity to experiment   *)
(*                                             *)
(***********************************************)
vecrot(v,db,disl);
disl:=v;
sm:=0;
for i:=1 to 3 do sm:=sm+sqr(disl[i]);
sm:=sqrt(sm);
for i:=1 to 3 do disl[i]:=disl[i]/sm;
if disl[2]=0 then disl[2]:=1E-10
else if disl[2]<0 then for i:=1 to 3 do disl[i]:=-disl[i];
writeln('dislocation direction ',disl[1]:1:3,'  ',disl[2]:1:3,'  ',
                                                   disl[3]:1:3);
  dix:=patry*disl[1]/disl[2];
  diz:=patry*disl[3]/disl[2];

(***********************************************)
(*                                             *)
(*      Calculate transformation matrices      *)
(*        da  experiment to dislocation        *)
(*        dc  elasticity to dislocation        *)
(*                                             *)
(***********************************************)
(*                                             *)
(*     Dislocation axes :                      *)
(*        1  lies in plane of incidence        *)
(*        2                                    *)
(*        3  parallel to dislocation line      *)
(*                                             *)
(***********************************************)

  sm:=0;
  for i:=1 to 3 do begin
    da[3,i]:=disl[i];
    sm:=sm+sqr(da[3,i]);
  end;
  if (disl[1]=0) and (disl[3]=0) then begin
    da[1,1]:=1;
    da[1,2]:=0;
    da[1,3]:=0;
  end else begin
    sp:=sqrt(sqr(disl[1])+sqr(disl[3]));
    da[1,1]:=disl[3]/sp;
    da[1,2]:=0;
    da[1,3]:=-disl[1]/sp;
  end;
  for i:=1 to 3 do da[3,i]:=da[3,i]/sqrt(sm);
  for i:=1 to 3 do begin
    m:=np[i];
    n:=nq[i];
    da[2,i]:=da[1,n]*da[3,m]-da[1,m]*da[3,n];
  end;
```

```
(**********************************************)
(*                                            *)
(*            Calculate dc=da*db              *)
(*                                            *)
(**********************************************)

 for i:=1 to 3 do begin
   for j:=1 to 3 do begin
     dc[i,j]:=0;
     for k:=1 to 3 do dc[i,j]:=dc[i,j]+da[i,k]*db[k,j];
   end;
 end;

(**********************************************)
(*                                            *)
(*   Read in elastic constants and print out  *)
(*                                            *)
(**********************************************)

  for i:=1 to 10 do read(bt[i]); readln(bt[11]);
  for i:=12 to 21 do read(bt[i]);
  for m:=1 to 6 do begin
    for n:=1 to 6 do begin
      mn:=m+trunc((12-n)*(n-1)/2);
      cc[m,n]:=bt[mn];
      cc[n,m]:=bt[mn];
    end;
  end;
  for i:=1 to 6 do begin
    for j:=1 to i do write(cc[i,j]:8:3);
    writeln;
  end;
  tensrot(c,cc,dc);
  vecrot(gd,dc,rf);
  for i:=1 to 3 do v[i]:=b[i]*q/2;
  vecrot(bd,dc,v);
  defcalc(h,el,em,a2,p,c);
  for i:=1 to 3 do begin
    su[i].re:=0;
    su[i].im:=0;
    for k:=1 to 3 do begin
      su[i].re:=su[i].re+gd[k]*a2[k,i].re;
      su[i].im:=su[i].im+gd[k]*a2[k,i].im;
    end;
    cmult(su[i],p[i],d[i]);
  end;
  for i:=1 to 3 do begin
    for l:=1 to 3 do begin
      u[i,l].re:=0;
      u[i,l].im:=0;
      for j:=1 to 3 do begin
        u[i,l].re:=u[i,l].re+em[i,j].re*h[j,l];
        u[i,l].im:=u[i,l].im+em[i,j].im*h[j,l];
      end;
    end;
  end;
  for i:=1 to 3 do begin
    for l:=1 to 3 do cmult(d[i],u[i,l],v2[i,l]);
  end;
  for i:=1 to 3 do begin
    for l:=1 to 3 do  u[i,l].im:=v2[i,l].re*p[i].re+v2[i,l].im*p[i].im;
  end;
  for j:=1 to 3 do begin
    cn[j+6]:=p[j].re;
    cn[j+9]:=sqr(p[j].im);
```

```
        cn[j]:=0;
        cn[j+3]:=0;
        for l:=1 to 3 do begin
          cn[j]:=cn[j]+v2[j,l].re*bd[l];
          cn[j+3]:=cn[j+3]+u[j,l].im*bd[l];
        end;
      end;
    end;
```

APPENDIX D2

```
(**********************************************)
(*                                            *)
(* 21/11/86 Segment checked and comments added *)
(*                                            *)
(**********************************************)
(*                                            *)
(* References:                                *)
(*                                            *)
(* Hirth & Lothe  "Theory of Dislocations" p418 *)
(* Stroh          Phil. Mag. 3 p625 (1958)    *)
(*                                            *)
(**********************************************)

#include "globals.h"
#include "complex.h"
#include "newton.h"

type quadratic=array[1..3] of real;
     ivector=array[1..3] of integer;
     cmatrix=array[1..3,1..3] of complex;
     cvector=array[1..3] of complex;


procedure defcalc(var h:matrix;var el,em,a:cmatrix;var p:cvector;c:tensor);

var i,j,k,l,m,n,n2,i1,i2,j1,j2,ni,nk,mk,t,k1,k2:integer;
    q1,q2,q3,q4,q5,q6:quadratic;
    qq2,qq3,qq:coefficients;
    z,dum,dum1,dum2,pp,sq,x,y,del,aum,zero:complex;
    np,nq,mm,nn:ivector;
    b:matrix;
    d:cmatrix;


begin
  np[1]:=2;  np[2]:=3;  np[3]:=1;
  nq[1]:=3;  nq[2]:=1;  nq[3]:=2;
  mm[1]:=1;  mm[2]:=6;  mm[3]:=5;
  nn[1]:=6;  nn[2]:=2;  nn[3]:=4;
  zero.re:=0; zero.im:=0;

(**********************************************)
(*                                            *)
(*    Coefficients of (13-86) Hirth & Lothe   *)
(*                                            *)
(**********************************************)

  q1[1]:=c[1,1];  q1[2]:=2*c[1,6];       q1[3]:=c[6,6];
  q2[1]:=c[6,6];  q2[2]:=2*c[2,6];       q2[3]:=c[2,2];
  q3[1]:=c[5,5];  q3[2]:=2*c[4,5];       q3[3]:=c[4,4];
  q4[1]:=c[1,6];  q4[2]:=c[1,2]+c[6,6];  q4[3]:=c[6,2];
  q5[1]:=c[1,5];  q5[2]:=c[1,4]+c[6,5];  q5[3]:=c[6,4];
  q6[1]:=c[5,6];  q6[2]:=c[6,4]+c[2,5];  q6[3]:=c[4,2];

(**********************************************)
(*                                            *)
(*    Coefficients of (13-85) Hirth & Lothe   *)
(*                                            *)
(**********************************************)

  for i:=1 to 7 do qq[i]:=zero;
  for i:=1 to 3 do begin
    for j:=1 to 3 do begin
      for k:=1 to 3 do begin
        t:=i+j+k-2;
        qq[t].re:=qq[t].re+q3[i]*q2[j]*q1[k]+2*q6[i]*q5[j]*q4[k]
```

```
                 -q6[i]*q6[j]*q1[k]-q5[i]*q5[j]*q2[k]-q4[i]*q4[j]*q3[k];
      end;
    end;
  end;

(*************************************************)
(*                                               *)
(*      Solution of (13-85) Hirth & Lothe        *)
(*                                               *)
(*************************************************)

  for i:=1 to 7 do begin
                     qq[i].re:=qq[i].re/qq[7].re;
                     qq[i].im:=0;
                   end;
  z.re:=0.1; z.im:=1;
  solve(6,qq,qq2,z,false);
  p[1].re:=z.re;
  p[1].im:=abs(z.im);
  z.im:=-z.im;
  solve(5,qq2,qq3,z,false);
  z.re:=0.5; z.im:=0.9;
  solve(4,qq3,qq2,z,false);
(*solve(6,qq,qq3,z,false);*)
  p[2].re:=z.re;
  p[2].im:=abs(z.im);
  z.im:=-z.im;
  solve(3,qq2,qq3,z,false);
  z.re:=-z.re;
  solve(2,qq3,qq2,z,false);
(*solve(6,qq,qq3,z,false);*)
  p[3].re:=z.re;
  p[3].im:=abs(z.im);

(*************************************************)
(*                                               *)
(*     Sort solutions Pn into correct order      *)
(*                                               *)
(*************************************************)

  z.re:=-c[4,5]/c[4,4];
  z.im:=sqrt(abs(c[4,4]*c[5,5]-sqr(c[4,5])))/c[4,4];
  for n2:=1 to 2 do
  begin
    if (sqr(z.re-p[n2].re)-sqr(z.im-p[n2].im)
     - -sqr(z.re-p[n2+1].im)-sqr(z.im-p[n2+1].im))<0 then
    begin
      dum:=p[n2];
      p[n2]:=p[n2+1];
      p[n2+1]:=dum;
    end;
  end;

(*************************************************)
(*                                               *)
(* Calculate d(i,k)=aik(n) (13-86) Hirth & Lothe *)
(*                                               *)
(*************************************************)

  for n:=1 to 3 do begin
    pp:=p[n];
    sq.re:=sqr(pp.re)-sqr(pp.im);
    sq.im:=2*pp.re*pp.im;
    d[1,1].re:=c[1,1]+2*c[1,6]*pp.re+c[6,6]*sq.re;
    d[1,1].im:=2*c[1,6]*pp.im+c[6,6]*sq.im;
    d[2,2].re:=c[6,6]+2*c[2,6]*pp.re+c[2,2]*sq.re;
```

```
    d[2,2].im:=2*c[2,6]*pp.im+c[2,2]*sq.im;
    d[3,3].re:=c[5,5]+2*c[4,5]*pp.re+c[4,4]*sq.re;
    d[3,3].im:=2*c[4,5]*pp.im+c[4,4]*sq.im;
    d[1,2].re:=c[1,6]+(c[1,2]+c[6,6])*pp.re+c[2,6]*sq.re;
    d[1,2].im:=(c[1,2]+c[6,6])*pp.im+c[2,6]*sq.im;
    d[2,1]:=d[1,2];
    d[1,3].re:=c[1,5]+(c[1,4]+c[5,6])*pp.re+c[4,6]*sq.re;
    d[1,3].im:=(c[1,4]+c[5,6])*pp.im+c[4,6]*sq.im;
    d[3,1]:=d[1,3];
    d[2,3].re:=c[5,6]+(c[4,6]+c[2,5])*pp.re+c[2,4]*sq.re;
    d[2,3].im:=(c[4,6]+c[2,5])*pp.im+c[2,4]*sq.im;
    d[3,2]:=d[2,3];

(**************************************************)
(*                                                *)
(*      Solve (13-87) to get a(k,n)=Ak(n)         *)
(*                                                *)
(**************************************************)

    i:=np[n];
    j:=nq[n];
    for k:=1 to 3 do begin
      l:=np[k];
      m:=nq[k];
      cmult(d[i,l],d[j,m],dum1);
      cmult(d[i,m],d[j,l],dum2);
      csub(dum1,dum2,a[k,n]);
    end; (* k loop *)
  end; (* n loop *)

(**************************************************)
(*                                                *)
(* Calculate Bi2k(n)      (13-90) Hirth & Lothe   *)
(*    and hence                                   *)
(* el(i,n)=Bi2k(n)Ak(n)                           *)
(*        =Li(a)                     (14) Stroh   *)
(*                                                *)
(**************************************************)

  for i:=1 to 3 do begin
    ni:=nn[i];
    for n:=1 to 3 do begin
      x.re:=0;
      x.im:=0;
      for k:=1 to 3 do begin
        nk:=nn[k];
        mk:=mm[k];
        y.re:=c[ni,mk]+c[ni,nk]*p[n].re;
        y.im:=c[ni,nk]*p[n].im;
        cmult(y,a[k,n],dum1);
        cadd(x,dum1,x);
      end; (* k loop *)
      el[i,n]:=x;
    end; (* n loop *)
  end; (* i loop *)

(**************************************************)
(*                                                *)
(*     Calculate em(j,k)=Mai      (37) Stroh      *)
(*                                                *)
(**************************************************)

  for j:=1 to 3 do begin
    j1:=np[j];
    j2:=nq[j];
    for k:=1 to 3 do begin
```

```
      k1:=np[k];
      k2:=nq[k];
      cmult(el[j1,k1],el[j2,k2],dum1);
      cmult(el[j1,k2],el[j2,k1],dum2);
      csub(dum1,dum2,em[k,j]);
    end; (* k loop *)
  end; (*j loop *)
  del.re:=0;
  del.im:=0;
  for j:=1 to 3 do begin
    cmult(el[3,j],em[j,3],dum1);
    cadd(del,dum1,del);
  end; (* j loop *)
  aum.re:=del.re/(sqr(del.re)+sqr(del.im));
  aum.im:=-del.im/(sqr(del.re)+sqr(del.im));
  for j:=1 to 3 do begin
    for k:=1 to 3 do begin
      cmult(em[j,k],aum,dum1);
      em[j,k]:=dum1;
    end; (* k loop *)
  end; (* j loop *)

(**************************************************)
(*                                                *)
(*    Calculate b[i,j]=Bij          (40) Stroh    *)
(*                                                *)
(**************************************************)

  for i:=1 to 3 do begin
    for j:=1 to 3 do begin
      b[i,j]:=0;
      for k:=1 to 3 do begin
        cmult(a[i,k],em[k,j],dum1);
        b[i,j]:=b[i,j]-dum1.im;
      end; (* k loop *)
    end; (* j loop *)
  end; (* i loop *)

(**************************************************)
(*                                                *)
(*        Calculate h[i,j]=inverse of Bij         *)
(*                                                *)
(**************************************************)

  for i:=1 to 3 do begin
    i1:=np[i];
    i2:=nq[i];
    for j:=1 to 3 do begin
      j1:=np[j];
      j2:=nq[j];
      h[i,j]:=b[i1,j1]*b[i2,j2]-b[i1,j2]*b[i2,j1];
    end; (* j loop *)
  end; (* i loop *)
  del.re:=b[3,1]*h[3,1]+b[3,2]*h[3,2]+b[3,3]*h[3,3];
  for i:=1 to 3 do begin
    for j:=1 to 3 do  h[i,j]:=h[i,j]/del.re;
  end; (* i loop *)

end;
```

Appendix E

A procedure *CYLINDER.P*, written in Pascal, is listed, and represents the strain code for a cylindrical inclusion.

```
(*************************************************)
(*                                               *)
(*  24/4/91 Procedures for calculating the       *)
(*          strain-field & inputting the         *)
(*          defect data for a cylindrical        *)
(*          defect.                              *)
(*                                               *)
(*                                               *)
(*************************************************)

#include "globals.h"
#include "algebra.h"
#include "crystal.h"
#include "cylinder.h"                                (*** cylinder ***)

type ivector=array[1..3] of integer;

const pi=3.14159;

var xcyl0,ycyl0,zcyl0,vfrac,xsi,psi,eps,zcrit,clength,dir:real;

procedure diffcyl(var dsh:real;x,y,z,xsi,psi,eps:real;gd:vector);

var acyl,s,t,u,ess,ett,est,ets,gs,gt1,gt2,gt,shs,sht:real;      (** u **)
    t1,t2,u1,u2:real;                                           (** u **)
    xcrit,ycrit,cylinc,ucrit,ucrit1,ucrit2:real;                (** u **)
    utest1,utest2,psitest,epstest:boolean;                      (** u **)

begin
  acyl:=-vfrac*1.28/2.16;    (*** FOR Si ONLY, i.e. nu = 0.28 ***) ---- line A
  if psi=90.0*pi/180.0 then psitest:=true;     --+
  if psi=270.0*pi/180.0 then psitest:=true;      |
  if eps=90.0*pi/180.0 then epstest:=true;       |-- section α
  if eps=270.0*pi/180.0 then epstest:=true;      |
  if psitest then begin                          |
          psi:=psi - 2.0*pi/180.0                |
               end;                              |
  if epstest then begin                          |
          eps:=eps - 2.0*pi/180.0                |
               end;                            --+
  cylinc:=(zcrit-zcyl0)/(cos(eps)*cos(psi)); ---- line B
  u1:=sin(psi)*cos(eps)*(x-xcyl0);
  u2:=sin(eps)*(y-ycyl0) + cos(psi)*cos(eps)*(z-zcyl0);
  u:=u1+u2;
  if zcrit=zcyl0 then begin                    --+
         xcrit:=xcyl0 + clength*cos(eps);        |
         ycrit:=ycyl0 + clength*sin(eps)         |
                      end                        |
    else begin                                   |-- section β
              xcrit:=xcyl0 + cylinc*cos(eps)*sin(psi);
              ycrit:=ycyl0 + cylinc*sin(eps)     |
              end;                             --+
  ucrit1:=sin(psi)*cos(eps)*(xcrit-xcyl0);     --+
  ucrit2:=sin(eps)*(ycrit-ycyl0) + cos(psi)*cos(eps)*(zcrit-zcyl0); -- section γ
  ucrit:=ucrit1 + ucrit2;                      --+
    if u >= 0.0 then utest1:=true; ---- line C
    if u <= ucrit then utest2:=true;
    if utest1 and utest2 then begin
  s:=cos(psi)*(x-xcyl0) - sin(psi)*(z-zcyl0);
  t1:=-sin(psi)*sin(eps)*(x-xcyl0);
  t2:=cos(eps)*(y-ycyl0) - cos(psi)*sin(eps)*(z-zcyl0);
  t:=t1 + t2;
  ess:=acyl*sqr(xsi)*(sqr(s) - sqr(t))/sqr(sqr(s) + sqr(t));
  ett:=-ess;
  est:=acyl*sqr(xsi)*2.0*s*t/sqr(sqr(s) + sqr(t));
```

```
  ets:=est;
  gs:=gd[1]*cos(psi) - gd[3]*sin(psi);
  gt1:=-gd[1]*sin(eps)*sin(psi) + gd[2]*cos(eps);
  gt2:=-gd[3]*sin(eps)*cos(psi);
  gt:=gt1 + gt2;
  shs:=-cos(psi)*sin(dir) - sin(psi)*cos(dir);
  sht:=sin(eps)*sin(psi)*sin(dir) - sin(eps)*cos(psi)*cos(dir);
  dsh:=shs*(gs*ess + gt*ets) + sht*(gs*est + gt*ett)
          end
    else dsh:=0.0;
end;

procedure cyldef(var vfrac,xsi,psi,eps,xcyl0,ycyl0,zcyl0,zcrit,clength:real;
                 var gd:vector;a,ang,rn,rf:vector);

const pi=3.14159;

var v:vector;
    i,m,n:integer;
    sm,sn,sp:real;
    g,r,dr,db:matrix;
    np,nq:ivector;

begin
  np[1]:=2; np[2]:=3; np[3]:=1;
  nq[1]:=3; nq[2]:=1; nq[3]:=2;
  readln(vfrac);
  readln(xsi);
  readln(psi);
  readln(eps);
  readln(xcyl0,ycyl0,zcyl0);
  readln(zcrit,clength);
  xsi:=xsi*1.0E-06;
  psi:=psi*pi/180;
  eps:=eps*pi/180;
  xcyl0:=xcyl0*1.0E-06;
  ycyl0:=ycyl0*1.0E-06;
  zcyl0:=zcyl0*1.0E-06;
  zcrit:=zcrit*1.0E-06;
  clength:=clength*1.0E-06;

(*************************************************)
(*                                               *)
(*   Calculate transformation matrices and       *)
(*    transform  rf recip to elasticity          *)
(*               rn recip to elasticity          *)
(*                                               *)
(*************************************************)

 writeln(rf[1], rf[2], rf[3]);

  crystal(g,r,dr,a,ang);
  vecrot(v,r,rf);
  vecrot(rf,dr,v);
  vecrot(v,r,rn);
  vecrot(rn,dr,v);

(*************************************************)
(*                                               *)
(*      Calculate transformation matrices        *)
(*        db  elasticity to experiment           *)
(*                                               *)
(*************************************************)
(*                                               *)
(*     Experiment axes :                         *)
(*       -x  proj of diffraction vector on surf *)
```

```
(*        y  perpendicular to incidence plane     *)
(*        z  inward perpendicular to surface      *)
(*                                                *)
(************************************************)

  sm:=0; sn:=0; sp:=0;
  for i:=1 to 3 do begin
    sm:=sm+sqr(rn[i]);
    sn:=sn+rn[i]*rf[i];
  end;
  for i:=1 to 3 do begin
    db[3,i]:=rn[i]/sqrt(sm);
    db[1,i]:=rn[i]*sn/sm-rf[i];       (* 9/3/88  db[1,i]:=rf[i]-rn[i]*sn/sm;   *)
    sp:=sp+sqr(db[1,i]);
  end;
  sm:=0;
  sp:=sqrt(sp);
  for i:=1 to 3 do begin
    db[1,i]:=db[1,i]/sp;
  end;
  for i:=1 to 3 do begin
    m:=np[i];
    n:=nq[i];
    db[2,i]:=db[1,n]*db[3,m]-db[1,m]*db[3,n];
  end;

  vecrot(gd,db,rf);

  writeln;
  writeln('In experimental coordinates diffraction vector is');
  writeln(gd[1],'  ',gd[2],'  ',gd[3]);
  writeln;
  writeln('CYLINDRICAL INCLUSION');
  writeln;
  writeln('X,Y,Z COORDS (microns) NEAR PT. OF INCLUSION ARE : ');
  writeln(xcyl0*1E06,ycyl0*1E06,zcyl0*1E06);
  writeln;
  writeln('RADIUS OF INCLUSION (microns) IS : ');
  writeln(xsi*1.0E06);
  writeln;
  writeln('VALUES OF ANGLES PSI, EPSILON (degrees) ARE : ');
  writeln(psi*180.0/pi,eps*180.0/pi);
  writeln(' ',' ',' ','respectively');
  writeln
end;
```

Appendix F

A procedure $CYLBOX.P$, written in Pascal, is listed, and represents the strain code for a cylindrical distribution of precipitates.

```
(**********************************************)
(*                                            *)
(*  1/12/86 Segment checked and comments added *)
(*  11/1/87 Altered for point defect          *)
(*  12/2/87 Diffpoint added                   *)
(*  9/3/88  db corrected and output added     *)
(*  9/3/88  diffpoint corrected               *)
(*                                            *)
(**********************************************)

#include "globals.h"
#include "algebra.h"
#include "crystal.h"
#include "cylbox.h"

type ivector=array[1..3] of integer;

const pi=3.14159;

var xbox,ybox,zbox:zarray;


procedure diffbox(var dsh:real;x,y,z,shx,shz,c:real;gd:vector);

var rsqr,t1,t2,dhdx1,dhdx3:real;
begin
  rsqr:=sqr(x)+sqr(y)+sqr(z);
  t2:=gd[1]*x+gd[2]*y+gd[3]*z;
  t1:=sqrt(sqr(rsqr)*rsqr);
  dhdx1:=(gd[1]-3*x*t2/rsqr)/t1;
  dhdx3:=(gd[3]-3*z*t2/rsqr)/t1;     (*  9/3/88  *)
  dsh:=dhdx1*shx+dhdx3*shz;          (*  9/3/88  *)
  dsh:=c*dsh;
end;

procedure boxdef(var c:real;var ptno,ptlim,iseed:integer;var psi,eps:real;
                 x,y,z:real;var xcyl0,ycyl0,zcyl0:real;
                 var rmax,zcrit,clength:real;var xbox,ybox,zbox:zarray;
                 var gd:vector;a,ang,rn,rf:vector);


var v:vector;
    i,m,n:integer;
    sm,sn,sp:real;
    g,r,dr,db:matrix;
    np,nq:ivector;
    rbox,thetrnd:real;
    psitest,epstest:boolean;
    cylinc,u1,u2,u,xcrit,ycrit,ucrit1,ucrit2,ucrit:real;
    sbox,tbox,ubox:zarray;
    xbox1,xbox2,zbox1,zbox2:real;

begin
  np[1]:=2; np[2]:=3; np[3]:=1;
  nq[1]:=3; nq[2]:=1; nq[3]:=2;
  readln(c);
  readln(ptlim);
  readln(psi,eps);
  readln(xcyl0,ycyl0,zcyl0);
  readln(rmax,zcrit,clength);
    psi:=psi*pi/180;
    eps:=eps*pi/180;
    xcyl0:=xcyl0*1.0E-06;
    ycyl0:=ycyl0*1.0E-06;
    zcyl0:=zcyl0*1.0E-06;
```

section α

```
  rmax := rmax*1E-06;
  zcrit := zcrit*1E-06;
  clength:=clength*1.0E-06;


if psi=90.0*pi/180.0 then psitest:=true;
if psi=270.0*pi/180.0 then psitest:=true;
if eps=90.0*pi/180.0 then epstest:=true;
if eps=270.0*pi/180.0 then epstest:=true;
if psitest then begin
        psi:=psi - 2.0*pi/180.0
                end;
if epstest then begin
        eps:=eps - 2.0*pi/180.0
                end;
cylinc:=(zcrit-zcyl0)/(cos(eps)*cos(psi));
u1:=sin(psi)*cos(eps)*(x-xcyl0);
u2:=sin(eps)*(y-ycyl0) + cos(psi)*cos(eps)*(z-zcyl0);
u:=u1+u2;
if zcrit=zcyl0 then begin
       xcrit:=xcyl0 + clength*cos(eps);
       ycrit:=ycyl0 + clength*sin(eps)
                     end
  else begin
             xcrit:=xcyl0 + cylinc*cos(eps)*sin(psi);
             ycrit:=ycyl0 + cylinc*sin(eps)
             end;
ucrit1:=sin(psi)*cos(eps)*(xcrit-xcyl0);                             ─┐
ucrit2:=sin(eps)*(ycrit-ycyl0) + cos(psi)*cos(eps)*(zcrit-zcyl0);     ├── section β
ucrit:=ucrit1 + ucrit2;                                               ─┘

iseed:=seed(wallclock);                                               ─┐
  for ptno:=1 to ptlim do begin                                        │
      rbox:=rmax*random(0);                                            ├── section γ
      thetrnd:=2*pi*random(0);                                         │
      sbox[ptno]:=rbox*cos(thetrnd);                                   │
      tbox[ptno]:=rbox*sin(thetrnd);                                   │
      ubox[ptno]:=ucrit*random(0);                                    ─┘
      xbox1:=sbox[ptno]*cos(psi)-tbox[ptno]*sin(psi)*sin(eps);
      xbox2:=ubox[ptno]*sin(psi)*cos(eps)+xcyl0;
      xbox[ptno]:=xbox1+xbox2;
      ybox[ptno]:=tbox[ptno]*cos(eps)+ubox[ptno]*sin(eps)+ycyl0;
      zbox1:=-sbox[ptno]*sin(psi)-tbox[ptno]*cos(psi)*sin(eps);
      zbox2:=ubox[ptno]*cos(psi)*cos(eps)+zcyl0;
      zbox[ptno]:=zbox1+zbox2
                         end;


(**********************************************)
(*                                            *)
(*   Calculate transformation matrices and    *)
(*    transform  rf recip to elasticity       *)
(*               rn recip to elasticity       *)
(*                                            *)
(**********************************************)

crystal(g,r,dr,a,ang);
vecrot(v,r,rf);
vecrot(rf,dr,v);
vecrot(v,r,rn);
vecrot(rn,dr,v);

(**********************************************)
(*                                            *)
(*     Calculate transformation matrices      *)
```

```
(*        db  elasticity to experiment            *)
(*                                                *)
(**************************************************)
(*                                                *)
(*     Experiment axes :                          *)
(*       -x  proj of diffraction vector on surf  *)
(*        y  perpendicular to incidence plane    *)
(*        z  inward perpendicular to surface     *)
(*                                                *)
(**************************************************)

  sm:=0; sn:=0; sp:=0;
  for i:=1 to 3 do begin
    sm:=sm+sqr(rn[i]);
    sn:=sn+rn[i]*rf[i];
  end;
  for i:=1 to 3 do begin
    db[3,i]:=rn[i]/sqrt(sm);
    db[1,i]:=rn[i]*sn/sm-rf[i];       (* 9/3/88  db[1,i]:=rf[i]-rn[i]*sn/sm;   *)
    sp:=sp+sqr(db[1,i]);
  end;
  sm:=0;
  sp:=sqrt(sp);
  for i:=1 to 3 do begin
    db[1,i]:=db[1,i]/sp;
  end;
  for i:=1 to 3 do begin
    m:=np[i];
    n:=nq[i];
    db[2,i]:=db[1,n]*db[3,m]-db[1,m]*db[3,n];
  end;

  vecrot(gd,db,rf);

  writeln;
  writeln('In experimental coordinates diffraction vector is');
  writeln(gd[1],'  ',gd[2],'  ',gd[3]);
  writeln;
  writeln('CYLINDRICAL DISTN. OF PRECIPITATES');
  writeln;
  writeln('Size parameter is ',c);
  writeln;
  writeln('Total no. of precipitates is ',ptlim);
  writeln;
end;
```

Appendix G

A procedure *STRIP.P*, written in Pascal, is listed, and represents the strain code for an oxide film or device on the surface of a silicon substrate.

```
(*  7/2/92 Procedures for calculating the                    *)
(*                                                           *)
(*         strain-field & inputting the                      *)
(*                                                           *)
(*         defect data for an oxide strip                    *)
(*                                                           *)
(*         on a substrate.                                   *)
(*                                                           *)
(*                                                           *)
(***********************************************************)


#include "globals.h"
#include "algebra.h"
#include "crystal.h"
#include "strip.h"

type ivector=array[1..3] of integer;

const pi=3.14159;

procedure diffstrip(var dsh:real;x,y,z,flnth,ymod,delta,horiz,shx,shz:real;
                    gd:vector);

var x0,chi0,tau,dudx1,dudx2,dudz1,dudz2,ddx,ddz:real;

begin
  x0 := x*cos(delta) + y*sin(delta);            ┐
  chi0 := -x0 - horiz*cos(delta);               ┘ section α
  tau := 2.56*flnth/(pi*ymod);                  — line A
  dudx1 := 0.72*((chi0/(sqr(chi0)+sqr(z)))-(x0/(sqr(x0)+sqr(z))));   ┐
  dudx2 := sqr(z)*((x0/sqr(sqr(x0)+sqr(z)))-(chi0/sqr(sqr(chi0)+sqr(z))));  section β
  dudz1 := 0.72*z*((1/(sqr(chi0)+sqr(z)))-(1/(sqr(x0)+sqr(z))));
  dudz2 := z*((sqr(chi0)/sqr(sqr(chi0)+sqr(z)))-(sqr(x0)/sqr(sqr(x0)+sqr(z))));
  ddx := tau*sqr(cos(delta))*(dudx1 + dudx2);
  ddz := tau*cos(delta)*(dudz1 + dudz2);        ┘
  dsh := gd[1]*shx*ddx + gd[1]*shz*ddz;         — line B
end;


procedure stripdef(var flnth,ymod,delta,xedge,yedge,horiz,zdispl:real;
                   var gd:vector;a,ang,rn,rf:vector);

 var v:vector;
     i,m,n:integer;
     sm,sn,sp:real;
     g,r,dr,db:matrix;
     np,nq:ivector;


begin
  np[1]:=2; np[2].=3; np[3]:=1;
  nq[1]:=3; nq[2]:=1; nq[3]:=2;
readln(flnth);
readln(ymod);
readln(delta);
readln(xedge,yedge);
readln(horiz);
readln(zdispl);
delta := delta*pi/180;
xedge := xedge*1E-06;
yedge := yedge*1E-06;
horiz := horiz*1E-06;
zdispl := zdispl*1E-06;
```

```
(*********************************************)
(*                                           *)
(*   Calculate transformation matrices and   *)
(*    transform  rf recip to elasticity      *)
(*               rn recip to elasticity      *)
(*                                           *)
(*********************************************)

  crystal(g,r,dr,a,ang);
  vecrot(v,r,rf);
  vecrot(rf,dr,v);
  vecrot(v,r,rn);
  vecrot(rn,dr,v);

(*********************************************)
(*                                           *)
(*      Calculate transformation matrices    *)
(*        db  elasticity to experiment       *)
(*                                           *)
(*********************************************)
(*                                           *)
(*     Experiment axes :                     *)
(*       -x  proj of diffraction vector on surf *)
(*        y  perpendicular to incidence plane   *)
(*        z  inward perpendicular to surface    *)
(*                                           *)
(*********************************************)

  sm:=0; sn:=0; sp:=0;
  for i:=1 to 3 do begin
    sm:=sm+sqr(rn[i]);
    sn:=sn+rn[i]*rf[i];
  end;
  for i:=1 to 3 do begin
    db[3,i]:=rn[i]/sqrt(sm);
    db[1,i]:=rn[i]*sn/sm-rf[i];       (* 9/3/89  db[1,i]:=rf[i]-rn[i]*sn/sm;   *)
    sp:=sp+sqr(db[1,i]);
  end;
  sm:=0;
 sp:=sqrt(sp);
  for i:=1 to 3 do begin
    db[1,i]:=db[1,i]/sp;
  end;
  for i:=1 to 3 do begin
    m:=np[i];
    n:=nq[i];
    db[2,i]:=db[1,n]*db[3,m]-db[1,m]*db[3,n];
  end;

  vecrot(gd,db,rf);

  writeln;
  writeln('In experimental coordinates diffraction vector is');
  writeln(gd[1],'  ',gd[2],'  ',gd[3]);
  writeln;
  writeln('OXIDE STRIP');
  writeln;
  writeln('Force p.u. length = ',flnth,' N/m');
  writeln;
  writeln('Youngs Modulus = ',ymod,' N/(m*m)');
  writeln;
  writeln('Layer angle = ',delta*180/pi,' degrees');
  writeln;
  writeln('Value of xedge = ',xedge*1E06,' microns');
```

```
  writeln;
  writeln('Value of yedge = ',yedge*1E06,' microns');
  writeln;
  writeln('Horiz. sepn. edges = ',horiz*1E06,' microns');
  writeln;
  writeln('Depth of Oxide Strip = ',zdispl*1E06,' microns');
  writeln
end;
```

Appendix H

A list of input data files, for several types of defect, used to generate the simulations.

Example template of input file H1

defect-code imperfect crystal code

$$kperfo$$

$$\lambda \;\; \Theta_B \;\; \alpha \;\; \mu$$

$$\chi_o$$

$$\chi_{\overline{h}}$$

$$\chi_h$$

$$elem \;\; t \;\; \Delta\Theta \;\; w$$

$$a \;\; b \;\; c \;\; \cos\alpha \;\; \cos\beta \;\; \cos\gamma$$

$$rn \;\; rf$$

$$height \;\; pzy$$

$$prlim$$

$$C$$

$$x_{min} \;\; x_{max}$$

$$y_{min} \;\; y_{max}$$

$$z_{min} \;\; z_{max}$$

where $kperfo$ = apodisation factor,
λ = wavelength of X-radiation,
Θ_B = Bragg angle,
α = asymmetry angle,
μ = absorption coefficient,
χ = susceptibility,
$elem$ = vertical integration step,
t = crystal thickness,
$\Delta\Theta$ = beam divergence,
w = source slit width,
a, b, c = cubic lattice parameters,
$\cos(\alpha, \beta, \gamma)$ = crystallographic direction cosines,
rn = surface normal indices,
rf = reflection indices,
$height$ = image height,
pzy = ratio of no. of image points in x and y-directions,
$prlim$ = total number of precipitates,
C = precipitate deformation parameter,
x_{min} = min. allowable x-coordinate of precipitate distribution,
x_{max} = max. allowable x-coordinate of precipitate distribution, etc.

```
2  0
1.0e+00
 7.0930e-11 19.8362 15.4282  1.44777737226662e+02
-3.17024021407409e-06
-7.26358584679206e-07  -7.42290983940664e-07
-7.42290979918242e-07   7.26358588789857e-07
 4.0000e-06  4.2400e-04 0.0000 0.0000
 5.4307e-10  5.4307e-10  5.4307e-10  0.0 0.0 0.0
0 0 -1  3 3 3
 2.9000e-04  1.0
 1
 6.5E-19
 18.9  19.1
 144.9  145.1
 29.9  30.1
```

H1: Input data file for a single precipitate, used to generate the simulation in Fig. 4.9.

```
2  0
1.0e+00
 7.0930e-11 21.6798 -21.6798  1.44777737226662e+02
-3.17024021407409e-06
-1.37779404673066e-06  -1.59323952096261e-08
-1.37779404673066e-06  -1.59323952096261e-08
 3.0000e-06  3.0000e-04 0.0000 0.0000
 5.4307e-10  5.4307e-10  5.4307e-10  0.0 0.0 0.0
0 0 -1  -4 4 0
 3.0000e-04  1.0
 860
 2.0E-22
 -119.0  119.0
 0.0  150.0
 30.0  270.0
```

H2: Input data file for a silicon crystal containing a random distribution of precipitates, with denuded zones at the top and bottom surfaces, used to generate the simulation in Fig. 4.23(c).

```
1  0
1.0e+00
 7.0930e-11 12.5089 5.0395  1.44777737226662e+02
-3.17024021407409e-06
-9.36450501684652e-07   9.20518104756206e-07
-9.20518106484829e-07  -9.36450499985439e-07
 3.0000e-06  5.0000e-04 0.0000 0.0000
 5.4307e-10  5.4307e-10  5.4307e-10  0.0 0.0 0.0
0 0 -1  -1 3 1
 2.0000e-04  1.0
 0.0  0.5  0.5    0  -1  1
 2.0000e-04  0.0000e+00
 16.6 6.39 6.39 0.0 0.0 0.0 16.6 6.39 0.0 0.0 0.0
 16.6 0.0 0.0 0.0 7.96 0.0 0.0 7.96 0.0 7.96
```

H3: Input data file for an edge dislocation, used to generate the corresponding simulation in Fig. 5.11.

```
7  0
 1.0000000000000E+00
 7.0930000000000E-11   12.509   5.040   1.4477773722666E-03
-3.1702401676546E-06
-9.3645061555406E-07    9.2051802611298E-07
-9.2051822168686E-07   -9.3645042330760E-07
 5.0000000000000E-06 5.0000000000000E-04     0.000000 0.0000000000000E+00
 5.4307000000000E-10 5.4307000000000E-10 5.4307000000000E-10   0   0   0
  0   0   -1           -1   3   1
 2.0000000000000E-04 1.0000000000000E+00
 0.55
 0.08
 316.5
 12.9
 200.0   0.0   0.0
 618.0   290.0

12/17/90
14:26:56
penetration depth =   4.7827554872772E-05
                      3.4773469270924E-05
```

H4: Input data file for a cylindrical inclusion with radius, ξ, equal to $0.08\mu m$, used to generate the corresponding simulation in Fig. 5.11.

```
12  0
 1.0000000000000E+00
 7.0930000000000E-11   12.509   5.040   1.4477773722666E-03
-3.1702401676546E-06
-9.3645061555406E-07    9.2051802611298E-07
-9.2051822168686E-07   -9.3645042330760E-07
 3.0000000000000E-06 5.0000000000000E-04     0.000000 0.0000000000000E÷00
 5.4307000000000E-10 5.4307000000000E-10 5.4307000000000E-10   0   0   0
  0   0   -1           -1   3   1
 2.0000000000000E-04 1.0000000000000E+00
 0.0   0.5   0.5         0   -1   1
 2.0000E-04       0.0000E+00
 16.6 7.96 7.96 0.0 0.0 0.0 16.6 7.96 0.0 0.0 0.0
 16.6 0.0 0.0 0.0 6.4 0.0 0.0 6.4 0.0 6.4
 4.0E-22
 52
 316.5   12.9
 200.0   0.0   0.0
 5.0   618.0   290.0

12/17/90
14:26:56
penetration depth =   4.7827554872772E-05
                      3.4773469270924E-05
```

H5: Input data file for an edge dislocation decorated with a cylindrical distribution of precipitates with C-value of $4\times10^{-22}m^3$, used to generate the simulation in Fig. 5.14(f).

```
8  0
 1.0000000000000E+00
 7.0930000000000E-11  12.509  5.040  1.4477773722666E-03
-3.1702401676546E-06
-9.3645061555406E-07   9.2051802611298E-07
-9.2051822168686E-07  -9.3645042330760E-07
 3.0000000000000E-06 5.0000000000000E-04    0.000000 0.0000000000000E+00
 5.4307000000000E-10 5.4307000000000E-10 5.4307000000000E-10  0  0  0
  0  0  -1          -1  3  1
 2.0000000000000E-04 1.0000000000000E+00
 0.0  0.5  0.5        0  -1  1
 2.0000E-04      0.0000E+00
 16.6 7.96 7.96 0.0 0.0 0.0 16.6 7.96 0.0 0.0 0.0
 16.6 0.0 0.0 0.0 6.4 0.0 0.0 6.4 0.0 6.4
 0.55
 0.06
 316.5
 12.9
 200.0  0.0  0.0
 618.0  290.0

12/17/90
14:26:56
penetration depth =  4.7827554872772E-05
                     3.4773469270924E-05
```

H6: Input data file for an edge dislocation and associated cylindrical inclusion of radius $0.06\mu m$, used to generate the simulation in Fig. 5.15(f).

```
10  0
3.0e+00
 5.5940e-11 8.3763 -8.3763  7.16920254480028e+01
-1.96771202401224e-06
-1.22772064107734e-06  -6.03582801399665e-09
-1.22772064109220e-06  -6.03582499228010e-09
 3.0000e-06  1.3300e-03 0.0000 0.0000
 5.4307e-10  5.4307e-10  5.4307e-10  0.0 0.0 0.0
0 0 -1  2 2 0
 6.8000e-04  1.0
 10
 2.0E02
 1.7E11
 30.0
 0.0  340.0
 3300.0
 0.0
```

H7: Input data file for an oxide film on the surface of a silicon crystal, used to generate the simulation in Fig. 6.6(a).

Appendix I

A set of diagrams representing the reflection geometries studied in this work.

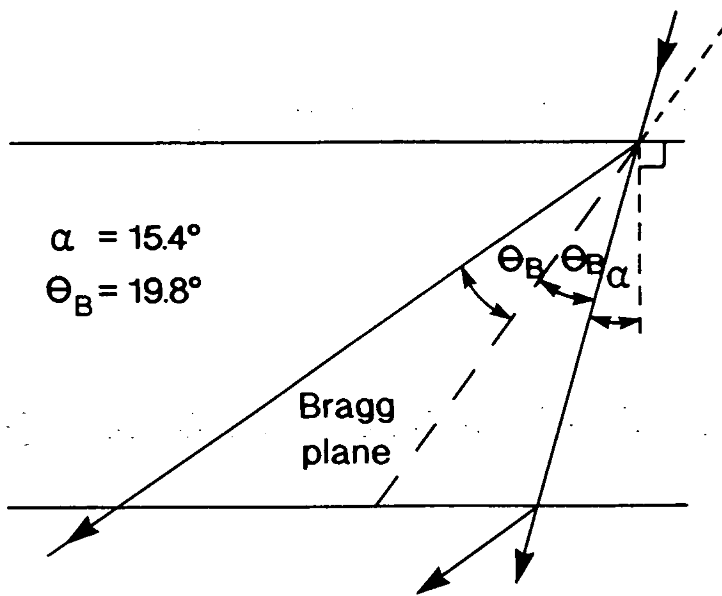

I1: Diffraction geometry for (001) oriented crystal, imaged using MoK_{α_1} radiation in the 333 reflection.

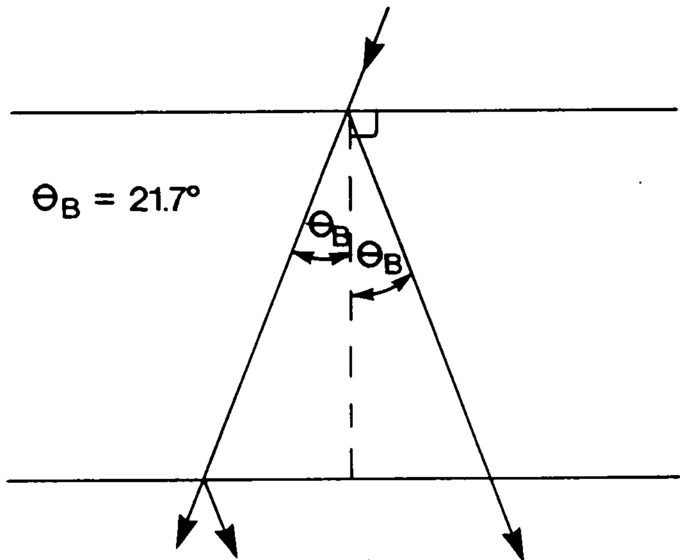

I2: Diffraction geometry for (001) oriented crystal, imaged using MoK_{α_1} radiation in either the 440 or the $\bar{4}40$ reflection.

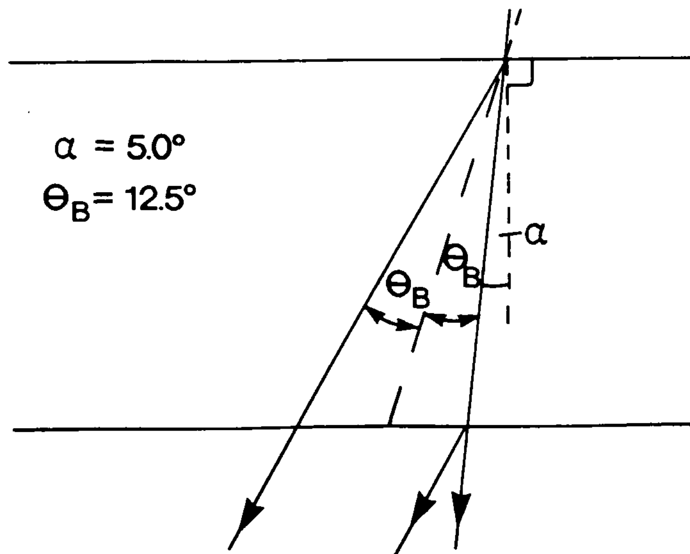

I3: Diffraction geometry for (001) oriented crystal, imaged using MoK_{α_1} radiation in the $\bar{1}31$ reflection.

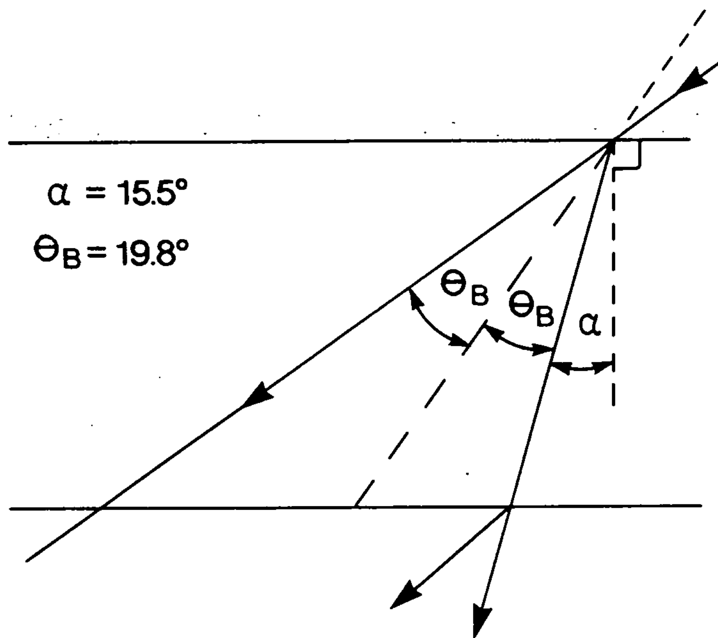

I4: Diffraction geometry for (001) oriented crystal, imaged using MoK_{α_1} radiation in the $3\overline{3}\overline{3}$ reflection.

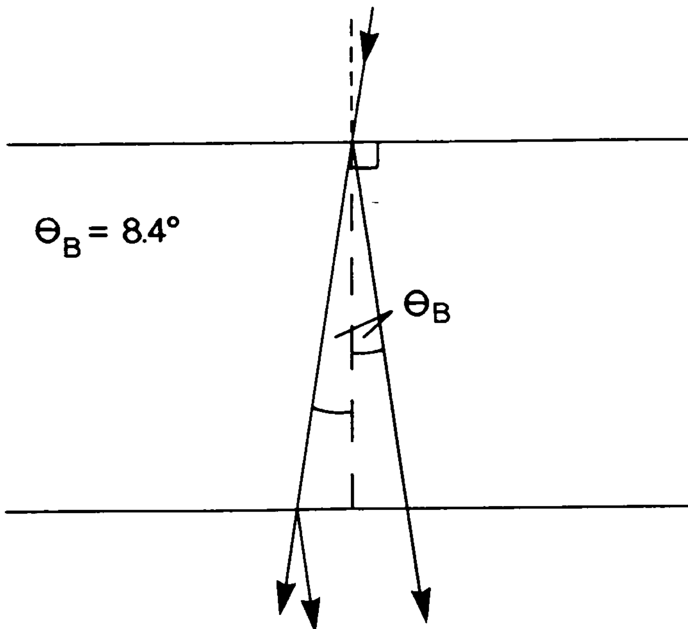

I5: Diffraction geometry for (001) oriented crystal, imaged using MoK_{α_1} radiation in the 220 reflection.

Appendix J

A set of simulations showing matching of the cylindrical inclusion model to the associated decorated dislocation, for several values of precipitate line density, ρ_p.

$\overline{1}31$

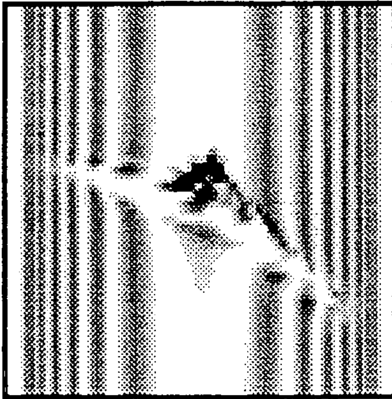

dislocation

100μm

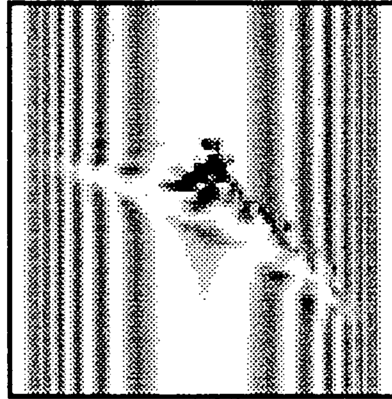

$C = 1\times10^{-22} m^3$

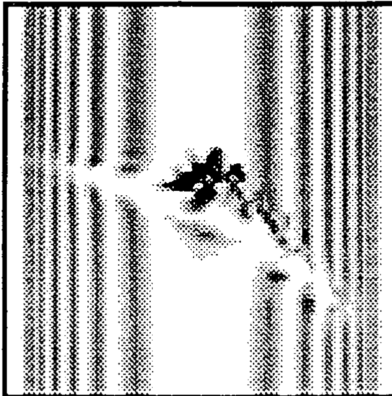

$C = 2\times10^{-22}\ m^3$

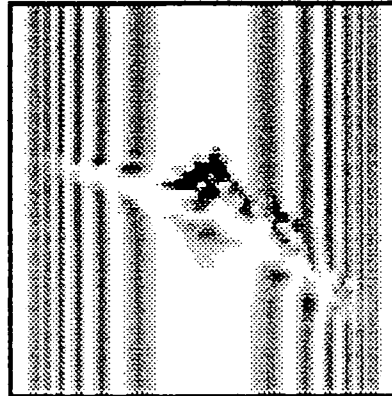

$C = 5\times10^{-22}\ m^3$

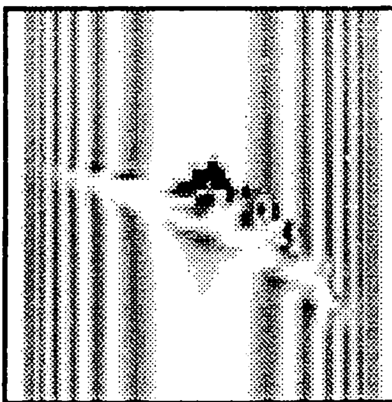

$C = 2\times10^{-21}\ m^3$

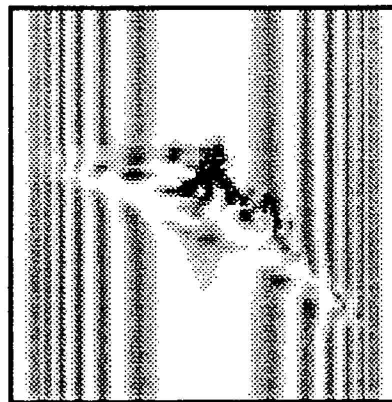

$C = 4\times10^{-21} m^3$

Dislocation with cylindrical distribution of precipitates, for precipitate line density, ρ_p, of $1.56\times10^4 m^{-1}$, in the $\overline{1}31$ reflection.

$\bar{1}31$

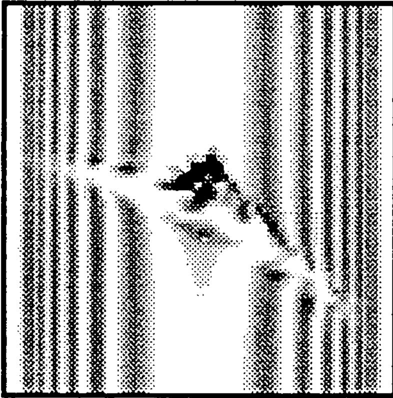

dislocation

$100 \mu m$

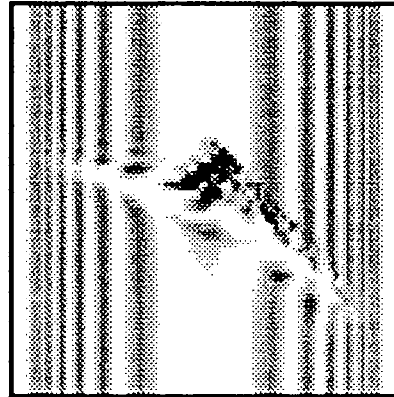

$\xi = 0.01 \mu m$

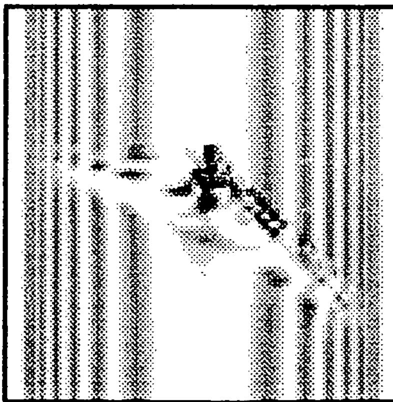

$\xi = 0.02 \mu m$

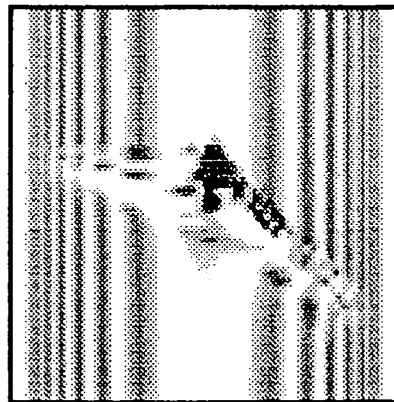

$\xi = 0.025 \mu m$

Dislocation with cylindrical inclusion, for precipitate line density, ρ_p, of $1.56 \times 10^4 m^{-1}$, in the $\bar{1}31$ reflection.

$\overline{1}31$

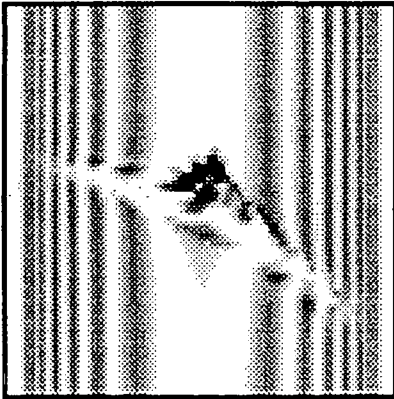

dislocation

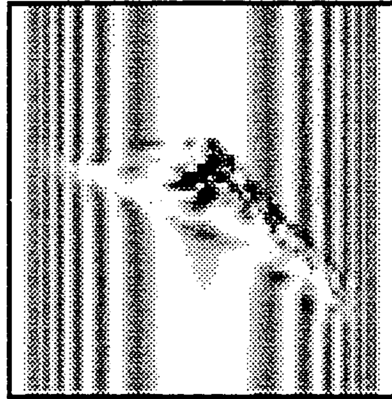

$C = 1\times10^{-22}\,m^3$

$100\mu m$

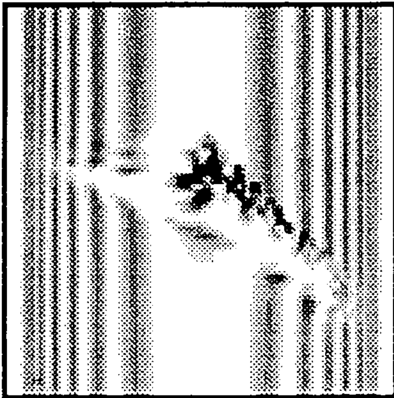

$C = 2\times10^{-22}\,m^3$

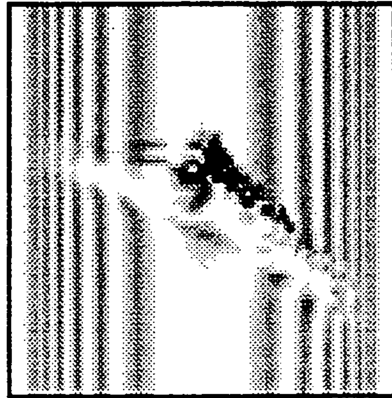

$C = 5\times10^{-22}\,m^3$

$C = 2\times10^{-21}m^3$

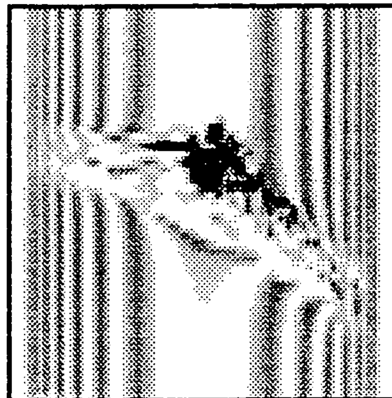

$C = 4\times10^{-21}\,m^3$

Dislocation with cylindrical distribution of precipitates, for precipitate line density, ρ_p, of $1.81\times10^5 m^{-1}$, in the $\overline{1}31$ reflection.

$\bar{1}31$

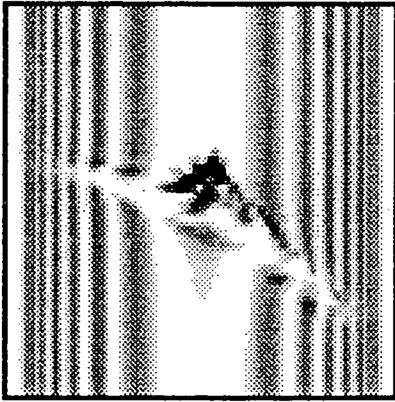

dislocation

100μm

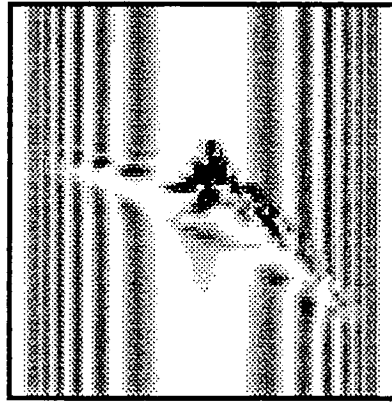

$\xi = 0.015\mu m$

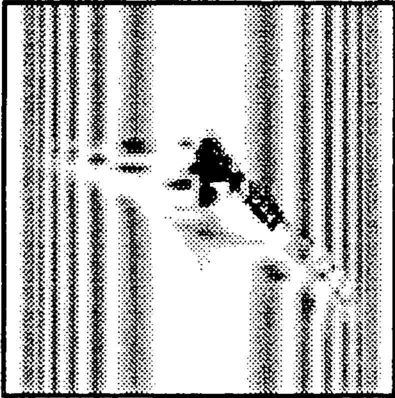

$\xi = 0.025\mu m$

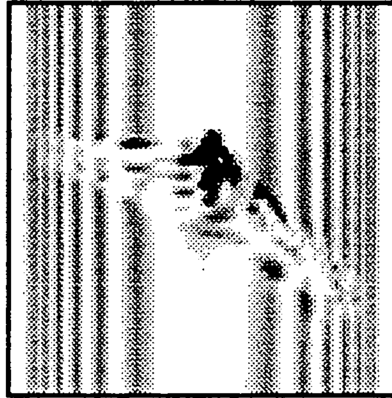

$\xi = 0.04\mu m$

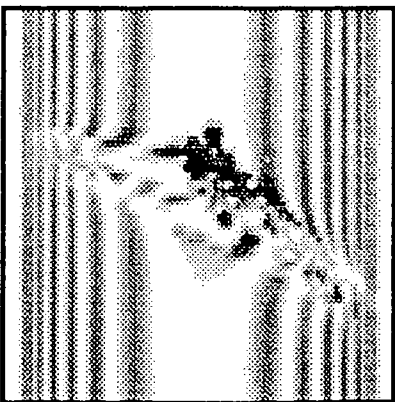

$\xi = 0.085\mu m$

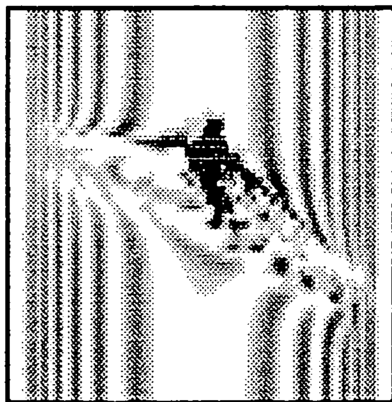

$\xi = 0.011\mu m$

Dislocation with cylindrical inclusion, for precipitate line density, ρ_p, of $1.81 \times 10^5 m^{-1}$, in the $\bar{1}31$ reflection.

$\leftarrow$
$\bar{1}31$

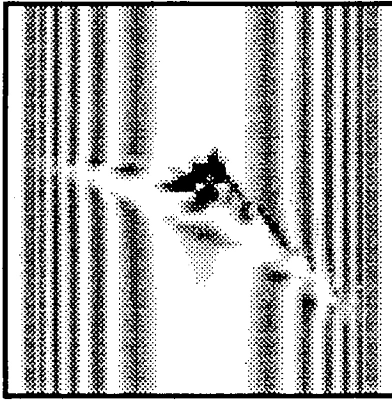

dislocation

100μm

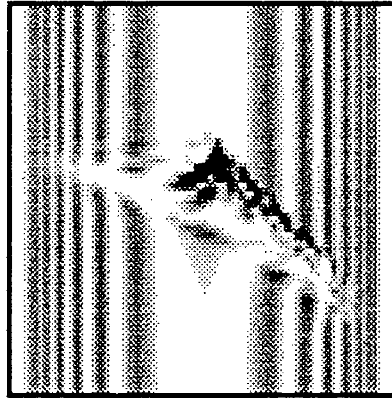

$C = 1\times 10^{-22}\, m^3$

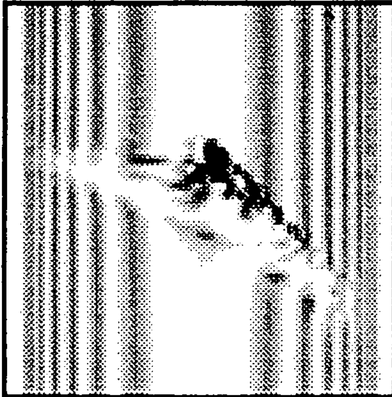

$C = 2\times 10^{-22}\, m^3$

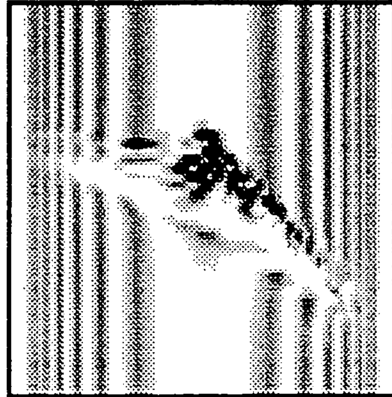

$C = 5\times 10^{-22}\, m^3$

$C = 2\times 10^{-21}\, m^3$

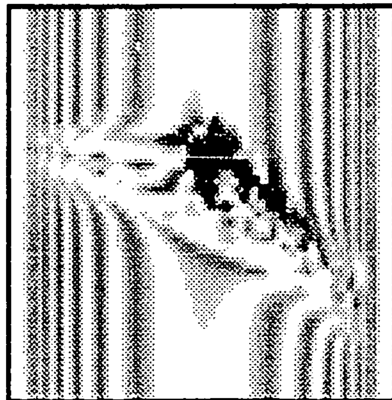

$C = 4 \times 10^{-21}\, m^3$

Dislocation with cylindrical distribution of precipitates, for precipitate line density, ρ_p, of $3.62\times 10^5 m^{-1}$, in the $\bar{1}31$ reflection.

$\bar{1}31$

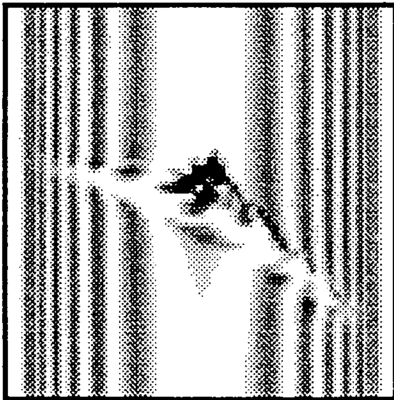

dislocation

100μm

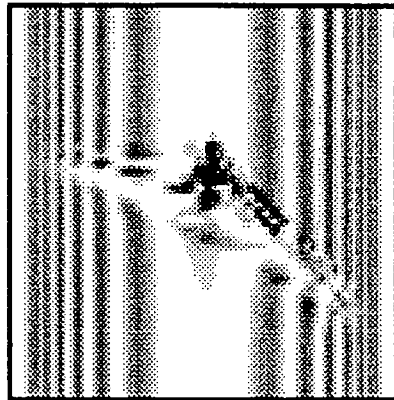

$\xi = 0.02\mu m$

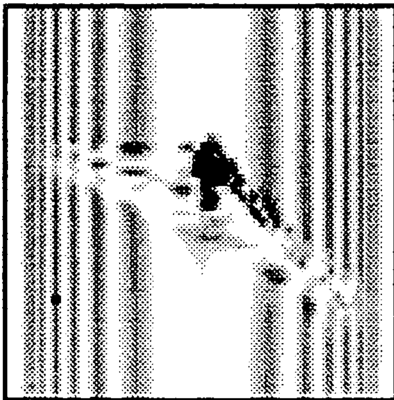

$\xi = 0.03\mu m$

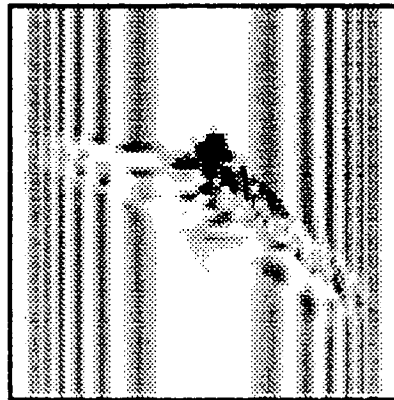

$\xi = 0.05\mu m$

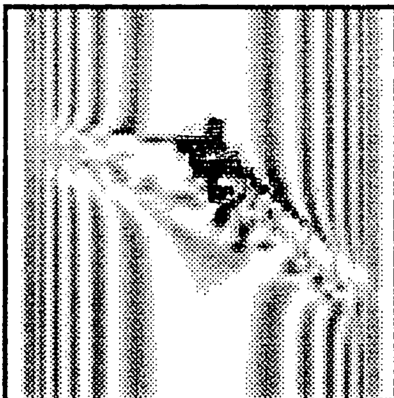

$\xi = 0.1\mu m$

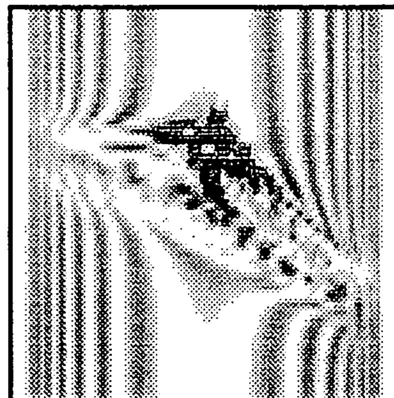

$\xi = 0.14\mu m$

Dislocation with cylindrical inclusion, for precipitate line density, ρ_p, of $3.62\times10^5 m^{-1}$, in the $\bar{1}31$ reflection.

Appendix K

A series of simulations for decorated dislocation pairs of different separation, κ, showing the effect of defect strain on resolvability.

$\bar{1}31$

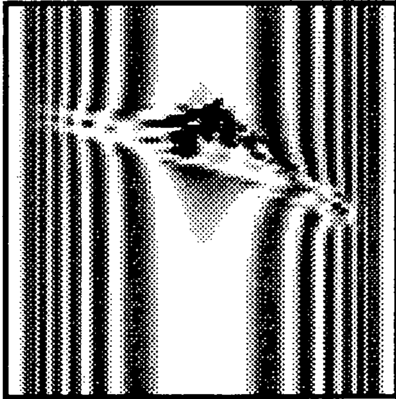

bare dislocations

100μm

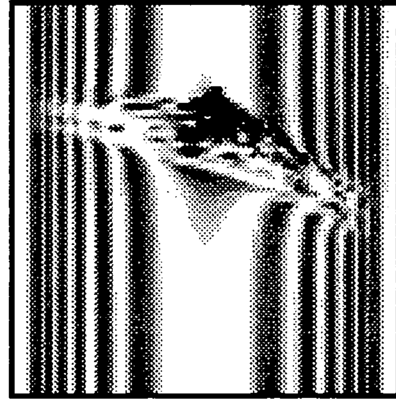

$\xi = 0.03\mu m$

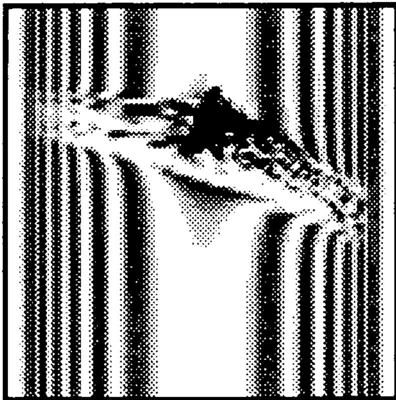

$\xi = 0.05\mu m$

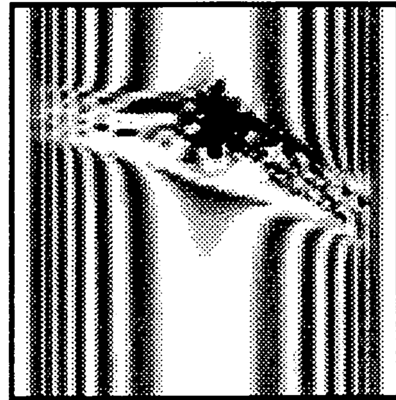

$\xi = 0.07\mu m$

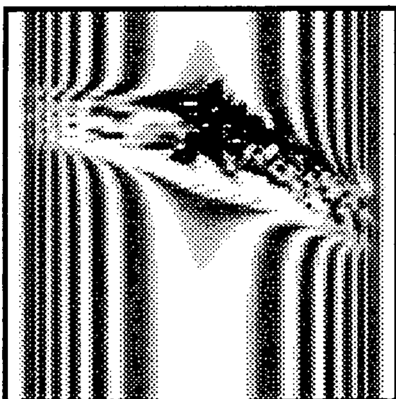

$\xi = 0.09\mu m$

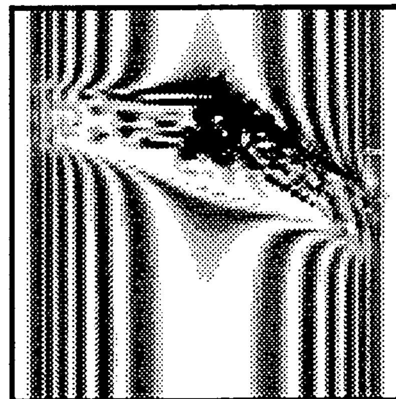

$\xi = 0.11\mu m$

Separation, κ, of decorated dislocations is 19.0μm.

$\bar{1}31$

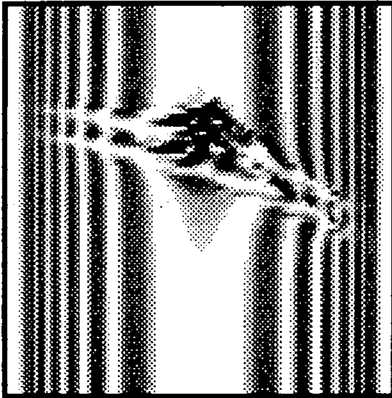

bare dislocations

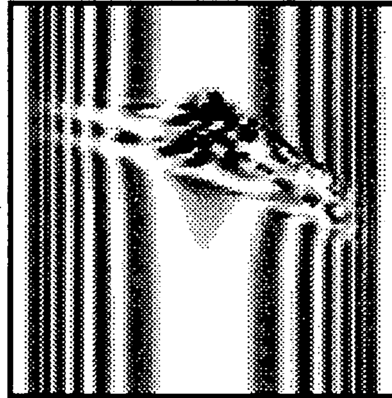

$\xi = 0.02\mu m$

100μm

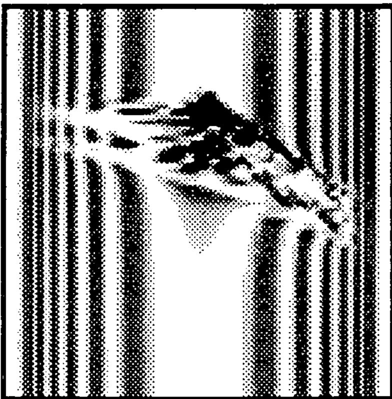

$\xi = 0.03\mu m$

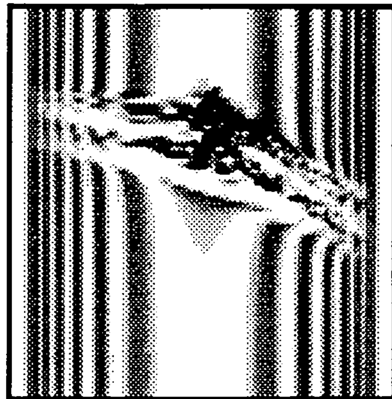

$\xi = 0.05\mu m$

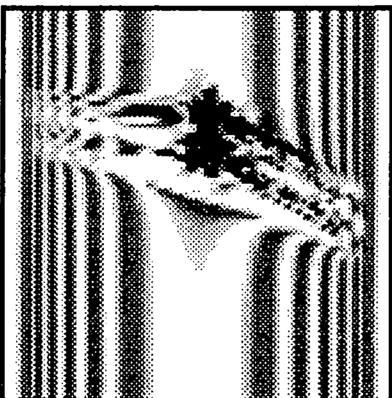

$\xi = 0.07\mu m$

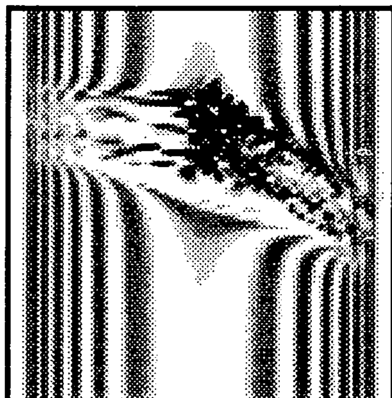

$\xi = 0.1\mu m$

Separation, κ, of decorated dislocations is 28.5μm.

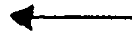

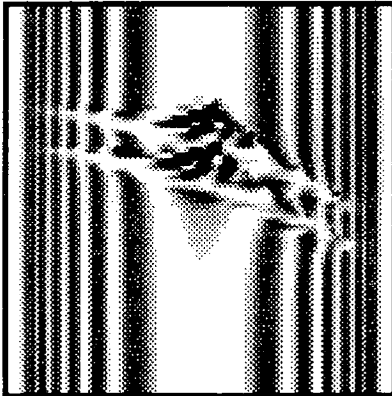

bare dislocations

$\vdash$ $100\mu m$ $\dashv$

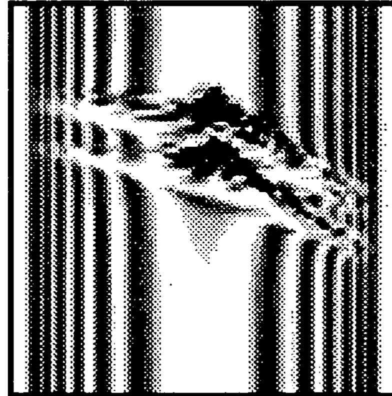

$\xi = 0.04\mu m$

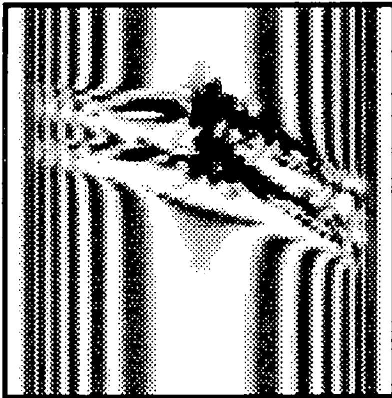

$\xi = 0.07\mu m$

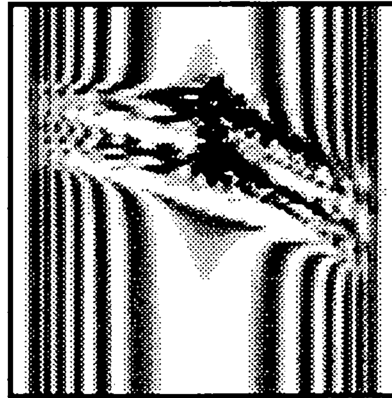

$\xi = 0.09\mu m$

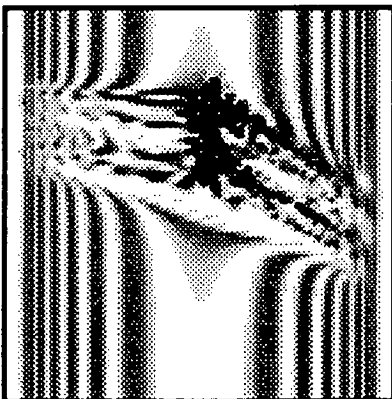

$\xi = 0.11\mu m$

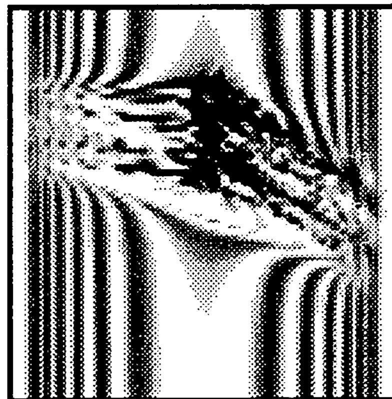

$\xi = 0.13\mu m$

Separation, κ, of decorated dislocations is $38.0\mu m$.

$\bar{1}31$

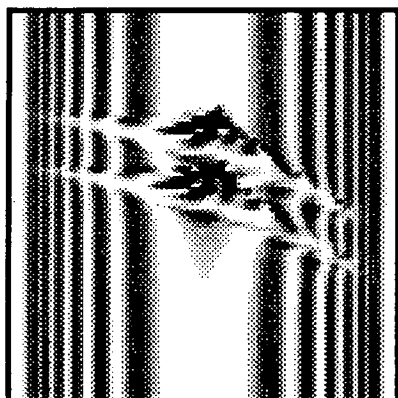

bare dislocations

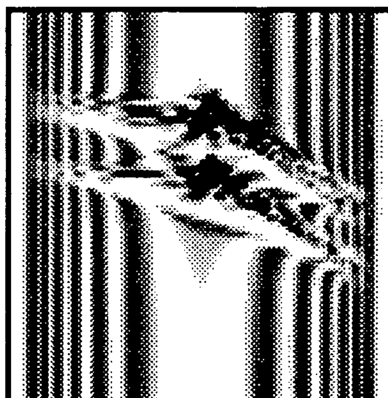

$\xi = 0.05\mu m$

$100\mu m$

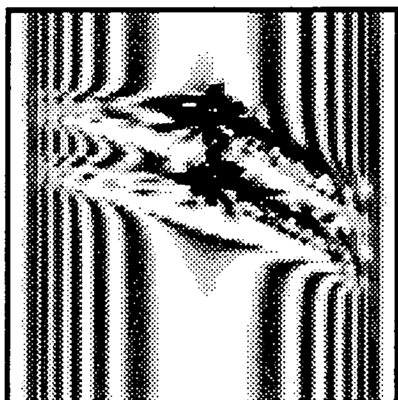

$\xi = 0.09\mu m$

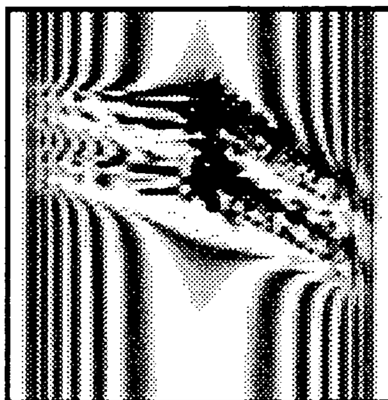

$\xi = 0.12\mu m$

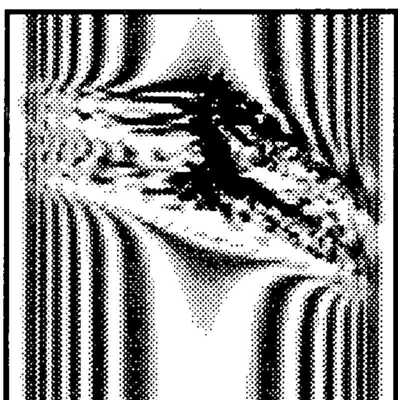

$\xi = 0.14\mu m$

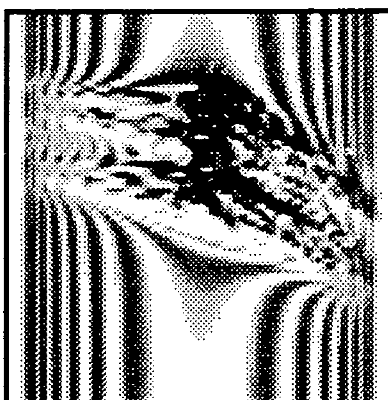

$\xi = 0.16\mu m$

Separation, κ, of decorated dislocations is $47.5\mu m$.

$\bar{1}31$

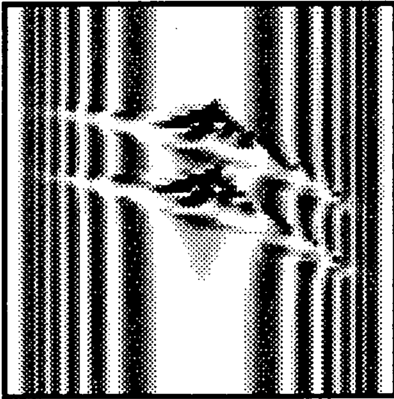

bare dislocations

100μm

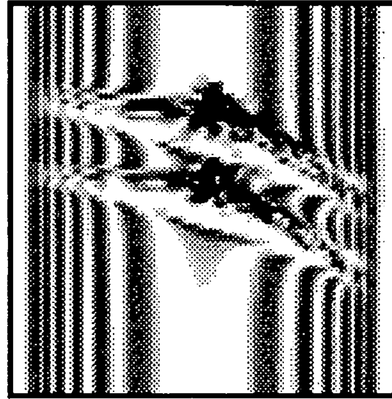

$\xi = 0.06\mu m$

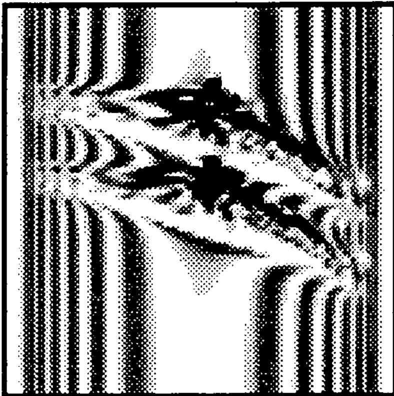

$\xi = 0.09\mu m$

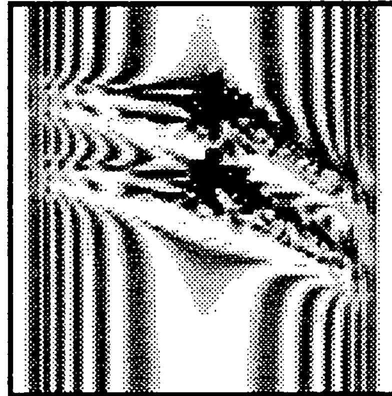

$\xi = 0.12\mu m$

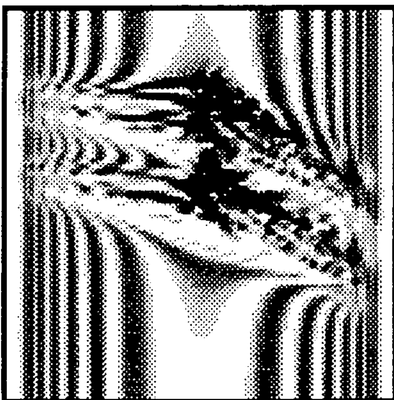

$\xi = 0.14\mu m$

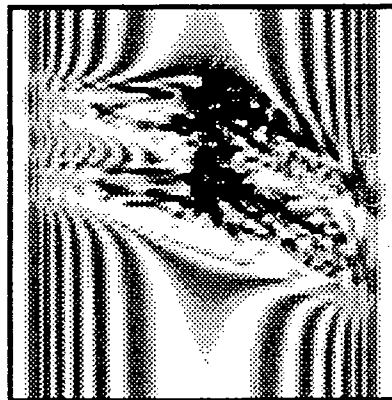

$\xi = 0.17\mu m$

Separation, κ, of decorated dislocations is $57.0\mu m$.

$\bar{1}31$

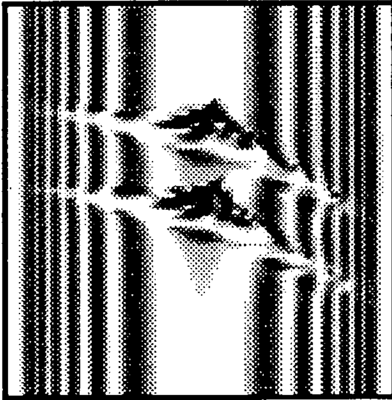

bare dislocations

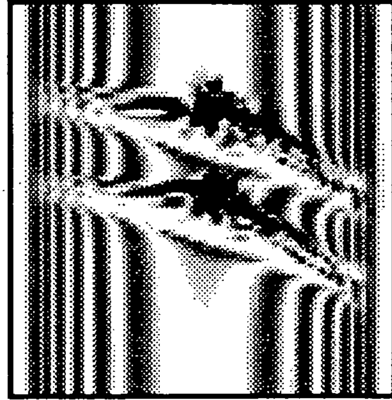

$\xi = 0.07\mu m$

$100\mu m$

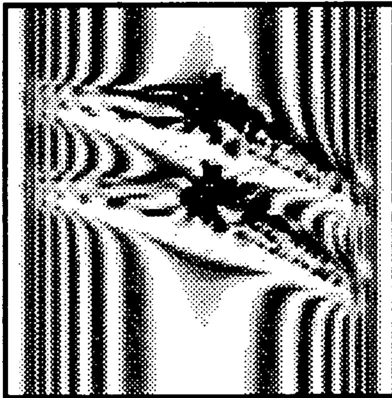

$\xi = 0.11\mu m$

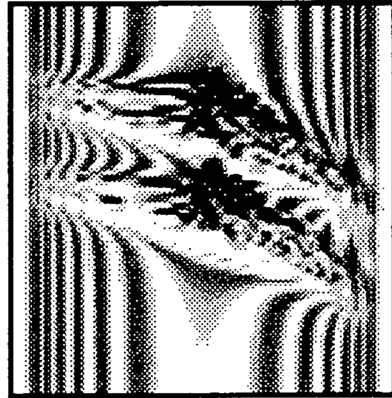

$\xi = 0.14\mu m$

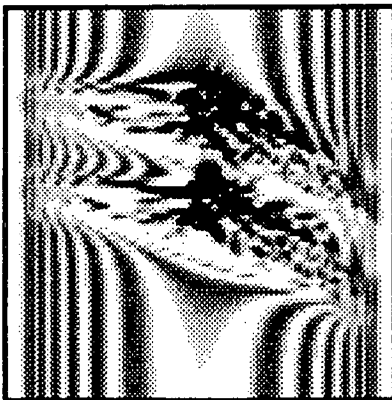

$\xi = 0.16\mu m$

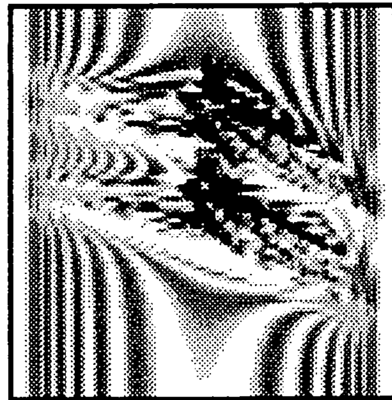

$\xi = 0.19\mu m$

Separation, κ, of decorated dislocations is $66.5\mu m$.

$\overline{1}31$

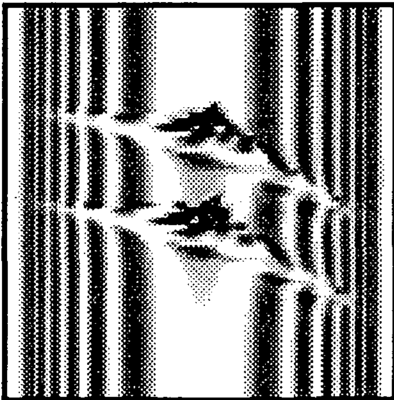

bare dislocations

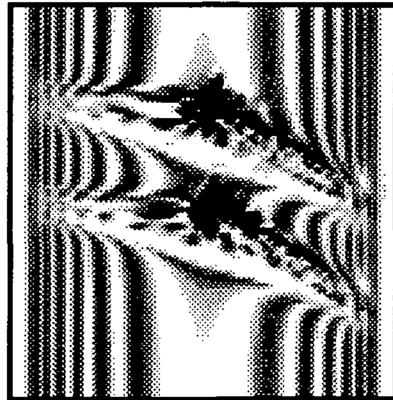

$\xi = 0.1\mu m$

$100\mu m$

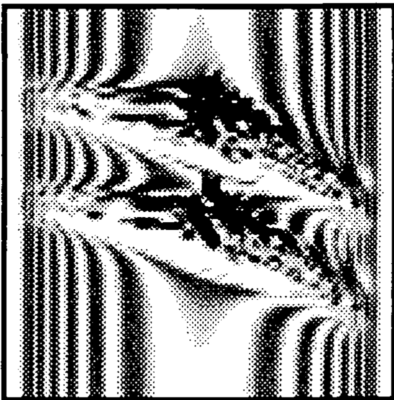

$\xi = 0.13\mu m$

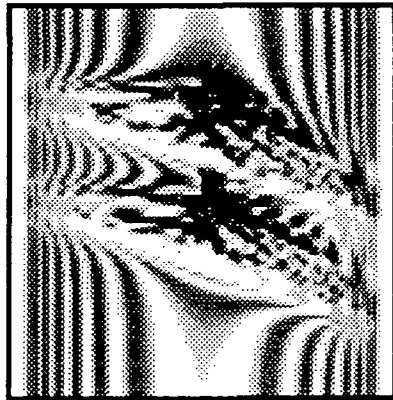

$\xi = 0.17\mu m$

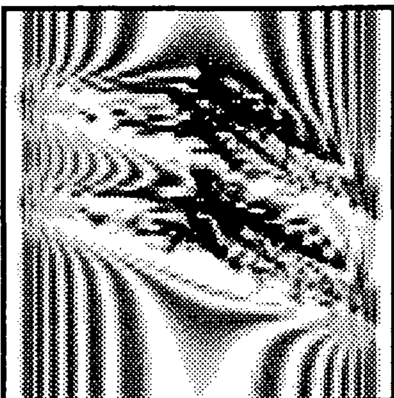

$\xi = 0.2\mu m$

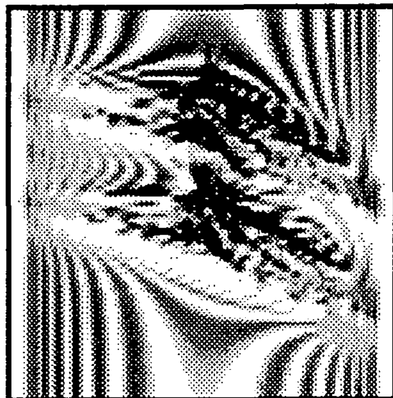

$\xi = 0.23\mu m$

Separation, κ, of decorated dislocations is $76.0\mu m$.

Appendix L

A series of simulations to determine the minimum detectable device width, W_{min}, for several values of force, S, per unit length of device edge.

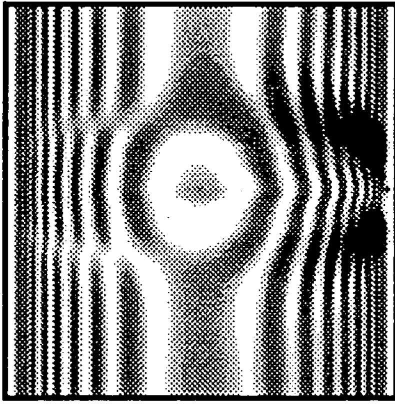

$W = 3\mu m$

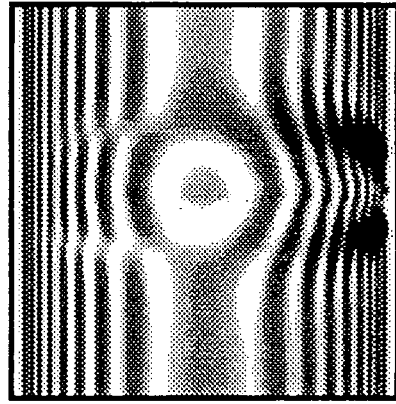

$W = 2.5\mu m$

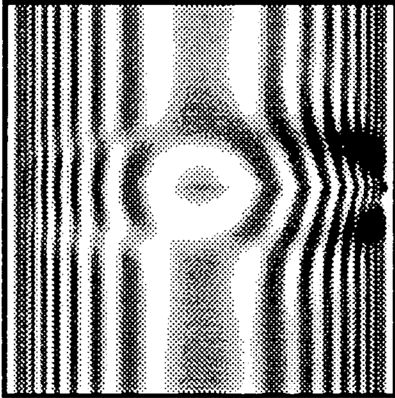

$W = 2\mu m$

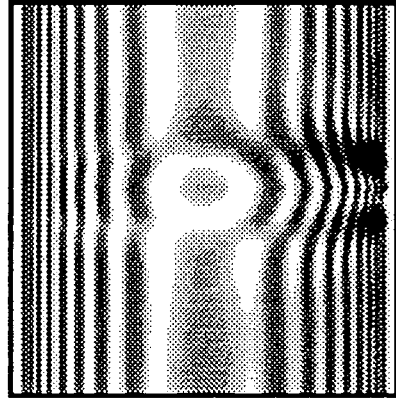

$W = 1.5\mu m$

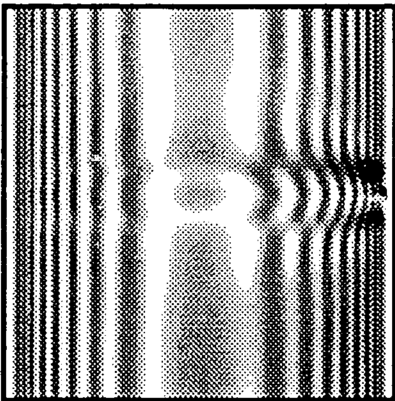

$W = 1\mu m$

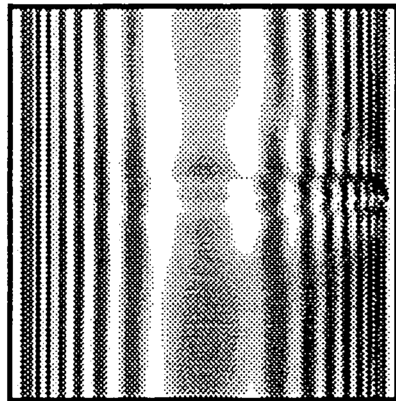

$W = 0.5\mu m$

Force, S, per unit length = $450Nm^{-1}$.

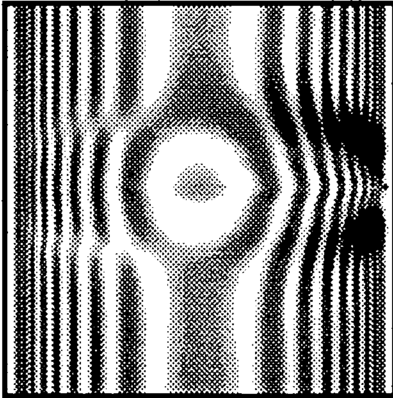

$W = 3\mu m$

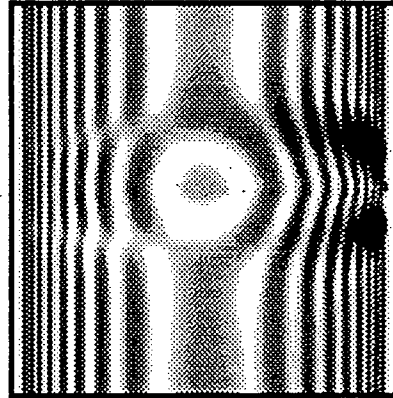

$W = 2.5\mu m$

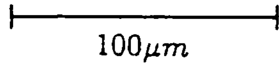

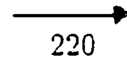

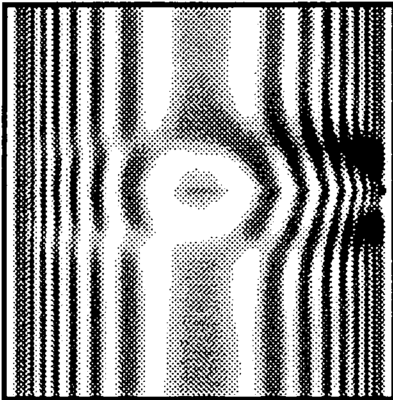

$W = 2\mu m$

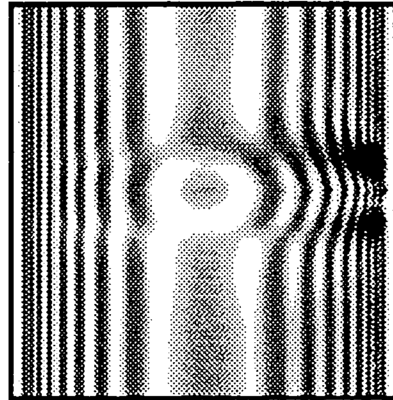

$W = 1.5\mu m$

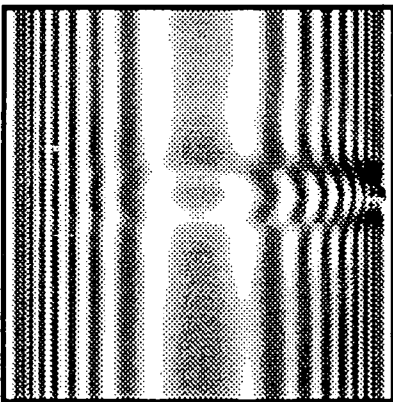

$W = 1\mu m$

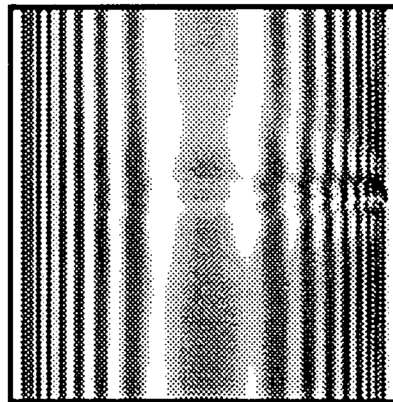

$W = 0.5\mu m$

Force, S, per unit length $= 400Nm^{-1}$.

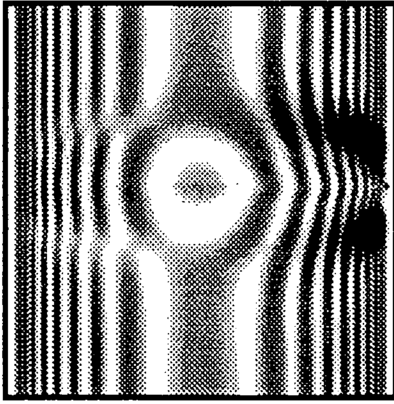
$W = 3\mu m$

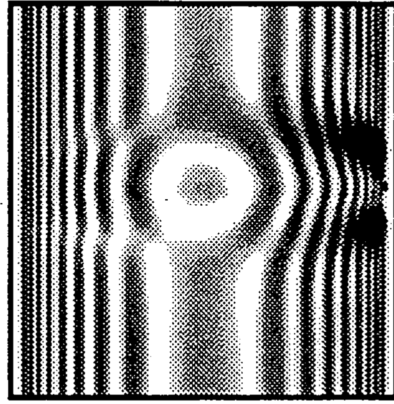
$W = 2.5\mu m$

100μm

220

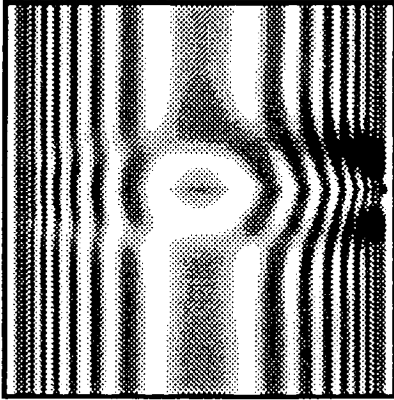
$W = 2\mu m$

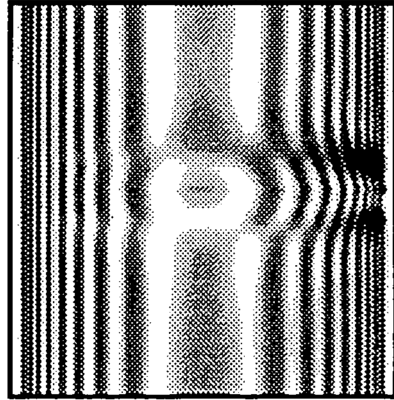
$W = 1.5\mu m$

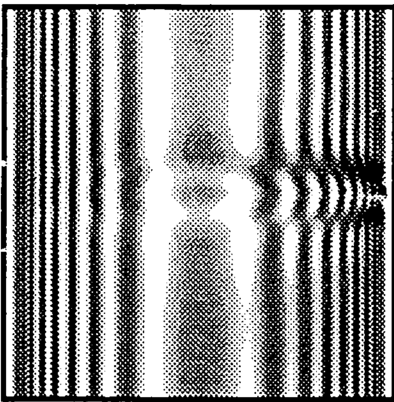
$W = 1\mu m$

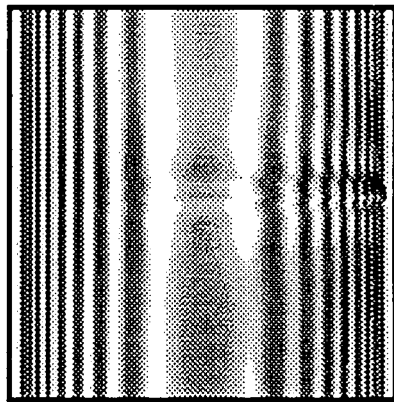
$W = 0.5\mu m$

Force, S, per unit length = $350 N m^{-1}$.

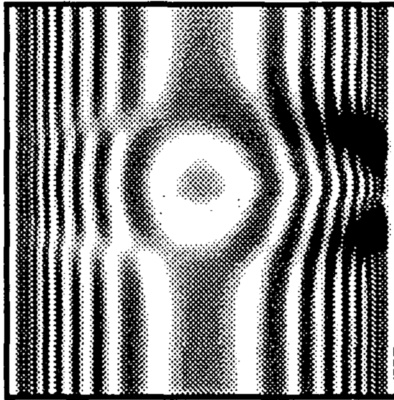

$W = 3.5\mu m$

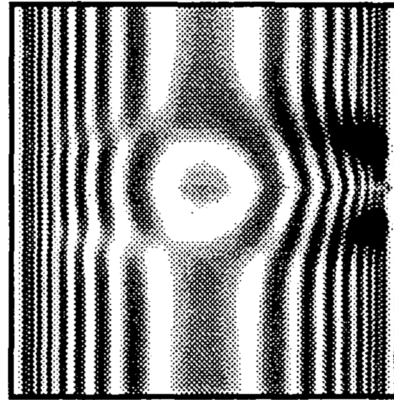

$W = 3.0\mu m$

100μm

220

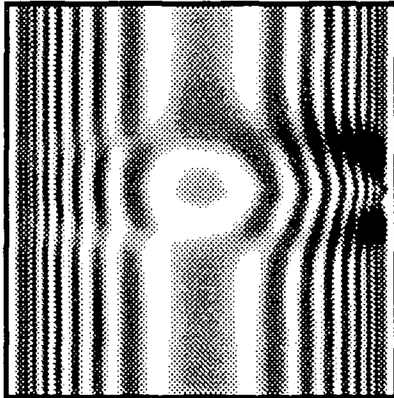

$W = 2.5\mu m$

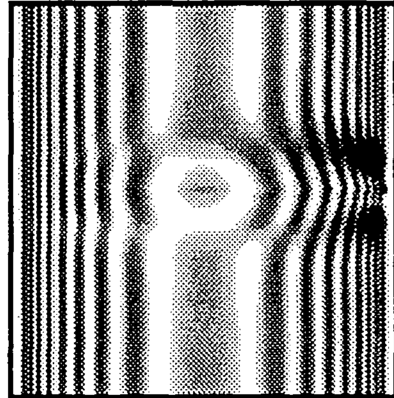

$W = 2.0\mu m$

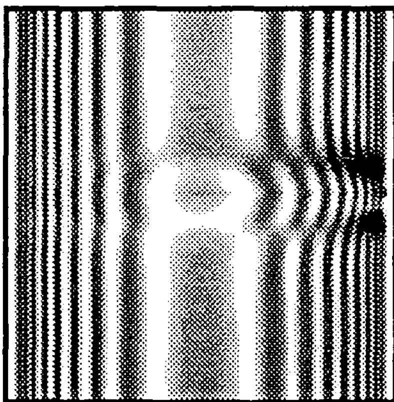

$W = 1.5\mu m$

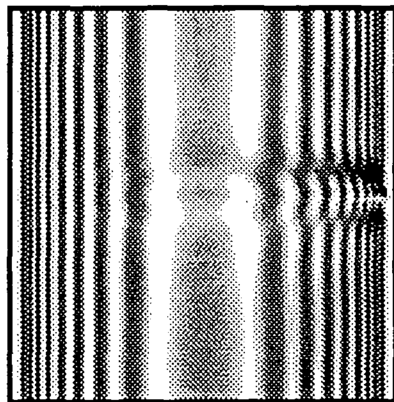

$W = 1.0\mu m$

Force, S, per unit length = $300Nm^{-1}$.

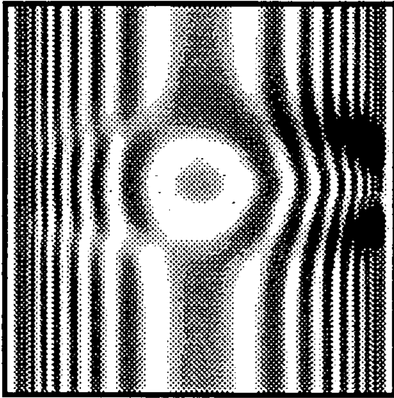

$W = 3.5\mu m$

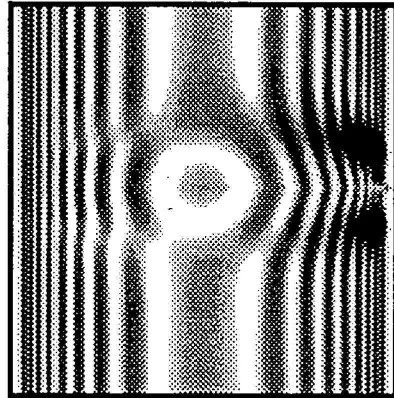

$W = 3.0\mu m$

$100\mu m$

220

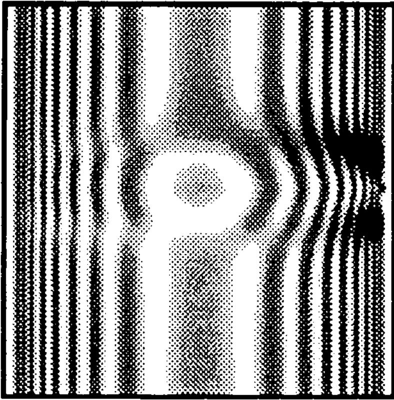

$W = 2.5\mu m$

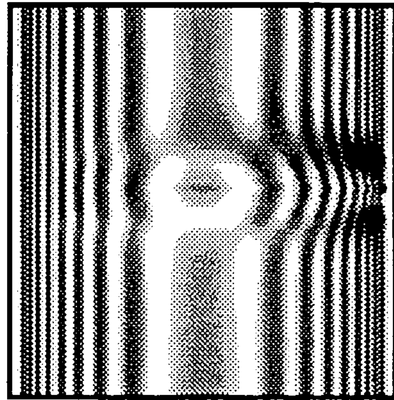

$W = 2.0\mu m$

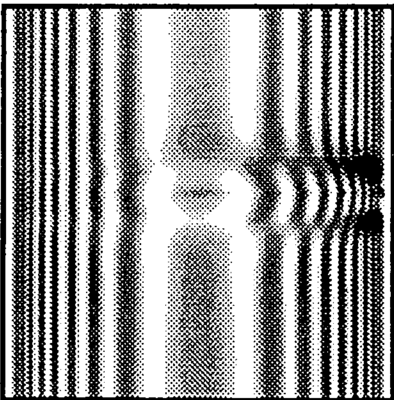

$W = 1.5\mu m$

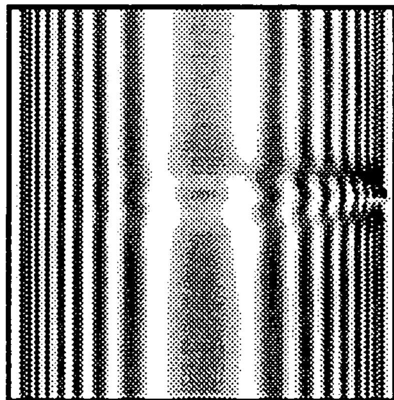

$W = 1.0\mu m$

Force, S, per unit length = $250 N m^{-1}$.

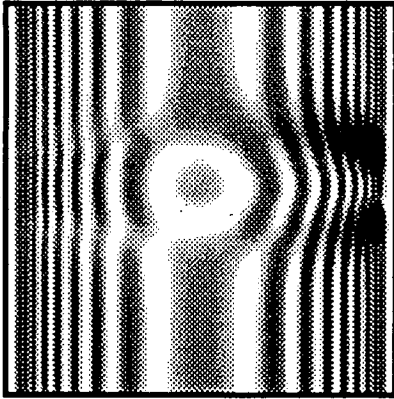

$W = 3.5\mu m$

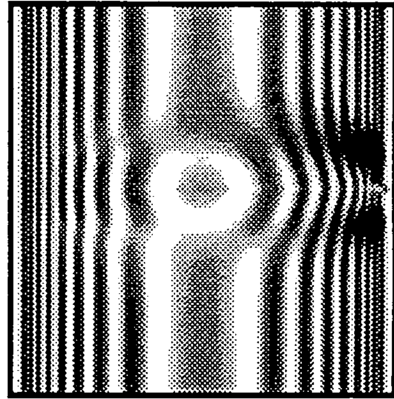

$W = 3.0\mu m$

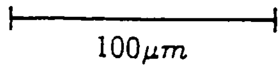

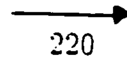

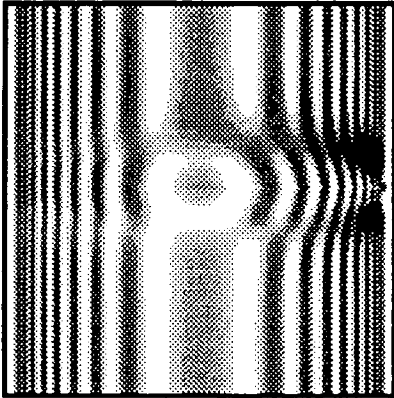

$W = 2.5\mu m$

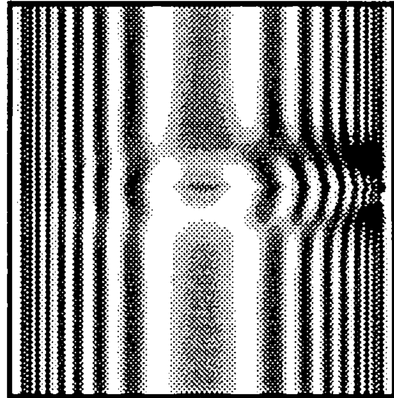

$W = 2.0\mu m$

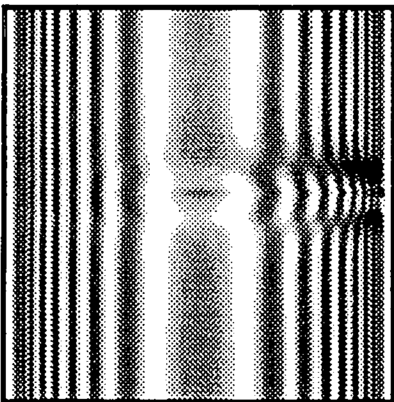

$W = 1.5\mu m$

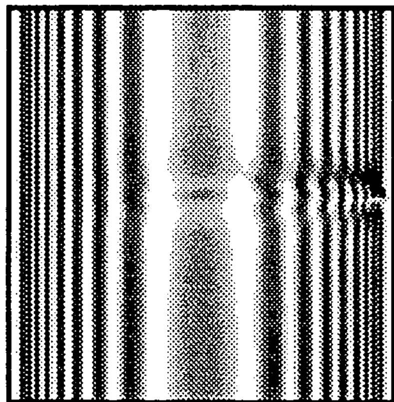

$W = 1.0\mu m$

Force, S, per unit length = $200Nm^{-1}$.

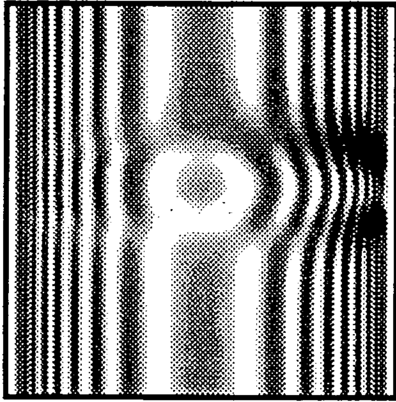

$W = 3.5\mu m$

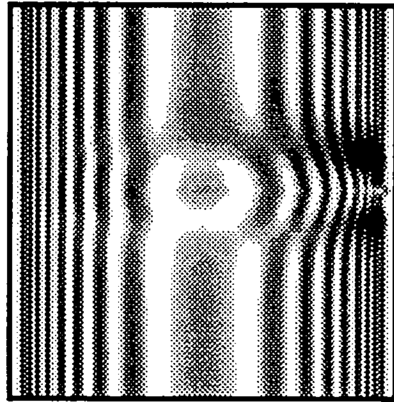

$W = 3.0\mu m$

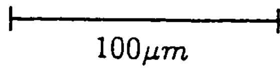

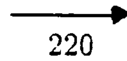

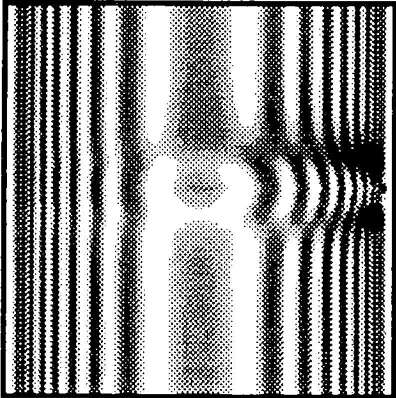

$W = 2.5\mu m$

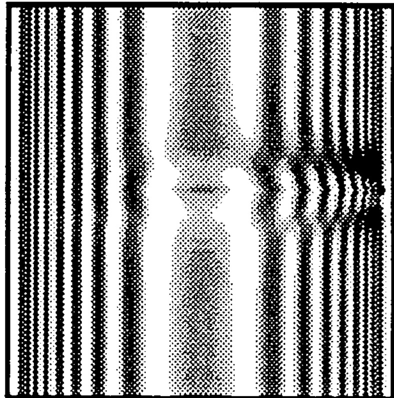

$W = 2.0\mu m$

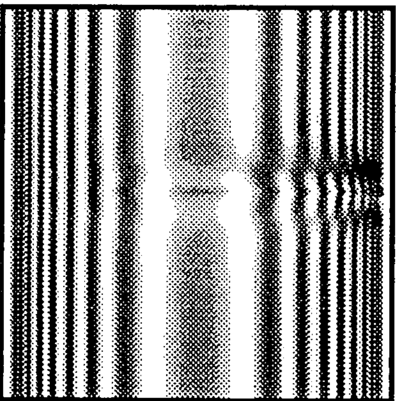

$W = 1.5\mu m$

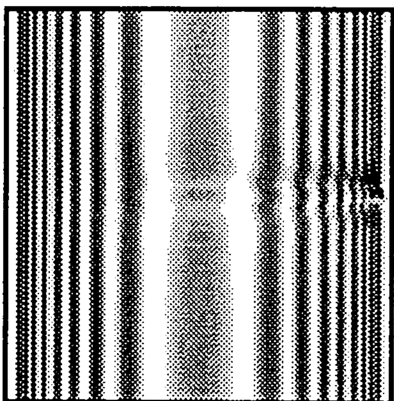

$W = 1.0\mu m$

Force, S, per unit length = $150Nm^{-1}$.

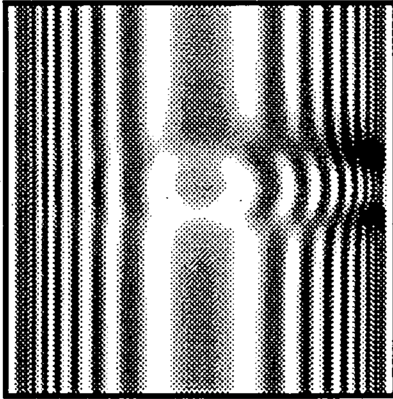

$W = 3.5\mu m$

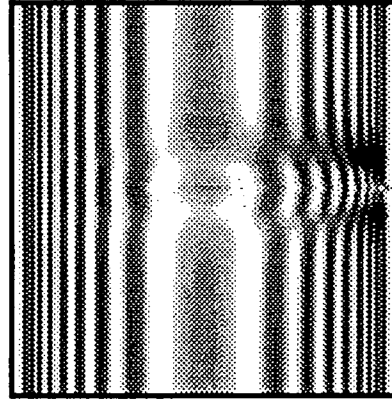

$W = 3.0\mu m$

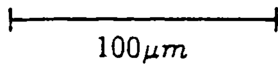

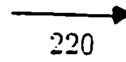

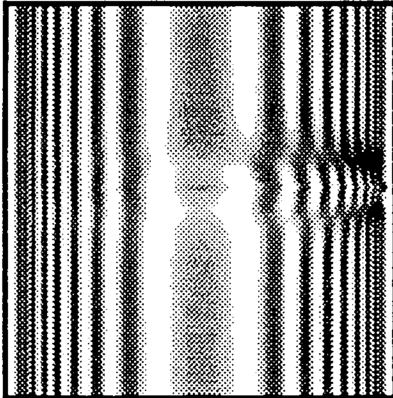

$W = 2.5\mu m$

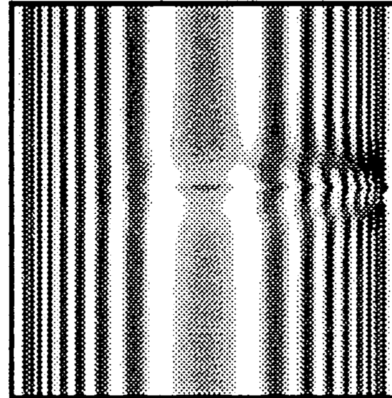

$W = 2.0\mu m$

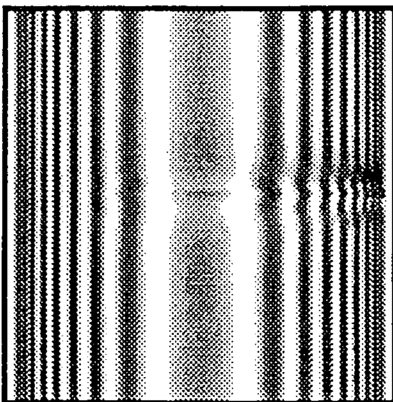

$W = 1.5\mu m$

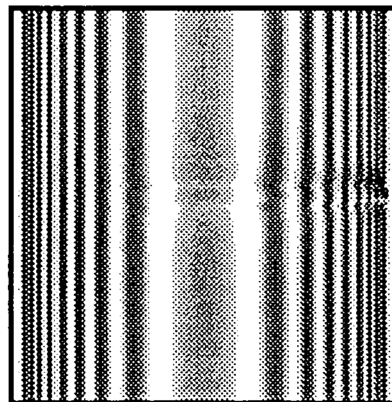

$W = 1.0\mu m$

Force, S, per unit length $= 100Nm^{-1}$.

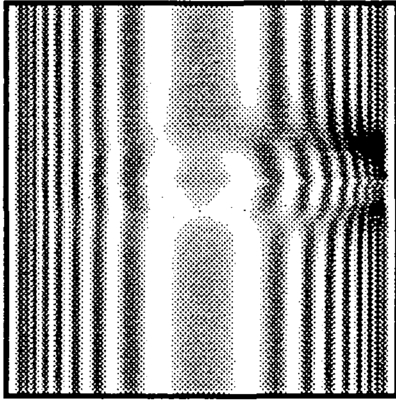

$W = 6.5\mu m$

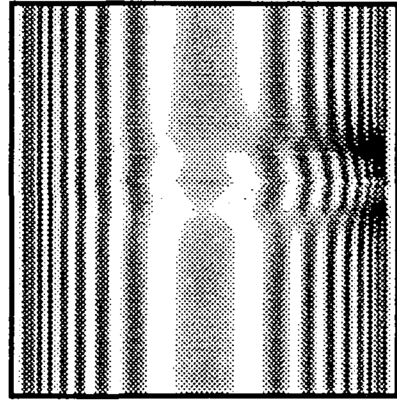

$W = 6.0\mu m$

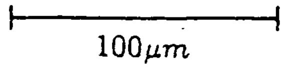

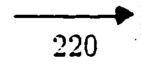

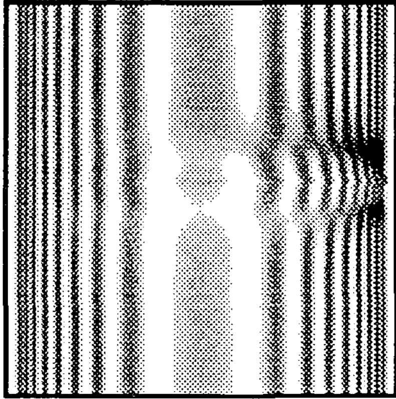

$W = 5.5\mu m$

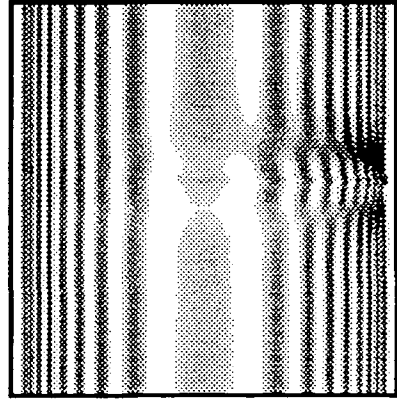

$W = 5.0\mu m$

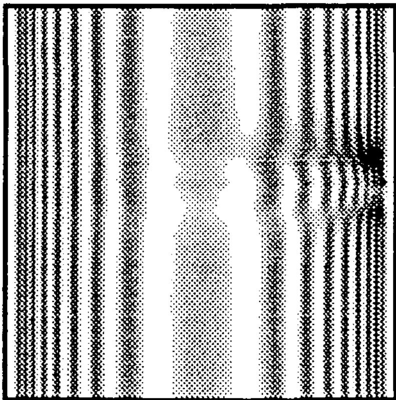

$W = 4.5\mu m$

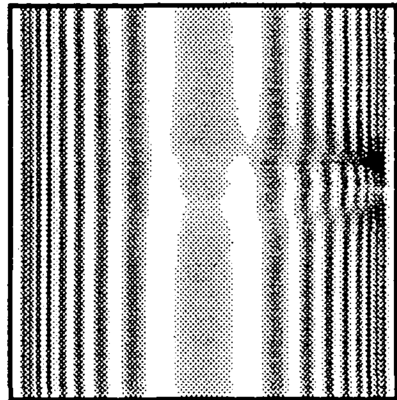

$W = 4.0\mu m$

Force, S, per unit length = $50Nm^{-1}$.

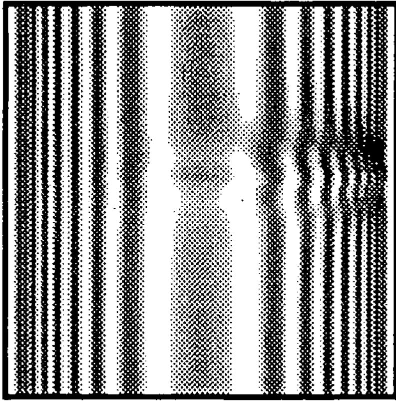

$W = 8.0\mu m$

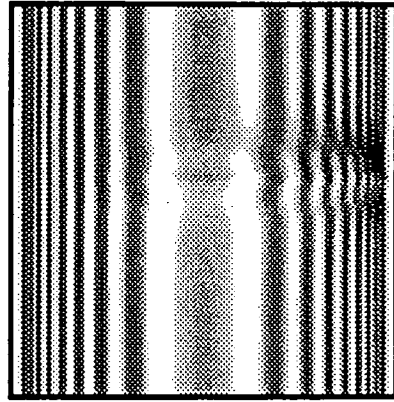

$W = 7.5\mu m$

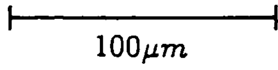

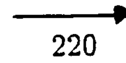

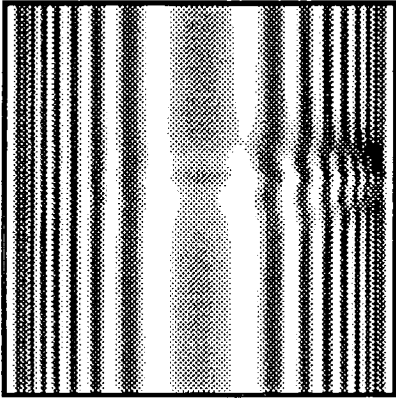

$W = 7.0\mu m$

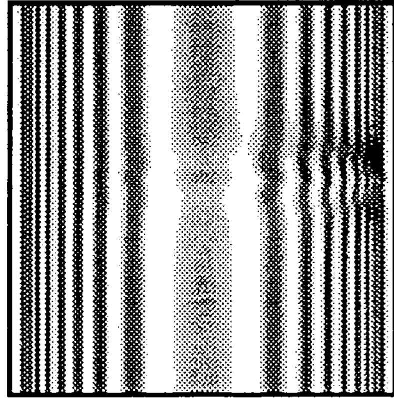

$W = 6.5\mu m$

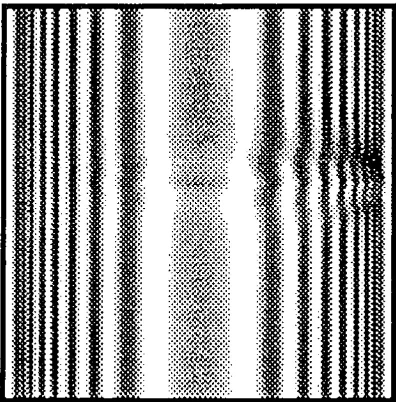

$W = 6.0\mu m$

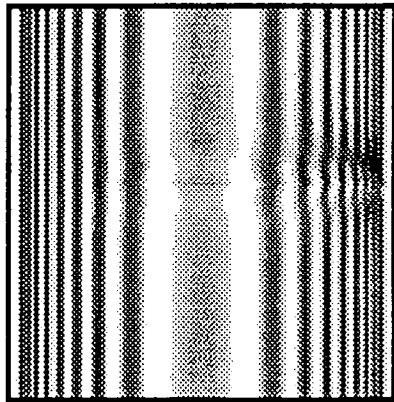

$W = 5.5\mu m$

Force, S, per unit length = $25Nm^{-1}$.

Bibliography

[1] A. Authier, (1967), Adv. X-ray analysis, Plenum, **10**, 9.

[2] B.K. Tanner, (1976), *X-ray Diffraction Topography*, Pergamon, Oxford.

[3] A.R. Lang, (1978), *Diffraction and Imaging Techniques in Material Science*, vol.2, 2nd rev. ed., (ed. S. Amelinckx, R. Gevers and J. Van Landuyt), North-Holland, p.623.

[4] U. Bonse, M. Hart and J.B. Newkirk, (1967), Adv. X-ray Analysis, Plenum, **10**, 1.

[5] C.S. Barrett, (1945), Trans. AIME, **161**, 15.

[6] A.R. Lang, (1958), J. Appl. Phys., **29**, 597.

[7] A.R. Lang, (1957), Acta Cryst., **10**, 839.

[8] A.R. Lang, (1959), Acta Cryst., **12**, 249.

[9] N. Kato and A.R. Lang, (1959), Acta Cryst., **12**, 787.

[10] A.R. Lang, (1980), *Characterization of Crystal Growth Defects by X-ray Methods*, (ed. B.K. Tanner and D.K. Bowen), Plenum, New York, p.163.

[11] A.R. Lang, (1963), Brit. J. Appl. Phys., **14**, 904.

[12] W.L. Bond and J. Andrus, (1952), Am. Mineralogist, **37**, 622.

[13] U. Bonse and E. Kappler, (1958), Z. Naturforschung, **13a**, 348.

[14] B. Davis and C.M. Slack, (1926), Phys. Rev., **27**, 18.

[15] T. Tuomi, K. Naukkarinen, E. Laurila and P. Rabe, (1973), Acta polytech. Scand., **Ph100**, 1.

[16] T. Tuomi, K. Naukkarinen and P. Rabe, (1974), Phys. Stat. Sol. (a), **25**, 93.

[17] D.K. Bowen, (1988), Adv. Materials Science, Pergamon, **1**, 522.

[18] B.K. Tanner and D.K. Bowen, (1992), Materials Science Reports, 369.

[19] D.H. Templeton and L.K. Templeton, (1988), J. Appl. Cryst., **21**, 151.

[20] R. Docherty, A. El-Korashy, H.-D. Jennissen, H. Klapper, K.J. Roberts and T. Scheffen-Lauenroth, (1988), J. Appl. Cryst., **21**, 406.

[21] D. Hohlwein, D.P. Siddons and J.B. Hastings, (1988), J. Appl. Cryst., **21**, 911.

[22] S.R. Stock, Y.H. Chung and Z.U. Rek, (1989), J. Appl. Cryst., **22**, 70.

[23] B.K. Tanner and J.K. Cringean, (1987), Prog. Cryst. Growth and Charact., **14**, 403.

[24] S. Tohno, S. Shinoyama, A. Katsui and H. Takaoka, (1985), J. Crystal Growth, North-Holland, Amsterdam, **73**, 190.

[25] B.K. Tanner, M. Safa, D. Midgley and J. Bordas, (1976), J. Magnetism and Magnetic Materials, North-Holland, **1**, 337.

[26] M. Hart, (1975), J. Appl. Cryst., **8**, 436.

[27] Y. Chikaura, M. Imai and T. Ishikawa, (1987), Jap. J. Appl. Phys., **26**, L889.

[28] G.D. Yao, J. Wu, M. Dudley, V. Shastry and P. Anderson, (1991), Mat. Res. Soc. Symp. Proc., **209**, 707.

[29] J. Baruchel, *Synchrotron radiation topography : Present Achievements, and Prospects at the ESRF*, ESRF Publication, Dec. 1990.

[30] Y. Epelboin, A. Jeanne-Michaud and A. Zarka, (1979), J. Appl. Cryst., **12**, 201.

[31] S. Mardix, (1974), J. Appl. Phys., **45**, 5103.

[32] A. Segmüller, IBM J. Res. Develop., Nov. 1968, p.448.

[33] Y. Nanishi, S. Ishida and S. Miyazawa, (1983), Jap. J. Appl. Phys., **22**, L54.

[34] R.N. Pangborn, S. Weissmann and I.R. Kramer, (1981), Metallurgical Transactions A, **12**, 109.

[35] J. Auleytner, J. Bak, Z. Furmanik, M. Maciaszek and A. Saulewicz, (1980), Kristall und Technik, **15**, 3.

[36] M.P. Scott, (1985), *Defect Recognition and Image Processing in 3-5 Compounds*, (ed. J.P. Fillard), Elsevier, Amsterdam, p.41.

[37] T. Abe and J.H. Matlock, *Solid State Technology*, Nov. 1990, p.39.

[38] E.S. Meieran, (1980), *Characterization of Crystal Growth Defects by X-ray Methods*, (ed. B.K. Tanner and D.K. Bowen), Plenum, New York, p.1.

[39] R. Falster and W. Bergholz, (1990), J. Electrochem. Soc., **137**, 1548.

[40] S. Hahn, C.Y. Tung, J. Lee, T. Tuomi and J. Partanen, (1988), Mat. Res. Soc. Symp. Proc., **105**, 103.

[41] D. Tänzer, C. Hansch, R. Bertoldi, H. Richter, S. Lingel, H. Möhr and J. Godau, (1985), Materials Letters, Elsevier, North-Holland, **3**, 478.

[42] M.v. Laue, W. Fridrich and P. Knipping, (1913), Ann. Physik., **41**, 971.

[43] C. Darwin, (1914), Phil. Mag., **27**, 315.

[44] P.P. Ewald, (1916), Ann. Physik., **49**, 117.

[45] M.v. Laue, (1931), Ergeb. Exact. Naturw., **10**, 133.

[46] Z.G. Pinsker, (1978), *Dynamical Scattering of X-rays in Crystals*, Springer-Verlag.

[47] R.W. James, (1948), *The Optical Principles of the Diffraction of X-rays*, Bell.

[48] M. Hart, (1980), *Characterization of Crystal Growth Defects by X-ray Methods*, (ed. B.K. Tanner and D.K. Bowen), Plenum, New York, p.216.

[49] B.W. Batterman and H. Cole, (1964), Rev. Mod. Phys., **36**, 681.

[50] R.D. Heidenreich, (1942), Phys. Rev., **62**, 291.

[51] J.M. Cowley and A.F. Moodie, (1957), Acta Cryst., **10**, 609.

[52] P. Hirsch, A. Howie and M.J. Whelan, (1960), Trans. Roy. Soc. A, **252**, 499.

[53] A. Howie and M.J. Whelan, (1961), Proc. Roy. Soc. A, **263**, 217.

[54] A. Howie and M.J. Whelan, (1962), Proc. Roy. Soc. A, **267**, 206.

[55] S. Takagi, (1962), Acta Cryst., **15**, 1131.

[56] S. Takagi, (1969), J. Phys. Soc. Jpn., **26**, 1239.

[57] D. Taupin, (1964), Bull. Soc. Fr. Min. Crist., **87**, 469.

[58] Y. Epelboin, (1985), Materials Science and Engineering, **73**, 1.

[59] Y. Epelboin, (1987), Prog. Crystal Growth Charact., **14**, 465.

[60] T. Uragami, (1969), J. Phys. Soc. Jpn., **27**, 147.

[61] F. N. Chuhkovskii, (1974), Sov. Phys. - Crystallogr., **19**, 301.

[62] F. N. Chukhovskii and P. V. Petrashen, (1977), Acta Cryst., **A33**, 311.

[63] F. N. Chukhovskii, K. T. Gabryelyan and P. V. Petrashen, (1978), Acta Cryst., **A34**, 610.

[64] A. Authier, C. Malgrange and M. Tournarie, (1968), Acta Cryst., **A24**, 126.

[65] C. Nourtier and D. Taupin, (1981), J. Appl. Cryst., **14**, 432.

[66] P. V. Petrashen, (1976), Fiz. Tverd. Tela, **18**, 3729.

[67] Y. Epelboin, (1981), Acta Cryst., **A37**, 132.

[68] Y. Epelboin, (1983), Acta Cryst., **A39**, 761.

[69] F. Balibar and A. Authier, (1967), Phys. Stat. Sol. (a), **21**, 413.

[70] J. C. Brice, (1965), *The Growth of Crystals from the Melt,*, Vol. 5 - *Selected Topics in Solid State Physics*, (ed. E. P. Wohlfarth), North-Holland.

[71] D. J. J. Hurle, (1973), *Crystal Growth : an Introduction*, (ed. P. Hartman), North-Holland/Elsevier, p. 210.

[72] K. Hoshi, N. Isawa, T. Suzuki and Y. Okhubo, (1985), J. Electrochem. Soc., **132**, 693.

[73] Z. H. Mai, Z. X. Mao, S. F. Cui, C. Y. Wang, L. S. Wu, H. Li, G. X. Chen, S. R. Zhou and S. Ye, *International Conference on Science and Technology of Defect Control*, Sept. 1989, Japan.

[74] Z. X. Mao, Z. H. Mai, S. R. Zhou and S. Ye, (1989), Chinese Phys. Lett., Science Press, Beijing, Springer-Verlag, **6**, 507.

[75] K. Hoshikawa, (1982), Japan J. Appl. Phys., **21**, L545.

[76] W. Kaiser, P. H. Keck and C. F. Lange, (1956), Phys. Rev., **101**, 1264.

[77] J. W. Corbett, R. S. McDonald and G. D. Watkins, (1964), J. Phys. Chem. Solids, Pergamon Press, **25**, 873.

[78] W. L. Bond and W. Kaiser, (1960), J. Phys. Chem. Solids, Pergamon Press, **16**, 44.

[79] W. Kaiser, (1957), Phys. Rev., **105**, 1751.

[80] K. W. Böer, (1990), *Survey of Semiconductor Physics*, Vol. 1, Van Nostrand Reinhold, New York, p. 431.

[81] H. Furuya, I. Suzuki, Y. Shimanuki and K. Murai, (1988), J. Electrochem. Soc., **135**, 677.

[82] Y. Shimanuki, H. Furuya and I. Suzuki, (1989), J. Electrochem. Soc., **136**, 2058.

[83] S. Gupta, S. Messoloras, J. R. Schneider, R. J. Stewart and W. Zulehner, (1991), J. Appl. Cryst., **24**, 576.

[84] W. Bergholz, J. L. Hutchison and P. Pirouz, (1985), J. Appl. Phys., **58**, 3419.

[85] J. R. Patel, (1973), J. Appl. Phys., **44**, 3903.

[86] H. Bender, (1984), Phys. Stat. Sol. (a), **86**, 245.

[87] J. Partanen, T. Tuomi and K. Katayama, (1992), J. Electrochem. Soc., **139**, 599.

[88] F. S. Ham, (1958), J. Phys. Chem. Solids, **6**, 335.

[89] C. P. Flynn, (1972), *Point Defects and Diffusion*, Clarendon Press, Oxford.

[90] K. Wada, N. Inoue and K. Kohra, (1980), J. Crystal Growth, **49**, 749.

[91] K. Wada, H. Nakanishi, H. Takaoka and N. Inoue, (1982), J. Cryst. Growth, **57**, 535..

[92] F. Agullo-Lopez, C. R. A. Catlow and P. D. Townsend, (1988), *Point Defects in Materials*, Academic Press, p. 39.

[93] S. Messoloras, R. C. Newman, R. J. Stewart and J. H. Tucker, (1987), Semicond. Sci. Technol., **2**, 14.

[94] M. J. Binns, W. P. Brown, J. G. Wilkes, R. C. Newman, F. M. Livingston, S. Messoloras and R. J. Stewart, (1983), Appl. Phys. Lett., **42**, 525.

[95] W. Patrick, E. Hearn, W. Westdorp and A. Bohg, (1979), J. Appl. Phys., **50**, 7156.

[96] K. H. Yang, H. F. Kappert and G. H. Schwuttke, (1978), Phys. Stat. Sol. (a), **50**, 221.

[97] W. Bergholz, M. J. Binns, G. R. Booker, J. C. Hutchison, S. H. Kinder, S. Messoloras, R. C. Newman, R. J. Stewart and J. G. Wilkes, (1989), Phil. Mag. B, **59**, 499.

[98] J. D. Eshelby, (1956), *Solid State Physics - Advances in Research and Applications*, (ed. F. Seitz and D. Turnbull), Academic Press, New York, p. 79.

[99] C. Teodosiu, (1982), *Elastic Models of Crystal Defects*, Springer-Verlag, p. 287.

[100] G. G. Green, N. Loxley and B. K. Tanner, (1991), J. Appl. Cryst., **24**, 304.

[101] G. S. Green, S. F. Cui and B. K. Tanner, (1990), Phil. Mag. A, **61**, 23.

[102] S. F. Cui, G. S. Green and B. K. Tanner, (1989), Mat. Res. Soc. Symp. Proc., **139**, 71.

[103] M. Lefeld-Sosnowska, J. Gronkowski and A. Andrejczuk, (1988), Proc. 8th Int. Sch. on Defects in Crystals, World Scientific Press, p. 91.

[104] A. J. Holland, G. S. Green, B. K. Tanner and Z. H. Mai, (1991), Mat. Res. Soc. Symp. Proc., **209**, 475.

[105] S. F. Cui, Z. H. Mai and L. Z. Qian, (1984), Scientia Sinica, **A27**, 213.

[106] Z. H. Mai, S. F. Cui, J. Lin and Y. Lu, (1984), Acta Phys. Sinica, **33**, 922.

[107] E. S. Meieran and I. A. Blech, (1972), J. Appl. Phys., **43**, 265.

[108] N. Kato, (1963), J. Phys. Soc. Jpn., **18**, 1785.

[109] N. Kato, (1964), J. Phys. Soc. Jpn., **19**, 67.

[110] M. Hart, (1966), Z. Phys., **189**, 269.

[111] G. E. White and H. Chen, (1984), Materials Lett., **2**, 347.

[112] G. S. Green and B. K. Tanner, (1987), Inst. Phys. Conf. Ser. No. 87: Section 9, I. O. P. Publishing Ltd., 627.

[113] F. N. Chukhovskii and P. V. Petrashen, (1975), Sov. Phys. J. E. T. P., **42**, 243.

[114] T. Tuomi, S. Hahn, M. Tilli, C. C. D. Wong and O. Borland, (1986), Mat. Res. Soc. Symp. Proc., **71**, 47.

[115] T. Tuomi, M. Tilli and O. Anttila, (1985), Mat. Res. Soc. Symp. Proc., **41**, 101.

[116] J. R. Patel, (1964), Discuss. Faraday Soc., **38**, 201.

[117] F. Seitz, (1950), Phys. Rev., **79**, 723.

[118] L. Fiermans and J. Vennik, (1967), Phys. Stat. Sol. (a), **21**, 627.

[119] L. Fiermans and J. Vennik, (1967), Phys. Stat. Sol. (a), **22**, 463.

[120] S. M. Hu and M. R. Poponiak, (1972), J. Appl. Phys., **43**, 2067.

[121] T. Y. Tan and W. K. Tice, (1976), Phil. Mag., **34**, 615.

[122] D. M. Maher, A. Staudinger and J. R. Patel, (1976), J. Appl. Phys., **47**, 3813.

[123] W. K. Tice and T. Y. Tan, (1976), Appl. Phys. Lett., **28**, 564.

[124] T. Y. Tan, E. E. Gardner and W. K. Tice, (1977), Appl. Phys. Lett., **30**, 175.

[125] P. Bai, G. R. Yang and T. M. Lu, (1990), J. Appl. Phys., **68**, 3313.

[126] A. Ourmazd and W. Schröter, (1984), Appl. Phys. Lett., **45**, 781.

[127] W. K. Tice and T. Y. Tan, (1981), Mat. Res. Soc. Symp. Proc., **2**, 367.

[128] K. Graff, (1989), Materials Science and Engineering, **B4**, 63.

[129] T. A. Baginski and J. R. Monkowski, (1986), J. Electrochem. Soc., **133**, 762.

[130] L. Rivaud, C. N. Anagnostopoulos and G. R. Erikson, (1988), J. Electrochem. Soc., **135**, 437.

[131] G. A. Adegboyega and A. Poggi, (1990), Phys. Stat. Sol. (a), **121**, 181.

[132] D. Gilles, E. R. Weber and S. Hahn, (1990), Phys. Rev. Lett., **64**, 196.

[133] K. Graff, H. A. Hefner and W. Hennerici, (1988), J. Electrochem. Soc., **135**, 952.

[134] W. Wijaranakula, J. H. Matlock and H. Mollenkopf, (1988), J. Electrochem. Soc., **135**, 3113.

[135] V. V. Batavin, (1967), Sov. Phys. - Solid State, **8**, 2478.

[136] D. Maroudas and R. A. Brown, (1991), Mat. Res. Soc. Symp. Proc., **209**, 597.

[137] J. T. Yue and H. J. Ruiz, (1977), Electrochem. Soc. Ex. Abs., **77-1**,535.

[138] A. Bourret, J. Thibault-Desseaux and D. N. Seidman, (1984), J. Appl. Phys., **55**, 825.

[139] P. Kidd, D. J. Stirland and G. R. Booker, (1990), Materials Lett., **9**, 521.

[140] B. K. Tanner, (1984), Phil. Mag. A, **49**, 435.

[141] E. J. Kramer and C. L. Bauer, (1967), Phil. Mag., **15**, 1189.

[142] S. A. Ivanov, A. L. Kolesnikova and A. E. Romanov, (1982), Phys. Stat. Sol. (a), **73**, K31.

[143] I. A. Blech and E. S. Meieran, (1967), J. Appl. Phys., **38**, 2913.

[144] J. E. A. Miltat and D. K. Bowen, (1975), J. Appl. Cryst., **8**, 657.

[145] I. Fabian, E. K. Pal and T. Kormany, (1992), Semicond. Sci. Technol., **7**, A163.

[146] S. Isomae, Y. Tamaki, A. Yajima, M. Nanba and M. Maki, (1979), J. Electrochem. Soc., **126**, 1014.

[147] M. Tamura and H. Sunami, (1972), Japan J. Appl. Phys., **8**, 1097.

[148] K. Haruta and W. J. Spencer, (1966), J. Appl. Phys., **37**, 2232.

[149] G. H. Schwuttke and J. K. Howard, (1968), J. Appl. Phys., **39**, 1581.

[150] J. R. Patel and N. Kato, (1968), Appl. Phys. Lett., **13**, 40.

[151] N. Kato and J. R. Patel, (1968), Appl. Phys. Lett., **13**, 42.

[152] N. Kato and J. R. Patel, (1973), J. Appl. Phys., **44**, 965.

[153] J. R. Patel and N. Kato, (1973), J. Appl. Phys., **44**, 971.

[154] Y. Ando, J. R. Patel and N. Kato, (1973), J. Appl. Phys., **44**, 4405.

[155] G. Filscher, (1976), Phys. Stat. Sol. (a), **33**, K81.

[156] P. V. Petrashen and I. L. Shulpina, (1983), Phys. Stat. Sol. (a), **78**, K105.

[157] S. M. Hu, (1979), J. Appl. Phys., **50**, 4661.

[158] *C.R.C. Handbook of Chemistry and Physics*, (1988), 69th edn., C.R.C. Press.

[159] *Gmelins Handbuch der Anorganischen Chemie*, (1959), Set B, vol. 15, Verlag-Chemie.

[160] S. Isomae, (1981), J. Appl. Phys., **52**, 2782.

[161] Y. Epelboin, (1988), J. Appl. Phys., **64**, 109.

[162] S. P. Timoshenko and J. N. Goodier, (1970), *Theory of Elasticity*, McGraw-Hill, New York.

[163] N. Loxley, (1988), Ph.D. Thesis, Durham University.

[164] M. W. Dellow, P. H. Beton, M. Henini, P. C. Main and L. Eaves, (1991), Electronics Lett., **27**, 134.